Universitat Autònoma de Barcelona

Centre Nacional de Microelectrònica IMB

CSIC Consejo Superior de Investigaciones Científicas

Doctorado en Ciencia de Materiales
Departamento de Física

TESIS DOCTORAL 2015

ENZYMATIC MICROFLUIDIC FUEL CELLS: FROM ACTIVE TO PASSIVE POWER SOURCES

MªJosé González Guerrero

Directores

Neus Sabaté Vizcarra

F. Javier del Campo García

Tutor

Javier Rodríguez Viejo

El presente trabajo titulado ***Enzymatic Microfluidic Fuel Cells: From Active to Passive Power Sources*** ha sido realizado por Mª José González Guerrero para optar al título de Doctora en Ciencia de Materiales por la Universidad Autónoma de Barcelona, dentro del grupo *Microenergy Sources and Sensors* del Instituto de Microelectrónica de Barcelona, IMB-CNM (CSIC). Dicha tesis doctoral se ha llevado a cabo bajo la dirección de la Dr. Neus Sabaté Vizcarra y el Dr. F. Javier del Campo García del Instituto de Microelectrónica de Barcelona, IMB-CNM (CSIC), así como bajo la tutela del Dr. Javier Rodríguez Viejo del departamento de Física de la Universidad Autónoma de Barcelona.

Bellaterra, Cerdanyola del Vallès

Octubre, 2015

Dr. Neus Sabaté Vizcarra Dr. F. Javier del Campo García Dr. Javier Rodriguez Viejo

Contents

3. PLASTIC-BASED MICROFLUIDIC BIOFUEL CELL

4. PAPER-BASED MICROFLUIDIC BIOFUEL CELL

5. PAPER-BASED MICROFLUIDIC BIOFUEL CELL FUNCTIONING FOR IN-VITRO APPLICATIONS AT PHYSIOLOGICAL CONDITIONS

CHAPTER

1

Introduction

An increasing societal demand for portable devices capable of operating for extended periods without recharging has resulted in a surge of investigation in the development of miniaturized power sources [1-2]. In the last fifteen years, micro fuel cells have been considered possible power sources for applications ranging from portable computing and communication systems (cell phones, laptop computers, personal organizers) to MEMS devices (small integrated biosensors for diagnostic tests or global positioning devices) [3-4]. To date, research on microfuel cells has addressed mostly miniaturization of their functional components leaving long lifetime issues of these power sources as one of the major challenges [1].

1.1 BIOFUEL CELLS

Fuel cells are electrochemical devices that convert chemical energy to electrical energy. One electrode (anode) facilitates electrochemical oxidation of a fuel, while the other (cathode) promotes electrochemical reduction of oxidant an [5]. The oxidation releases electrons, which travel to the cathode via an external circuit - and thus realizing electrical work - and completing the reduction reaction once reaching the cathode. A catalyst, such as platinum, is often used to speed up the reactions at the electrodes. The circuit is closed by the movement of a compensating charge through the electrolyte often in the form of positive ions [6]. The electrolyte also serves as an effective separator of the anode and cathode cells reactions as it prevents mixing of electrolytes or fuels from the anodic and the cathodic compartments. The region of contact of the electrolyte, the electrode and the fuel is called the triple phase boundary (TPB) and it is where the electrochemical reactions of the fuel cell take place [7]. Therefore, a high performing fuel cell electrode should have a large TPB area. For this reason, fuel cell electrodes are usually porous (in order to guarantee fuel access to the active sites) and highly conductive (so electrical current flows with minimal loss) to increase the cell performance. A basic scheme of a H_2-O_2 fuel cell is shown in figure 1.1 (a) whereas the reactions occurring are the TPB are depicted in figure 1.1 (b).

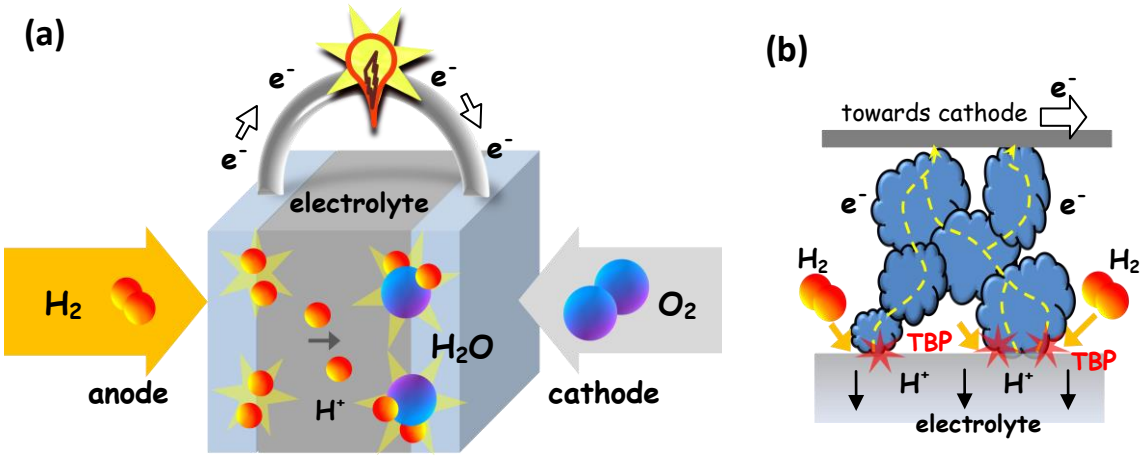

Figure 1.1 (a) Schematic representation of the main parts and the operating process in a fuel cell. (b) Representations of the triple phase boundary (TPB) zones (in red color) for a an electronic conductor in contact with an electrolyte showing the movement of protons from the TPB to the anode through the electrolyte side and the movement of the electrons produced in the TPB toward the cathode.

Fuel cells can process a wide variety of fuels and oxidants, although most reported fuels are natural gas (and derivatives) and hydrogen, while the most used oxidant is oxygen form air [8]. However, it is frequent to classify fuel cells according to the nature of the electrolyte used. Generally, this classification determines the kind of electrochemical reactions taking place in the cell, the type of catalysts required, the temperature range in which the cell operates and the fuel among other factors. Based on this, fuel cells are classified as: (i) alkaline fuel cells (AFC) that use an alkaline solution electrolyte (such as potassium hydroxide, KOH), (ii) phosphoric acid fuel cells (PAFC) with acidic solution electrolyte (such as phosphoric acid), (iii) solid proton exchange

membrane fuel cells (PEMFC) that are based on a polymer electrolyte membrane, (iv) molten carbonate fuel cells (MCFC) with molten carbonate salt electrolyte and (v) solid oxide fuel cells (SOFC) that generally use a ceramic ion conducting electrolyte in solid oxide form [9]. Table 1.1 lists the various types of fuel cells along with the most important characteristics.

	AFC	PAFC	PEMFC	MCFC	SOFC
Mobile ion	OH^-	H^+	H^+	CO_3^{2-}	O^{2-}
Operating temperature	50-200 °C	≈200 °C	30-100 °C	≈650 °C	500-1000 °C
Electrolyte	Potassium hydroxide	Phosphoric acid	Solid proton conducting polymer	Molten carbonate	Ceramic
Catalyst	Pt, Pt/Au, Ag	Pt, Pt/Ni	Pt, Pt/Ru	Ni, Ni/Cr	Ni/ZrO_2
Applications	Submarine, spaceships	Power station, 200kW CHP systems	Vehicles, mobile applications, low power CHP systems	Power station, up to MW CHP systems	Power station, 2kW to MW
References	[10]	[11]	[12]	[13]	[14]

Table 1.1 Principle properties of five main types of conventional fuel cells.

Among portable fuel cells, PEMFC is considered to be the most promising technology. They generally possess low weight and volume compared with other fuel cells. They operate at relatively low temperatures (25-80 °C), offer quick start-up times and the polymeric electrolyte reduces corrosion and electrolyte management problems. [15]. Hydrogen can be fed to the fuel cell system directly or can be generated within the fuel cell system by reforming hydrogen-rich fuels such as methanol, ethanol, and hydrocarbon fuels [16]. In any case, hydrogen is difficult to store in sufficient quantity within small and lightweight containers, compromising the portability and operational longevity of PEMFC. In this sense, the use of liquid fuels avoids the difficulties associated to the H_2 storage and handling. Therefore, direct alcohol fuel cells (DMFCs), which are powered by methanol or ethanol, are an attractive alternative to overcome the hydrogen issues restrictions [17]. In this direction, direct alcohol fuel cells have been extensively studied and considered as possible power production systems for portable electronic devices. However, because of the high cost of platinum-based catalysts, a number of research groups have oriented their efforts mainly towards the development: a) of low or non platinum electrocatalysts (anodes and cathodes) and b) of nanostructured electrocatalysts based on non-noble metals [18]. In this respect, biological fuel cells (BFC) have drawn significant attention due to their unique advantages over metal-based conventional fuel cells. In these fuel cells, the metal catalyst is replaced by a biological catalyst (bacteria, enzyme) which makes them extremely cost-effective [6, 19-22]. Moreover, they are considered more environmental friendly compared with traditional chemical fuel cells, because they use sustainable energy sources such as sugars and alcohols. In this sense, the fuel substance can be selected from a wide range of organic sources as there is a large variety

of reactions that can be promoted with properly selected biocatalysts. This is in contrast to fossil fuel and organic solvent fuel sources that are non-renewable and potentially harmful to the environment. BFCs can work under ambient temperature and atmospheric pressure conditions and they generally utilize neutral electrolyte. These features make these devices extremely easy to operate.

Metal-based fuel cells generate power ranging from a few watts to several hundreds of megawatts, whereas to date, BFCs have been shown to produce a few hundred microwatts at most (see figure 1.2). The difference between the power output of traditional fuel cells and BFCs is represented as the *credibility gap* [6], which is the power improvement that these devices have to experience to be considered competitive; it is estimated that BFCs will need to increase power production up to 10 mW to bridge this so-called *credibility gap* of power generation [23]. Consequently, many research groups are currently devoted to increase the power output and current density of BFC systems.

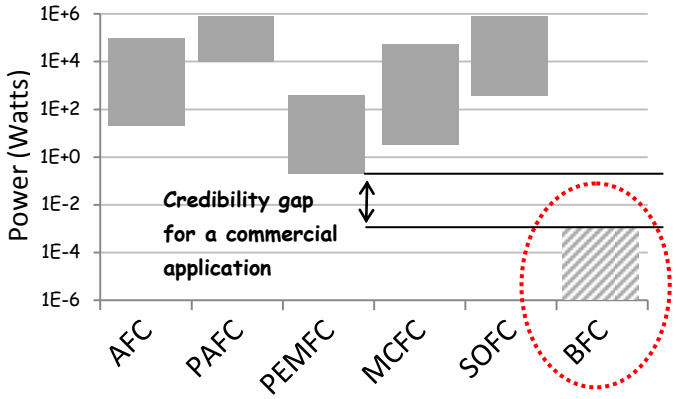

Figure 1.2 Range of power application of different conventional fuel cells and biological fuel cells showing the credibility gap between both technologies.

Although today the power output of BFC is not large enough for many portable applications, they can be suited to supply energy to devices only needing power in the few mili or microwatt range. This includes devices such as pacemakers, hearing aids, drug delivery systems and many more [24]. Indicative power consumption of some of these devices is depicted in figure 1.3.

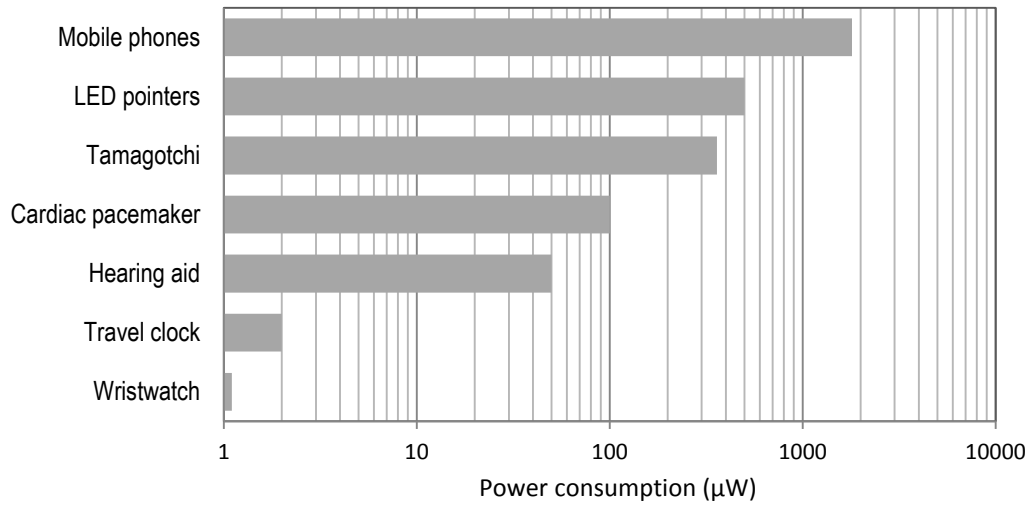

Figure 1.3 Graphic of power consumption of various small electronic devices [25-26].

There are two types of biological fuel cells, namely *microbial* fuel cells and *enzymatic* fuel cells, depending on the biocatalysts used. Microbial fuel cells (MFCs) use whole living organisms whereas enzymatic biofuel cells (EFCs) manage isolated and purified enzymes. EFCs yield significantly higher power densities than MFCs [27], which makes them more attractive to power small electronic devices. The use of single enzymes (or enzyme cascades) allow to have defined reaction pathways on the electrode surface and to overcome the limited output performance of MFCs, which is thought to be due to mass transfer resistance across the cellular membrane [23]. Moreover, unlike MFCs, EFCs do not require nutrients or biomass acclimation so the electrochemical process occurring in the fuel cell can be easily controlled. Consequently, they are simpler to engineer into a miniaturized system [28]. Yet, enzymes cannot compete with microbes in terms of long-term stability and complete oxidation of the biofuel [29], which are the main hurdles for EFCs to reach the market.

1.2 ENZYMATIC BIOFUEL CELLS

In enzymatic fuel cells, organic fuels and oxygen are converted into electrons, CO_2 and/or oxidized fuel by-products and water [19, 30-33]. Enzymes have the added advantage of specificity, which in some cases eliminates the need for a membrane between anolyte and catholyte solutions [27]. In figure 1.4 a basic structure of a membraneless enzymatic fuel cell is shown. Anode and cathode are both immersed in a single electrolyte solution. At the anode, a specific enzyme catalyzes fuel oxidation, while at the cathode the enzyme catalyzes the reduction of the oxidant.

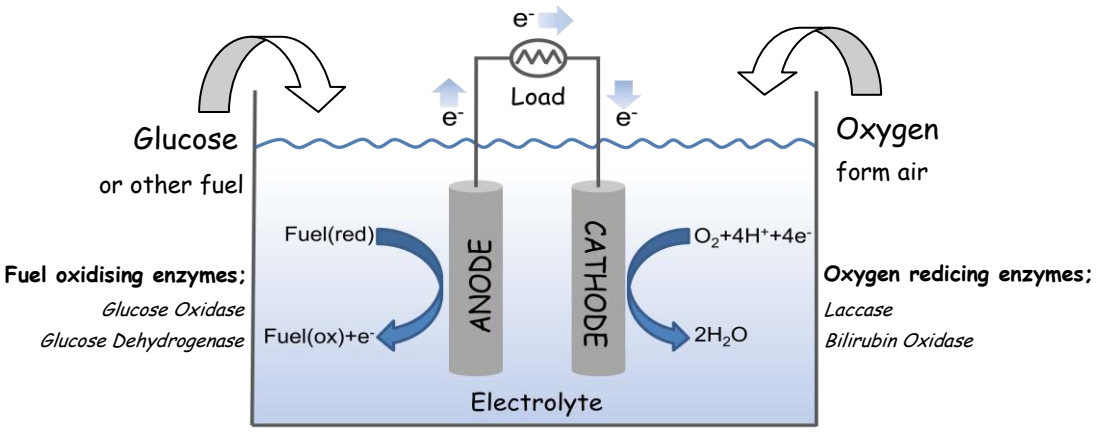

Figure 1.4 General scheme of an enzymatic fuel cell. At the anode the oxidation of the fuel is catalyzed by oxidase enzymes suitable for conversion of the fuel of choice. For the cathode, the oxygen reduction usually features oxidoreductase enzymes that use molecular oxygen as the ultimate electron acceptor and catalyzes the reduction of O_2 to water.

Fuel-oxidant configurations reported in the literature are: glucose/O_2, fructose/O_2, lactose/O_2, methanol/O_2, ethanol/O_2, glycerol/O_2, pyruvate/O_2, glucose/H_2O_2, and ethanol/H_2O_2. However, **glucose/O_2 enzymatic fuel cell** is the most commonly described [34]. Glucose possesses high energy density, 2805 kJ mol^{-1} if glucose is oxidized to carbon dioxide, that is to say ≈ $16 \cdot 10^6$ J kg^{-1} and ≈ 5 kWh kg^{-1} of electrical energy [35]. Glucose has gained so much interest with respect to other candidates because it is highly abundant in nature, it is an important metabolic intermediate and a key source of energy for most living organisms. In fact, glucose and oxygen play an essential role in human metabolism. This allows to envisage the possibility of using glucose-based fuel cells to feed devices for in-vivo applications (peacemakers, active implants, etc) [36]. Oxygen is an excellent oxidant, it has a high reduction potential, it is widely available [33] and it is essential for the respiration in all aerobic organisms.

Theoretically, the oxidation of one molecule of glucose at the anode liberates 24 electrons if it is completely oxidized to CO_2 (equation 1.1):

$$C_6H_{12}O_6 + 6H_2O \rightarrow 6CO_2 + 24H^+ + 24e^- \quad \textbf{(1.1)}$$

However, in practice only a partial oxidation of the glucose takes place and the number of electrons obtained from the anodic reaction are two (equation 1.2). The reduction of O_2 to water [22, 37] is shown in equation 1.3 together with the overall reaction in equation 1.4 [38]:

$$\text{Anode:} \quad C_6H_{12}O_6 \rightarrow C_6H_{10}O_6 + 2H^+ + 2e^- \quad \textbf{(1.2)}$$

$$\text{Cathode:} \quad {}^1/_2\, O_2 + 2H^+ + 2e^- \rightarrow H_2O \quad \textbf{(1.3)}$$

$$\text{Overall:} \quad C_6H_{12}O_6 + {}^1/_2\, O_2 \rightarrow C_6H_{10}O_6 + H_2O \quad \textbf{(1.4)}$$

1.2.1 Enzymatic electron transfer processes

A key issue in the development of enzymatic biofuel cells is to ensure that there is an efficient electron transfer between the enzyme – which oxidizes or reduces a particular molecule - and the electrode – which is responsible of collecting or supply electrons from or to the catalytic reactions. Enzymes are proteins with a complex three-dimensional structure. They consist of an apoenzyme (the protein component of an enzyme) and the cofactor or active site [39]. The cofactor is the location where the electron transfer with the fuel or oxidant takes place. When an enzyme is capable of transferring electrons directly to the electrode surface of the fuel cell the process is termed direct electron transfer (DET) [29]. However, sometimes the active site is deeply buried inside the enzyme, giving rise to inefficient electron conduction between de redox centre of the enzyme and the conductive electrode support. In order to lower the electron transfer kinetic barrier, low-molecular-weight and redox active species called *mediators* are introduced in the system [27, 40-41]. In the anodic compartment of the fuel cell, mediators are reduced when they catch the electrons coming from fuel oxidation in the enzyme and they are oxidized upon the delivery of electrons to the electrode. After that, they are ready to accept electrons from the enzyme again. This redox cycle takes place also in the cathode but in the opposite way. The use of mediators result in a significant increase of the electron transfer rate between the active site of the enzyme and the electrode surface [23]. The process is called mediated electron transfer (MET) [22, 27, 42]. Compared with MET, DET systems are easier to implement and present advantages for implantable applications because they avoid use of mediators that can be potentially toxic for the human bpdy. However, although MET-based bioelectrodes preparation is more complex as they require additional species, MET is generally preferred over DET, because it generates higher output powers, often orders of magnitude larger than the direct mechanism [43]. In figure 1.5 the two enzymatic electron transfer processes are represented.

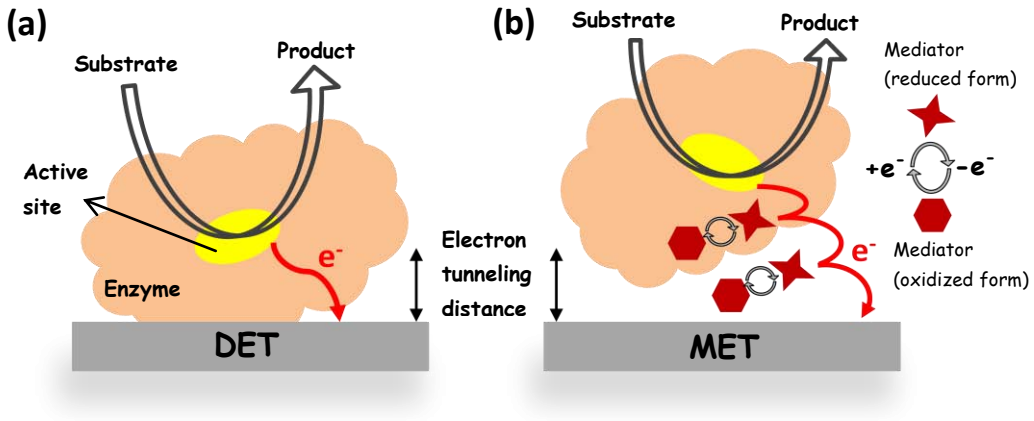

Figure 1.5 Scheme illustrating a simple arrangement for (a) direct electron transfer (DET) and (b) mediated electron transfer (MET), between the active site of an electrochemically-active enzyme and a solid electrode, during the oxidation of a substrate.

In MET-systems, the working potential of the electrodes is dominated by the redox potential of the mediator-enzyme couple. The operating potential of a biofuel cell comprising two such MET-electrodes will be primarily determined by the difference in redox potential of the mediator couples placed at both electrodes. In principle, mediators should be selected taking into account three factors; i) the redox potential of the mediator molecule should be thermodynamically favorable with respect to the enzyme redox potential [44] and ii) the electron transfer rate of the couple enzyme-mediator should be high enough to produce large currents, this means that the mediator should be able to react rapidly with the reduced enzyme or coenzyme and (iii) they should exhibit reversible behaviour. [45]. Furthermore, the mediator should have stable oxidized and reduced forms, and the reduced form should not react with oxygen in order to present crossover effects.

Osmium and ruthenium complexes, polypyrrole, phthalocyanines, organic dyes, and other molecules are the most used mediators in enzymatic devices [46]. Among them, osmium complexes are very attractive for enzymatic biofuel cells because by changing the substituent on the ligands of the complex, it is possible to modify their redox potential, which normally ranges from −0.17 to 0.79 vs Ag/AgCl [43]. This broad voltage range makes them suitable both for anode and cathode processes. Nevertheless, the toxicity of some Os-mediators limits their utilization as in the case of medical implant applications [47].

1.2.2 Anode for glucose oxidation

Among the enzymes performing the oxidation of glucose, glucose oxidase GOx is the most widely used [48]. Glucose oxidase is composed of two identical subunits, each one carrying one molecule of a coenzyme called flavin adenine dinucleotide (FAD) [49-50]. FAD acts as an electron acceptor from the glucose and it is reduced to $FADH_2$ (equation 1.5). $FADH_2$ is then oxidized by the final electron acceptor (a mediator or the electrode itself). In this process, the conversion of glucose to gluconolactone, which spontaneously hydrolyzes to gluconic acid, takes place (see figure 1.6 (a)). The natural electron acceptor for GOx is molecular oxygen which is reduced to hydrogen peroxide (H_2O_2) - see equation 1.6. This means that in the presence of an oxygen atmosphere, GOx would rather transfer its electrons directly to oxygen than to the anode resulting in an overall decrease of the fuel cell oxidation current and an undesired production of H_2O_2. In the case of membraneless fuel cell configuration, using GOx may result in a diminution of the O_2 concentration available for reduction at the cathode; consequently the performance of the fuel cell can be also affected.

$$GOx(FAD) + glucose \rightarrow GOx(FADH_2) + gluconolactone \quad \textbf{(1.5)}$$

$$GOx(FADH_2) + O_2 \rightarrow GOx(FAD) + H_2O_2 \quad \textbf{(1.6)}$$

For these reasons, another enzyme that has been widely used in biofuel cell applications is glucose dehydrogenase, GDH. Unlike GOx enzyme, GDH does not donate electrons to oxygen [39, 51].

Glucose dehydrogenases are classified according to their redox cofactors: nicotinamide adenine dinucleotide (NAD), nicotine adenine dinucleotide phosphate (NADP), pyrroloquinoline quinone (PQQ) and FAD [39]. Each GDH cofactor owns special characteristics and must be selected depending on the specific application. For example, the PQQ-GDH presents broad substrate specificity (e.g. the presence of maltose in the sample along with glucose generates additional oxidation currents that leads to errors in certain glucose meters [52]). Interestingly, whereas FAD-GOxs are able to interact with oxygen, FAD-harboring GDHs are unable to utilize it, despite having the same redox cofactor and significant structural similarities with GOx [51-53]. Furthermore, GOx only oxidizes the α-form glucose, which is only 36% in the solution, while the rest is of β-form. FAD-GDH has the affinity towards both forms of glucose [54], which results in a higher oxidation current. For this reason, FAD-GDH has been selected to implement fuel cell anodes in this thesis.

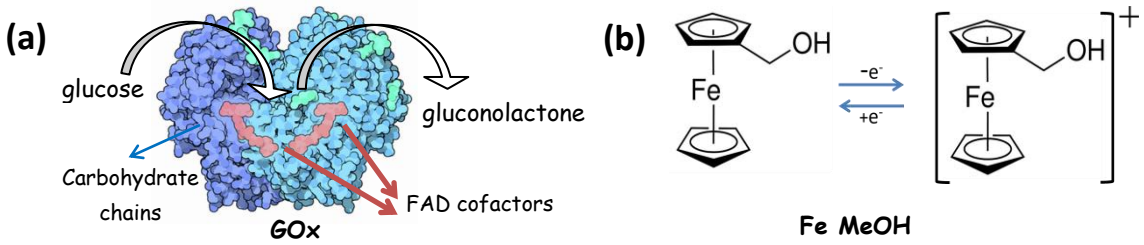

Figure 1.6 (a) Half view of GOx. The active sites are deep inside the shell and it is covered with carbohydrate chains [55]. (b) Sketch of the mono-electronic oxidation of ferrocenemethanol acting as mediator for GOx [56].

Under normal circumstances, DET between GOx or GDH and the electrode material is very slow because the catalytic centers for both enzymes are deeply buried inside the protein [57-58]. Even though systems employing GOx are typically mediated, it is possible to achieve DET using nanostructured electrodes [21, 59]. However, their power output is lower when compared with the fuel cells based on MET [40, 60]. In the case of the utilization of mediators, literature shows that ferrocene (redox potential of 0.2 V vs Ag/AgCl), their derivatives (figure 1.6 (b)) and quinone derivatives possess the desired characteristics to function as good electron acceptors for GOx [61]. Besides, azine dye-based mediators are employed for the GDH [29] whereas Os-based redox hydrogels have shown good performance for both enzymes.

1.2.3 Cathode for oxygen reduction

Multi-copper oxidases are one of the most reported enzymes for electro-reduction of oxygen to water. Examples include plant and fungal laccases and bilirubin oxidase (BOx) [62-63]. For fuel cell applications, laccases produced by fungi are preferred because reduction takes place at a higher potentials than with plant laccases [33]. Laccases from fungi present their highest activity at pH in

the region of 3-5, which makes them unsuitable for certain applications requiring pH close to neutrality. In contrast, BOx presents its highest activity at a higher pH, around 7 [21, 29].

The catalytic active site of multi-copper oxidases contains four metal copper ions, classified into three types; T1, T2, T3 [33, 64]. The four copper atoms are distributed in three redox sites (one in each T1 and T2 sites, and two in T3 site). Each redox site has a different function: type 1 catalyzes the electron transfer, type 2 activates molecular oxygen and type 3, is responsible for the oxygen uptake [65]. Therefore, catalysis in multi-copper oxidases involves T1-Cu reduction by an electron coming from the anode followed by internal electron transfer from T1-Cu to T2 and T3-Cu and finally, dioxygen reduction at T2 and T3 sites [66-69]. Figure 1.7 (a) shows a representation of a multi-copper oxidase enzyme with the catalytic active site formed by the four copper metal ions.

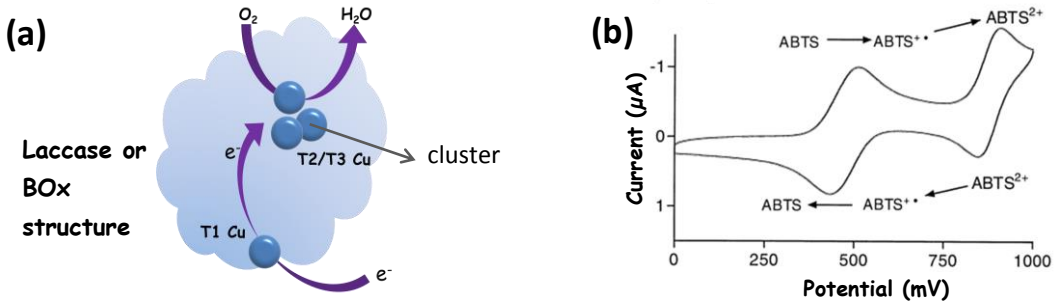

Figure 1.7 (a) Representation of a multi-copper oxidase enzyme with the four cooper ions responsible of the catalytic electro-reduction of oxygen to water. (b) Two step oxidation/reduction reaction of the mediator ABTS, taken from [70].

The mechanism of oxygen reduction of laccase and BOx can also be DET or MET. Direct electron transfer have been reported in the case of laccase adsorbed on carbon nanomaterials [71], carbon nanotubes [72], or carbon electrodes [73]. BOx, however, has been used on spectrographic graphite (SPG) [38]. In all cases, the mechanism of the DET reaction depends strongly on the type of supporting material [29]. Multi-copper oxidases using mediated electron transfer allow the utilization of a wide variety of mediators –always taking into account that the selected mediator presents a reduction potential between that of oxygen and the reduction potential of type I cooper of laccase or BOx [74]. Mediators for multicopper oxidases include Osmium-polymers and the mediator 2,2'-azino-bis(3-ethylbenzothiazoline-6-sulphonic acid (ABTS). ABTS - shown in figure 1.7 (b) - represents the most widely exploited mediator due to its high electron transfer rate [29].

1.2.4 Electrode performance characterization by cyclic voltammetry

Cyclic voltammetry (CV) is a simple and fast technique to evaluate the catalytic performance of a fuel cell, as it characterizes the processes occurring on its enzymatic-based electrodes. The most common configuration for running this electrochemical experiment involves the use of three

electrodes; the working electrode, a counter (auxiliary) electrode and a reference electrode, all connected to a potentiostat. The potentiostat applies a scanning voltage to the working electrode using a triangular potential wave form and the corresponding flow of current is monitored. This is used to evaluate independently the anode and the cathode of the biofuel cell. CVs are utilized to determine the electron transfer kinetics of the reactions occurring between enzymes, mediators and the solid electrode as the current versus voltage dependence measured in the working electrode can be directly related the electrochemical reaction rate. CV curves also enable the determination of the potentials where oxidation and reduction reaction occurs (redox potentials), which allow to predict the open circuit potential of the fuel cell.

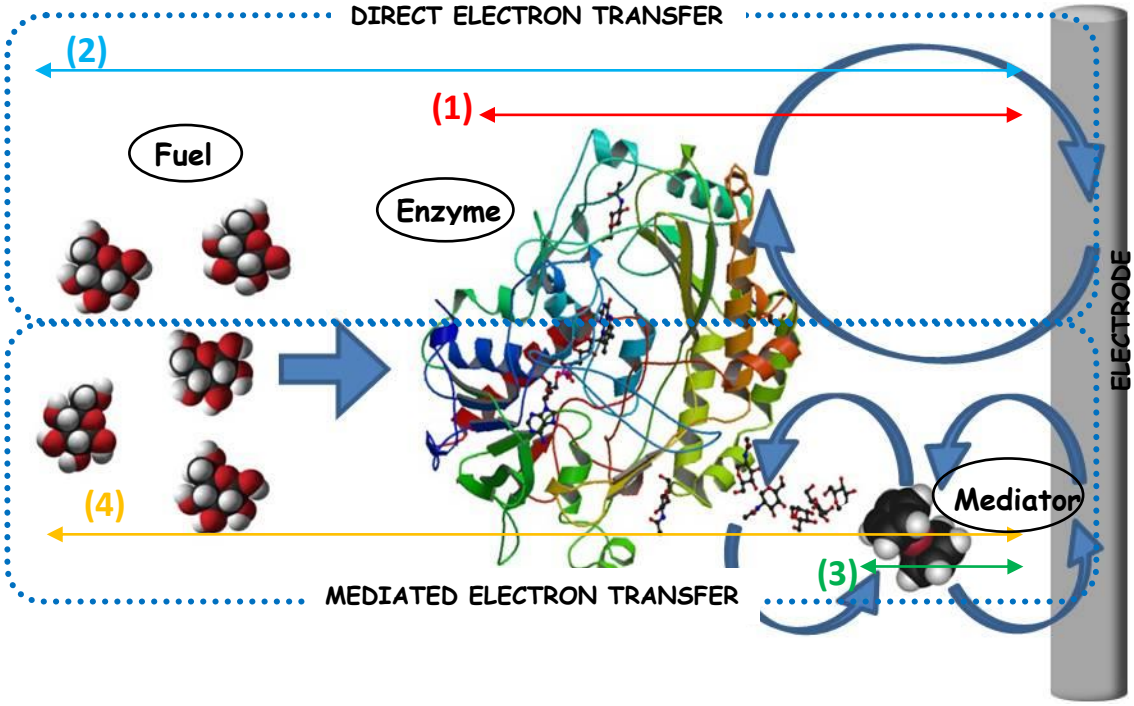

Figure 1.8 Oxidation of glucose by the enzyme glucose oxidase (and the mediator ferrocene) for DET (1 and 2) and MET reactions (3 and 4). The numbers indicate the species interacting with the electrode. (1) enzyme/electrode, (2) fuel/enzyme/electrode, (3) mediator/electrode and (4) fuel/enzyme/mediator/electrode.

Different shapes of voltammograms can be obtained while working with bioelectrodes depending on whether the enzyme is directly interacting with the electrode (DET) or it is the mediator the responsible for transferring the electrons to the conductive support (MET). The characteristics of the CV depend mainly on the rate of the electron transfer reaction taking place, the chemical reactivity of the electroactive species and on the scan rate, *v*.

As an example, figure 1.8 shows both kinds of electron transfer reactions for the specific case of glucose oxidation by the enzyme glucose oxidase when assisted with a ferrocene mediator. At the same time DET and MET are divided according to the species interacting with the electrode in: (1)

enzyme/electrode and (2) fuel/enzyme/electrode for DET, (3) mediator/electrode and (4) fuel/enzyme/mediator/electrode for MET.

The CVs of the different interactions within the electrode are depicted in figure 1.9 (numbers and its color are related to those of figure 1.8) and they are characterized generally by two current peaks and two potential positions corresponding to the oxidation and reduction reactions. For the case of the direct electron transfer (figure 1.9 (a)) two different voltammetric shapes can be observed. The first one, with red line, shows the GOx directly exchanging electrons with the electrode surface, case (1). Two peaks corresponding to the oxidation and reduction of the active site of the GOx (FAD/$FADH_2$) can be appreciated. In case (2), glucose is added into the electrolyte and the CV is changed giving an increase in current belonging to the oxidation of glucose. However, the magnitude of current (I_{ox}) is not very high because of the difficulty for GOx to performing DET with the electrode.

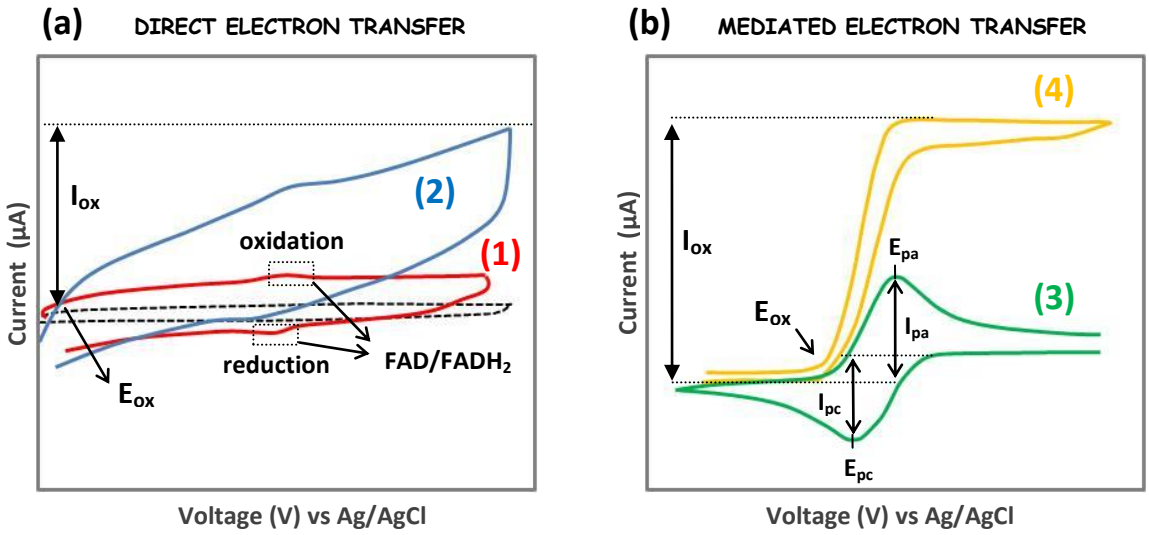

Figure 1.9 Cyclic voltammogram for (a) DET reaction between GOx/electrode, (1) in red, and glucose/GOx/electrode, (2) blue line, dotted line corresponds to a plain electrode and (b) MET electron transfer of mediator/electrode, (3) in green, and glucose/GOx/mediator/electrode, (4) yellow line.

Figure 1.9 (b) depicts the voltammetric curves commonly obtained in a MET process. Curve (3) shows the typical CV of an ideal reversible mediator with well-defined oxidation/reduction current peaks. One of the most interesting parameters that can be obtained from this reversible voltammogram is the peak current that follows the *Randles–Ševčik* equation [75-76]:

$$i_p = \pm 0.4463\, nFAC \left(\frac{nFD}{RT} v\right)^{1/2} \qquad \textbf{(1.7)}$$

where, $\pm$ indicate if it is an oxidative or reductive process, i_p the peak current (A), n is the number of electrons F is the Faraday's constant (96485 C mol^{-1}), R the universal gas constant (8.314 V C K^{-1} mol^{-1}), A is the electrode surface area of the working electrode (m^2), D is the diffusion coefficient

of the redox species ($m^2 \cdot s^{-1}$), *C* is the bulk concentration of the redox diffusing species ($mol \cdot m^{-3}$) and $v^{1/2}$ the voltage scan rate ($V \cdot s^{-1}$). Accordingly, the current of the redox mediator is directly proportional to concentration and increases with the square root of the scan rate, $v^{1/2}$. The ratio of the reverse-to-forward peak currents, I_{pa}/I_{pc} is 1 for a simple reversible couple. This peak ratio can be strongly affected by chemical reactions coupled to the redox process. The current peaks are commonly measured by extrapolating the preceding baseline current. The position of the peaks on the potential axis is related to the formal potential of the redox process. The formal potential, E^0, for a reversible couple is centered between E_{pa} and E_{pc}:

$$E^{0'} \approx \frac{E_{pa} + E_{pc}}{2} \quad \textbf{(1.8)}$$

The separation between the anodic and the cathodic peak potentials (for the case of reversibility) is:

$$\Delta E_p = E_{pa} - E_{pc} \quad \textbf{(1.9)}$$

where, ΔE_p can be used to as a criterion for a Nernstian behavior that should be approximately 59 mV (at 298 K and n=1) and will be independent of the applied scan rate [77-79]. When glucose is incorporated into the system, case (4), an enlargement in the oxidation current proportional to the glucose concentration can be observed, until the glucose saturation is reached. This is when the enzyme is working at its best rate. From the voltammogram potential at which glucose oxidation takes place (E_{ox}) can be easily extracted as well as the oxidation current (I_{ox}).

1.3 ENZYMATIC IMMOBILIZATION IN MINIATURIZED BIOFUEL CELLS

Although enzymatic fuel cells are a young technology, important progress has been made in the area where it is possible to distinguish between two types of cells, as represented in figure 1.10 and summarized in table 1.2. The first group represents the most simple configuration and it can be find those where bare electrodes are used and the enzyme catalysts flow in solution along with fuel and oxidant moieties, figure 1.10 (a) [80-81]. However, they were costly devices because enzymes were flowing inside the system. Then, the second group appeared with systems using bioelectrodes; that is, the catalytic enzymes are immobilized and/or electrically wired directly to the electrodes [30, 82]. At the same time they can be microfluidic, figure 1.10 (b), suitable for portable applications or non-microfluidic, figure 1.10 (c) appropriate in implantable devices.

Initial studies in the development of enzymatic biofuel cells attempted to produce current from enzyme solutions or suspensions allowing enzymes to freely diffuse in the anodic and cathodic compartment. These microfluidic fuel cells with enzymes in solution have been reported to yield significantly higher power densities than those featuring bioelectrodes (immobilized enzymes). Zebda et al. reported the generation of 0.5 mW cm^{-2} at 0.3 V for a fuel cell running with glucose/GOx and O_2/ABTS/laccase in solution at 0.3 ml min^{-1}. Nevertheless, the fuel cell

performance could be better if the system were not limited by the inefficiency of the electron transfer to the electrode surface because of convection and diffusion of the enzymes in the fuel solution [83]. Moreover, bioelectrode cells supply lower power densities, but are more cost effective to run because they require much smaller amounts of enzymes than fuel cells in the other group.

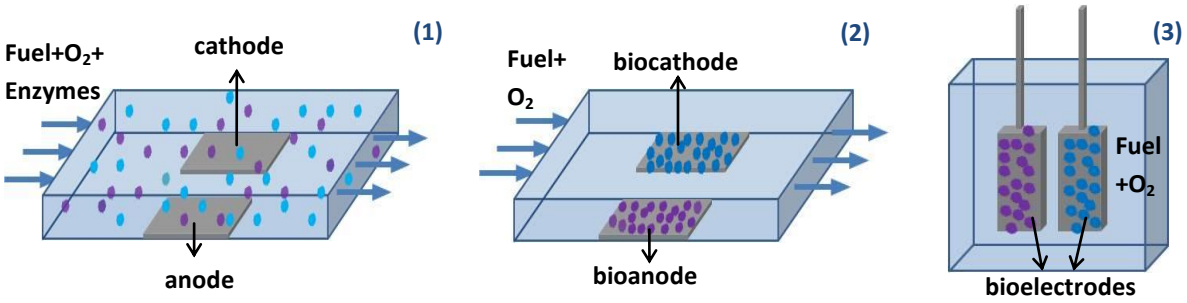

Figure 1.10 Representation of the different kinds of enzymatic fuel cells. (1) Flowing enzymes in solution. (2) Immobilized enzymes in flowing cells. (3) Immobilized enzyme in fuel reservoir.

Fuel Cell Type	Anode material	Anolyte	Cathode material	Catholyte	Flow rate ($\mu L\ min^{-1}$)	J_{max} ($\mu A\ cm^{-2}$)	P_{max} (μWcm^{-2})	Ref.
(1) Flowing enzymes in solution	Gold	Acetate ABTS	Gold	Laccase /ABTS/O_2	100	125	25	Lim and Palmor, 2007, [84]
	Gold	GOx and glucose	Gold	Laccase/O_2	1000	690	110	Zebda et al., 2009, [80]
(2) Immobilized enzymes in flowing cells	GDH and Dp enzymes and the mediator PLL-VK_3 with KB coated on gold	Glucose and NAD+	BOx adsorbed on KB on Au electrode	O_2 (air sat.)	300	160	70	Togo et al., 2007, [82]
	GDH and Dp enzymes and the mediator PLL-VK_3 and GDH with KB coated on gold	Glucose and NAD+	PDMS coated Pt or Ag/AgCl	O_2 (air sat.)	1000	130	32 and 20 at 37°C with Ag/AgCl and PDMS/Pt cathode	Togo et al., 2007, [85]
	GOx enzyme with SWCNTs on glass	Glucose and FEMOL	Laccase with SWCNTs on glass	O_2/ABTS	17	204 (covalent bonding) 346 (cross-linked bonding)	1.57 (covalent bonding) 0.27 (cross-linked binding)	Beneyton et al., 2013, [30]

Fuel Cell Type	Anode material	Anolyte	Cathode material	Catholyte	Flow rate ($\mu L\ min^{-1}$)	J_{max} ($\mu A\ cm^{-2}$)	P_{max} (μWcm^{-2})	Ref.
(3) Immobilized enzymes in fuel reservoir	GOx with Os-mediator on carbon fibers	Glucose	BOx with Os-mediator on carbon fiber	O_2 (air sat.)	NA	540 1040	290 at 25°C 540 at 37°C	Heller et al., 2001, [86]
	GOx with Os-mediator on carbon fibers	Glucose	Laccase with Os-mediator on carbon fibers	O_2 (air sat.)	NA	160 343	64 at 23°C 137 at 37°C	Chen et al., 2001, [87]
	GOx on gold/chrome	Glucose	COx enzyme with the mediator Cyt c on gold	O_2	NA	550	21	Katz and Wilner, 2003, [88]
	GOx on carbon fibers and Os-mediator	Glucose	BOx on carbon fibers and Os-mediator	O_2	NA	10	4.5	Mano et al., 2003, [89]
	GOx with MWCNTs	Glucose	Laccase with MWCNTs	O_2 (air sat.)	NA	NS	1250	Zebda et al., 2011, [90]
	GOx/NQ/catalase MWCNT	Glucose	Laccase with MWCNTs	O_2 (air sat.)	NA	4470	1100	Reuillard et al., 2013, [91]

NA; *Not applicable* ***NS;*** *Not specify* ***NQ;*** *Naphthoquinone* ***CP;*** *Carbon paper* ***KB;*** *Ketjenblack*

GDH*; Glucose Dehydrogense enzyme* ***Dp****; Diaphorase enzyme* ***PPF;*** *Pyrolyzed pohotoresist films* ***COx****; Cytochrome Oxidase enzyme* ***SWCNTs****; Single walled carbon nano tubes*

PLL-VK$_3$*; Vitamin K_3-modified poly-L-lysine mediator* ***BOx;*** *Bilirubin Oxidase enzyme* ***MWCNTs;*** *Multi walled carbon nano tubes*

Table 2.1 Overview of the state of the art of some enzymatic fuel cells

Thus, there are important benefits to be gained from the immobilization of enzymes despite their lower power output compared to fuel cells based on dissolved enzymes. On the one hand, the lifetime of the free enzymes in solution is typically only a few hours to a couple of days and changes in pH or temperature cause them to denature [92] whereas immobilized enzymes can have extended life be more protected from changes in the surrounding environments [93] [6, 27, 94-95]. But, the most significant advantages are; the cost savings brought about by the use of only

a small amount of enzyme and redox mediators and, that stabilization of the enzymes allows them to remain active longer when adequately immobilized [6, 83, 96-99].

More recently, Beneyton *et al.* reported the first microfluidic fuel cell with enzymes covalently attached to the electrodes [30] where they improved the efficiency through a better attachment of the enzyme catalysts to the electrodes, and succeeded at covalently binding glucose oxidase and laccase to carbon-nanotube-based electrodes produced by lift-off on a glass slide. By capturing the enzyme at the surface of the electrode the efficiency of the biofuel cell is improved as the electrons can more easily transport to the electrode surface [31]. There are four common techniques for immobilizing enzymes on electrode surfaces; a) adsorption, b) covalent binding, c) entrapment and d) membrane confinement [50, 100]. These methods are represented in figure 1.11.

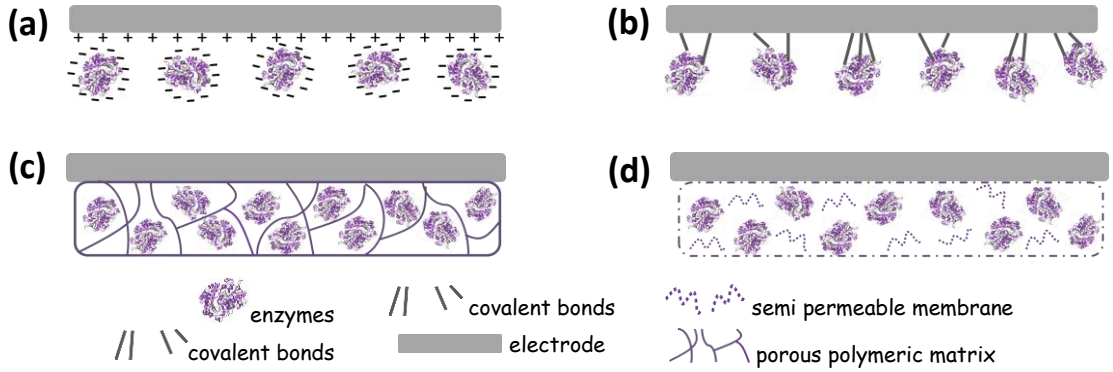

Figure 1.11 Schematic representations of common enzyme immobilization techniques [101]. (a) Enzyme electrostatically absorbed to an insoluble matrix. (b) Enzyme covalently attached to an insoluble matrix. (c) Enzyme entrapped within an insoluble matrix by a cross-linked polymer. (d) Enzyme confined within a semi-permeable membrane.

1.3.1 Materials structure for the electrodes

Besides the improvement of enzyme lifetime by enzymatic immobilization, another important challenge in enzyme-based systems is to optimize their usually poor electron transfer rates to solid electrodes [99-100]. The electrodes represent one of the most important components in an electrochemical fuel cell. The selection of the material is critical because performance can significantly vary with its choice. Ideally, electrodes should have a high electrical conductivity, provide a stable surface to enzymes, have a high surface-to-volume ratio to allow for a high enzyme load, and contain sufficiently large pore size to facilitate efficient mass transport of fuel and oxidant [23-24, 98, 102]. Out of the conductive and functionalized materials examined for use in bioelectrodes of EFCs [99, 103], the most favorable interfaces for biomolecular electron transfer are carbon-based materials. Their use is widespread due to their low cost, wide operational potential window, low background currents and high surface area [99, 103-106]. Different forms of carbon electrodes have been used to date [107]. Graphite rods, for example, are widely utilized

to measure enzymatic electrodes performance in a cell test due to their low cost, naturally high porosity and easy of handling. However, they are hard to shape for its use in a miniaturized fuel cells. On the other hand, increasing the surface roughness of an electrode by the addition of carbon nanomaterials, such as Ketjen Black (KB) and CNTs, has had a large impact on the development of EFCs because this fact is directly related to the enhancement of enzyme activity [29, 108]. It is known that different approaches exist to improve electron transfer between enzymes and electrodes, most of which rely on different forms of conducting polymers, and more recently on the use of anthracene-modified carbon nanotubes for laccase enzymes, figure 1.12, [63, 100, 103, 109].

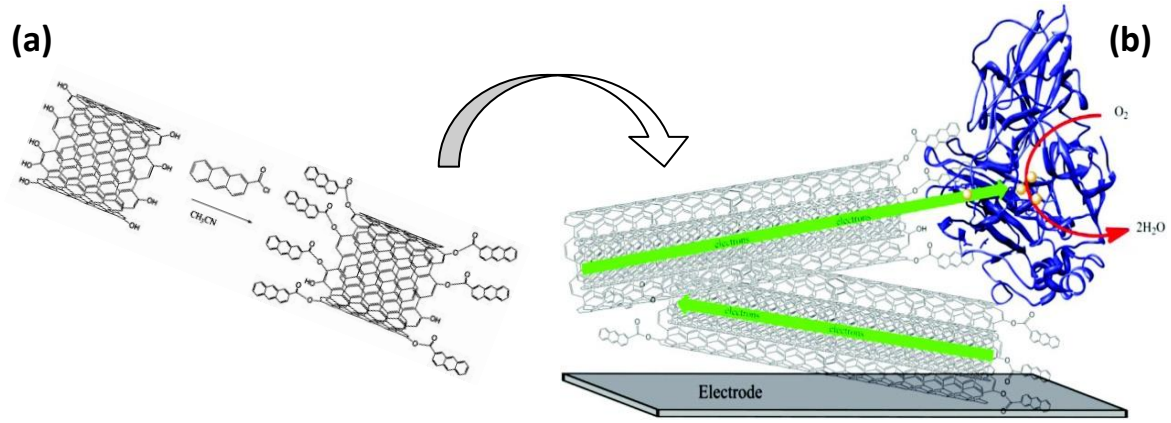

Figure 1.12 (a) Covalent attachment of anthracene groups to MWCNTs. (b) Idealized scheme of DET oxygen reduction by laccase to a carbon-paper electrode, oriented with T1 site near anthracene groups [110].

Diverse forms of carbon materials are commercially available, see figure 1.13. Between them, the most widely used is carbon-fiber paper which sometimes is combined with CNTs to further increase the available surface area [111]. Pyrolyzed photoresist films (PPF) electrodes show also attractive characteristics. They are synthesized from phenolic photoresists and therefore they can be shaped into a wide range of geometries using photolithography [112-114]. The properties of PPF are akin to those of commercial glassy carbon, but its synthesis is fully CMOS compatible (which can be very attractive for its application to silicon-based systems) and less costly [113, 115-117]. Furthermore, PPF electrodes are extremely flat (rms roughness ca. 0.2–0.7 nm) and display very low capacitive currents

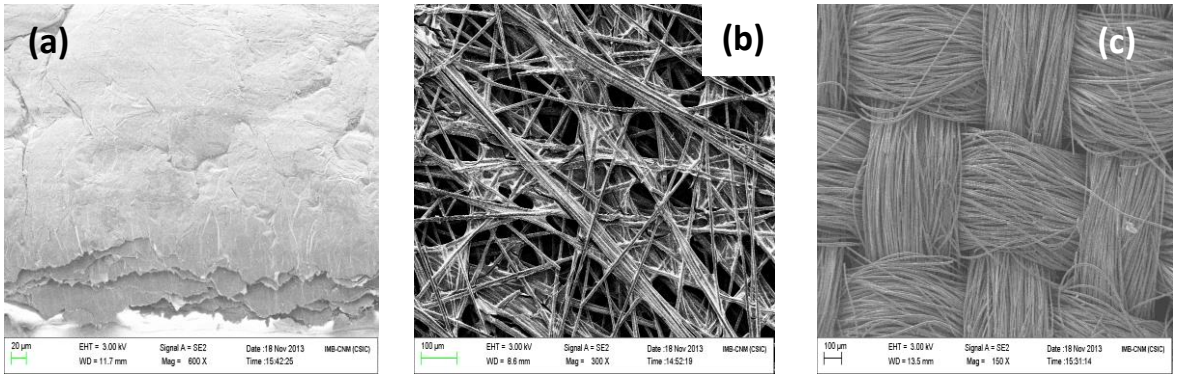

Figure 1.13 SEM images of different kinds of carbon materials that eventually could work as working electrode in a biofuel cell. (a) Carbon tape (b) Carbon Paper (c) Carbon cloth.

1.4 MICROFLUIDIC FUEL CELLS

As stated at the beginning of this chapter, fuel cells have been considered for many years a suitable source of power for micro-electro-mechanical-systems and, in order to be integrated within the devices to power they have been miniaturized at the microscale [85]. In the last 15 years, there has been much activity in this field developing packed fuel cells systems using Nafion separating the anode and cathode compartment, such as the micro direct methanol fuel cells (μDMFC) [118-119] and micro polymer electrolyte membrane fuel cells (μPEMFC) [120-122]. However, the use of Nafion adds complexity of fabrication and poses many obstacles to integration [123-124]. Other issues such as fuel cross-over through the membrane or its deformation due to the dehydration are also important disadvantages [3]. To address these drawbacks a novel conceptual design for micro-scale fuel cells was proposed in 2002 [125]. This configuration, named microfluidic fuel cell, proposes the elimination the fuel cell membrane and has been rapidly developed since their invention.

Microfluidic fuel cells are sometimes called membraneless fuel cells or laminar flow-based fuel cells and they operate in a co-laminar flow configuration without requiring a physical membrane. The main idea behind this kind of devices is that anolyte and catholyte flowing solutions can be kept effectively separated because their mixing is restricted to a narrow interdiffusion region between the two streams. Generally, the fluid flow inside a microchannel is expected to be laminar as the flow regime through it is characterized by a low Reynolds number:

$$R_e = \frac{\rho U D_h}{\mu} \qquad \textbf{(1.10)}$$

where, ρ is the fluid density (kg m^{-3}), U is the average velocity (m s^{-1}), D_h is the hydraulic diameter (m), and μ is the dynamic viscosity (kg m^{-1} s^{-1}). In general, turbulence occurs at a high Reynolds number (typically R_e>10^3) [126-127]. However, at low Reynolds numbers (R_e<<1) flow is laminar and viscous effects dominate over inertial effects and surface forces are more relevant than body

forces [50]. For maintaining laminar flow, D_h should range approximately from 200 µm to 3 mm [128], which means that even for flow rates as high as 1 ml min^{-1}, the Reynolds number will be lower than 1.

Another important peculiarity accompanying the microscale is the surface-to-volume ratio that increases inversely proportional to the length scaling factor, $\frac{R^2}{R^3} = R^{-1}$ [129]. Since electrochemical reactions are surface-based, the performance of the fuel cell benefits directly from the miniaturization [50]. However, the reduction of size has a limit; as the dimensions of the device are decreased, the energy load necessary to maintain the parallel flow increases with frictional losses.

The most common microfluidic fuel cell architecture reported to date is the **Y-shaped configuration**, where two streams are combined horizontally in a microchannel. One laminar stream contains the fuel and a second laminar stream contains the oxidant. Both of them flow over a reaction region where the fuel cell electrodes are placed. Depending on the design of the electrodes and its position inside the channel microfluidic fuel cells are classified into (i) flow-over type with planar electrodes (ii) flow through type with three dimensional porous electrodes and (iIi) the air-breathing cathode design. The most reported configuration is that of planar electrodes that are positioned in parallel at the bottom of the microchannel [81, 130]. Due to the fact that the stream solutions can be chosen independently, the reaction rates and cell voltage of the system can be optimized.

This dissertation focuses on the Y-shape microfluidic configuration with bottom electrodes positioned side by side at the bottom of it. In figure 1.14 a scheme of this kind of fuel cell is represented. For these flow systems, the mass transport is achieved by diffusion of molecules and convection transport as a result of the bulk motion of the fluids [126]. The relation between both is given by Péclet number,

$$P_e = \frac{UD_h}{D} \tag{1.11}$$

where, U is the average velocity of convective flow (m s^{-1}), D_h is the hydraulic diameter of the microchannel (m) and D is the diffusion coefficient of the fuel or oxidant (m^2 s^{-1}). High Péclet numbers indicate that the rate of mass transfer via crosswise diffusion is much lower than the streamwise convective velocity. Therefore, P_e can be adjusted through the choice of flow velocity and the selection of the dimensions of the system to keep reactants effectively separated in the absence of a solid membrane.

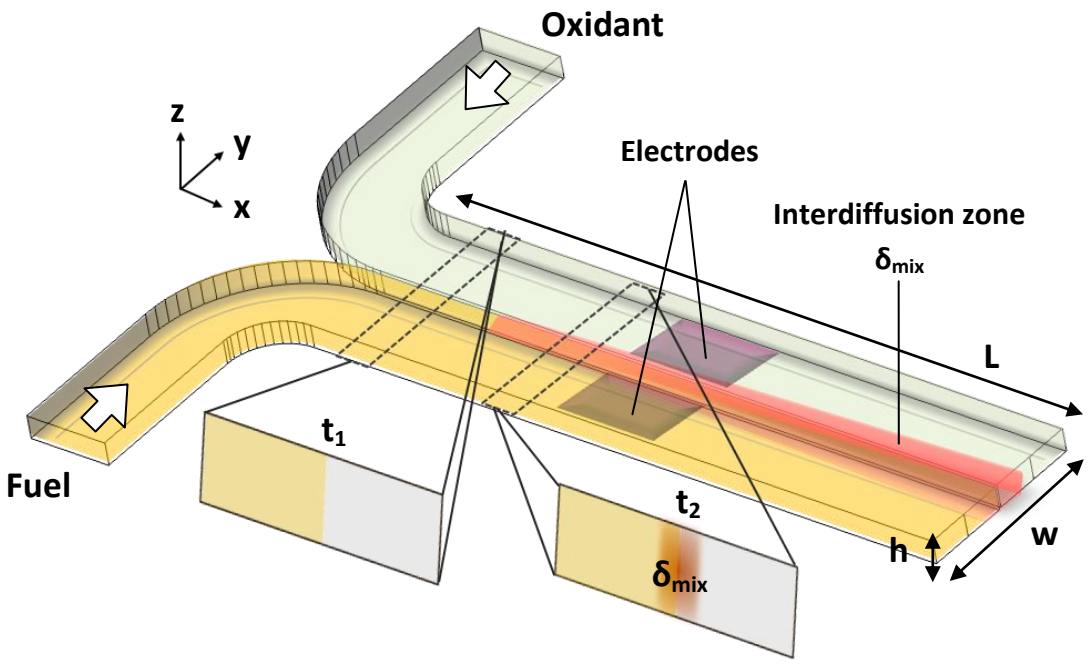

Figure 1.14 Membraneless laminar flow-based fuel cell with fuel and oxidant solutions flowing in the channel and electrodes on bottom. The region of fuel/oxidant crossover is indicated in red.

As stated before, the mixing of fluids is limited and only occurs by diffusion in an interfacial region along the liquid-liquid separation. The thickness of the interdiffusion zone, δ_{mix}, at a given downstream position can be calculated using:

$$\delta_{mix} = \left(\frac{Dhx}{U}\right)^{1/3} \quad \textbf{(1.12)}$$

where, *h* is the channel height, *x* is the downstream position calculated from the point where the two fluids are first in contact (m), and *U* is the linear flow velocity (m s^{-1}). Interdiffusive width between two streams (δ_{mix}) is highly dependent on the mean residence time stream in the channel [131]. Furthermore, the effect of the mixing width (δ_{mix}) of the streams on the fuel cell performance can be controlled by positioning the electrodes at x values where fuel and oxidant crossovers are prevented.

1.4.1 Microfluidic fuel cell fundamentals

The performance of any fuel cell can be evaluated by means of the open circuit voltage (OCV), the voltage-intensity and power-intensity polarization curves.

Open circuit voltage, OCV; It is the potential at which no load is applied to the cell and therefore it is the maximum output voltage. The OCV estimates the good behavior of the fuel cell but does not give information about the electrochemical processes occurring in the cell [132]. The value of OCV

is determined as the difference in the electrochemical potential between the anode and the cathode half cell potentials, $E_{cathode} - E_{anode}$, when they are measured in a in a three electrode setup, figure 1.15.

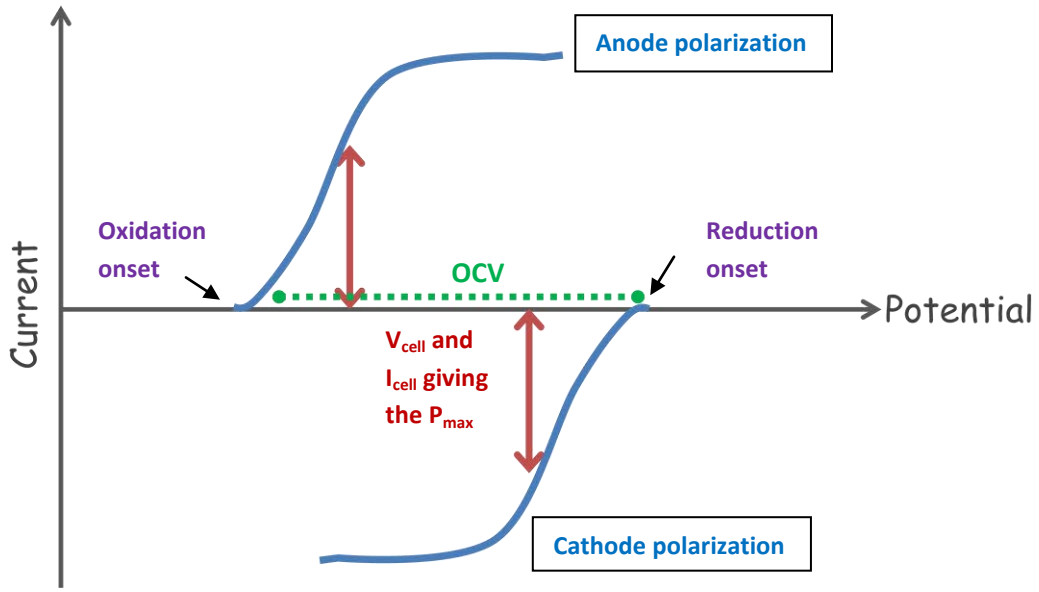

Figure 1.15 General scheme of anode and cathode tested separately in a three-electrode mode showing voltage and current operation. The operating voltage of a fuel cell has an upper limit dictated by the difference in potential between the oxidant and reductant and the potential difference between the final electron donor and initial acceptor at the electrodes [6].

Voltage-intensity polarization curves; A polarization curve is obtained by scanning its output voltage or current under a variable load. As a result, a potential is obtained as a function of the current, figure 1.16 (a). The slope of an I-V curve is due to different potential losses related to the fuel cell components. The cell voltage can be described as follows:

$$V_{cell} = \Delta E_{cell} - \eta_{ohm} - \eta_{act} - \eta_{conc} \quad \textbf{(1.13)}$$

where, ΔE_{cell}, represents the ideal thermodynamic potential between of the fuel cell and η_{act} , η_{ohm} and η_{conc} correspond to the activation, ohmic and mass transport losses, respectively [133]. In practice the V_{cell} can be slightly lower than ΔE_{cell} due to various voltage losses. These limiting factors contributing to the performance decrease can be described as follows:

$\boldsymbol{\eta_{act}}$ or activation losses. They are found at low currents due to a combination of $\eta_{act\ anode}$ and $\eta_{act\ cathode}$. They are also called charge transfer losses and are caused by the slow reaction kinetics at the electrodes. Choosing the appropriate electrocatalyst and increasing the active surface area of the electrodes are key methods to reduce these limitations. The choice of electrolyte media and pH may also influence the electrode kinetics.

$\boldsymbol{\eta_{ohm}}$ or ohmic losses. In the middle of the graph the ohmic losses, $\eta_{ohm} = RI$, predominates. They are the result of ionic charge transfer resistance in the electrolyte ($R_{electrolyte}$) and electrical resistance in electrodes, contacts and wires ($R_{external}$). They need to be minimized for an efficient fuel cell system. The co-laminar streams must have relatively high ionic conductivity to facilitate good ionic charge transport between the electrodes and to close the electrical circuit [134]. Ohmic resistance for ionic transport ($R_{electrolyte}$) in the channel can be expressed in terms of anode-to-cathode spacing distance (d), cross-sectional area of charge transport (A) and the resistivity (ρ);

$$R_{electrolyte} = \rho \frac{d}{A} \quad \textbf{(1.14)}$$

Equation 1.14 indicates that a supporting electrolyte with small resistivity (or high conductivity ($\sigma=\rho^{-1}$) and high microchannel with a small electrode-to-electrode distance will minimize the electrical resistance, R.

$\boldsymbol{\eta_{conc}}$ or concentration losses. At high current densities, concentration losses dominates as a consequence of two main factors; (i) the formation of a depletion zone over the electrodes and (ii) the cross diffusional mixing of the two streams (δ_{mix});

(i) The depletion zone is the result of the consumption of fuel and oxidant over the corresponding electrode while the oxidation or reduction reactions occur [135]. It happens along the length of the microchannel and it can be motivated for a slow replenishment of reactants over the electrodes [136-137].

(ii) Cross diffusional mixing across the liquid–liquid boundary occurs along the width of the microchannel [138] leading to the reduction in the concentrations of fuel/oxidant streams.

Both contributions can be lowered by increasing the flow velocity of reactants or/and their concentrations. Apart from these, it is known that the performance of membraneless laminar flow-based fuel cell running on dissolved O_2 will be limited by the cathode side. This is because oxygen in aqueous media is presented in low concentration due to its low solubility in water-based electrolytes. The content of oxygen is 2.2 mM at room temperature and standard pressure conditions [139]. Furthermore, O_2 dissolved in aqueous media presents very low diffusivity ($\approx 2 \times 10^{-5}$ cm^2 s^{-1}). The access of more oxygen into the cell can be achieved by the use of an air-breathing cathode. In fact, the content of oxygen in air is about 10 mM with a diffusivity of 0.2 cm^2 s^{-1}, four order of magnitude higher than that in aqueous media [3].

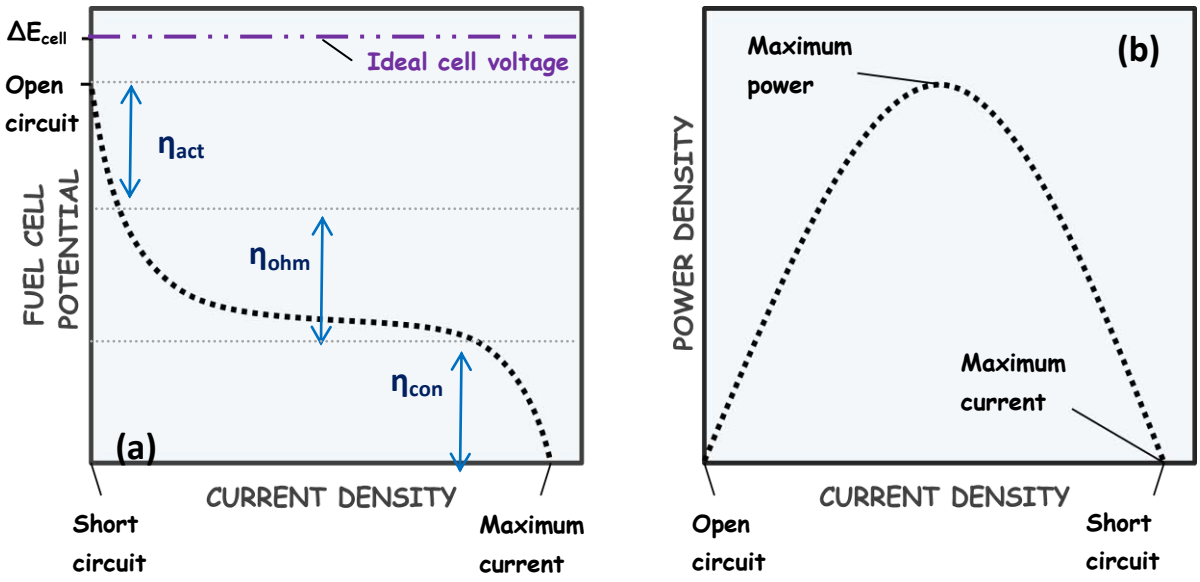

Figure 1.16 Overall cell polarization curves as a sum of anode and cathode polarizations. (a) Polarization curve of a biofuel cell with the major losses of cell voltage and the approximate range of current density in with these losses occur. (b) Power curve consequence of the integral of the voltage by the current.

Power-intensity polarization curve: The power curve is an overall measure of the device level performance and it is achieved by multiplying the cell voltage and the current density:

$$P_{cell} = V_{cell} \cdot I \tag{1.15}$$

Most of the times the power is expressed as power density in order to give a value comparable with other electrodes using different active areas. It is obtained by normalizing the power with respect to the cross-sectional electrode area (*A*):

$$Power\ density = \frac{P_{cell}}{A} \tag{1.16}$$

Figure 1.16 (b) exhibits the characteristic profile of power density as a function of the current density. The curve is defined by the open circuit and the short circuit voltage and allows the determination of the maximum power density that the fuel cell can generate and the potential at which this occurs. Usual power outputs for enzymatic fuel cells are in the range of several hundred of microwatts per cm^2 at voltages between 0.5-0.2 V. Moreover, individual cells can be stacked and scaled up to achieve higher voltage and power and meet the applications requirements.

1.5 OBJECTIVES AND OUTLOOK

This thesis presents different types of electrochemical devices biologically catalyzed by enzymes and using glucose as fuel and oxygen as reductant agent. Throughout this work the initial primitive microfluidic system fabricated has been evolved toward a compact an efficient microfluidic device. The final purpose is to use these systems to power microelectronic devices demanding low power consumption.

The thesis is divided in four experimental chapters according to the different technologies used for the construction of the microfluidic systems. At the same time these chapters have been separated in two sections; *section 1* (chapter 2 and chapter 3), in which devices used external pressure systems for the supply of liquids chapter 2 and chapter 3, therefore not all the energy obtained from these devices will be net energy ready to use. On the other hand, in *section 2* (chapter 4 and 5) devices utilized the capillary action of paper to cause the movement of liquids. In these paper-based devices, fluids flow through capillary transport mechanisms, so no external appliance for pumping the solution to the inner is needed. As a result, passive fuel delivery is obtained and all the power achieved can be available for powering miniature portable electronics.

Finally, general conclusions of the thesis have been presented in addition to the directions that the future work may take.

REFERENCES

1. Choban, E.R., L.J. Markoski, A. Wieckowski, and P.J.A. Kenis, *Microfluidic fuel cell based on laminar flow.* Journal of Power Sources, 2004. **128**(1): p. 54-60.
2. Hsu, T.-R. *Miniaturization–A paradigm shift in advanced manufacturing and education*. in *Internat ional conference on Advanced Manufacturing Technologies and Education in the 21st Century*. 2002.
3. Mousavi Shaegh, S.A., N.-T. Nguyen, and S.H. Chan, *A review on membraneless laminar flow-based fuel cells.* International Journal of Hydrogen Energy, 2011. **36**(9): p. 5675-5694.
4. Davis, F. and S.P.J. Higson, *Biofuel cells—Recent advances and applications.* Biosensors and Bioelectronics, 2007. **22**(7): p. 1224-1235.
5. Ramani, V. *Fuel Cells*. 2006; Available from: www.electrochem.org/dl/interface/spr/spr06/spr06_p41-44.pdf.
6. Bullen, R.A., T.C. Arnot, J.B. Lakeman, and F.C. Walsh, *Biofuel cells and their development.* Biosensors and Bioelectronics, 2006. **21**(11): p. 2015-2045.
7. Ruiz-Morales, J.C., D. Marrero-López, M. Gálvez-Sánchez, J. Canales-Vázquez, C. Savaniu, and S.N. Savvin, *Engineering of materials for solid oxide fuel cells and other energy and environmental applications.* Energy & Environmental Science, 2010. **3**(11): p. 1670-1681.
8. Scott, K., E.H. Yu, M.M. Ghangrekar, B. Erable, and N.M. Duteanu, *Biological and Microbial Fuel Cells.* Comprehensive Renewable Energy, Vol 4: Fuel Cells and Hydrogen Technology, 2012: p. 277-300.

9. Carrette, L., K.A. Friedrich, and U. Stimming, *Fuel cells: principles, types, fuels, and applications.* ChemPhysChem, 2000. **1**(4): p. 162-193.
10. Merle, G., M. Wessling, and K. Nijmeijer, *Anion exchange membranes for alkaline fuel cells: A review.* Journal of Membrane Science, 2011. **377**(1): p. 1-35.
11. Ganguly, S., S. Das, K. Kargupta, and D. Banerjee, *Reduced Order Inferential Model-Based Optimization of a Phosphoric Acid Fuel Cell (PAFC) Stack.* Industrial & Engineering Chemistry Research, 2013. **52**(22): p. 7104-7115.
12. Ghenciu, A.F., *Review of fuel processing catalysts for hydrogen production in PEM fuel cell systems.* Current opinion in solid state and materials science, 2002. **6**(5): p. 389-399.
13. Nguyen, Q.M., *Technological status of nickel oxide cathodes in molten carbonate fuel cells—a review.* Journal of Power Sources, 1988. **24**(1): p. 1-19.
14. Stambouli, A.B. and E. Traversa, *Solid oxide fuel cells (SOFCs): a review of an environmentally clean and efficient source of energy.* Renewable and Sustainable Energy Reviews, 2002. **6**(5): p. 433-455.
15. Mekhilef, S., R. Saidur, and A. Safari, *Comparative study of different fuel cell technologies.* Renewable and Sustainable Energy Reviews, 2012. **16**(1): p. 981-989.
16. Girard, J.E. and J. Girard, *Principles of environmental chemistry*. 2013: Jones & Bartlett Publishers.
17. kumar, J.A., P. Kalyani, and R. Saravanan, *Studies on PEM fuel cells using various alcohols for low power applications.* International Journal of Electrochemical Science, 2008. **3**(8): p. 961-969.
18. Brouzgou, A., F. Tzorbatzoglou, and P. Tsiakaras. *Direct alcohol fuel cells: challenges and future trends*. in *Energetics (IYCE), Proceedings of the 2011 3rd International Youth Conference on*. 2011: IEEE.
19. Lee, J.w. and E. Kjeang, *A perspective on microfluidic biofuel cells.* Biomicrofluidics, 2010. **4**(4): p. -.
20. Katz, E., A. Shipway, and I. Willner, *Handbook of Fuel Cells—Fundamentals, Technology and Applications. (Chapter 21—biochemical fuel cells).* 2003.
21. Osman, M.H., A.A. Shah, and F.C. Walsh, *Recent progress and continuing challenges in bio-fuel cells. Part I: Enzymatic cells.* Biosensors and Bioelectronics, 2011. **26**(7): p. 3087-3102.
22. Shukla, A.K., P. Suresh, S. Berchmans, and A. Rajendran, *Biological fuel cells and their applications.* Current Science, 2004. **87**(4): p. 455-468.
23. Calabrese Barton, S., J. Gallaway, and P. Atanassov, *Enzymatic biofuel cells for implantable and microscale devices.* Chemical reviews, 2004. **104**(10): p. 4867-4886.
24. Falk, M., C.W. Narváez Villarrubia, S. Babanova, P. Atanassov, and S. Shleev, *Biofuel cells for biomedical applications: colonizing the animal kingdom.* ChemPhysChem, 2013. **14**(10): p. 2045-2058.
25. Romero, E., *Powering Biomedical Devices*. 2013: Elsevier Science.
26. Flipsen, B., A. Bremer, A. Jansen, and M. Veefkind, *Towards a selection method for designing alternative energy systems in consumer products.* Proc. TMCE 2004 (Lausanne, Switzerland, April 12-16), 2004: p. 1-8.
27. Minteer, S.D., B.Y. Liaw, and M.J. Cooney, *Enzyme-based biofuel cells.* Current Opinion in Biotechnology, 2007. **18**(3): p. 228-234.
28. Moore, E. *Microfluidic biofuel cells*. 2009; Available from: www.tyndall.ie/content/microfluidic-biofuel-cells.
29. Ivanov, I., T. Vidaković-Koch, and K. Sundmacher, *Recent advances in enzymatic fuel cells: experiments and modeling.* Energies, 2010. **3**(4): p. 803-846.

30. Beneyton, T., I.P.M. Wijaya, C. Ben Salem, A.D. Griffiths, and V. Taly, *Membraneless glucose/O-2 microfluidic biofuel cells using covalently bound enzymes.* Chemical Communications, 2013. **49**(11): p. 1094-1096.
31. Lee, J.w. and E. Kjeang, *A perspective on microfluidic biofuel cells.* Biomicrofluidics, 2010. **4**(4): p. 041301.
32. Zhou, M., C. Chen, Y. Du, B. Li, D. Wen, S. Dong, and E. Wang, *An IMP-Reset gate-based reusable and self-powered "smart" logic aptasensor on a microfluidic biofuel cell.* Lab on a Chip, 2010. **10**(21): p. 2932-2936.
33. Cracknell, J.A., K.A. Vincent, and F.A. Armstrong, *Enzymes as working or inspirational electrocatalysts for fuel cells and electrolysis.* Chemical Reviews, 2008. **108**(7): p. 2439-2461.
34. Kavanagh, P., S. Boland, P. Jenkins, and D. Leech, *Performance of a Glucose/O2 Enzymatic Biofuel Cell Containing a Mediated Melanocarpus albomyces Laccase Cathode in a Physiological Buffer.* Fuel Cells, 2009. **9**(1): p. 79-84.
35. Shukla, A., P. Suresh, S. Berchmans, and A. Rajendran, *Biological fuel cells and their applications.* Current Science, 2004. **87**(4): p. 455-468.
36. Cuevas-Muñiz, F.M., M. Guerra-Balcázar, J.P. Esquivel, N. Sabaté, L.G. Arriaga, and J. Ledesma-García, *Glucose microfluidic fuel cell based on silver bimetallic selective catalysts for on-chip applications.* Journal of Power Sources, 2012. **216**(0): p. 297-303.
37. Song, C. and J. Zhang, *Electrocatalytic Oxygen Reduction Reaction*, in *PEM Fuel Cell Electrocatalysts and Catalyst Layers*, J. Zhang, Editor. 2008, Springer London. p. 89-134.
38. Ramirez, P., N. Mano, R. Andreu, T. Ruzgas, A. Heller, L. Gorton, and S. Shleev, *Direct electron transfer from graphite and functionalized gold electrodes to T1 and T2/T3 copper centers of bilirubin oxidase.* Biochimica et Biophysica Acta (BBA)-Bioenergetics, 2008. **1777**(10): p. 1364-1369.
39. Leech, D., P. Kavanagh, and W. Schuhmann, *Enzymatic fuel cells: Recent progress.* Electrochimica Acta, 2012. **84**: p. 223-234.
40. Meredith, M.T. and S.D. Minteer, *Biofuel Cells: Enhanced Enzymatic Bioelectrocatalysis.* Annual Review of Analytical Chemistry, 2012. **5**(1): p. 157-179.
41. Shan, D., W. Yao, and H. Xue, *Electrochemical study of ferrocenemethanol-modified layered double hydroxides composite matrix: Application to glucose amperometric biosensor.* Biosensors and Bioelectronics, 2007. **23**(3): p. 432-437.
42. Gao, F., O. Courjean, and N. Mano, *An improved glucose/O2 membrane-less biofuel cell through glucose oxidase purification.* Biosensors and Bioelectronics, 2009. **25**(2): p. 356-361.
43. Aquino Neto, S. and A.R. De Andrade, *New energy sources: the enzymatic biofuel cell.* Journal of the Brazilian Chemical Society, 2013. **24**: p. 1891-1912.
44. Kavanagh, P. and D. Leech, *Mediated electron transfer in glucose oxidising enzyme electrodes for application to biofuel cells: recent progress and perspectives.* Physical Chemistry Chemical Physics, 2013. **15**(14): p. 4859-4869.
45. Armstrong, F.A. and J. Hirst, *Reversibility and efficiency in electrocatalytic energy conversion and lessons from enzymes.* Proceedings of the National Academy of Sciences of the United States of America, 2011. **108**(34): p. 14049-14054.
46. Sarma, A.K., P. Vatsyayan, P. Goswami, and S.D. Minteer, *Recent advances in material science for developing enzyme electrodes.* Biosensors and Bioelectronics, 2009. **24**(8): p. 2313-2322.

47. Gupta, G., C. Lau, B. Branch, V. Rajendran, D. Ivnitski, and P. Atanassov, *Direct bio-electrocatalysis by multi-copper oxidases: Gas-diffusion laccase-catalyzed cathodes for biofuel cells.* Electrochimica Acta, 2011. **56**(28): p. 10767-10771.
48. Wilson, R. and A.P.F. Turner, *Glucose oxidase: An ideal enzyme.* Biosensors and Bioelectronics, 1992. **7**(3): p. 165-185.
49. Leskovac, V., S. Trivic, G. Wohlfahrt, J. Kandrac, and D. Pericin, *Glucose oxidase from Aspergillus niger: the mechanism of action with molecular oxygen, quinones, and one-electron acceptors.* International Journal of Biochemistry & Cell Biology, 2005. **37**(4): p. 731-750.
50. Zhao, T., *Micro Fuel Cells: Principles and Applications*. 2009: Elsevier Science.
51. Tsujimura, S., S. Kojima, K. Kano, T. Ikeda, M. Sato, H. Sanada, and H. Omura, *Novel FAD-dependent glucose dehydrogenase for a dioxygen-insensitive glucose biosensor.* Bioscience, biotechnology, and biochemistry, 2006. **70**(3): p. 654-659.
52. Ferri, S., K. Kojima, and K. Sode, *Review of glucose oxidases and glucose dehydrogenases: a bird's eye view of glucose sensing enzymes.* Journal of diabetes science and technology, 2011. **5**(5): p. 1068-1076.
53. Zafar, M.N., N. Beden, D. Leech, C. Sygmund, R. Ludwig, and L. Gorton, *Characterization of different FAD-dependent glucose dehydrogenases for possible use in glucose-based biosensors and biofuel cells.* Analytical and Bioanalytical Chemistry, 2012. **402**(6): p. 2069-2077.
54. Fapyane, D., S.-J. Lee, S.-H. Kang, D.-H. Lim, K.-K. Cho, T.-h. Nam, J.-P. Ahn, J.-H. Ahn, S.-W. Kim, and I.S. Chang, *High performance enzyme fuel cells using a genetically expressed FAD-dependent glucose dehydrogenase [small alpha]-subunit of Burkholderia cepacia immobilized in a carbon nanotube electrode for low glucose conditions.* Physical Chemistry Chemical Physics, 2013. **15**(24): p. 9508-9512.
55. *RCSB Protein Data Bank*. Available from: www.rcsb.org/pdb/101/motm.do?momID=77.
56. *Sigma Aldrich*. Available from: www.sigmaaldrich.com/catalog/product/aldrich/335061?lang=es&region=ES.
57. Wang, J., *Electrochemical glucose biosensors.* Chemical reviews, 2008. **108**(2): p. 814-825.
58. Felice, A.K., C. Sygmund, W. Harreither, R. Kittl, L. Gorton, and R. Ludwig, *Substrate specificity and interferences of a direct-electron-transfer-based glucose biosensor.* Journal of diabetes science and technology, 2013. **7**(3): p. 669-677.
59. Wang, J., *Nanomaterial-based electrochemical biosensors.* Analyst, 2005. **130**(4): p. 421-426.
60. Xu, W., L. Gao, D. Danilov, V. Pop, and P. Notten. *BIO-INSPIRED FUEL CELLS FOR MINIATURIZED BODY-AREA-NETWORKS APPLICATIONS*. in *Proceedings of The 10th International Workshop on Micro and Nanotechnology for Power Generation and Energy Conversion Applications, Dec*.
61. Chaubey, A. and B.D. Malhotra, *Mediated biosensors.* Biosensors and Bioelectronics, 2002. **17**(6–7): p. 441-456.
62. Jenkins, P., S. Tuurala, A. Vaari, M. Valkiainen, M. Smolander, and D. Leech, *A comparison of glucose oxidase and aldose dehydrogenase as mediated anodes in printed glucose/oxygen enzymatic fuel cells using ABTS/laccase cathodes.* Bioelectrochemistry, 2012. **87**(0): p. 172-177.
63. Ammam, M. and J. Fransaer, *Glucose/O2 biofuel cell based on enzymes, redox mediators, and Multiple-walled carbon nanotubes deposited by AC-electrophoresis then stabilized by*

electropolymerized polypyrrole. Biotechnology and Bioengineering, 2012. **109**(7): p. 1601-1609.

64. Shleev, S., J. Tkac, A. Christenson, T. Ruzgas, A.I. Yaropolov, J.W. Whittaker, and L. Gorton, *Direct electron transfer between copper-containing proteins and electrodes.* Biosensors & Bioelectronics, 2005. **20**(12): p. 2517-2554.
65. Klis, M., J. Rogalski, and R. Bilewicz, *Voltammetric determination of catalytic reaction parameters of laccase based on electrooxidation of hydroquinone and ABTS.* Bioelectrochemistry, 2007. **71**(1): p. 2-7.
66. Palmore, G.T.R. and H.-H. Kim, *Electro-enzymatic reduction of dioxygen to water in the cathode compartment of a biofuel cell.* Journal of Electroanalytical Chemistry, 1999. **464**(1): p. 110-117.
67. Madhavi, V. and S.S. Lele, *LACCASE: PROPERTIES AND APPLICATIONS*. 2009. Vol. 4. 2009.
68. Fernández-Sánchez, C., T. Tzanov, G.M. Gübitz, and A. Cavaco-Paulo, *Voltammetric monitoring of laccase-catalysed mediated reactions.* Bioelectrochemistry, 2002. **58**(2): p. 149-156.
69. Shumakovich, G., S. Shleev, O. Morozova, P. Khohlov, I. Gazaryan, and A. Yaropolov, *Electrochemistry and kinetics of fungal laccase mediators.* Bioelectrochemistry, 2006. **69**(1): p. 16-24.
70. Bourbonnais, R., D. Leech, and M.G. Paice, *Electrochemical analysis of the interactions of laccase mediators with lignin model compounds.* Biochimica Et Biophysica Acta-General Subjects, 1998. **1379**(3): p. 381-390.
71. Kamitaka, Y., S. Tsujimura, N. Setoyama, T. Kajino, and K. Kano, *Fructose/dioxygen biofuel cell based on direct electron transfer-type bioelectrocatalysis.* Physical Chemistry Chemical Physics, 2007. **9**(15): p. 1793-1801.
72. Zheng, W., H.M. Zhou, Y.F. Zheng, and N. Wang, *A comparative study on electrochemistry of laccase at two kinds of carbon nanotubes and its application for biofuel cell.* Chemical Physics Letters, 2008. **457**(4–6): p. 381-385.
73. Shleev, S., A. Jarosz-Wilkolazka, A. Khalunina, O. Morozova, A. Yaropolov, T. Ruzgas, and L. Gorton, *Direct electron transfer reactions of laccases from different origins on carbon electrodes.* Bioelectrochemistry, 2005. **67**(1): p. 115-124.
74. Cañas, A.I. and S. Camarero, *Laccases and their natural mediators: Biotechnological tools for sustainable eco-friendly processes.* Biotechnology Advances, 2010. **28**(6): p. 694-705.
75. Randles, J.E.B., *A CATHODE RAY POLAROGRAPH .2. THE CURRENT-VOLTAGE CURVES.* Transactions of the Faraday Society, 1948. **44**(5): p. 327-&.
76. Comminges, C., R. Barhdadi, M. Laurent, and M. Troupel, *Determination of viscosity, ionic conductivity, and diffusion coefficients in some binary systems: Ionic liquids plus molecular solvents.* Journal of Chemical and Engineering Data, 2006. **51**(2): p. 680-685.
77. Kissinger, P.T. and W.R. Heineman, *CYCLIC VOLTAMMETRY.* Journal of Chemical Education, 1983. **60**(9): p. 702-706.
78. Nicholso.Rs, *THEORY AND APPLICATION OF CYCLIC VOLTAMMETRY FOR MEASUREMENT OF ELECTRODE REACTION KINETICS.* Analytical Chemistry, 1965. **37**(11): p. 1351-&.
79. Armstrong, F.A., H.A.O. Hill, and N.J. Walton, *DIRECT ELECTROCHEMISTRY OF REDOX PROTEINS.* Accounts of Chemical Research, 1988. **21**(11): p. 407-413.
80. Zebda, A., L. Renaud, M. Cretin, C. Innocent, F. Pichot, R. Ferrigno, and S. Tingry, *Electrochemical performance of a glucose/oxygen microfluidic biofuel cell.* Journal of Power Sources, 2009. **193**(2): p. 602-606.

81. Zebda, A., L. Renaud, M. Cretin, C. Innocent, R. Ferrigno, and S. Tingry, *Membraneless microchannel glucose biofuel cell with improved electrical performances.* Sensors and Actuators B: Chemical, 2010. **149**(1): p. 44-50.
82. Togo, M., A. Takamura, T. Asai, H. Kaji, and M. Nishizawa, *Structural studies of enzyme-based microfluidic biofuel cells.* Journal of Power Sources, 2008. **178**(1): p. 53-58.
83. Moehlenbrock, M.J. and S.D. Minteer, *Extended lifetime biofuel cells.* Chemical Society Reviews, 2008. **37**(6): p. 1188-1196.
84. Lim, K.G. and G.T.R. Palmore, *Microfluidic biofuel cells: The influence of electrode diffusion layer on performance.* Biosensors and Bioelectronics, 2007. **22**(6): p. 941-947.
85. Togo, M., A. Takamura, T. Asai, H. Kaji, and M. Nishizawa, *An enzyme-based microfluidic biofuel cell using vitamin K3-mediated glucose oxidation.* Electrochimica Acta, 2007. **52**(14): p. 4669-4674.
86. Heller, A., *Miniature biofuel cells.* Physical Chemistry Chemical Physics, 2004. **6**(2): p. 209-216.
87. Chen, T., S.C. Barton, G. Binyamin, Z. Gao, Y. Zhang, H.-H. Kim, and A. Heller, *A miniature biofuel cell.* Journal of the American Chemical Society, 2001. **123**(35): p. 8630-8631.
88. Katz, E. and I. Willner, *A Biofuel Cell with Electrochemically Switchable and Tunable Power Output.* Journal of the American Chemical Society, 2003. **125**(22): p. 6803-6813.
89. Mano, N., F. Mao, and A. Heller, *Characteristics of a miniature compartment-less glucose-O2 biofuel cell and its operation in a living plant.* Journal of the American Chemical Society, 2003. **125**(21): p. 6588-6594.
90. Zebda, A., C. Gondran, A. Le Goff, M. Holzinger, P. Cinquin, and S. Cosnier, *Mediatorless high-power glucose biofuel cells based on compressed carbon nanotube-enzyme electrodes.* Nat Commun, 2011. **2**: p. 370.
91. Reuillard, B., A. Le Goff, C. Agnès, M. Holzinger, A. Zebda, C. Gondran, K. Elouarzaki, and S. Cosnier, *High power enzymatic biofuel cell based on naphthoquinone-mediated oxidation of glucose by glucose oxidase in a carbon nanotube 3D matrix.* Physical Chemistry Chemical Physics, 2013. **15**(14): p. 4892-4896.
92. Grunwald, P., *Biocatalysis: Biochemical Fundamentals and Applications*. 2009: Imperial College Press.
93. Brena, B.M. and F. Batista-Viera, *Immobilization of Enzymes*. 2006. p. 15-30.
94. Armstrong, F.A. and G.S. Wilson, *Recent developments in faradaic bioelectrochemistry.* Electrochimica Acta, 2000. **45**(15–16): p. 2623-2645.
95. Rubenwolf, S., S. Kerzenmacher, R. Zengerle, and F. von Stetten, *Strategies to extend the lifetime of bioelectrochemical enzyme electrodes for biosensing and biofuel cell applications.* Applied Microbiology and Biotechnology, 2011. **89**(5): p. 1315-1322.
96. Fessner, W.D., *Biocatalysis: From Discovery to Application*. 2000: Springer.
97. Zebda, A., C. Innocent, L. Renaud, M. Cretin, F. Pichot, R. Ferrigno, and S. Tingry, *Enzyme-Based Microfluidic Biofuel Cell to Generate Micropower*. Biofuel's Engineering Process Technology. 2011.
98. Atanassov, P., C. Apblett, S. Banta, S. Brozik, S.C. Barton, M. Cooney, B.Y. Liaw, S. Mukerjee, and S.D. Minteer, *Enzymatic biofuel cells.* Interface-Electrochemical Society, 2007. **16**(2): p. 28-31.
99. Kim, J., H. Jia, and P. Wang, *Challenges in biocatalysis for enzyme-based biofuel cells.* Biotechnology Advances, 2006. **24**(3): p. 296-308.
100. Osman, M.H., A.A. Shah, and F.C. Walsh, *Recent progress and continuing challenges in bio-fuel cells. Part II: Microbial.* Biosensors and Bioelectronics, 2010. **26**(3): p. 953-963.

101. Chaplin, M. *Enzyme Technology. Methods of immobilisation*. 2014; Available from: http://www1.lsbu.ac.uk/water/enztech/immethod.html.
102. Narváez Villarrubia, C.W., R.A. Rincón, V.K. Radhakrishnan, V. Davis, and P. Atanassov, *Methylene Green Electrodeposited on SWNTs-Based "Bucky" Papers for NADH and l-Malate Oxidation.* ACS Applied Materials & Interfaces, 2011. **3**(7): p. 2402-2409.
103. Minteer, S.D., P. Atanassov, H.R. Luckarift, and G.R. Johnson, *New materials for biological fuel cells.* Materials Today, 2012. **15**(4): p. 166-173.
104. Park, B.Y. and M.J. Madou, *Design, fabrication, and initial testing of a miniature PEM fuel cell with micro-scale pyrolyzed carbon fluidic plates.* Journal of Power Sources, 2006. **162**(1): p. 369-379.
105. Arechederra, R.L. and S.D. Minteer, *Complete Oxidation of Glycerol in an Enzymatic Biofuel Cell.* Fuel Cells, 2009. **9**(1): p. 63-69.
106. Lacher, N.A., K.E. Garrison, R.S. Martin, and S.M. Lunte, *Microchip capillary electrophoresis/ electrochemistry.* Electrophoresis, 2001. **22**(12): p. 2526-2536.
107. Pant, D., G. Van Bogaert, L. Diels, and K. Vanbroekhoven, *A Comparative Assessment of Bioelectrochemical Systems and Enzymatic Fuel Cells.* Microbial Biotechnology: Energy and Environment, 2012: p. 39.
108. Armstrong, F.A. and J. Hirst, *Reversibility and efficiency in electrocatalytic energy conversion and lessons from enzymes.* Proceedings of the National Academy of Sciences, 2011. **108**(34): p. 14049-14054.
109. Minson, M., M.T. Meredith, A. Shrier, F. Giroud, D. Hickey, D.T. Glatzhofer, and S.D. Minteer, *High Performance Glucose/O2 Biofuel Cell: Effect of Utilizing Purified Laccase with Anthracene-Modified Multi-Walled Carbon Nanotubes.* Journal of the Electrochemical Society, 2012. **159**(12): p. G166-G170.
110. Meredith, M.T., M. Minson, D. Hickey, K. Artyushkova, D.T. Glatzhofer, and S.D. Minteer, *Anthracene-Modified Multi-Walled Carbon Nanotubes as Direct Electron Transfer Scaffolds for Enzymatic Oxygen Reduction.* ACS Catalysis, 2011. **1**(12): p. 1683-1690.
111. Holzinger, M., A. Le Goff, and S. Cosnier, *Carbon nanotube/enzyme biofuel cells.* Electrochimica Acta, 2012. **82**(0): p. 179-190.
112. Gross, A.J. and A.J. Downard, *Regeneration of Pyrolyzed Photoresist Film by Heat Treatment.* Analytical Chemistry, 2011. **83**(6): p. 2397-2402.
113. del Campo, F.J., P. Godignon, L. Aldous, E. Pausas, M. Sarrión, M. Zabala, R. Prehn, and R.G. Compton, *Fabrication of PPF Electrodes by a Rapid Thermal Process.* Journal of the Electrochemical Society, 2011. **158**(1): p. H63-H68.
114. Rehacek, V., I. Hotovy, M. Vojs, M. Kotlar, T. Kups, and L. Spiess, *PYROLYZED PHOTORESIST FILM ELECTRODES FOR APPLICATION IN ELECTROANALYSIS.* Journal of Electrical Engineering-Elektrotechnicky Casopis, 2011. **62**(1): p. 49-53.
115. Ueda, A., D. Kato, R. Kurita, T. Kamata, H. Inokuchi, S. Umemura, S. Hirono, and O. Niwa, *Efficient Direct Electron Transfer with Enzyme on a Nanostructured Carbon Film Fabricated with a Maskless Top-Down UV/Ozone Process.* Journal of the American Chemical Society, 2011. **133**(13): p. 4840-4846.
116. Ranganathan, S., R. McCreery, S.M. Majji, and M. Madou, *Photoresist-Derived Carbon for Microelectromechanical Systems and Electrochemical Applications.* Journal of the Electrochemical Society, 2000. **147**(1): p. 277-282.

117. Fischer, D.J., W.R. Vandaveer, R.J. Grigsby, and S.M. Lunte, *Pyrolyzed Photoresist Carbon Electrodes for Microchip Electrophoresis with Dual-Electrode Amperometric Detection.* Electroanalysis, 2005. **17**(13): p. 1153-1159.
118. Falcão, D.S., V.B. Oliveira, C.M. Rangel, and A.M.F.R. Pinto, *Review on micro-direct methanol fuel cells.* Renewable and Sustainable Energy Reviews, 2014. **34**: p. 58-70.
119. Lu, G., C. Wang, T. Yen, and X. Zhang, *Development and characterization of a silicon-based micro direct methanol fuel cell.* Electrochimica Acta, 2004. **49**(5): p. 821-828.
120. Shah, K., W. Shin, and R. Besser, *A PDMS micro proton exchange membrane fuel cell by conventional and non-conventional microfabrication techniques.* Sensors and Actuators B: Chemical, 2004. **97**(2): p. 157-167.
121. Wang, Y., K.S. Chen, J. Mishler, S.C. Cho, and X.C. Adroher, *A review of polymer electrolyte membrane fuel cells: technology, applications, and needs on fundamental research.* Applied Energy, 2011. **88**(4): p. 981-1007.
122. Wang, Y., L. Pham, G.P.S. de Vasconcellos, and M. Madou, *Fabrication and characterization of micro PEM fuel cells using pyrolyzed carbon current collector plates.* Journal of Power Sources, 2010. **195**(15): p. 4796-4803.
123. Lee, J., K.G. Lim, G.T.R. Palmore, and A. Tripathi, *Optimization of microfluidic fuel cells using transport principles.* Analytical Chemistry, 2007. **79**(19): p. 7301-7307.
124. Bojorquez, J.P.E., *Microfabricated Fuel Cells as Power Sources for MEMS*. 2011: Universitat Autònoma de Barcelona.
125. Ferrigno, R., A.D. Stroock, T.D. Clark, M. Mayer, and G.M. Whitesides, *Membraneless Vanadium Redox Fuel Cell Using Laminar Flow.* Journal of the American Chemical Society, 2002. **124**(44): p. 12930-12931.
126. Atencia, J. and D.J. Beebe, *Controlled microfluidic interfaces.* Nature, 2005. **437**(7059): p. 648-655.
127. Brody, J.P., P. Yager, R.E. Goldstein, and R.H. Austin, *Biotechnology at low Reynolds numbers.* Biophysical journal, 1996. **71**(6): p. 3430-3441.
128. Kandlikar, S.G. and W.J. Grande, *Evolution of Microchannel Flow Passages--Thermohydraulic Performance and Fabrication Technology.* Heat Transfer Engineering, 2003. **24**(1): p. 3-17.
129. Lo, R.C., *Application of Microfluidics in Chemical Engineering.* Nature, 2013. **442**: p. 368-373.
130. Zebda, A., L. Renaud, M. Cretin, F. Pichot, C. Innocent, R. Ferrigno, and S. Tingry, *A microfluidic glucose biofuel cell to generate micropower from enzymes at ambient temperature.* Electrochemistry Communications, 2009. **11**(3): p. 592-595.
131. Kamholz, A.E., B.H. Weigl, B.A. Finlayson, and P. Yager, *Quantitative analysis of molecular interaction in a microfluidic channel: the T-sensor.* Analytical Chemistry, 1999. **71**(23): p. 5340-5347.
132. Minteer, S.D., H.R. Luckarift, and P. Atanassov, *Electrochemical Evaluation of Enzymatic Fuel Cells and Figures of Merit*, in *Enzymatic Fuel Cells*. 2014, John Wiley & Sons, Inc. p. 4-11.
133. Meredith, M.T. and S.D. Minteer, *Biofuel Cells: Enhanced Enzymatic Bioelectrocatalysis.* Annual Review of Analytical Chemistry, Vol 5, 2012. **5**: p. 157-179.
134. Kjeang, E., *Microfluidic Fuel Cells and Batteries*. 2014: Springer.
135. Shaegh, S.A.M., N.-T. Nguyen, and S.H. Chan, *An air-breathing microfluidic formic acid fuel cell with a porous planar anode: experimental and numerical investigations.* Journal of Micromechanics and Microengineering, 2010. **20**(10).

136. Yang, J., S. Ghobadian, P.J. Goodrich, R. Montazami, and N. Hashemi, *Miniaturized biological and electrochemical fuel cells: challenges and applications.* Physical Chemistry Chemical Physics, 2013. **15**(34): p. 14147-14161.
137. Hassanshahi, R. and M. Fathipour, *Improved Control of Concentration Boundary Layer in Microfluidic Fuel Cells.* International Journal of Renewable Energy Research (IJRER), 2013. **3**(4): p. 901-905.
138. Kjeang, E., N. Djilali, and D. Sinton, *Microfluidic fuel cells: A review.* Journal of Power Sources, 2009. **186**(2): p. 353-369.
139. Eibl, D. and R. Eibl, *Disposable Bioreactors II*. 2014: Springer Berlin Heidelberg.

SECTION I

ACTIVE MICROFLUIDIC FUEL CELLS AS LAB-ON-A-CHIP POWER SOURCES

Since their early appearance, the development of microfluidic devices was centred on the enhancement of analytical performance attained by the system miniaturization [1]. Further developments showed that the use of advanced microfluidic platforms also involved diminution of the reagents volume, higher automation and reduction of manufacturing costs. These promising features led to the birth of a new generation of microsystems able to perform a "total analysis" of a particular sample, the so called Lab-on-a-Chip (LoC) devices. Over the last 10–20 years, LoC devices have demonstrated their potential and benefits for many applications, including point-of-care diagnostics [2], genomic and proteomic research [3], analytical chemistry [4], environmental monitoring [5] and the detection of biohazards [6]. These miniaturized systems offer many advantages compared to bulkier and “historical” analytical instruments: they support precise control of liquids flowing usually under laminar regime, minimize consumption of reagents and samples, favour short reaction times, enable highly parallel and multiplexed analysis, require little

or less power to operate, are potentially portable, and if rapid prototyping techniques are used, have low cost of production [7-8].

Generally, most of these systems require external components such as pumps, power sources and control electronics to perform a complete sample analysis. These elements increase device complexity and limit portability and flexibility of the Lab-on-a-Chip (LoC) device. For this reason it is often mentioned that microfluidic chips are microscale devices coupled to macroscale experimental setups. In this sense, the achievement of a higher degree of integration of the ancillary components, especially micropumps and power sources, which are needed to run a microfluidic platform is currently being pursued to obtain totally autonomous devices [9].

One way of increasing the integration level of LoC systems is to directly integrate the power source inside the microfluidic platform. This implies that the power sources must be developed using the same materials and processes required in the fabrication of the microfluidic device. In this section, microfluidic fuel cell prototypes fabricated with materials and processes typically used in the development of LoC devices are presented.

I.I MATERIALS USED IN THE DEVELOPMENT OF MICROFLUIDIC DEVICES

Microfluidic platforms date from the early nineties, where MEMS technology allowed for the microstructuring of silicon and glass channels. However, they required heavy infrastructure to be implemented, such us etching procedures, originally developed for microelectronics industry. Starting the 2000's, to overcome the limitations that glass and silicon presented, a new generation of microfluidic devices based on polymeric materials emerged offering low-cost and fast production time devices [10]. Among polymeric materials, silicones such as PDMS (polydimethylsiloxane) [11] have been the most popular choice. The high biocompatibility, elasticity, low cost and simple manufacturing process made PDMS an ideal material for the construction of microfluidic channel structures [12-15] which were typically sealed by plasma treatment to a solid substrate harbouring the electrodes [16]. The fabrication of a PDMS structure is typically achieved by casting the PDMS on photolithographically patterned photoresists, however, any design change requires a repetition of the photolithographic process which represents a limiting step in the creation of microfluidic systems. In this context, the use of laminate materials provide a possible solution to the photolithography fabrication hurdles presented by PDMS. Microstructures can be patterned on laminate materials by using a cutting plotter (a plotter fit with a knife blade). This brings the possibility to fabricate rapid an inexpensive microfluidic devices out of clean rooms [17-19]. Moreover, the low cost of this kind of materials allow the affordability of devices to be disposable after a single use [19]. The most typically used laminated materials are thermoplastics, a kind of material that become deformable or flexible at relatively high temperature [20]. Among the most popular it can be find poly(methyl methacrylate) (PMMA) [21], polyethylene terephthalate (PET) [22], polypropylene (PP) [23], or cyclic olefin

(co)polymers (COC/COP) [24-28]. Another advantage of using thermoplastics is that the bonding process to obtain sealed layers can be easily performed by using thermal bonding or adhesives and glues that are incorporated directly on the laminated material [25, 29-30].

I.II NET POWER OF ACTIVE MICROFLUIDIC FUEL CELLS

Fuel cell systems require other sub-components to provide the necessary control over the processes involved in the energy conversion. These ancillary devices [31] are typically filters to remove contaminants, heaters to enhance catalytic reactions, thermal management systems or fluid pumps to supply the fuel.

In active microfluidic fuel cells, the laminar flow inside the microchannel is achieved by the use of external pressure systems such as syringe pumps being these the main power consumer in the fuel cell Balance of Plant (BoP). This pumping power (*W*) required to sustain the steady laminar flow in the microchannel can be estimated by the following equation [32];

$$W = \Delta p \cdot Q = \frac{32\mu LU}{D_h^2} Q \qquad \textbf{(I.1)}$$

where, Δp is the pressure drop, Q is the flow rate, μ is the dynamic viscosity, L is the length of the channel, U is the average velocity, D_h is the hydraulic diameter and the contributions from the inlets and outlets are neglecting.

The Balance of Plant represents a significant fraction of the weight and volume of most microfluidic fuel cell systems restricting severely the device portability, because these BoP components are usually bigger than the fuel cell itself. Consequently, the final overall net power output of the fuel cell to the external load (P_T) is impacted directly by the difference of the parasitic power consumed by the BoP devices (P_P) relative to the net power developed by the fuel cell (P_{FC}) [33].

$$P_T = P_{FC} - P_P \qquad \textbf{(I.2)}$$

If P_{FC} is not high enough, the parasitic power losses associated with the devices can reduce or even eliminate the advantage of using microfluidics for powering small-scale devices [33-35]. Therefore, to obtain net energy from the cell the power consumed by the balance of plant devices should be maintained as low as possible. The parasitic power (P_p) depends on the fuel cell technology and the type of auxiliary components employed for each fuel cell [36]. In this dissertation the fuel cell needs were kept to minimum only considering the pumping needs of electrolytes in the channel, keeping them as low as possible.

CONTENTS OF SECTION I

In **Chapter 2,** a microfluidic prototype partially fabricated with microfabrication technologies is presented achieving the first approximation of microfluidic devices working with enzymes. The main components of the device are: PDMS microchannels and gold electrodes over glass-based substrates. Biocatalysts are introduced into the system using a syringe pump allowing to obtain a co-laminar flow. The crossover of the streams was studied as well as the power generated from the fuel cell as a function of flow rate. The fuel utilization of the system was also evaluated and some reflexions about the viability of this device to be a commercial application are exposed.

Chapter 3 has been devoted to the improvement of the first microfluidic device exposed at chapter 2. Two fuel cells are fabricated using two types of electrode materials: gold or PPF and they are combined with a microchannel made on plastic. The use of plastic materials turns the system light, non-rigid and compatible with large-scale manufacturing. In this chapter enzymes have been immobilized at the electrode surfaces for a better use of the catalytic solutions. These solutions are introduced into the fuel cell using a syringe pump. The operation of the enzymatic fuel well was tested at different flow rates. In next chapters, the system simplification and the enhancement of power output has been addressed.

Table I.1 summarizes the achievements obtained in these chapters (in terms of current and power denisties):

Fuel Cell Type	Anode material	Anolyte	Cathode material	Catholyte	Flow rate ($\mu L\ min^{-1}$)	J_{max} ($\mu A\ cm^{-2}$) P_{max} (μWcm^{-2})	P_P (μWcm^{-2})	Chapter
Non-bioelectrode based and enzymes in solution	Gold	GOx and glucose	Gold	Laccase /ABTS/O_2	80	52.5 9	1.3	**2**
Bioelectrode based and microfluidic	GOx enzyme and the mediator Fc-C6-LPEI on gold	Glucose	MWCNT/ laccase/TB AB nafion on gold	O_2 (air sat.)	50	142 33	0.2	**3**
	GOx enzyme and the mediator Fc-C6-LPEI on PPF	Glucose	MWCNT/ laccase/TB AB nafion on PPF	O_2 (air sat.)	70	423 64	0.4	

Table I.1 Types of microfluidic fuel cells developed in Chapter 2 and Chapter 3 displaying the electrode material, the electrolytes and the maximum current, power and parasitic power densities obtained at a given flow rate.

REFERENECES

1. Manz, A., N. Graber, and H.á. Widmer, *Miniaturized total chemical analysis systems: a novel concept for chemical sensing.* Sensors and Actuators B: Chemical, 1990. **1**(1): p. 244-248.
2. Jung, W., J. Han, J.-W. Choi, and C.H. Ahn, *Point-of-care testing (POCT) diagnostic systems using microfluidic lab-on-a-chip technologies.* Microelectronic Engineering, 2015. **132**: p. 46-57.
3. Sanders, G.H. and A. Manz, *Chip-based microsystems for genomic and proteomic analysis.* TrAC Trends in Analytical Chemistry, 2000. **19**(6): p. 364-378.
4. Figeys, D. and D. Pinto, *Lab-on-a-chip: a revolution in biological and medical sciences.* Analytical chemistry, 2000. **72**(9): p. 330 A-335 A.
5. Gardeniers, J.G.E. and A. van den Berg, *Lab-on-a-chip systems for biomedical and environmental monitoring.* Analytical and bioanalytical chemistry, 2004. **378**(7): p. 1700-1703.
6. Yager, P., T. Edwards, E. Fu, K. Helton, K. Nelson, M.R. Tam, and B.H. Weigl, *Microfluidic diagnostic technologies for global public health.* Nature, 2006. **442**(7101): p. 412-418.
7. Mark, D., S. Haeberle, G. Roth, F. von Stetten, and R. Zengerle, *Microfluidic lab-on-a-chip platforms: requirements, characteristics and applications.* Chemical Society Reviews, 2010. **39**(3): p. 1153-1182.
8. Temiz, Y., R.D. Lovchik, G.V. Kaigala, and E. Delamarche, *Lab-on-a-chip devices: How to close and plug the lab?* Microelectronic Engineering, 2015. **132**: p. 156-175.
9. Sabaté, N., *Fuel cell-powered microfluidic platform for lab-on-a-chip applications.* Lab Chip, 2012. **12**: p. 74-79.
10. Becker, H. and L.E. Locascio, *Polymer microfluidic devices.* Talanta, 2002. **56**(2): p. 267-287.
11. McDonald, J.C. and G.M. Whitesides, *Poly(dimethylsiloxane) as a Material for Fabricating Microfluidic Devices.* Accounts of Chemical Research, 2002. **35**(7): p. 491-499.
12. McDonald, J.C., D.C. Duffy, J.R. Anderson, D.T. Chiu, H.K. Wu, O.J.A. Schueller, and G.M. Whitesides, *Fabrication of microfluidic systems in poly(dimethylsiloxane).* Electrophoresis, 2000. **21**(1): p. 27-40.
13. Sia, S.K. and G.M. Whitesides, *Microfluidic devices fabricated in poly(dimethylsiloxane) for biological studies.* Electrophoresis, 2003. **24**(21): p. 3563-3576.
14. Kjeang, E., N. Djilali, and D. Sinton, *Microfluidic fuel cells: A review.* Journal of Power Sources, 2009. **186**(2): p. 353-369.
15. Duffy, D.C., O.J.A. Schueller, S.T. Brittain, and G.M. Whitesides, *Rapid prototyping of microfluidic switches in poly(dimethyl siloxane) and their actuation by electro-osmotic flow.* Journal of Micromechanics and Microengineering, 1999. **9**(3): p. 211-217.
16. Reymond, F., J.S. Rossier, and H.H. Girault, *Polymer microchips bonded by O2-plasma activation.* Electrophoresis, 2002. **23**: p. 782-790.
17. Whitesides, G.M. and A.D. Stroock, *Flexible methods for microfluidics.* Physics Today, 2001. **54**(6): p. 42.
18. Yuen, P.K. and V.N. Goral, *Low-cost rapid prototyping of flexible microfluidic devices using a desktop digital craft cutter.* Lab on a Chip, 2010. **10**(3): p. 384-387.
19. Fredrickson, C.K., Z. Xia, C. Das, R. Ferguson, F.T. Tavares, and Z.H. Fan, *Effects of fabrication process parameters on the properties of cyclic olefin copolymer microfluidic devices.* Journal of Microelectromechanical Systems, 2006. **15**(5): p. 1060-1068.

20. Tominaka, S., H. Nishizeko, J. Mizuno, and T. Osaka, *Bendable fuel cells: on-chip fuel cell on a flexible polymer substrate.* Energy & Environmental Science, 2009. **2**(10): p. 1074-1077.
21. Chen, Y., L. Zhang, and G. Chen, *Fabrication, modification, and application of poly(methyl methacrylate) microfluidic chips.* Electrophoresis, 2008. **29**(9): p. 1801-1814.
22. Li, J.M., C. Liu, H.C. Qiao, L.Y. Zhu, G. Chen, and X.D. Dai, *Hot embossing/bonding of a poly(ethylene terephthalate) (PET) microfluidic chip.* Journal of Micromechanics and Microengineering, 2008. **18**(1).
23. Shim, J.S., W. Jung, C. Park, K.H. Kim, W. Chung, K. Namkoong, J.H. Kim, and N. Huh. *A low-cost valve and pump with polypropylene (PP) fabricated by uv/ozone-assisted thermal fusion bonding*. in *Proceedings of the 16th International Conference on Miniaturized Systems for Chemistry and Life Sciences, MicroTAS 2012*. 2012.
24. Azouz, A.B., S. Murphy, S. Karazi, M. Vazquez, and D. Brabazon, *Fast Fabrication Process of Microfluidic Devices Based on Cyclic Olefin Copolymer.* Materials and Manufacturing Processes, 2014. **29**(2): p. 93-99.
25. Lysko, J.M., D. Pijanowska, A. Baraniecka, M. Nieprzecki, and P. Grabiec, *Microfluidic devices for biomedical applications.* Przeglad Elektrotechniczny, 2012. **88**(3A): p. 212-214.
26. Illa, X., O. Ordeig, D. Snakenborg, A. Romano-Rodriguez, R.G. Compton, and J.P. Kutter, *A cyclo olefin polymer microfluidic chip with integrated gold microelectrodes for aqueous and non-aqueous electrochemistry.* Lab on a Chip, 2010. **10**(10): p. 1254-1261.
27. Jena, R.K. and C.Y. Yue, *Cyclic olefin copolymer based microfluidic devices for biochip applications: Ultraviolet surface grafting using 2-methacryloyloxyethyl phosphorylcholine.* Biomicrofluidics, 2012. **6**(1).
28. Piruska, A., I. Nikcevic, S.H. Lee, C. Ahn, W.R. Heineman, P.A. Limbach, and C.J. Seliskar, *The autofluorescence of plastic materials and chips measured under laser irradiation.* Lab on a Chip, 2005. **5**(12): p. 1348-1354.
29. Wang, X., D. Nilsson, and P. Norberg, *Printable microfluidic systems using pressure sensitive adhesive material for biosensing devices.* Biochimica et Biophysica Acta (BBA) - General Subjects, 2013. **1830**(9): p. 4398-4401.
30. Tsao, C.-W. and D.L. DeVoe, *Bonding of thermoplastic polymer microfluidics.* Microfluidics and Nanofluidics, 2009. **6**(1): p. 1-16.
31. Energy, U.S.D.o., ed. *Fuel Cell Handbook, seventh edition*. 2004, National Energy Technology Laboratory: Morgantown, WV.
32. Zebda, A., L. Renaud, M. Cretin, F. Pichot, C. Innocent, R. Ferrigno, and S. Tingry, *A microfluidic glucose biofuel cell to generate micropower from enzymes at ambient temperature.* Electrochemistry Communications, 2009. **11**(3): p. 592-595.
33. Gemmen, R. and C. Johnson, *Evaluation of fuel cell system efficiency and degradation at development and during commercialization.* Journal of Power Sources, 2006. **159**(1): p. 646-655.
34. Pei, P., M. Ouyang, Q. Lu, H. Huang, and X. Li, *Testing of an automotive fuel cell system.* International Journal of Hydrogen Energy, 2004. **29**(10): p. 1001-1007.
35. Elgowainy, A., L. Gaines, and M. Wang, *Fuel-cycle analysis of early market applications of fuel cells: Forklift propulsion systems and distributed power generation.* International Journal of Hydrogen Energy, 2009. **34**(9): p. 3557-3570.
36. Elgowainy, A. and M. Wang, *Fuel cycle comparison of distributed power generation technologies*. 2008, Argonne National Laboratory (ANL).

CHAPTER

2

Microfluidic biofuel cells based on solid glass substrates

The chapter presents a first approach to the development of a microfluidic fuel cell built on glass substrates, PDMS and gold electrodes. The components were fabricated with silicon microfabrication technologies and the enzymatic solutions were flown through the channel using a syringe pump. The suitability of the catalytic solutions was tested in separate electrochemical cells. Finally, the performance of the fuel cell was measured at different flow rates obtaining the best conditions for optimum power output and fuel utilization.

2.1 DESIGN AND FABRICATION

The device developed in this chapter can be divided in three parts; the microchannel, the electrodes and the external housing. The first step in the construction of the micro fuel cell was the fabrication of the Y-shaped microchannel in PDMS [1-2]. The next stage was to define the electrodes. Finally, an external casing was designed to place and fix all the previous components. Its main function was to prevent electrolyte leak from the device and to provide the necessary fluidic connections. Figure 2.1 shows a scheme of the device where its different components are identified.

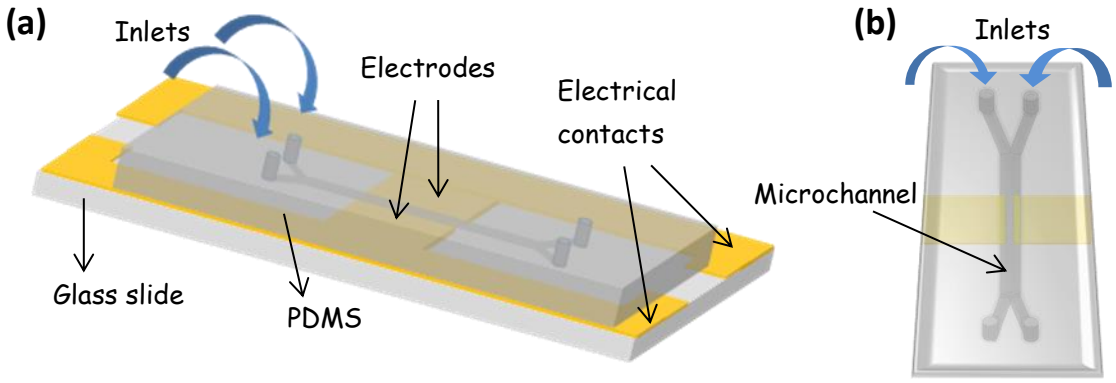

Figure 2.1 (a) Schematic representation of the microfluidic Y-shaped microfluidic fuel cell showing the main parts. (b) Top view of the microfluidic channel in PDMS.

2.1.1 Fabrication of the microchannel

Due to its many advantages such as flexibility, transparency, ease to mould and bio-compatibility and because it is the most widely used material in microfluidic device fabrication, PDMS was selected for the construction of the Y-shaped microfluidic channel. Structures in PDMS are typically fabricated using soft lithography techniques [3-4] that involve the replication of a master in this elastomer.

In this case, the fabrication process of the microfluidic channel began with the design of the SU-8 structures that were to be used as the PDMS mould. A low-resolution photolithographic mask was designed to generate a master. The layout drawing was made in AutoCAD software and printed afterwards on a plastic slide with a resolution of 3600 dpi.

The fabrication of the SU-8 structures comprised the following steps. First, a silicon wafer was dehydrated for 30 minutes at 200 °C. After cooling down the wafer, the surface was coated with a thin layer of SU-8 (2025) photoresist [5-7] using a spin coater (spinner *Karl Suss Delta 80*) applying a rotational speed of 3500 rpm for 45 seconds. These two parameters allow obtaining a thickness of 75 µm. This determines the height of the final PDMS microchannel. The wafer was then soft

baked in an oven in three different thermal steps. A first heating step of the wafer at 21 °C during 30 minutes was applied, then the wafer was heated again at 65 °C for 3 minutes and finally the temperature was increased to 95 °C for 15 additional minutes.

The SU-8 layer was exposed to 11 mW cm^{-2} of UV-light for 25 seconds in a *Karl Suss MA6* using the plastic photolithography mask previously defined. After the exposure, a post bake step in a hot plate consisting of 2 minutes at 65 °C and 10 minutes at 95 °C was performed. The resist was then developed by dipping the wafer into a bath of AZ R600 developer for approximately 45 seconds. In this way, the unexposed SU-8 regions were dissolved. The final stage was the hard bake process that consisted in introducing the wafer into the oven again for 2 minutes at 65 °C and 15 minutes more at 95 °C. At the end, the SU-8 master obtained was a positive relief of the microchannel. Figure 2.2 (a) shows the final silicon wafer with the SU-8 structures that were used as a master for fabricating the PDMS microchannels. The final dimensions of the microchannels were 25 mm in length, 4 mm in width and 75 µm of height.

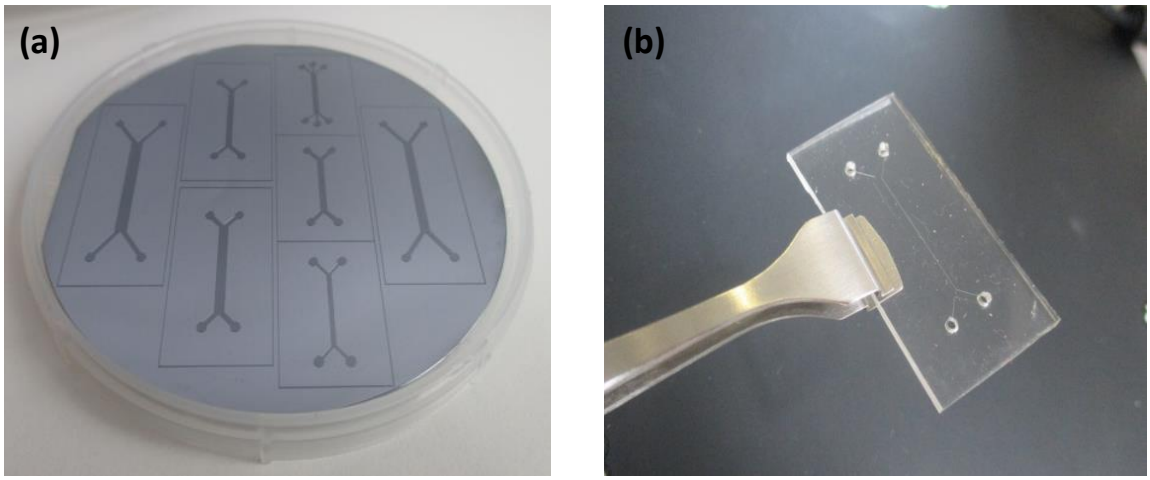

Figure 2.2 (a) Silicon wafer with some different designs of microchannels impressed on it. (b) Individual piece of PDMS cut from the silicon wafer once the PDMS as poured on it and cured. The holes correspond to the liquid inlet and outlet.

The PDMS elastomer, Syligard™ 184, was supplied as a two-part kit: a liquid silicone rubber base and a catalyst or curing agent, being 10:1 (w/w) the mixing ratio between them. Both parts were mixed and then poured over the SU-8 master. The wafer was then heated for 15 minutes at 150 °C in a hotplate. This allowed curing the liquid mixture and obtaining a solid PDMS microstructured slab. The PDMS slab was then peeled off from the master and cut into indivicual pieces. To allow tubing connexion, the patterned circles corresponding to the two inlets and two outlets of the PDMS microchannel were perforated using a 2 mm diameter biopsy punch. Figure 2.2 (b) shows a picture of the final PDMS microfluidic structure.

2.1.2 Fuel cell electrode construction

A microscope glass slide with dimensions of 75 mm by 26 mm and approximately 1 mm thickness was used as the device substrate. Electrodes were defined on this substrate and separated 1 mm from each other. The fabrication process is schematically represented in figure 2.3 (a) and described below.

First, the glass slide was coated with a gold layer of 100 nm over 15 nm titanium by sputtering metallization. After this, the samples were dehydrated for 10 minutes at 200°C and then the slides cooled down. Next, a positive photoresist (*6512*) was spin coated (spinner POLOS MCD TFM indeck) on the surface at 3500 rpm for 45 seconds. Straightaway, the slides were heated at 100°C for 15 minutes and then exposed to UV-light for 12 seconds in a *Suss MA 1006* mask aligner. The photomask used to pattern the electrodes is shown in figure 2.3 (b). After that, the slides were immersed in the resist developer (*OPD 4252*) bath to remove the unexposed parts. The slides were placed again in the oven for the hard bake process consisting of 10 minutes at 115°C. Metal etching was then performed with a solution containing iodine/iodide, that removes the layer of gold, and a solution of hydrogen fluoride/propylene glycol to remove the titanium layer. Once the electrode metallic structures were defined on the glass surface the remaining resist was removed with acetone.

2.1.3 Microfluidic device assembly

The Y-shaped PDMS-microchannel was bonded to the glass-slide substrate by previously applying an O_2 plasma treatment to both components [8-9]. Due to the small dimensions of the microchannel, the correct positioning of the PDMS on top of the gold electrodes was assisted with a magnifying glass. At the end, the PDMS microchannel was aligned to cover the same area of both electrodes. Figure 2.3 (c) displays the glass substrate with patterned titanium/gold electrodes and the PDMS-microchannel aligned on top of it.

Therefore, the ensemble electrode/microchannel was placed between two PMMA pieces to enable easy device handling. Furthermore, the PMMA-plates acted as a rigid interface for tubing connection with the syringe pump in charge of the supplying liquids and the microfluidic system. Figure 2.4 (a) shows the PMMA casing and the electrodes with the PDMS-channel.

The machining of the pieces was performed using a BASIC 540-16 CNC milling machine (*STEP-FOUR GmbH*). The different parts were made from a 5 mm-thick methacrylate plate obtaining final external dimensions of 5 cm x 7 cm. The holes for the screws at the edges were set to 4 mm diameter and inlets and outlets for tubing connexions were of 3 mm diameter. Finally, the system was assembled with screws. The pressure applied in the sandwich had to be adjusted carefully because if it exceeded a certain value it caused the deformation of the PDMS-microchannel which presented the correct flowing of the fuel cell electrolytes. By contrast, a too loose system resulted

in flow leakage at the liquid inlets. Electrical connections were available at the ends of the glass slide (as PMMA casing were designed to be 5 mm shorter). Figure 2.4 (b) shows an image of the double syringe pump (*NE-4000*) used during the fuel cell operation.

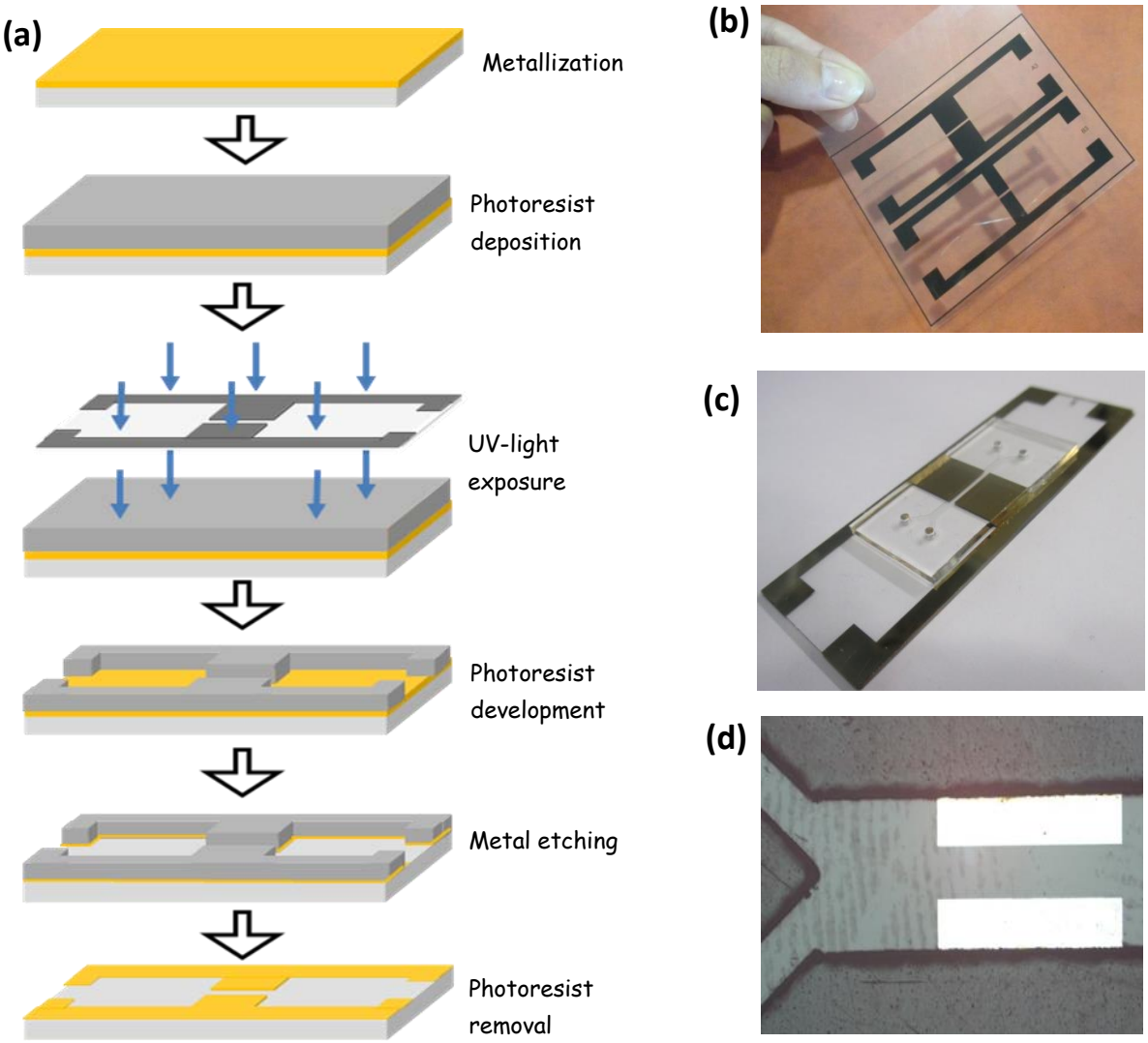

Figure 2.3 (a) Stages of the etching process. (b) Photomask used during the current collector lithography. (c) PDMS-microchannels over a glass slide with gold electrodes impressed and joined together by O_2 treatment. (d) Optical microscope image showing the aspect of the PDMS channel over the Ti/Au electrodes

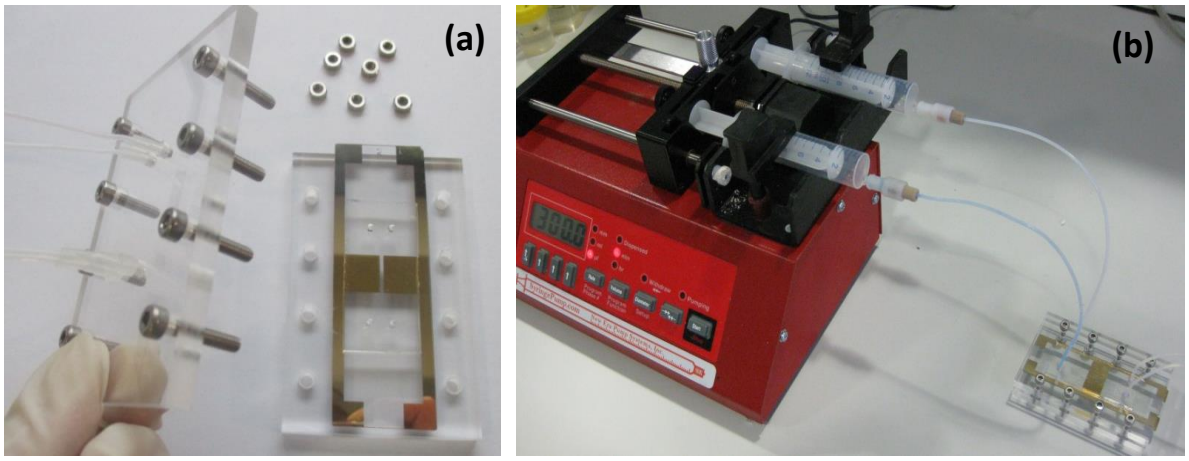

Fig 2.4 (a) Methacrylate pieces housing the electrodes and the PDMS-microchannel. (b) Syringe pump used during the performance measures of the fuel cell.

2.2 ENZYMATIC ANOLYTE AND CATHOLYTE CHARACTERIZATION

Before introducing the enzymes in the fuel cell, their performance was characterized in a separate electrochemical cell. The anolyte and the catholyte, that consisted of the enzymes and mediators dissolved along with the electrolyte, were tested in a three electrode system to analyze glucose oxidation and oxygen reduction reactions [10].

The anolyte used for the glucose oxidation was the mixture of the enzyme glucose oxidase (GOx, 5 mg ml^{-1}) and the ferrocenemethanol (FeMeOH, 2 mM) mediator in 100 mM phosphate buffer at pH 7. On the other hand, the catholyte for the oxygen reduction reaction combined the enzyme laccase and the ABTS mediator in 150 mM citrate buffer at pH 4.

2.2.1 Reagents and electrochemical set up

Glucose oxidase (GOx) type VII from *Aspergillus niger* (162 U mg^{-1}, EC 1.1.3.4, product reference G2133) and laccase produced by *Trametes versicolor* (13.6 U mg^{-1}, EC 1.10.3.2, product reference 51639), ABTS, FeMeOH and the salts for the buffers were purchased from Sigma Aldrich. Phosphate buffer was prepared with the mixing of; 8.5 g sodium nitrate ($NaNO_3$), 6.9 g of sodium phosphate monobasic ($NaH_2PO_4 \cdot H_2O$) and 7.0 g of sodium phosphate dibasic (Na_2HPO_4) to obtain a final concentration of 100 mM in 1 litter of distilled water. Citrate buffer was made by the combination of 11.0 g of sodium citrate dihydrate ($C_6H_5Na_3O_7 \cdot 2H_2O$) and 7.8 g of citric acid monohydrate ($C_6H_8O_7 \cdot H_2O$) in 1 litter of distilled water for finally obtaining a concentration of 150 mM. The pHs of the solutions were adjusted with HCl or NaOH. A stock solution of 1 M glucose (α-D(+)-Glucose) was prepared in distilled water at least 24 hours before use to establish the anomeric equilibrium between α and β forms of D-glucose [11].

All the experiments in this section were performed using a potentiostat μAutolab Type III and tests were carried out in phosphate buffer at pH 7 or citrate buffer at pH 4 as supporting electrolyte for the anolyte or catholyte measurements, respectively. For the electrochemical measurements in a three system mode a glassy carbon working electrode with 2 mm diameter, a commercial reference electrode of Ag/AgCl (3M) and a platinum counter electrode were used. Glassy carbon electrodes were polished carefully before each experiment with 0.05 μm alumina particles on cloth followed by rinsing with distilled water, then sonicated in acetone and dried in air before use.

2.2.2 Performance of glucose oxidase anolyte in solution phase

The enzyme glucose oxidase (GOx) along with the redox mediator FeMeOH were selected for carrying out the oxidation of the glucose. The mechanism of electron transfer taking place in the system glucose/GOx/FeMeOH follows the next steps [12]:

$$GOx\ (ox) + glucose \rightleftarrows GOx\ (red) + gluconolactone \quad \textbf{(2. 1)}$$

$$2FeMeOH^{+}(ox) + GOx\ (red) \rightleftarrows GOx\ (ox) + 2FeMeOH\ (red) \quad \textbf{(2. 2)}$$

$$FeMeOH\ (red) \rightleftarrows FeMeOH^{+}\ (ox) + e^{-} \quad \textbf{(2. 3)}$$

GOx reaction is divided into a reductive and an oxidative step. In the reductive half reaction, GOx catalyzes the oxidation of glucose to gluconolactone, which is non-enzymatically hydrolyzed to gluconic acid. In turn, the FAD ring of GOx is reduced to $FADH_2$ (GOx reduced). In the oxidative half reaction, the reduced GOx is reoxidized to FAD (GOx oxidized) by the redox mediator [13].

The theoretical redox potential for the GOx (from *Aspergillus Niger*) and for the FeMeOH are: -0.08 vs Ag/AgCl [14] and 0.21 V vs. Ag/AgCl [15], respectively. These values validate the potential of this combination to be a suitable couple for a mediated electron transfer because their redox potentials are quite close to each other. Another important aspect for a good mediation is that FeMeOH presents high electron transfer to the electrode. It can be evaluated from the electrochemical parameters involved in the voltammetric curves, e.g. peak potentials and peak currents as a function of scan rate in cyclic voltammetry as well as by the diffusion coefficient of the species.

The diffusion coefficient was measured by cyclic voltammetry in 100 mM phosphate buffer containing 2mM of FeMeOH. The range of scan rates explored was comprised between 5 mV s^{-1} and 100 mV s^{-1} and figure 2.5 (a) shows the voltammetries obtained. In each case, a well-defined oxidation peak was observed along with its corresponding reduction peak. The characteristic electrochemical parameters were extracted from the cyclic voltammograms and represented in table 2.1.

The i_p was plotted as a function of the square root of the scanning rate and a linear relationship was observed with a correlation coefficient of 0.99, figure 2.5 (b). This linear behaviour indicated a clear diffusion controlled process. Combining the slope of the fit, $b = \frac{i_p}{v^{1/2}} = 7.13 \cdot 10^{-5}$ A $V^{-1/2}$ $s^{1/2}$, with the Randles-Ševčik equation (equation 1.7) the diffusion coefficient for FeMeOH can be calculated. Using the electrode area of the glassy carbon electrode A=0.07 cm^2, n=1 the electrons exchange in the reduction/oxidation reaction of the FeMeOH and C the concentration of FeMeOH, 2 mM. Finally, the diffusion constant was found to be $D_{FeMeOH} = 4.36 \cdot 10^{-6}$ $cm^2 \cdot s^{-1}$, in accordance with previous reported values [16].

Looking at table 2.1 in more detail, at each scan rate, the ratio of the anodic peak current, ip_a, to the cathodic peak current, ip_c, was close to 1 and as stated before, ip_a and ip_c were proportional to $v^{1/2}$. Furthermore, the separation between peaks was ≈ 67 mV suggesting that the reaction was highly reversible. All these characteristics showed that mass transfer of FeMeOH to the electrode surface was diffusion-controlled. The fast reversible electron transfer along with its formal experimental potential of $E^{0'}$ ≈ 0.20 V indicated that FeMeOH was a good mediator when combined with the enzyme GOx and glucose.

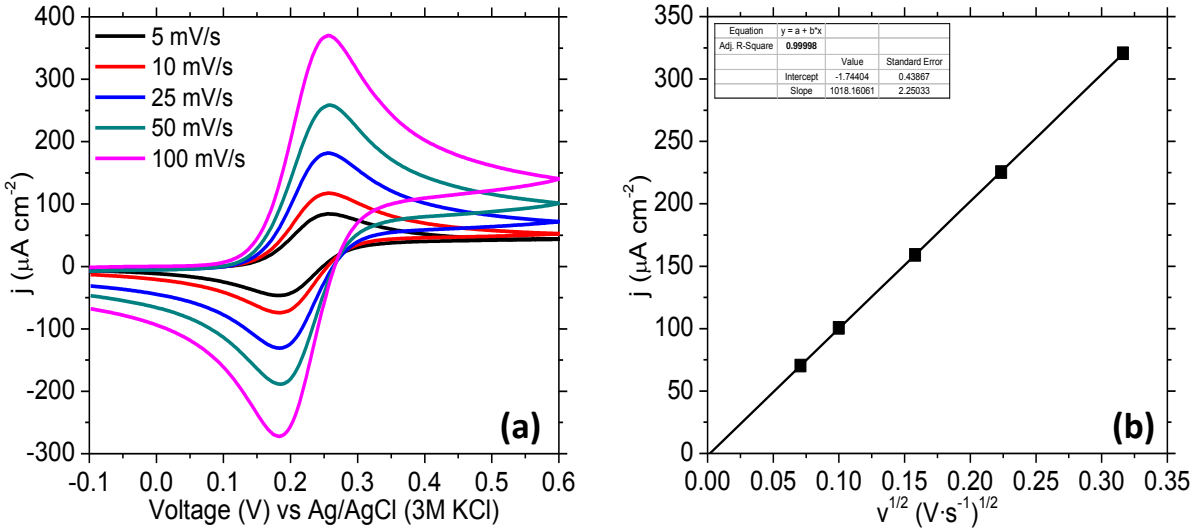

Figure 2.5 (a) Cyclic voltammetries responses at different scan velocities of 2 mM of FeMeOH in 100 mM phosphate buffer at pH 7 for a glassy carbon working electrode. (b) Intensity peak heights as a function of the square root of the scanning rate. Slope= $7.13 \cdot 10^{-5}$ A $V^{-1/2}$ $s^{1/2}$.

V (V/s)	E_{pa} (V)	I_{pa} (μA/cm^2)	E_{pc} (V)	$\lvert I_{pc} \rvert$ (μA/cm^2)	ΔE_p (V)	$E^{0'}$ (V)	i_{pa}/i_{pc}
0.005	0.255	$4.916 \cdot 10^{-6}$	0.184	$4.725 \cdot 10^{-6}$	0.070	0.204	1.041
0.010	0.255	$7.034 \cdot 10^{-6}$	0.188	$6.769 \cdot 10^{-6}$	0.074	0.206	1.039
0.025	0.255	$1.113 \cdot 10^{-5}$	0.188	$1.073 \cdot 10^{-5}$	0.070	0.206	1.037
0.050	0.255	$1.578 \cdot 10^{-5}$	0.188	$1.519 \cdot 10^{-5}$	0.071	0.206	1.038
0.100	0.255	$2.244 \cdot 10^{-5}$	0.188	$2.163 \cdot 10^{-5}$	0.072	0.206	1.037

Table 2.1 Electrochemical parameters obtained from voltammograms of figure 2.5 (a) showing the redox profiles of FeMeOH at different scan rates.

When 100 mM glucose were introduced into the system containing 2 mM FeMeOH in phosphate buffer at pH 7, no catalytic response was observed, figure 2.6 (a-1). The voltammogram obtained only exhibited a diffusion-controlled wave coming from the redox couple, FeMeOH. In contrast, the addition of 5 mg ml^{-1} GOx (corresponding to 810 units of enzyme per millilitre of buffer) displayed a very strong catalytic effect shown in figure 2.6 (a-2). This led to a sigmoidal response that at the same time caused the reduction peak to disappear. The catalytic process was fast as compared to diffusion predominating when only the mediator was in solution [17]. The catalytic electro-oxidation of glucose happened at approximately 10 mV vs Ag/AgCl reaching the plateau at ≈ 500 mV and 470 µA cm^{-2}.

The system was then purged with nitrogen to remove the potential interference of oxygen gas present in the solution and the current density increased to 630 µA cm^{-2}, figure 2.6 (a-3). Taking into account that the natural co-substrate of GOx is O_2 [18-19], the differences between voltammograms 2 and 3 were due to the oxygen competition against FeMeOH for the electrons produced by GOx from the oxidation of glucose. That demonstrated how O_2 in anolyte affected the response of the anode [20]. Moreover, if there is no oxygen present in solution the production of H_2O_2 is avoided [21-22].

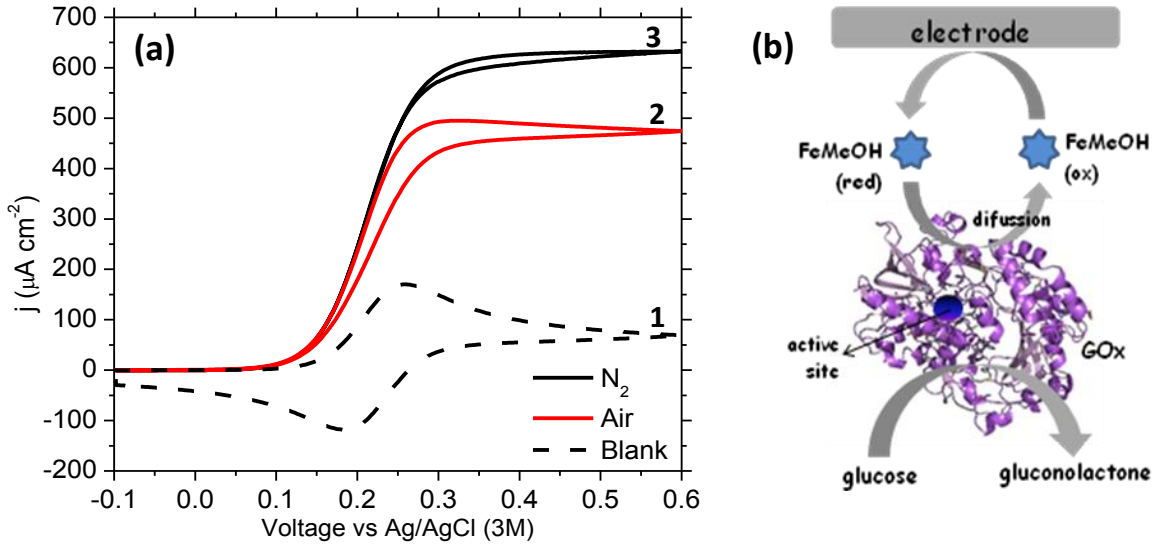

Figure 2.6 (a-1) Glassy carbon response of a solution containing 2 mM FeMeOH and 5 mg ml^{-1} GOx in 100 mM phosphate buffer at pH 7 at v_{scan}=0.025V s^{-1} (a-2) after the addition of 100 mM glucose in air saturated conditions (a-3) after the addition of 100 mM glucose in nitrogen saturated conditions. (b) Scheme of the electron transfer steps occurring at the electrode surface in a system containing FeMeOH, GOx and glucose.

2.2.3 Performance of laccase catholyte in solution phase

The ABTS mediator, with a theoretical redox potential of 0.47 V [23], was chosen for the mediation of the oxygen reduction reaction along with the laccase enzyme (from *Trametes Versicollor*) with redox potential around 0.58 V vs Ag/AgCl [24]. The process occurring at the surface of the electrode is schematically sketched in figure 2.8 (b) and the electronic path followed by the ABTS/laccase pair reducing the oxygen to water is summarized as follows;

$$ABTS^{+\cdot}(red) + Laccase\ (ox) \rightarrow Laccase\ (red) + ABTS\ (ox) \quad \textbf{(2. 4)}$$

$$Laccase\ (red) + \tfrac{1}{2} O_2 \rightleftarrows Laccase\ (ox) + H_2O \quad \textbf{(2. 5)}$$

$$ABTS\ (ox) + e^- \rightleftarrows ABTS^{+\cdot}(red) \quad \textbf{(2. 6)}$$

Interpreting the previous equations, laccase catalytically oxidizes the ABTS (equation 2.4). Then, oxygen is reduced by laccase (equation 2.5) and an electronic step involving the reduction and regeneration of the oxidized form of ABTS happens (equation 2.6).

In order to characterize the electrochemical behaviour of the ABTS, cyclic voltammetry experiments were carried out in a solution containing 150 mM citrate buffer at pH 4 and 0.1 mM ABTS. Figure 2.7 (a) shows the obtained curves measured at different scan rates ranging from 5 mV s^{-1} to 100 mV s^{-1}. It can be seen how anodic and cathodic peak currents increased as the scan rate was higher. This is because the diffusion layer thickness (depletion zone around the electrode) decreases with increasing scan rates and the current in the voltammogram is proportional to the flux of ABTS toward the electrode that is smaller at slow scan rates. From these voltammograms the most important parameters were extracted and summarized in table 2.2. The ratios for the anodic and cathodic peak heights were close to 1 as in a reversible process occurs. However, the difference between the ABTS oxidation peak potential (0.57 V) and the peak potential for the negative going scan (0.46 V) was $\Delta E_p \approx 0.14$ V. This value was almost triple the theoretical value for an ideal reversible system, 0.059 V. Therefore, the ABTS mediator follows a quasi reversible redox process [25-26]. Even though, it is known that ABTS undergoes rapid electron transfer on glassy carbon electrodes and therefore it will be a good option for the mediated electron transfer at the cathode [27-28]. Its experimental formal potential corresponds to 0.44 V that was obtained from the average of the redox potentials recorded for each scans rate.

Plotting the maximum peak currents, from figure 2.7 (a), as a function of the square root velocity a linear relation was obtained. The corresponding graphic is represented in figure 2.7 (b) and was adjusted with a linear fit obtaining a slope of $7.53 \cdot 10^{-6}$ A $V^{-1/2}$ $s^{1/2}$. Applying the Randles-Ševčik relation, the diffusion constant for the ABTS was determined, using n=1 for the number of electrons exchange between ABTS/$ABTS^{+\cdot}$, the surface of the glassy carbon working electrode 0.07 cm^2 and 0.1 mM the concentration of ABTS. Finally, D_{ABTS} was found to be $4.0 \cdot 10^{-6}$ cm^2 s^{-1}, in agreement with the literature $D_{ABTS} = 4.6 \cdot 10^{-6}$ cm^2 s^{-1} for a glassy carbon electrode in PBS at pH 4.4 [29].

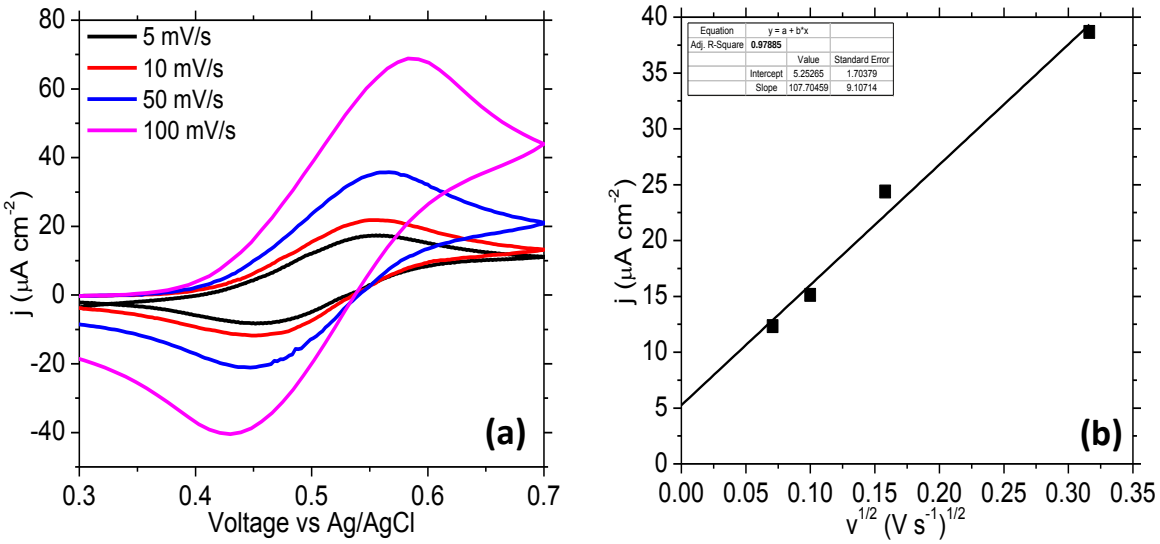

Fig 2.7 (a) Cyclic voltammograms of ABTS 0.1 mM at pH 4 in citrate buffer 150 mM at different scan velocities using a glassy carbon electrode. (b) Current peaks of ABTS as a function of the square root of the scanning rate. Slope= $7.5 \cdot 10^{-6}$ A $V^{-1/2}$ $s^{1/2}$.

v (V s^{-1})	E_{pa} (V)	I_{pa} (µA cm^{-2})	E_{pc} (V)	$\lvert I_{pc} \rvert$ (µA cm^{-2})	ΔE_p (V)	$E_{1/2}$ (V)	i_{pa}/i_{pc}
0.005	0.594	$8.240 \cdot 10^{-7}$	0.465	$9.001 \cdot 10^{-7}$	0.129	0.361	0.915
0.010	0.574	$9.990 \cdot 10^{-7}$	0.458	$1.118 \cdot 10^{-6}$	0.166	0.370	0.893
0.025	0.556	$1.596 \cdot 10^{-6}$	0.457	$1.818 \cdot 10^{-6}$	0.099	0.505	0.877
0.100	0.574	$2.336 \cdot 10^{-6}$	0.458	$3.078 \cdot 10^{-6}$	0.116	0.561	0.758

Table 2.2 Characteristics parameter from voltammetries of ABTS measured at different scan rates extracted from figure 2.7 (a).

Once the mediator was characterized, 5 mg ml^{-1} of laccase (equivalent to 68 units of enzyme each millilitre) were introduced into the buffer citrate at pH=4 previously containing 0.1 mM of ABTS. Figure 2.8 (a) shows the results with a disappearance of the anodic process due to the catalytic oxidation of the mediator, and a significant enlargement of the cathodic process related to the reduction of the oxidized form of the mediator generated by the enzymatic reaction.

The catalytic electro-reduction of O_2 began at 620 mV vs Ag/AgCl with 10 µA cm^{-2} and at 370 mV the plateau was achieved with a current density of -42 µA cm^{-2}. Then, the total current density obtained for the oxygen electro-reduction was found to be 52 µA cm^{-2}. This current can be enhanced by means of the increase of the enzyme amount or enhancing the content of oxygen present in solution.

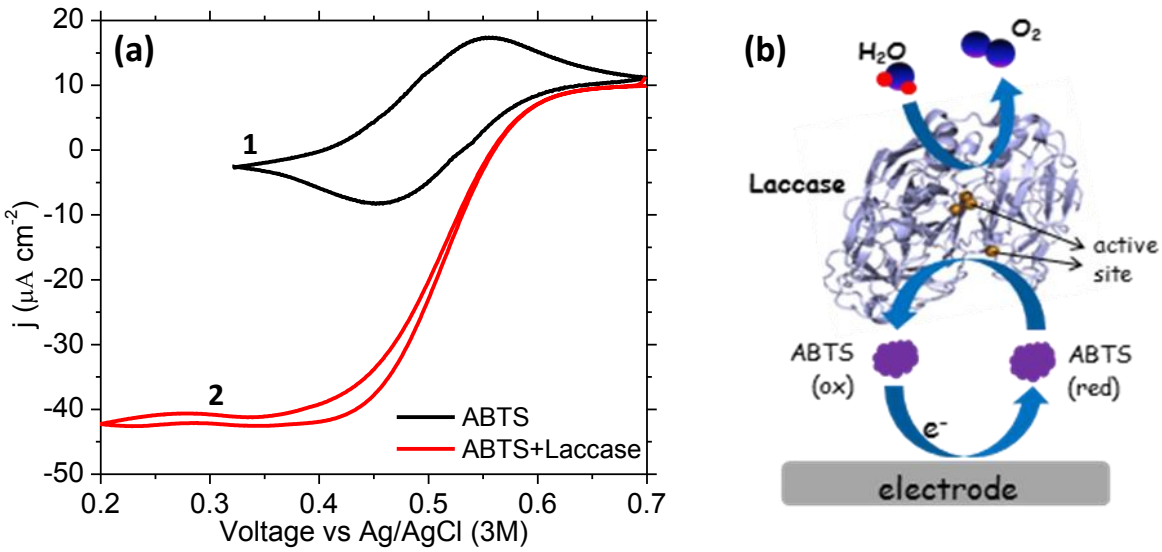

Figure 2.8 (a) Response of a glassy carbon electrode in 150 mM citrate buffer at pH 4 and 0.1 mM ABTS and 5 mg ml^{-1} laccase with v_{scan} = 0.025 V s^{-1} at room temperature (1) in N_2-saturated conditions (2) in air-saturated atmosphere. (b) Schematic representation of laccase-catalysed redox cycle in the presence of the redox mediator ABTS. Adapted from [30].

2.3 MICROFLUIDIC FUEL CELL PERFORMANCE

The anolyte and catholyte solutions tested in the previous sections were introduced in the microfluidic fuel cell presented in Section 2.1. As stated before, the fuel cell was based on a Y-shaped microfluidic channel that takes advantage of laminar flow to keep anolyte and catholyte physically separated. This fact allowed the use of two different stream compositions for fuel and oxidant and different solution pHs that ensured the optimal performance of each enzyme. Figure 2.9 schematically depicts the reactions taking place at each solution streams that will flow over the anode and cathode electrodes. For clarity, also the voltages associated with the reactions that were obtained experimentally in the previous section have been added.

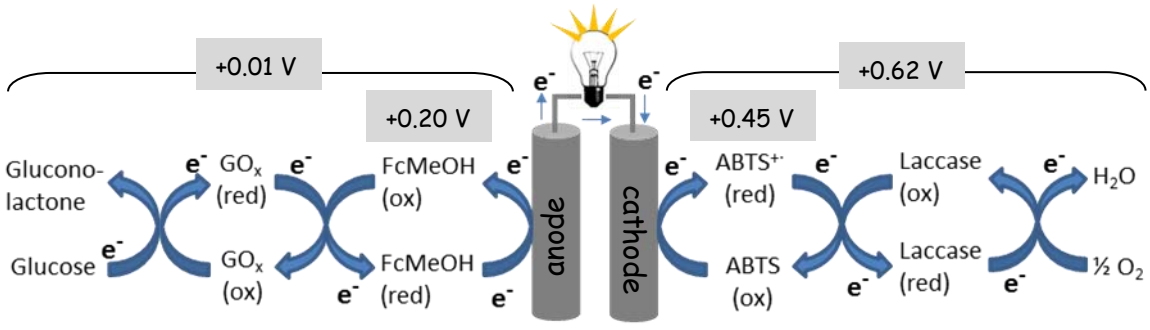

Figure 2.9 Electron transfer steps occurring at the bioanode and biocathode of the glucose/O_2 microfluidic fuel cell with the formal potentials of the enzymes and mediators. Redox mediators were chosen with a formal potential close to the enzymes because the open circuit potential will be partially controlled by them [31].

One important parameter to take into account when designing a microfluidic fuel cell is δ_{mix}, which is the thickness of the interdiffusion region that is established when the two parallel streams are put in contact (see equation 1.12). Generally, the mixing of anolyte and catholyte results in a negative effect on the fuel cell performance as unwanted species can interact directly with the electrodes and give rise to a parasitic current that diminishes the fuel cell output current. In this particular case, the species that can affect the fuel cell performance in case of reaching the electrode in the opposite of the channel were the mediators. The position of the electrodes of the fuel cell (of 10 mm in length) was already designed to be at the centre of the microchannel (length: 25 mm, width: 4 mm) and separated 1 mm from each other. The width of the mixing region in function of the distance to the inlets and the flow rate can be calculated to prevent interaction with the electrodes.

δ_{mix} was calculated for different flow rates ranging from 1 µl min^{-1} to 100 µl min^{-1}. Figure 2.10 shows a schematic top view of the fuel cell where the computed δ_{mix} profiles of the anode and cathode mediators (for the highest and lowest experimental flow rate values) were depicted. The mixing profile was calculated for ABTS because it was the mediator with faster diffusion coefficient. It can be seen that δ_{mix} becomes wider at decreasing flow rates. At 100 µl min^{-1} this region was very narrow but at 1 µl min^{-1}, δ_{mix} ranges from 450 µm at a distance of 7.5 mm to 1050 µm at 17.5 mm. Although there was an overlap of 50 µm at the end of the working electrodes, the effect of the mixing width was imperceptible. This means that even at the lowest tested flow rate, the mixing zone distance will not have any significant effect on the final power output of the fuel cell. Therefore, the degree of mixing of the two streams can be effectively controlled by tuning this parameter.

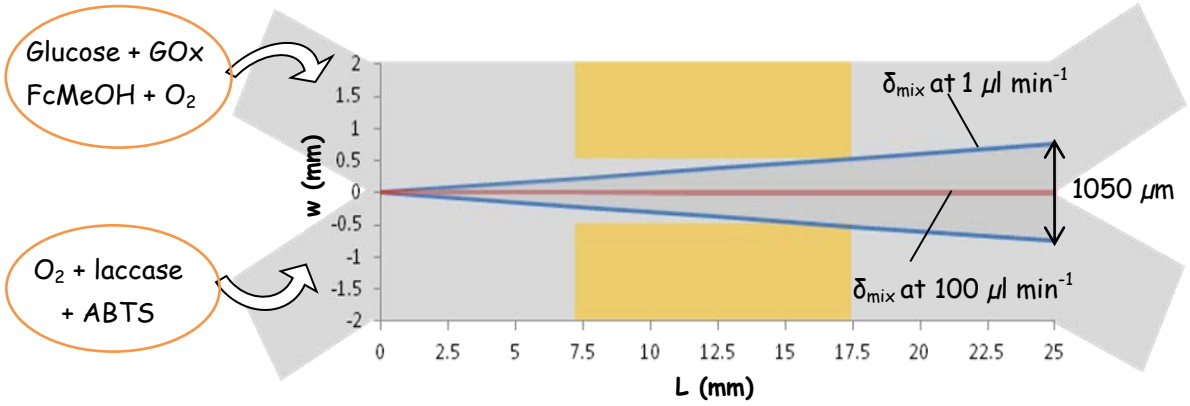

Figure 2.10 Top view of the fuel cell with the interfacial width (δ_{mix}) of the diffusive mixing represented for 1 µl min^{-1} (in blue) and 100 µl min^{-1} (in red). As flow rate increases, mixing zone becomes narrower.

2.3.1 Polarization and power curves

The microfluidic fuel cell performance was tested using a μAutolab Type III potentiostat. The measures were performed connecting the external counter and the reference electrodes to the fuel cell anode and working electrode to the cathode.

The polarization curves of the fuel cell were studied for flow rates ranging from 1 μl min^{-1} to an upper limit of 80 μl min^{-1} because at higher values the hydrodynamic pressure between PDMS-glass bonding caused leaks loses. The polarization curves, from figure 2.11 (a), show that the recorded open circuit potential corresponded to approximately 0.7 V, a little bit higher value than the 0.61 V expected from the individual CVs preformed in section 2.2.2 and 2.2.3. The maximum current density increased from 17 μA cm^{-2} at very low flow rates (1 μl min^{-1}) to 53 μA cm^{-2} at 80 μl min^{-1}. It can be observed that the concentration losses decrease when the convective transport (or pumping velocity) was increased. These concentration losses were related to the low concentration of oxygen dissolved in the electrolyte solution, 0.10 mM [32] as individual voltammetries showed that there was a difference of an order of magnitude between the GOx and laccase activities being the cathode the limiting electrode in the fuel cell performance. The power curves of the fuel cell are displayed in figure 2.11 (b) and the power output reached a maximum power density of 9 μW cm^{-2}, corresponding to an operational voltage of 0.25 V. The power required to pump the solution at 80 μl min^{-1} was calculated using equation I.1 (in Section I) and the parasitic power obtained was 1.3 μA cm^{-2}. Therefore, the real power it can be achieved form the fuel cell was 7.7 μW cm^{-2} and this represents a 15 % less than the maximum power extracted from figure 2.11.

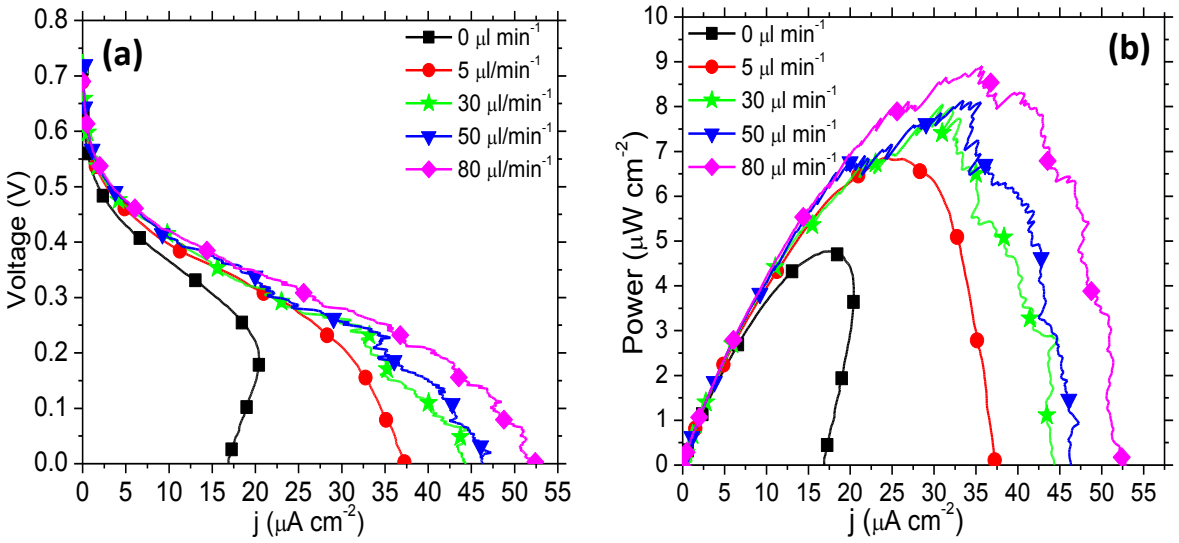

Figure 2.11 Plots generated from the microfluidic glucose/O_2 biofuel cell at different flow rates. At the anode glucose is oxidised by the GOx in the presence of the redox mediator FeMeOH. In the cathode, oxygen is reduced by the laccase in the presence of the redox mediator ABTS. v_{scan}= 1 mV s^{-1}. (a) Polarization curves. (b) Power curves.

High flow rates lead to higher power outputs but at the same time it may happen that a significant fraction of fuel cross the microchannel without being consumed by the electrodes, thus resulting in a reduction in fuel utilization (*FU*). The relevance of this contribution has been calculated by applying equation 2.7.

$$FU = \frac{I}{nFCv_{flow}} \tag{2.7}$$

where, *I* is the current measured at 0.25 V from figure 2.11 (a), *n*=2 the number of electrons exchanged by glucose, *F* the Faraday constant (96485 C mol^{-1}), *C* the concentration of the inlet glucose solution, 100 mM and v_{flow} the flow velocity in each case. Figure 2.12 shows the fuel utilization and the maximum power delivered by the fuel cell versus flow rate. It can be seen that the fuel utilization decreases as flow rate increases reaching a minimum of 0.3 % at 80 µl min^{-1}. On the contrary, fuel utilization rises up to 13% at the minimum tested flow rate of 1 µl min^{-1}. An optimized microfluidic fuel cell should balance fuel utilization with high output power. As shown in figure 2.12, a balanced fuel cell performance will be obtained at the crossing point between maximum power and fuel utilization lines, which was achieved at 3 µl min^{-1}. In the case in which the fuel costs are not relevant, it will be preferable to operate the fuel cell at faster flow rates so the power output requirements for a specific application can be obtained.

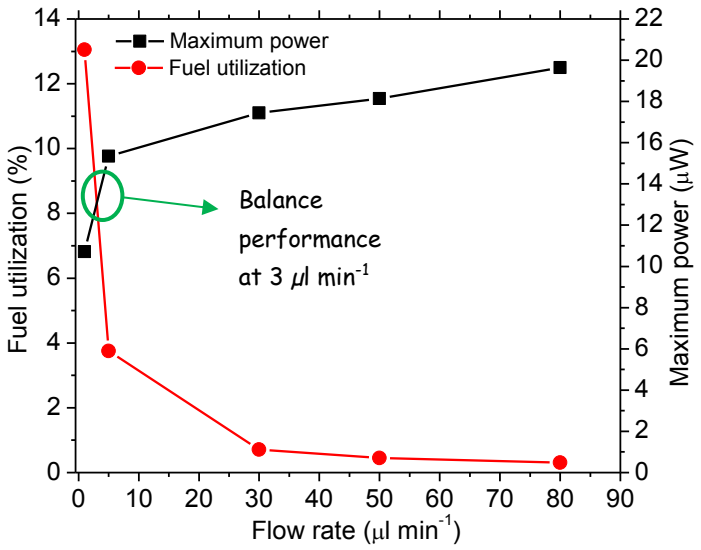

Figure 2.12 Fuel utilization as a function of the flow rate. Although lower flow rates utilize fuel more efficiently, maximum power is compromised.

2.4 SUMMARY AND CONCLUSIONS

In this chapter a glass-based microfluidic glucose/O_2 biofuel cell was presented. At the anode, glucose was oxidized by the enzyme GOx and electron transfer was mediated with FeMeOH. At the cathode, laccase enzyme with ABTS mediator reduced the O_2 to water. The components of the device presented, namely the electrodes and the microchannel, were partially fabricated with microfabrication technologies. The system was then completed using standard soft lithography procedure to build the channel in poly(dimethylsiloxane) (PDMS).

Before the assembly of the complete fuel cell, reactions taking place at the anode and at the cathode were studied separately by cyclic voltammetry in a three-electrode cell. The oxidation and reduction potentials of the couples GOx/FeMeOH and laccase/ABTS were determined to be appropriate for constituting the anolyte and the catholyte of the fuel cell.

The two solutions were introduced the Y-shaped microfluidic fuel cell using a double syringe-pump. The diffusive mixing region between the two streams flowing in parallel was studied for flow rates comprised between 1 µl min^{-1} and 100 µl min^{-1}. It was verified that there was no cross-over affecting the performance of the fuel cell. From these results, the fuel cell performance was tested obtaining that at 80 µl min^{-1} the current density was 53 µA cm^{-2} and the power density was set at 9 µW cm^{-2}. On the other hand, the power required to pump the solutions inside the fuel cell was found to be 1.3 µW cm^{-2} and this represents the 15 % of the net power output. The fuel utilization for these flow rates was also studied and the optimum balance of fuel cell was determined to be at 3 µl min^{-1}.

The work carried out in this chapter accounts for a successful first approximation of a microfluidic device running with enzymes flowing in solution. The device was simple and fast to fabricate and made possible the first electrochemical measurements with enzymes. In general, microfluidic fuel cells present relatively poor fuel utilization. Moreover, for this particular case biocatalysts were constantly flowing through the channel of the fuel cell therefore the device loses viability to be a commercial application because the utilization of enzymes along with the fuel makes the experiment very costly. In that case, the recirculation of the enzymatic solution could be an interesting solution but due to the mixing of solutions at the end of the channel it would be of interest to fabricate systems that work with single mixed anolyte and catholyte solutions. However, the best way to decrease the cost of power generation would be the immobilization of the catalytic solutions over the electrodes, being the fuel (glucose) and oxygen the only components continuously supplied to the fuel cell. This approximation will be addressed in the following chapters of the present dissertation.

REFERENCES

1. Zebda, A., L. Renaud, M. Cretin, C. Innocent, R. Ferrigno, and S. Tingry, *Membraneless microchannel glucose biofuel cell with improved electrical performances.* Sensors and Actuators B: Chemical, 2010. **149**(1): p. 44-50.
2. Zebda, A., L. Renaud, M. Cretin, F. Pichot, C. Innocent, R. Ferrigno, and S. Tingry, *A microfluidic glucose biofuel cell to generate micropower from enzymes at ambient temperature.* Electrochemistry Communications, 2009. **11**(3): p. 592-595.
3. Xia, Y. and G.M. Whitesides, *Soft Lithography.* Annual Review of Materials Science, 1998. **28**(1): p. 153-184.
4. Qin, D., Y. Xia, and G.M. Whitesides, *Soft lithography for micro- and nanoscale patterning.* Nat. Protocols, 2010. **5**(3): p. 491-502.
5. Jo, B.H., L.M. Van Lerberghe, K.M. Motsegood, and D.J. Beebe, *Three-dimensional micro-channel fabrication in polydimethylsiloxane (PDMS) elastomer.* Journal of Microelectromechanical Systems, 2000. **9**(1): p. 76-81.
6. Lorenz, H., M. Despont, N. Fahrni, N. LaBianca, P. Renaud, and P. Vettiger, *SU-8: a low-cost negative resist for MEMS.* Journal of Micromechanics and Microengineering, 1997. **7**(3): p. 121-124.
7. Friend, J. and L. Yeo, *Fabrication of microfluidic devices using polydimethylsiloxane.* Biomicrofluidics, 2010. **4**(2): p. 026502.
8. Sun, M., G. Velve Casquillas, S. Guo, J. Shi, H. Ji, Q. Ouyang, and Y. Chen, *Characterization of microfluidic fuel cell based on multiple laminar flow.* Microelectronic Engineering, 2007. **84**(5): p. 1182-1185.
9. Duffy, D.C., O.J.A. Schueller, S.T. Brittain, and G.M. Whitesides, *Rapid prototyping of microfluidic switches in poly(dimethyl siloxane) and their actuation by electro-osmotic flow.* Journal of Micromechanics and Microengineering, 1999. **9**(3): p. 211-217.
10. Andrieux, C.P., C. Blocman, J.M. Dumas-Bouchiat, F. M'Halla, and J.M. Savéant, *Homogeneous redox catalysis of electrochemical reactions: Part V. Cyclic voltammetry.* Journal of Electroanalytical Chemistry and Interfacial Electrochemistry, 1980. **113**(1): p. 19-40.
11. Bronsted, J.N. and E.A. Guggenheim, *Contribution to the theory of acid and basic catalysis. The mutarotation of glucose.* Journal of the American Chemical Society, 1927. **49**: p. 2554-2584.
12. Shan, D., W. Yao, and H. Xue, *Electrochemical study of ferrocenemethanol-modified layered double hydroxides composite matrix: Application to glucose amperometric biosensor.* Biosensors and Bioelectronics, 2007. **23**(3): p. 432-437.
13. Leskovac, V., S. Trivic, G. Wohlfahrt, J. Kandrac, and D. Pericin, *Glucose oxidase from Aspergillus niger: the mechanism of action with molecular oxygen, quinones, and one-electron acceptors.* International Journal of Biochemistry & Cell Biology, 2005. **37**(4): p. 731-750.
14. Vogt, S., M. Schneider, H. Schäfer-Eberwein, and G. Nöll, *Determination of the pH dependent redox potential of glucose oxidase by spectroelectrochemistry.* Analytical chemistry, 2014. **86**(15): p. 7530-7535.
15. Ahonen, P., V. Ruiz, K. Kontturi, P. Liljeroth, and B.M. Quinn, *Electrochemical gating in scanning electrochemical microscopy.* The Journal of Physical Chemistry C, 2008. **112**(7): p. 2724-2728.

16. Pearson, A. and A.P. O'Mullane, *Nanoparticle-electrode collisions as a dynamic seeding route for the growth of metallic nanostructures.* Chemical Communications, 2015. **51**(25): p. 5410-5413.
17. Bourdillon, C., C. Demaille, J. Moiroux, and J.M. Saveant, *New insights into the enzymic catalysis of the oxidation of glucose by native and recombinant glucose oxidase mediated by electrochemically generated one-electron redox cosubstrates.* Journal of the American Chemical Society, 1993. **115**(1): p. 1-10.
18. Bartlett, P.N., P. Tebbutt, and R.G. Whitaker, *Kinetic aspects of the use of modified electrodes and mediators in bioelectrochemistry.* Progress in Reaction Kinetics, 1991. **16**(2): p. 55-155.
19. Kavanagh, P. and D. Leech, *Mediated electron transfer in glucose oxidising enzyme electrodes for application to biofuel cells: recent progress and perspectives.* Physical Chemistry Chemical Physics, 2013. **15**(14): p. 4859-4869.
20. Beh, S.K., G.J. Moody, and J.D.R. Thomas, *Studies on enzyme electrodes with ferrocene and carbon paste bound with cellulose triacetate* Analyst, 1991. **116**(5): p. 459-462.
21. Bankar, S.B., M.V. Bule, R.S. Singhal, and L. Ananthanarayan, *Glucose oxidase — An overview.* Biotechnology Advances, 2009. **27**(4): p. 489-501.
22. Valdes, T.I. and F. Moussy, *In vitro and in vivo degradation of glucose oxidase enzyme used for an implantable glucose biosensor.* Diabetes technology & therapeutics, 2000. **2**(3): p. 367-76.
23. Bourbonnais, R., D. Leech, and M.G. Paice, *Electrochemical analysis of the interactions of laccase mediators with lignin model compounds.* Biochimica et Biophysica Acta (BBA)-General Subjects, 1998. **1379**(3): p. 381-390.
24. Ivnitski, D. and P. Atanassov, *Electrochemical studies of intramolecular electron transfer in laccase from Trametes versicolor.* Electroanalysis, 2007. **19**(22): p. 2307-2313.
25. Evans, D.H., *Theory for a homogeneous reaction following a quasireversible electrode reaction.* The Journal of Physical Chemistry, 1972. **76**(8): p. 1160-1165.
26. Bourbonnais, R., D. Leech, and M.G. Paice, *Electrochemical analysis of the interactions of laccase mediators with lignin model compounds.* Biochimica Et Biophysica Acta-General Subjects, 1998. **1379**(3): p. 381-390.
27. Palmore, G.T.R. and H.-H. Kim, *Electro-enzymatic reduction of dioxygen to water in the cathode compartment of a biofuel cell.* Journal of Electroanalytical Chemistry, 1999. **464**(1): p. 110-117.
28. Farneth, W.E., B.A. Diner, T.D. Gierke, and M.B. D'Amore, *Current densities from electrocatalytic oxygen reduction in laccase/ABTS solutions.* Journal of Electroanalytical Chemistry, 2005. **581**(2): p. 190-196.
29. Zeng, H., Z.-q. Tang, L.-w. Liao, J. Kang, and Y.-x. Chen, *Electrochemistry of ABTS at Glassy Carbon Electrodes.* Chinese Journal of Chemical Physics, 2011. **24**(6): p. 653-658.
30. Barton, S.C., J. Gallaway, and P. Atanassov, *Enzymatic biofuel cells for Implantable and microscale devices.* Chemical Reviews, 2004. **104**(10): p. 4867-4886.
31. Brunel, L., J. Denele, K. Servat, K.B. Kokoh, C. Jolivalt, C. Innocent, M. Cretin, M. Rolland, and S. Tingry, *Oxygen transport through laccase biocathodes for a membrane-less glucose/O2 biofuel cell.* Electrochemistry Communications, 2007. **9**(2): p. 331-336.
32. Bourbonnais, R., D. Leech, and M.G. Paice, *Electrochemical analysis of the interactions of laccase mediators with lignin model compounds.* Biochimica et Biophysica Acta (BBA) - General Subjects, 1998. **1379**(3): p. 381-390.

CHAPTER

3

Microfluidic biofuel cells based on flexible plastic substrates

This chapter describes the fabrication of a flexible and lightweight enzymatic device utilizing plastic materials and a combination of microfabrication and rapid prototyping techniques. Enzyme catalysts were immobilized over the electrodes of the fuel cell as a way to improve the enzymatic lifetime and decrease the cost involved in the power generation at small scale.

3.1 DESIGN, FABRICATION OF THE MICROFLUIDIC FUEL CELLS

The present section describes the design and fabrication of two glucose/oxygen microfluidic fuel cells. They were made utilizing a cutter plotter and laminated and flexible thermoplastic materials and used gold and pyrolyzed photoresist film (PPF) as electrode material. Moreover, between the first and the second system an important technological evolution has been achieved obtaining a compact fuel cell closer to a commercial device.

3.1.1 Rapid prototyping of microfluidic fuel cells

The use of laminated materials is relatively new in the fabrication of microfluidic devices, a field dominated by PDMS [1-2]. Although PDMS is an easily accessible and very affordable material ideally suited for the research laboratory, laminated materials allow for mass production using roll-to-roll processes [3-4]. The advantage of this approach compared to using PDMS is that masters and/or moulds are unnecessary and the fabrication process becomes continuous rather than in batches. In addition, the wide range of laminated materials available in the market allow for much more functionality and applicability than PDMS [5-7]. Consequently and resulting from its low cost, industry efforts have been put in the development of thermoplastic polymeric materials amenable for commercial and mass production [8]. Following this trend, in the present case, flexible and laminated thermoplastic materials have been selected for the construction of microfluidic fuel cell systems.

In the context of rapid prototyping of microfluidics, the most common fabrication method is *Xurograpghy*, which uses a cutting plotter to produce (micro)structures in flexible thermoplastic materials [9-11]. The benefits of using a cutting plotter over other prototyping methods are: (i) the flexibility of materials it can use (ii) the cost and the speed of fabrication that is a crucial advantage for rapid prototyping in LOC applications. Shortening the fabrication phase of a device leads to accelerate the design-fabrication-test cycle and therefore the product can be taken to market faster.

The type of thermoplastic material selected for a microfluidic device is an important aspect to take into account and depends on the features size of the channel and the resistance to chemicals needed in the microfluidic application. In general, the minimum feature size that can be defined by the cutting depends on material properties such as film thickness and the film hardness as well as on the blade used to cut it.

The most used thermoplastic materials for the construction of microfluidic devices are standard vinyl and cyclic olefin polymeric films (COP). Vinyl is a softer and easier to cut and can possess adhesive layers, in contrast to COP, which makes the staking process of a device very simple [12].

COP films normally display excellent optical properties, high chemical stability, resistance to acids, alkalis and most organic polar solvents (such as acetone, methanol, and isopropyl alcohol) [13].

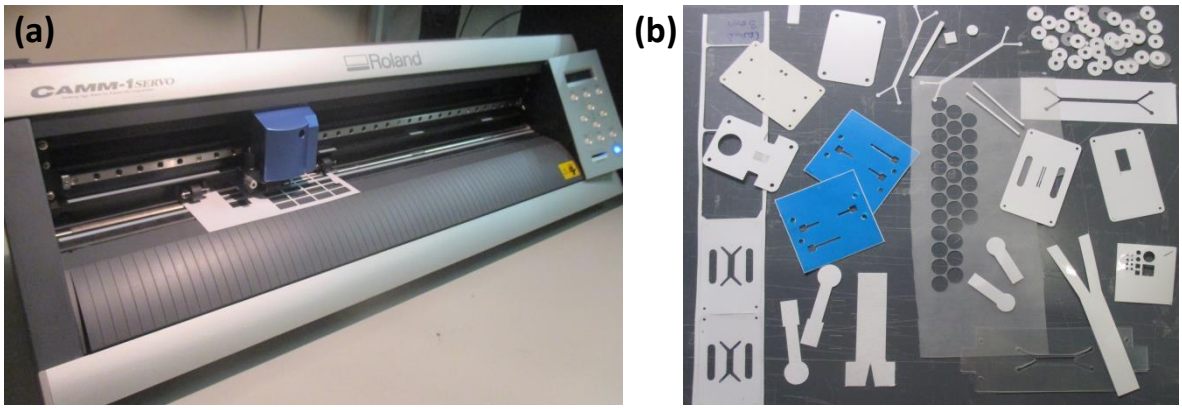

Figure 3.1 (a) Cutting plotter used for the fabrication of the different layers of the microfluidic devices. (b) Diverse structures performed by the cutter plotter in different thermoplastic materials.

For our microfluidic application, mild reagents were used and consequently both materials were suitable for the construction of the fuel cells. A combination of COP and adhesive vinyl substrates were used, in particular; Zeonex cyclo-olefin polymers, ZF14-100 and ZF14-188 sheets, purchased from Ibidi GmbH and AR8259, AR8939, and AR9067 adhesives obtained from Adhesives Research Europe. A *Roland GX-24* cutting plotter, with a mechanical resolution of 0.001 cm, was used and it is shown in figure 3.1 (a). Previously, device designs were generated with *Adobe Illustrator* and then loaded onto the cutter software (*Roland CutStudio™*).

3.1.2 Microfluidic fuel cell based on gold electrodes

The first microfluidic system fabricated in this chapter utilized gold electrodes impressed over COP substrates. The fuel cell was formed by two more layers, one of them incorporating the microchannels. In next paragraphs, the description of the process to obtain the final device is described.

3.1.2.1 Fuel cell electrode construction

COP substrates, with dimensions of 75 mm x 25 mm, were cut from a 100 µm thick sheet. The conditions applied to the cutting plotter were 250 grams-force and 1 cm s^{-1} of cutting speed. The substrates were then metalized with a layer of 150 nm of gold over a layer 15 nm of titanium by sputtering. Later, photolithography was applied to define the desired shape of electrodes on the surface of the metalized gold substrates. The process was similar to that described in Chapter 2, but adapted to thermoplastic substrates. The main steps of photolithography can be summarized

as follows: (1) The metalized COP slides were introduced in the oven for 30 minutes at 100°C to remove the moisture from their surface. (2) Resist (6512) was spin coated on the surface of the COP substrates at 3500 rpm for 45 seconds with a spinner *POLOS MCD TFM indeck*. (3) After that, the samples were placed into the oven for 30 minutes at 100 °C to evaporate the solvent in the resist and to densify it. (4) The slides were then exposed to the UV light in a *Suss MA 1006* aligner for 13 seconds by using a photomask (*Leicrom*, Spain) with a pattern of the electrodes. (5) At the post exposure baking, the slide was introduced in the oven 10 minutes more at 100 °C. (6) Then, the exposed resist was removed from the surface by stirring the substrate for 30 seconds in the developer solution (*AZ R600*). (7) The last step was a hard baking that consisted of heating the sample again into the oven for 30 minutes at 115°C. This process toughens the photoresist and improves the adhesion to the metalized COP-substrate. The metal etching was then accomplished sinking the sample in a solution containing iodine/iodide followed by hydrogen fluoride/propylene glycol solution for removing the layer of gold and titanium, respectively. The resist remaining was extracted with acetone. Figure 3.2 shows the patterned electrodes over a COP slide in which the electrodes, of 10 mm length, have been positioned in parallel in the middle of the substrate with an inter-electrode gap of 1 mm.

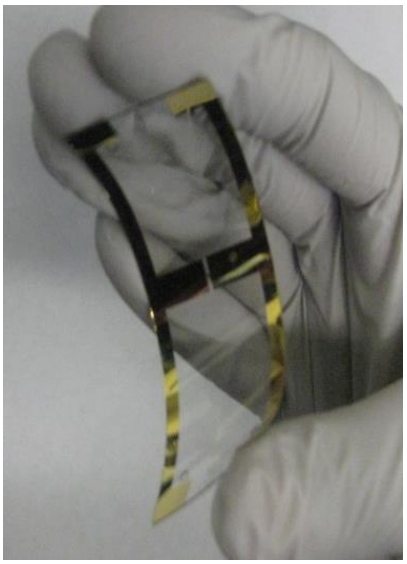

Figure 3.2 Demonstration of the flexibility of the COP substrate where gold electrodes have been impressed

3.1.2.2 Microchannel and cover system

The microfuel cell channel and the cover layer were cut with external dimensions of 75 mm x 25 mm to fit with the gold electrodes previously fabricated onto a COP substrate. This material was also used for the cover layer of the system. The microchannel was implemented using 130 µm thick double-sided pressure-sensitive adhesive (PET, AR8939). The dimensions of the microfluidic Y-shaped channel were 25 mm long and 3 mm wide. The conditions set to the cutting plotter for

the PSA material were 120 grams-force at 1 cm s^{-1}. Additionally, inlets and outlets for external tubing connection were perforated on the COP cover layer. Figure 3.3 (a) shows the different parts forming the microfluidic fuel cell.

3.1.2.3 Microfluidic device assembly

The final device assembly was performed through a four pin PMMA-holder fabricated with a *STEP-FOUR Basic 540* milling machine. The thermoplastic layers forming the fuel cell were perforated at the corners to match with the four pins of the PMMA-aligner allowing in this way the stacking process using this system. The Y-shaped microchannel was then easily placed on top of a COP substrate containing the gold electrodes and closed with the cover layer. Adhesion between the three components was provided by the adhesive layer present at both sides of the PSA microchannel material. The final effective working area of the device was determined by the electrode surface exposed in the microchannel corresponding to 20 mm^2 (10 mm^2 each electrode). Figure 3.3 (b) displays the PMMA-aligner with the microchannel centered between both electrode sides. The complete stacked fuel cell is shown in figure 3.4 (a) with their external tubing connection. The microfluidic connections consist of an adhesive washer, a plastic connector and a PTFE tube inserted on a piece of silicon. The inlets of PTFE tube were then coupled with the syringes of an external fluidic pump.

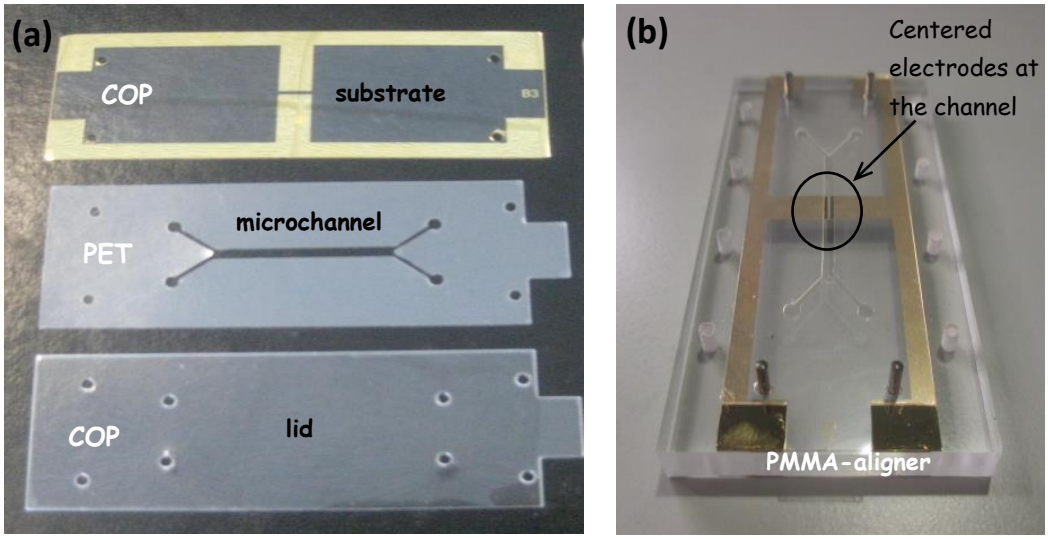

Figure 3.3 (a) Substrate, microchannel and cover system of the gold-based microfluidic fuel cell fabricated using rapid prototyping techniques. (b) PMMA structure accommodating the electrodes and channel of the fuel cell.

Once the microfluidic fuel cell was assembled, two separate coloured solutions were introduced into the device to verify the existence of a laminar flow and to check the sealing between the different layers of the device. Figure 3.4 (b) shows a top view of the fluidic structure in which the

two coloured solutions were flowing in parallel. However, after several minutes the washers holding the plastic ports started to lose adherence and leaks appeared trough the washers and the COP-cover. In order to prevent liquid outflow, the assembly was placed between a rigid PMMA structure that was held with screws. The top part of the PPMA piece hosted the ports to contact the plastic tubes which supplied the liquids to the fuel cell. The complete system with the holder and the tubing connection is displayed in figure 3.5.

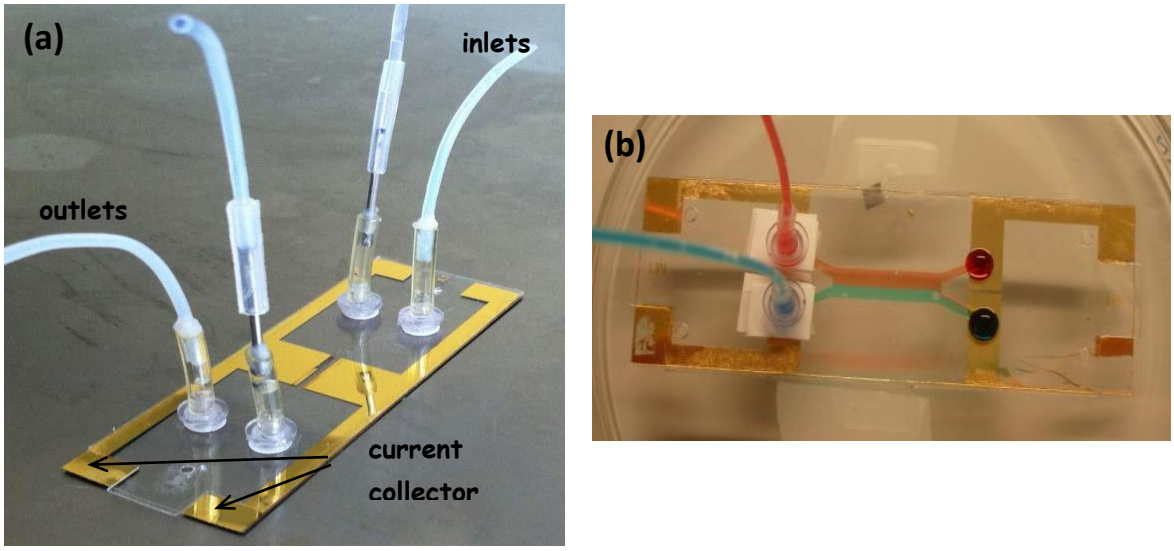

Figure 3.4 (a) Photograph of the assembled fuel cell showing the tubing connection. (b) Fuel cell testing by two coloured solutions. Laminar and parallel flow in the microfluidic channel is verified for both liquids.

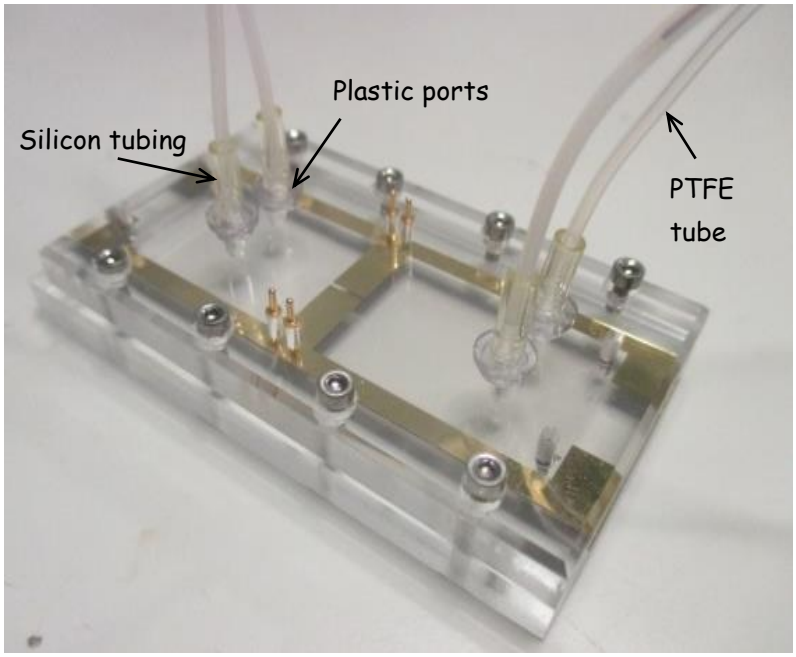

Figure 3.5 Methacrylate plates lodging the Au-biofuel cell inside.

3.1.3 Microfluidic fuel cell based on PPF electrodes

The second microfluidic device presented in this chapter was fabricated by incorporating a silicon chip that features pyrolyzed photoresist film (PPF) electrodes. PPF material possesses similar characteristics as glassy carbon electrodes, however is less costly and can be shaped into any geometry desired. The fabrication processes of the pyrolyzed photoresist electrodes, the Y-shaped microchannel and the thermoplastic layers forming the different levels of the device are detailed down below.

3.1.3.1 Working electrodes fabrication

Pyrolyzed photoresist films (PPF) electrodes were synthesized as follows; 20 µm of positive photoresist *AZ 4562* (*Clariant*) were spin coated on a silicon wafer (1 µm thermal oxide) at 1600 rpm. Next, the electrodes were patterned by photolithography through a bright-field mask (*Karl Suss MA56*). Due to the large size of the electrodes, a high-resolution transparency (*Leicrom*, Spain) was used instead of a chromium photomask. The undesired photoresist was removed during resist development, and the remaining structures were soft baked at 80 °C for 24 h to evaporate solvents and eliminate volatile impurities. The pyrolysis of the photoresist took place in a RTP (Rapid Thermal Process) oven (*Centrotherm*) in three different stages. First the temperature in the RTP oven was increased at 60 °C min^{-1} until reaching 1000 °C. Then this temperature was held for approximately 1 h, and finally the wafers were allowed to cool down to room temperature overnight. The overall diagram is represented in figure 3.6. After the PPF fabrication, the wafer (shown in figure 3.7 (a)) was diced into individual 20 × 20 mm chips featuring two PPF electrodes each between an insulating gap. One of these chips is displayed in figure 3.7 (b).

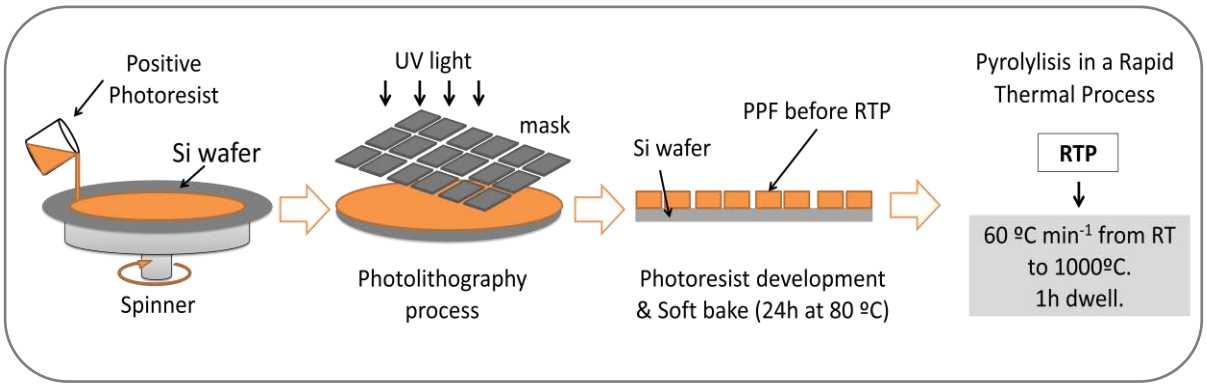

Figure 3.6 Summary of the steps used in the PPF fabrication process, previously reported at [14].

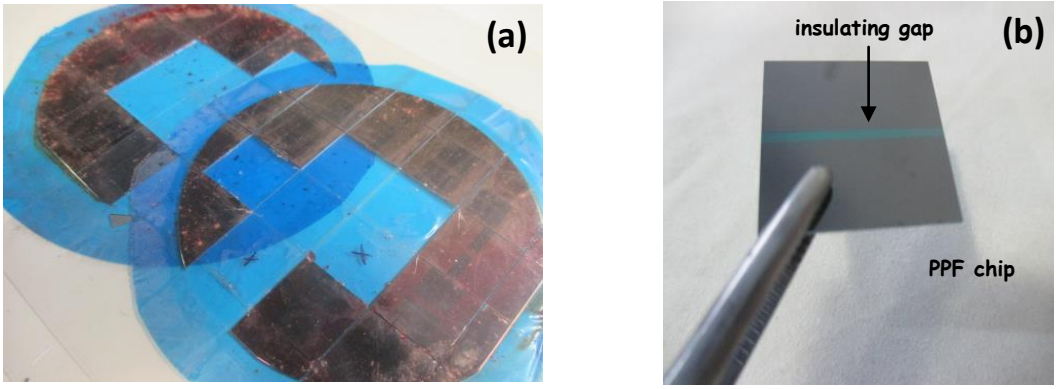

Figure 3.7 (a) Wafer showing the cut PPF chips, a covering resist has been located on the surface to protect the PPF electrodes. (b) Individual PPF chip extracted from the wafer with the protective resist removed.

3.1.3.2 Microchannel and layers constituting the device

The different polymeric layers of the microfluidic device were designed using *Vectorworks 2012 student edition* (Techlimits, Spain) and cut in a Roland GX-24 cutter plotter. The final device has a footprint dimension of 25 × 40 mm. The main channel was made in *AR8939*, a PET-two-side adhesive sheet of 130 µm thick. The dimensions of the channel were 10 mm long and 2 mm width. The chip frame consists of two layers of 160 micron *AR8259*, single side adhesive and a layer of *ZF14-188*, a 188 micron-thick Zeonex film. This combination of materials provides an optimal fit for the 500 micron silicon chip containing the PPF electrodes. The top part of the chip consists of a ZF14-100, 100 micron thick Zeonex layer and *AR9067*, a 99 micron polypropylene single-side adhesive. An additional lid layer (*AR8259*) was added to provide further (mechanical) stability to the chip underneath the silicon chip. Figure 3.8 shows the layers of different laminate materials forming the microfluidic system

The layers were manually aligned using a custom made PMMA holder that provided an assembly tolerance better than 0.1 mm, figure 3.9 (a). Once the layers were assembled, the device has an overall thickness of 1 mm. A PMMA casing was designed and milled (*Roland MDX-40*, Roland DG, Spain) to characterize the microfluidic fuel cell. Figure 3.9 (b) shows different pictures of the system. Fluidic connections were made with custom-made silicone gaskets, and spring-loaded pins (*preci-dip, CH*) were used for the electrical connections. Although not strictly necessary, a copper foil conducting tape was used to protect the PPF areas in contact with the spring-loaded pin connectors used in the holder, because PPF is a rather fragile material prone to mechanical damage. At the end, the exposed electrode surface area for each electrode was 5 mm^2.

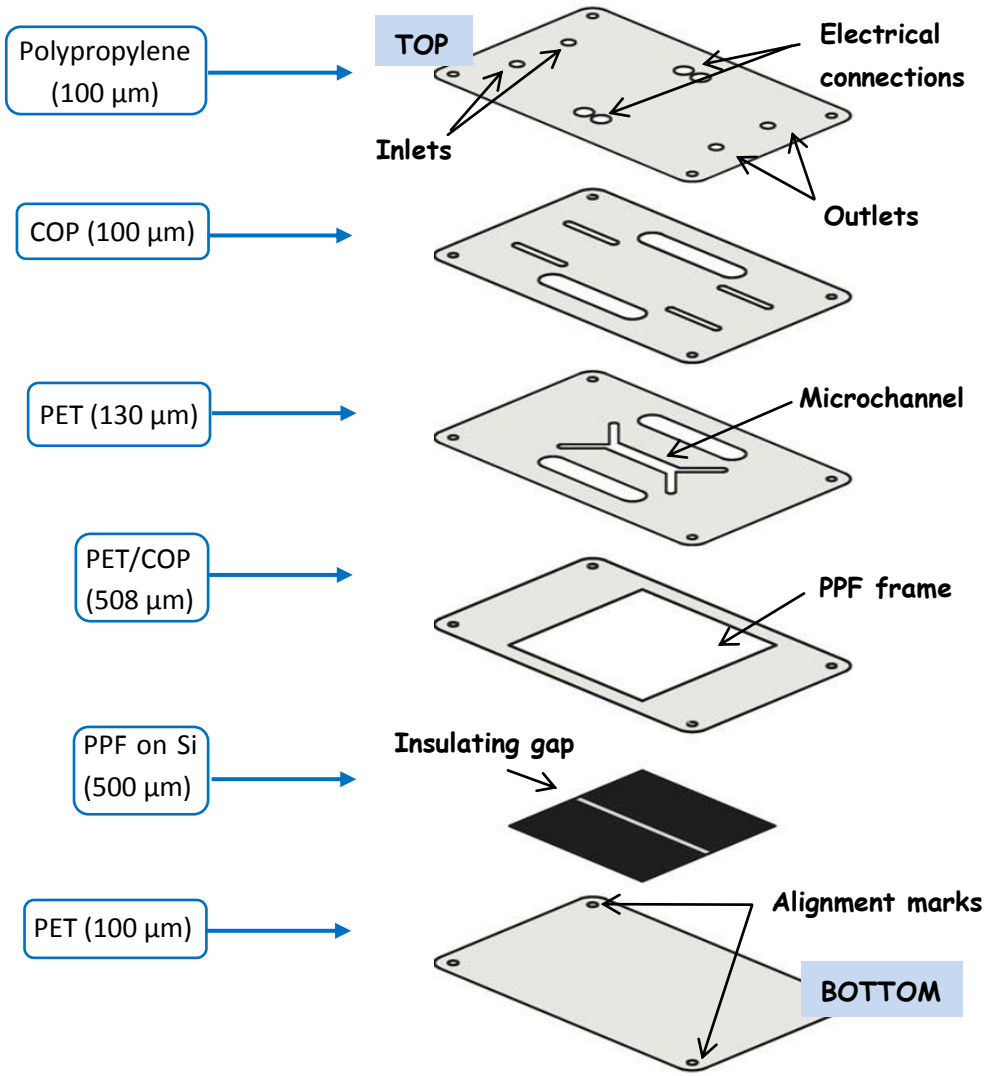

Figure 3.8 Exploded view of the multiple flexible layers forming the PPF-microfluidic fuel cell.

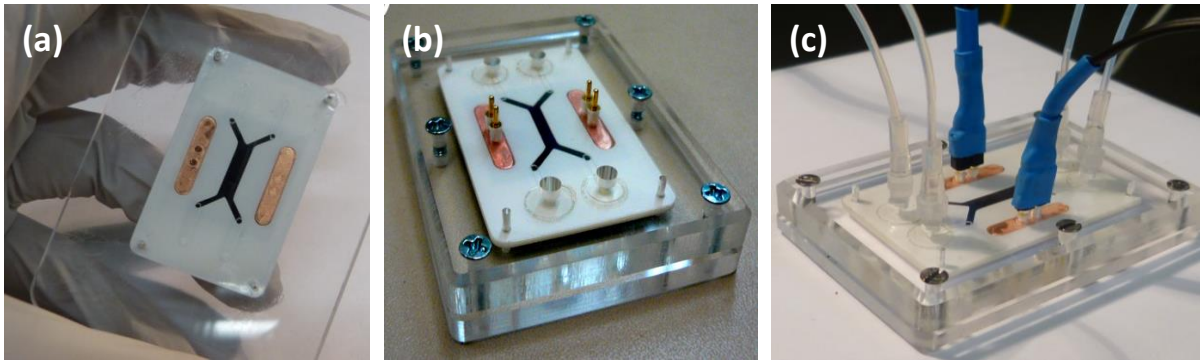

Figure 3.9 Photographs of the PPF fuel cell. a) Picture of the PMMA-aligner. b) Fuel cell device inside the PMMA-holder. (c) Electrical and fluidic connections through the PMMA casing.

3.2 ENZYMATIC IMMOBILIZATION

In this section the electrodes previously presented were catalytically modified trough enzymatic immobilization. Enzymatic immobilization consists of the attachment of a catalytic solution containing the enzymes into a solid support resulting in a restricted movement of these enzymes. There are multiple benefits to be gained by enzymatic immobilization, among them the most important is the cost savings involved running the fuel cell. This is because only a small amount of catalytic solution is needed to run the cell. Therefore, if the enzymes are retained on the electrode surface the same batch of enzyme can be repetitive used multiple times as long as they remain active. Consequently, it is a more efficient process as compared with the enzymes mixed in a solution along with the fuel [15] in which enzymes and mediators reached the end of the channel with a very low utilization level. Another important advantage of adequately immobilize the catalytic solutions on the electrode surface is that enzymes shelf life can be increased [16-19]. Dried enzymes can be stored remaining inactive and become active when an electrolyte is added to the system.

The enzymes to be immobilized on the electrodes generally come in a solution containing: (i) the enzymes and (ii) a conducting polymer. The function of the polymer is to respect thermal and operational enzyme stability and at the same time to enable ionic conductivity. TBAB (tetrabutylammonium bromide) modified Nafion has displayed to provide stabilizing properties when immobilizing enzymes. Moreover, a group of polymers that have also been shown to exhibit suitable characteristics in the presence of enzymes are polyamines, in particular poly-ethylenimines (PEI) that at the same time allow for electronic conduction [20-21].

Furthermore, depending on the type of electron transfer to the electrode, the enzyme solution includes other additional components. For the case of MET reactions, the conducting polymer to be incorporated into the catalytic solution presents redox properties. This is usually achieved by tethering a redox mediator to the polymer backbone. Moreover, a crosslinker agent, such as ethylene glycol diglycidyl ether (EGDGE), is normally introduced into the mixture to provide a better communication between the polymer, the enzyme and the electrode [22]. Figure 3.10 (a) shows a cross section scheme of an enzymatic solution performing mediated electron transfer process. On the other hand, in DET, carbon nanotubes are normally added to the catalytic solution. Then, the enzyme will be oriented to the ends of the carbon nanotubes and the electron transfer among the enzyme and the electrode can occur. In this way, the electron transfer between the enzyme and the electrode takes place trough the carbon nanotubes. A representative sketch of a solution performing direct electron transfer is represented in figure 3.10 (b).

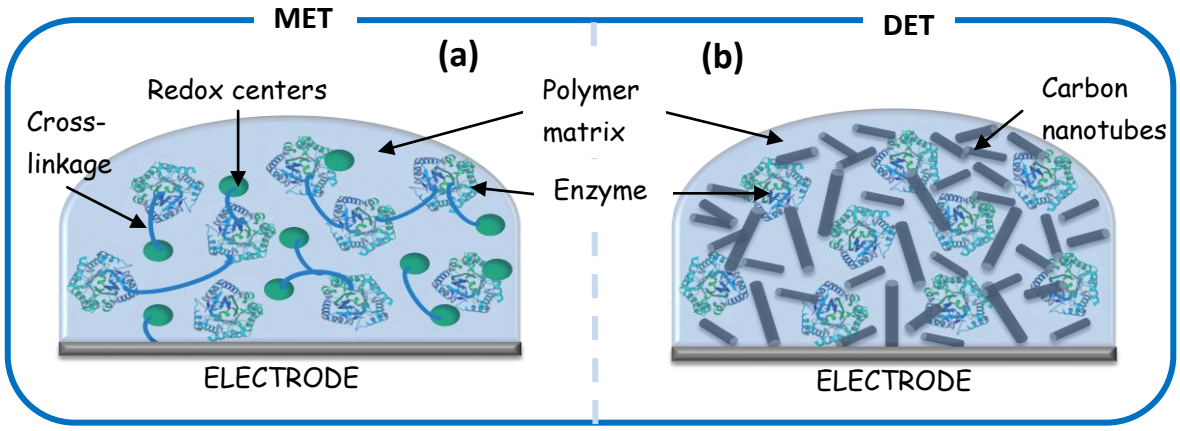

Figure 3.10 Representation of the catalytic enzymatic solution immobilized on the surface of an electrode for (a) a mediated electron transfer (MET) and (b) direct electron transfer (DET).

3.2.1 Chemicals and solutions

The necessary reagents and the procedures for preparing the catalytic solutions to be attached on the anodic and cathodic electrode surfaces as well as the electrolyte solutions used in the experiments are described down below:

3.2.1.1 Anode side

i) Anodic catalytic solution: The catalytic solution for the andode was prepared by the mixture of these three separate solutions: (i) the redox mediator polymer (Fc-C_6-LPEI) (ii) the solution containing the enzyme glucose oxidase from *Aspergillus niger* and (iii) the cross-linker reagent, ethylene glycol diglycidyl ether (EGDGE).

The redox polymer Fc-C_6-LPEI was synthesized as previously reported [23]. The ferrocene was attached to the linear poly(ethylenimine) (LPEI) backbone turning it in a redox polymer. This enables the efficient communication between glucose/GOx/electrode. The solid Fc-C_6-LPEI was dissolved in deionized water until the final concentration was 10 mg ml^{-1}. For the enzyme solution, GOx was diluted (EC 1.1.3.4, Type X-S, 175 units/mg of solid, 75% protein) in deionized water for a 10 mg ml^{-1} concentration. Finally, the cross-linker solution was prepared at 10% v/v of EGDGE in deionized water. Ethylene glycol diglycidyl ether (EGDGE) was purchased from Polyscience Inc., Warrington, PA. Combining these solutions in a ratio 14 : 6 : 0.75 (polymer : enzyme : cross-linker) and vortexing them together finally the catalytic solution for the anode was obtained. This procedure was realized according to a previously published protocol [24].

ii) Electrolyte for the anode: The anolyte solution used to run the fuel cell was phosphate buffer prepared with the blending of these three separate salts; sodium nitrate ($NaNO_3$), sodium phosphate monobasic (NaH_2PO_4) and sodium phosphate dibasic (Na_2HPO_4) until 100 mM concentration was achieved. The pH of the electrolyte was adjusted to 7.4 because it is around

this value where GOx presents it better activity. The fuel, glucose, was prepared in a stock solution of 1 M glucose (α-D(+)-Glucose) and allowed to mutarotate for 24 hours before it uses and subsequently stored at 4 °C. For the experiments, 100 mM glucose was utilized every time. The salts for preparing the electrolytes and the glucose were purchased from Sigma-Aldrich and used as received.

3.2.1.2 Cathode side

i) Cathodic catalytic solution: The catalytic solution to be immobilized at the cathode consisted of the mixture of: (i) the enzyme laccase solution from *Trametes Versicolor*, (ii) a solution containing anthracene-modified MWCNTs and (iii) TBAB-modified Nafion solution.

The laccase solution was obtained with 1.5 mg of laccase dissolved in 75 ml of 100 mM phosphate buffer (pH 7.0). Then, 7.5 mg of anthracene modified MWCNTs (10-30 μm length, 1.6% −OH functionalization purchased from cheaptubes.com) were added to the enzymatic solution and it was sonicated and vortexed until an ink-like mixture was obtained. Anthracene-2-carbonyl chloride for anthracene-modified MWCNTs was synthesized as previously published procedures [25-26]. Additionally, 25 μL of TBAB-modified Nafion (EW1100, purchased from Sigma-Aldrich) was added to the previous blend. TBAB-modified Nafion was also elaborated as previously reported [27]. The mixture was sonicated and vortexed again for 20 minutes. This mixing step is critical in the biocathode solution preparation to get homogeneous and reproducible cathodes. This protocol was also published previously [24].

ii) Electrolyte for the cathode: The electrolyte solution for the cathodic compartment was citrate buffer formed by the combination of sodium citrate dihydrate ($C_6H_5Na_3O_7 \cdot 2H_2O$) and citric acid monohydrate ($C_6H_8O_7 \cdot H_2O$) for a final concentration of 150 mM. These salts were used as received and purchased from Sigma-Aldrich. The pH of the buffer was adjusted to 4.5 in which laccase displays its highest activity. For the experiments, the citrate buffer was bubbled with air or nitrogen gas.

3.2.2 Enzymatic electrode functionalization

The catalytic solutions were deposited on the surface of COP/Ti/Au, PPF and commercial glassy carbon (BASi, West Lafayette, IN) electrodes. Prior setting up a complete microfluidic fuel cell, the objective was to study the electrochemical response of the coated solutions and their interaction with the electrode material used.

3.2.2.1 Catalytic modification over single electrodes

COP/Ti/Au and PPF films were cut in individual pieces using a cutter and a diamond tip, respectively, and chips of 5 x 30 mm^2 dimensions were obtained. On the contrary, glassy carbon

electrodes were used as received.

Before the catalytic modification, all the electrode surfaces were carefully cleaned. Glassy carbon electrodes were polished for approximately 5 minutes with 1 µm alumina powder solution. Then, rinsed with water and sonicated in isopropyl alcohol for a few minutes to ensure a complete removal of the alumina particles. By contrast and due to its brittle nature, COP/Ti/Au and PPF electrodes were cleaned by sonication in isopropyl alcohol for 10 minutes and rinsed with distilled water for finally air dried. A wire was bonded at the end of the COP/Ti/Au and PPF chips using a silver epoxy paste (*Electron Microscope Science*) to allow electrical connections. This connection was then encapsulated with a transparent thermoplastic that at the same time was used to define a 3 mm diameter working electrode area, corresponding to 7 mm^2. Figure 3.11 shows an individual PPF chip and the different parts forming the electrical connections. Then, a 3 µL drop of the corresponding enzymatic solution was deposited on the surface of the electrodes allowing them to dry overnight at 24 °C.

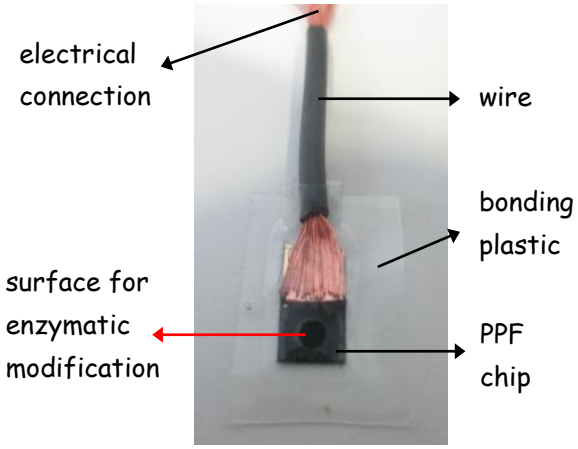

Figure 3.11 Individual PPF film with a bonding wire for external connection and a plastic encapsulation. The surface for enzymatic modification was 7 mm^2.

3.2.2.2 Catalytic modification on the electrodes of the fuel cell

The enzymatic solutions were deposited on the COP/Ti/Au and PPF electrodes forming the microfluidic fuel cells. Due to the liquid nature of the solutions they tend to spread in contact with a solid substrate. Then, three PDMS-strips aligned using a magnifier glass of 1 mm thickness and 1 mm width were used in order to confine the catalytic solutions in the desired region of the electrodes. One piece of PDMS was placed in the 1 mm gap separating the anode and the cathode electrodes. The other PDMS slices were positioned parallel side by side with 1 mm spacing between each one. At the end, the electrodes were modified with a drop of 4.3 µl of the catalytic solution. After the drying of the enzyme-coating solution, the PDMS-strips were removed and the COP/Ti/Au and PPF chips were embedded in the corresponding microfluidic fuel cell. Figure 3.12

displays a representation of a PPF chip catalytically modified and the electrochemical reactions occurring in each electrode side

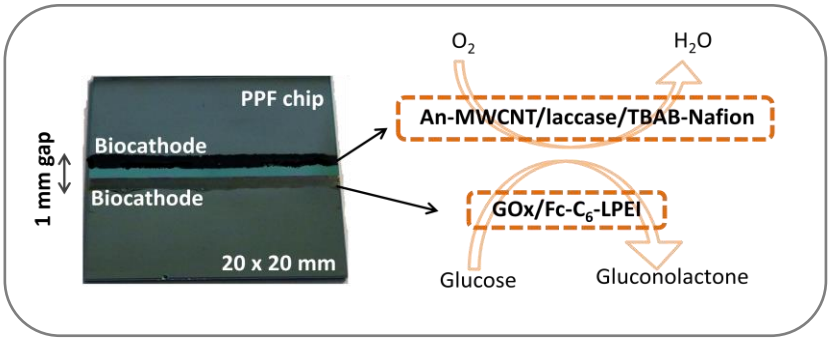

Figure 3.12 Enzyme electrode construction over a PPF electrode. This picture represents the drop cast immobilization of enzymes on pyrolyzed photoresist films before inserting the PPF in the frame of the microfluidic device. Also it is shown the chemical reaction taking place in anode and cathode.

3.3 MICROFLUIDIC FUEL CELL PERFORMANCE

The COP/Ti/Au and PPF electrodes coated with the enzymatic layers were characterized carrying out cyclic voltammetry experiments. The set up for the voltammetries consisted of a silver chloride electrode (Ag/AgCl), a platinum wire counter electrode and the corresponding working electrode. The goodness of the fuel cell enzymatic electrodes was evaluated by comparing their voltammetries with a commercial glassy carbon electrode, a widely used electrode material utilized as standard reference in electrochemical experiments. Afterwards, the performance of the microfluidic fuel cells formed by these electrodes was tested by pumping simultaneously the electrolyte solutions containing glucose and dissolved oxygen. Some aspects such as the influence of the electrode length, the effect of flow rate and the stability of the enzymes over time on the performance of the fuel cell were analyzed. Cyclic voltammetries, polarization and power curves were recorded using a *CH instruments* model 650A potentiostat (*Austin, TX*).

3.3.1 Microfluidic fuel cell performance with gold electrodes

3.3.1.1 Individual Au-bioelectrodes characterization

In order to assess the glucose-oxidative anode performance, cyclic voltammetries were run in the absence of glucose and when 100 mM glucose was present in the electrolyte (100 mM phosphate buffer). Both COP/Ti/Au and GC bioelectrodes (GOx/Fc-C_6-LPEI-electrodes) were tested and the results are shown in figure 3.13 (a). When no glucose was added in the electrolyte, the response was only due to the presence of the mediator, blue dotted line (for comparison with the other voltammograms only the GC electrode was measured without glucose). After the addition of 100 mM glucose, the glucose oxidation steady state current response was achieved. The open circuit

voltage (OCV) corresponded to approximately -0.15 V, in agreement with the experimental glucose oxidation onset. As it can be seen, GC electrode displays higher current density as compared with COP/Ti/Au electrodes being 379 ± 52 µA cm^{-2} and 335 ± 47 µA cm^{-2}, respectively.

Regarding the oxygen-reductive cathode, GC and COP/Ti/Au bioelectrodes (with the enzymatic layer of Laccase/MWCNTs) were tested in 150 mM citrate buffer in air and nitrogen saturated conditions. Results are shown in figure 3.13 (b). The dotted line shows the voltammetry of the GC electrode in citrate buffer after bubbling N_2 in the solution, namely background current. Under air saturated conditions, both electrodes showed the same value in terms of current density of approximately 113 ± 80 µA cm^{-2}. This value was obtained after substracting the background curve (blue dotted line) to the air bubbled CVs. The oxygen reduction onset was situated at 0.6 V.

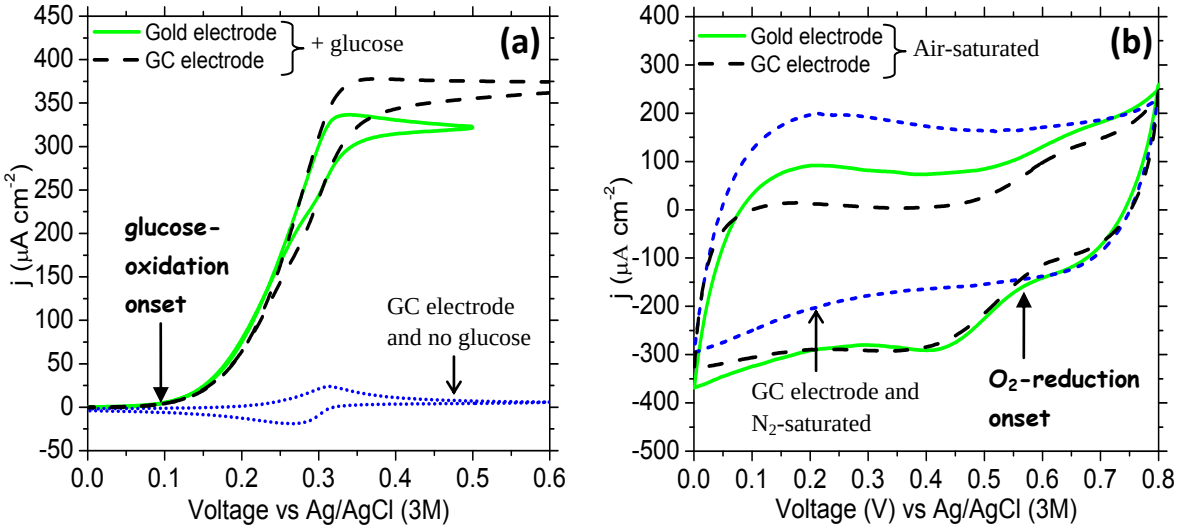

Figure 3.13 Cyclic voltammetries COP/Ti/Au and GC electrodes at 10 mV s^{-1} modified where it can be seen their respective catalytic onset for (a) GOx/Fc-C_6-LPEI in phosphate buffer with no glucose (blue line) and 100 mM glucose for a GC electrode (dashed line) and Au electrode (green solid line). (b) Laccase/MWCNTs in citrate buffer under N_2-saturated conditions (blue dotted line) and under air-saturated conditions for GC electrode (dashed line) and Au electrode (green solid line).

The bioanode and biocathode voltammetries obtained show that the COP/Ti/Au electrodes can be effectively coupled together in a biofuel cell, with an open circuit potential (being the combination of the open circuit voltages of the bioelectrodes half cells) of approximately 0.75 V.

3.3.1.1 Polarization and power curves

The performance of the fuel cell was evaluated for four different flow rates; 5, 10, 25, 50 µl min^{-1}. The open circuit voltage situated at approximately 0.65 V was found to be slightly below that the one predicted for the separated cyclic voltammetries due to internal losses inside the cell. As it was expected, the maximum power and current density increased with the enhancement of the

flow velocity achieving densities of 33 µW cm^{-2} and 142 µA cm^{-2}.

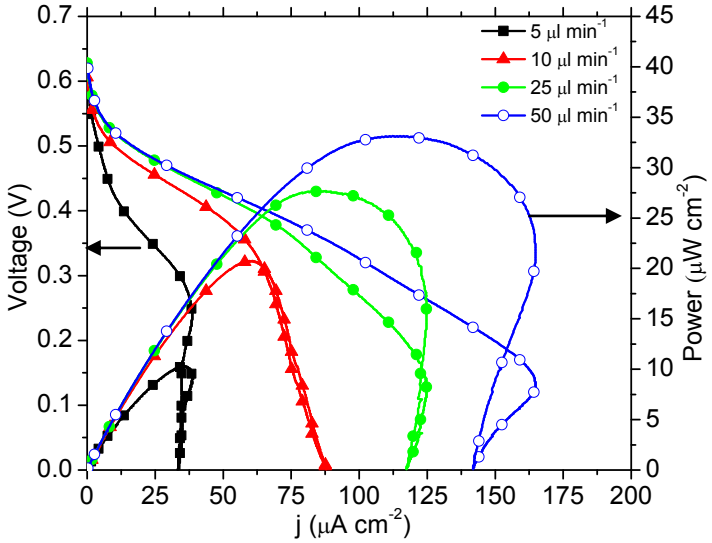

Figure 3.14 Polarization and power curves at different flow rates from the glucose enzymatic microfluidic using gold electrodes. Dashed lines represent the power curves. Solid lines are the polarization curves.

In the context of the evaluation of gold electrodes to be used in microfluidic fuel cell these results demonstrate their suitability to be operated along with the combination of catalytic solutions used in this chapter. The power invested for the syringe pump to introduce to keep in movement the solutions inside the fuel cell was calculated applying equitation I.1 from Section I. The parasitic power to drive the laminar flow (at 50 µl min^{-1}) was 0.2 µW cm^{-2} corresponding to the 0.6 % of the net power generated. Therefore, in this particular case the parasitic power can be neglected.

3.3.2 Microfluidic fuel cell performance with PPF electrodes

3.3.2.1 The importance of the PPF electrodes surface pre-treatment

Pyrolyzed photoresist films electrodes tend to oxidize it surface in contact with air after some time stored [28]. This can bring to no catalytic response when a surface of this kind is enzymatically modified. For this reason, the PPF-silicon wafer was covered with a layer of a protective resist after its fabrication that was removed with acetone just before its use (this is shown in figure 3.7). However, this measure was not 100 % effective and sometimes after all, the surfaces of the PPF electrodes were passivated. Therefore, prior to catalytic modification the surfaces of the PPF electrodes were cleaned and regenerated by immersing them in a solution containing H_2O_2, 30 % (w/w) in H_2O, and 50 mM KOH, with a ratio of 1:4, for at least 10 minutes.

To illustrate this fact, an oxidized PPF surface and a regenerated one were coated with the laccase-mediated solution and cyclic voltammetries were performed under air and nitrogen saturated atmospheres. Figure 3.15 shows the results obtained in the presence and absence of air. In (a), no

difference between scans can be observed, thus indicating that the PPF electrode was deteriorated. In (b), a completely different behavior can be seen. When the electrolyte solution was bubbled with air the electrochemical response of the oxygen reduction reaction showed an increase of current density of 150 µA cm^{-2} (in relation with the nitrogen bubbled curve).

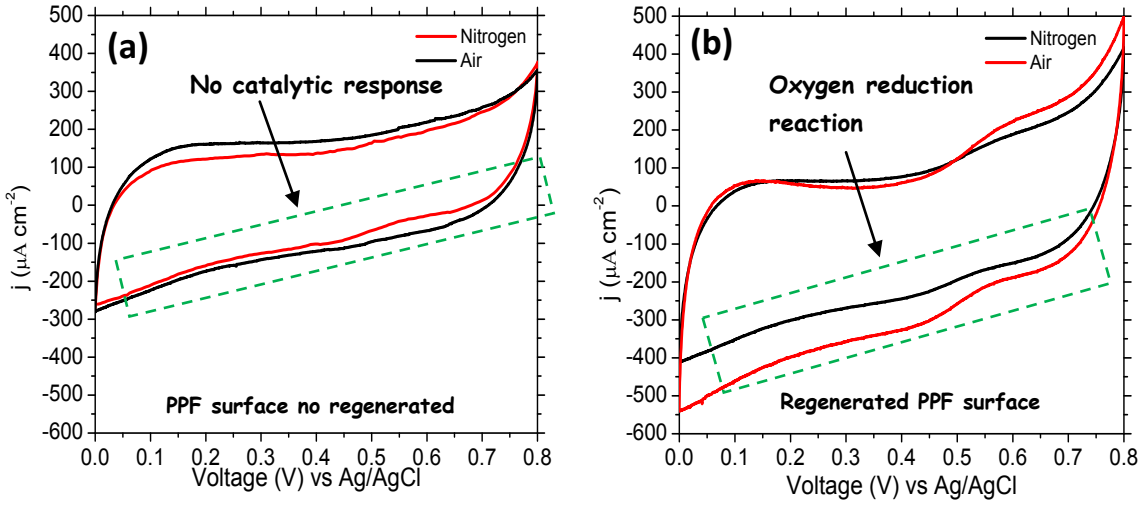

Figure 3.15 PPF enzymatically modified with the cathode solution (a) PPF after several months storage without any previous treatment (b) Activated PPF surface with KOH and H_2O_2 prior enzymatic modification.

3.3.2.2 Individual PPF-bioelectrodes characterization

Figure 3.16 displays the cyclic voltammograms of PPF and GC electrodes of: (a) GOx/Fc-C6-LPEI anode, in the absence of glucose and when 100 mM glucose was added in the phosphate buffer solution and (b) Laccase/MWCNTs cathode, in 150 mM citrate buffer electrolyte under air and nitrogen saturated conditions.

Although the current levels observed at GC and PPF electrodes differed slightly, both electrode materials behaved similarly in terms of peak potentials, and the differences in current density were attributed to variability of the surface modification procedure. As figure 3.16 shows, the PPF anode displayed higher current density than its GC counterpart (460 ± 45 µA cm^{-2} *vs.* 321 ± 36 µA cm^{-2}). However, the PPF cathode passed slightly less current than the GC cathode (113 ± 13 µA cm^{-2} *vs.* 165 ± 19 µA cm^{-2}). Despite these differences, it is proved that PPF material is a suitable electrode material for the construction of enzymatic fuel cells.

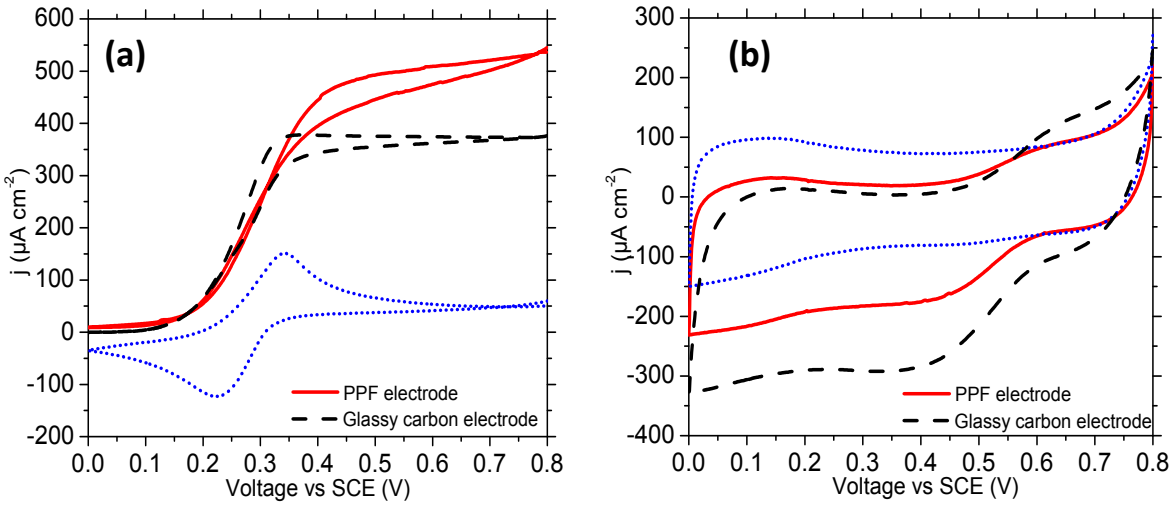

Figure 3.16 Representative cyclic voltammograms of enzymatic PPF and GC electrodes at 5 mV s^{-1}. (a) GOx/Fc-C_6-LPEI bioanodes in 100 mM sodium phosphate at pH 7.4 with (red) and without (blue) glucose. (b) An-MWCNTs/laccase/TBAB-Nafion biocathodes in 150 mM citrate buffer at pH 4.5. Blue line PPF under N_2-saturated conditions (blue), and under air saturated conditions (red). Solid lines correspond to PPF, and dotted lines to GC electrodes, respectively.

These data suggested that these electrodes should work when combined in a fuel cell, and that oxygen reduction at the cathode is likely to be the process limiting the fuel cell power output. This is not very surprising considering that the concentration of glucose in the anolyte was much higher, and therefore non-limiting, as long as the enzyme catalysts has high specific activity. However, dissolved oxygen in water is usually found in low concentrations, around 0.25 mM (8 ppm) which is defining a constraining feature. Given that increasing the concentration of O_2 above its solubility can only be achieved modifying thermodynamic parameters of the solution, such as pressure and temperature, this can potentially damage the enzyme activity [29-30]. Then, any enhancement of the cell performance needs to be efficiency improvements. To increase the rate of oxygen consumption in the cathode, the effect of increasing mass transport to the electrodes was next studied.

3.3.2.3 Effect of flow rate on the complete microfluidic fuel cell performance

After characterizing the enzyme-modified PPF electrodes separately, the complete glucose/O_2 microfluidic PPF biofuel cell was assembled combining them. Then, anolyte and catholyte were simultaneously pumped using a syringe pump and the polarization and power curves were studied as a function of the flow velocity.

The fuel cell was tested at different flow velocities, ranging from 1 μL min^{-1} to 80 μL min^{-1}. For the experiment, the potentiostat was set up with the working electrode connected to the cathode, and the auxiliary and reference electrode leads both connected to the anode. At each flow rate, the open circuit potential (OCP) was first measured and from that point the cell voltage dropped with increasing current draw was recorded. A set of polarization and power curves were

performed and the figures of merit for each curve were plotted in table 3.1. On the other side, figure 3.17 summarizes the effect of flow rate on power output density.

v (µl min^{-1})	V_{max} (V)	$j_{at\ Pmax}$ (µA cm^{-2})	P_{max} (µA cm^{-2})
1	0.51 (±0.01)	54.3 (±18.8)	11.9 (±4.3)
5	0.53 (±0.03)	98.0 (±22.4)	18.8 (±8.3)
10	0.57 (±0.02)	121.0 (±25.2)	27.3 (±10.7)
20	0.56 (±0.05)	170.7 (±18.5)	40.1 (±15.2)
25	0.55(±0.02)	195.3 (±33.5)	48.3 (±12.3)
30	0.54 (±0.04)	205.6 (±22.4)	51.2 (±12.8)
35	0.53(±0.02)	250.0 (±39.7)	56.6 (±20.3)
40	0.55 (±0.03)	263.6 (±46.7)	60.1 (±10.6)
45	0.55(±0.02)	280.1 (±65.0)	61.0 (±15.3)
50	0.52 (±0.05)	272.3 (±54.1)	62.1 (±20.3)
55	0.53(±0.02)	278.5 (±32.0)	62.1(±14.3)
60	0.50 (±0.04)	275.4 (±57.2)	61.3 (±15.9)
70	0.54 (±0.04)	290.2 (±38.3)	63.8 (±15.2)
80	0.49 (±0.05)	279.7 (±45.8)	63.2 (±10.7)

Table 3.1. Figures of merit of each curve used for the construction of the maximum biofuel cell power output as a function of flow rate (figure 3.16).

The data show two different power output zones as a function of flow rate. The first one, from 1 µL min^{-1} to 35 µL min^{-1} where the power density increases linearly with flow rate, and a second region in which the power density reaches a plateau from 40 µL min^{-1} onwards. It can be seen that the maximum output power increases more than 5 times in the first zone, delivering 12 µW cm^{-2} at 1 µL min^{-1} up to 60 µW cm^{-2} at 40 µL min^{-1}. The best results were obtained at a flow rate of 70 µL min^{-1}.

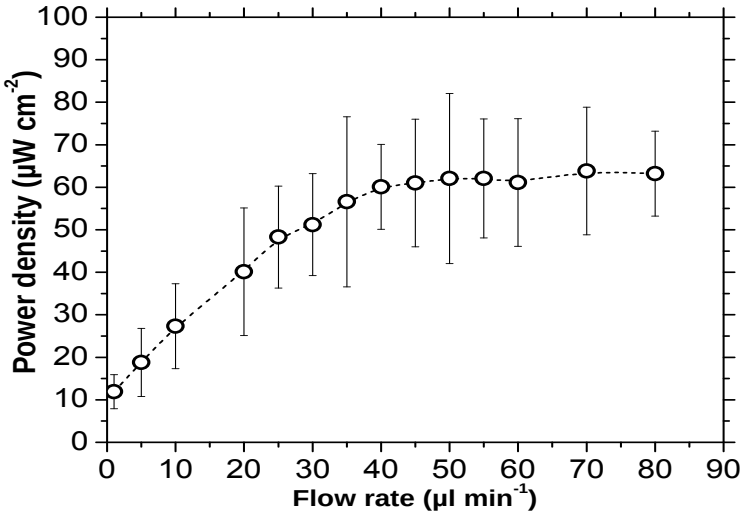

Figure 3.17 Maximum biofuel cell power output as a function of flow rate.

In this particular case, assuming a diffusion coefficient of 10^{-8} m^2 s^{-1} for protons, the fastest diffusing species in the system, the inter-diffusion thickness at the end of the cell (10 mm) was around 600 µm, while it is 370 µm for oxygen, and 230 µm for glucose. Note that protons were used to make a point, as it is the fastest diffusing species in our system. Therefore it was believed that was reasonably safe to disregard oxygen cross-diffusion as the most important factor limiting power output in this system. However, the presence of oxygen in the anode could cause the most important performance losses in our system. This was because oxygen is the natural substrate of glucose oxidase, and if it was found in sufficiently high concentrations it could disable the fuel cell. Our anolyte solutions were extensively purged with nitrogen, and the ferrocene concentration in the conducting polymer was sufficiently high to ensure that it was found in high concentration (compared to oxygen) in the vicinity of glucose oxidase.

The second factor, oxygen depletion at the cathode, was likely to be the true limiting factor in this system given the relatively low oxygen concentration in the catholyte. Thus, at low flow rates, it was possible that all the oxygen supplied to the cell is consumed and that this results in a decrease of power output. One way to increase the supply of oxygen to the cathode was to increase the flow rate. This worked while the rate of oxygen supply was below the enzymatic turnover rate.

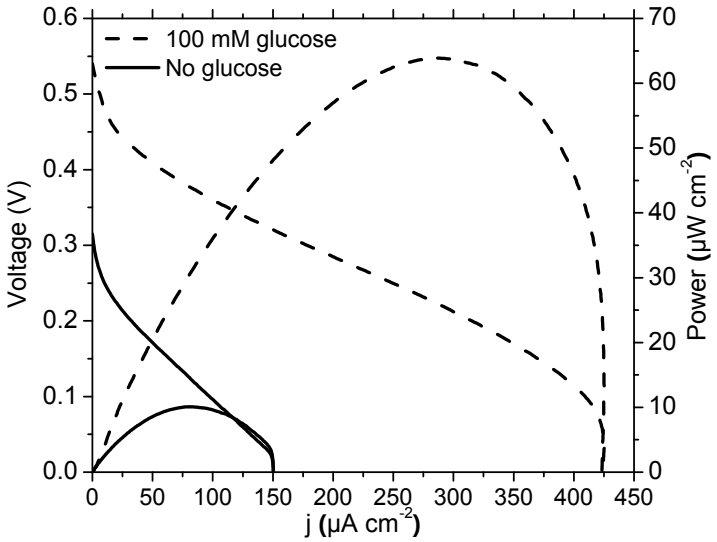

Figure 3.18 Polarization curves and power curves obtained from the glucose enzymatic microfluidic fuel cell at 70 µl min^{-1} at room temperature. Dashed lines with 100 mM glucose, solid lines without glucose

The best results were obtained at a flow rate of 70 µl min^{-1} as it is shown in figure 3.18 which displays representative polarization and power curves of the PPF-modified fuel cell in the absence and presence of 100 mM glucose under these flow conditions. The PPF biofuel cell showed a high open circuit voltage of 0.54 ± 0.04 V and delivered a maximum power density of 64 ± 5 µW cm^{-2} at a current density of 290 ± 28 µA cm^{-2} and a maximum current density of 423 µA cm^{-2}. The parasitic

power (introduced by the syringe pump) used to drive the flow through the microchannel at 70 µl min^{-1} can be calculated using equation I.1 (Section I). The parasitic power consumption was 0.40 ± 0.03 µW cm^{-2} (0.7 % of the net power) whereby this contribution to the net power output can be disregarded.

3.3.2.4 Stability system study after 24 hours of operation

The stability over time of the microfluidic biofuel cell was evaluated. For this, the power output of the cell was measured as a function of flow velocity in a time called, t=0. After that, the fuel cell was dried and stored at 4 °C in a refrigerator for 24 hours. Elapsed this time, the measures of the power output versus flow velocity were repeated obtaining the graphic of figure 3.19 (with triangle dots).

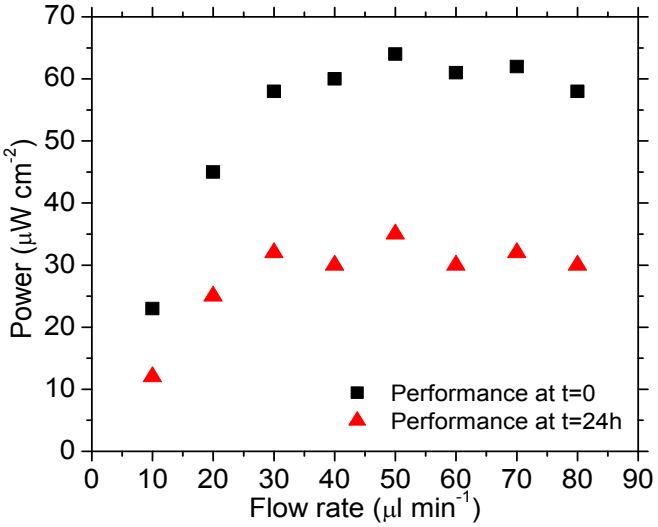

Figure 3.19 Power densities as a function of flow rates. In red, stability of the enzymatic microfluidic fuel cell after 24 hours of storage at 4°C. The power of density was calculated from the nominal active area of the electrode.

Although similar trends in the graphic can be appreciated, after a day of storage in the refrigerator a drop of power density just over 50% was observed. This behavior was attributed to the poor stability of the enzymatic electrodes, likely caused by the non-covalent attachment of enzymes and polymers to the electrodes. However, this short life may well be sufficient for disposable point of care devices with a limited sample supply and capable of providing an analytical result within minutes or, at worst, within a few hours.

3.4 SUMMARY AND CONCLUSIONS

In this work two microfluidic glucose/oxygen fuel cells built on flexible thermoplastic materials have been fabricated using a cutter plotter. This technique results in an inexpensive and very rapid prototyping method for microdevice fabrication. Furthermore, the thermoplastic materials and their assembly are compatible with large-scale manufacturing and roll-to-roll processes, which make these fuel cells more suitable for product development than fuel cell systems based on traditional microfluidic materials such as PDMS, glass and silicon.

The first fuel cell fabricated used gold electrodes, the second one utilized pyrolyzed photoresist film electrodes over a silicon wafer. The enzymatic solutions on charge of catalyzing the electrochemical reactions were immobilized at the electrode surface as a way to increase the enzymatic lifetime and to reduce the final cost of the devices. The electrode modification consisted of a bioanode made of a ferrocenium-based polyethyleneimine polymer linked to glucose oxidase (GOx/Fc-C_6-LPEI). The biocathode, was composed by a mixture of the enzyme laccase, anthracene-modified multi-walled carbon nanotubes, and tetrabutylammonium bromide-modified Nafion (MWCNTs/laccase/TBAB-Nafion) for performing direct electron transfer from the carbon material to the enzyme.

Several advances in the area of enzymatic microfluidic fuel cells have been presented in this chapter. For the first time the use of pyrolyzed photoresist films (PPFs) have been introduced as a suitable electrode material for the development of novel enzyme-based microfluidic fuel cells. A power density generation of 64 ± 5 μW cm^{-2} at 0.54 ± 0.04 V at room temperature and a solution flow rate of 70 μL min^{-1} have been achieved with negligible parasitic power consumption. However, the use of a syringe pump still represents a limitation in the device portability. Moreover, the electrochemical performance of the PPF electrodes was comparable to glassy carbon (GC) electrodes. In addition, and unlike GC, PPF offers the potential to be patterned by photolithography into any electrode shape desirable, and the whole process was CMOS compatible. This opened up the possibility to integrate carbon electrodes in microsystems that are produced either exclusively by standard microfabrication techniques or, as it was demonstrated here, combined with microfluidic devices produced in polymeric materials by less costly processes.

Future work will be focused on simplifying the system to increase the fuel cell power density. This will be done by introducing changes in the system design and architecture, and improving the quality of our bioelectrodes through better enzyme wiring which can be achieved by using alternative composition of the enzymatic inks. Rapid prototyping methods such as the ones described in this chapter accelerate the development cycle of the devices and make easier the optimization process.

REFERENCES

1. Berthier, E., E.W.K. Young, and D. Beebe, *Engineers are from PDMS-land, Biologists are from Polystyrenia.* Lab on a Chip, 2012. **12**(7): p. 1224-1237.
2. McDonald, J.C., D.C. Duffy, J.R. Anderson, D.T. Chiu, H. Wu, O.J.A. Schueller, and G.M. Whitesides, *Fabrication of microfluidic systems in poly(dimethylsiloxane).* Electrophoresis, 2000. **21**(1): p. 27-40.
3. Focke, M., D. Kosse, C. Mueller, H. Reinecke, R. Zengerle, and F. von Stetten, *Lab-on-a-Foil: microfluidics on thin and flexible films.* Lab on a Chip, 2010. **10**(11): p. 1365-1386.
4. Organic and Printed Electronics Association. http://oe-a.vdma.org.
5. Cassano, C.L. and Z.H. Fan, *Laminated paper-based analytical devices (LPAD): fabrication, characterization, and assays.* Microfluidics and Nanofluidics, 2013. **15**(2): p. 173-181.
6. Rohrman, B.A. and R.R. Richards-Kortum, *A paper and plastic device for performing recombinase polymerase amplification of HIV DNA.* Lab on a Chip, 2012. **12**(17): p. 3082-3088.
7. Godino, N., R. Gorkin, III, K. Bourke, and J. Ducree, *Fabricating electrodes for amperometric detection in hybrid paper/polymer lab-on-a-chip devices.* Lab on a Chip, 2012. **12**(18): p. 3281-3284.
8. Tiwari, A., *Advanced Healthcare Materials*. 2014: Wiley.
9. Bartholomeusz, D.A., R.W. Boutte, and J.D. Andrade, *Xurography: Rapid prototyping of microstructures using a cutting plotter.* Journal of Microelectromechanical Systems, 2005. **14**(6): p. 1364-1374.
10. Young, E.W.K., E. Berthier, D.J. Guckenberger, E. Sackmann, C. Lamers, I. Meyvantsson, A. Huttenlocher, and D.J. Beebe, *Rapid Prototyping of Arrayed Microfluidic Systems in Polystyrene for Cell-Based Assays.* Analytical Chemistry, 2011. **83**(4): p. 1408-1417.
11. Becker, H. and C. Gaertner, *Polymer microfabrication technologies for microfluidic systems.* Analytical and Bioanalytical Chemistry, 2008. **390**(1): p. 89-111.
12. Herold, K.E. and A. Rasooly, *Lab on a Chip Technology: Fabrication and microfluidics*. 2009: Caister Academic Press.
13. Jena, R.K. and C.Y. Yue, *Cyclic olefin copolymer based microfluidic devices for biochip applications: Ultraviolet surface grafting using 2-methacryloyloxyethyl phosphorylcholine.* Biomicrofluidics, 2012. **6**(1).
14. del Campo, F.J., P. Godignon, L. Aldous, E. Pausas, M. Sarrión, M. Zabala, R. Prehn, and R.G. Compton, *Fabrication of PPF Electrodes by a Rapid Thermal Process.* Journal of the Electrochemical Society, 2011. **158**(1): p. H63-H68.
15. Spahn, C. and S.D. Minteer, *Enzyme immobilization in biotechnology.* Recent patents on engineering, 2008. **2**(3): p. 195-200.
16. Bullen, R.A., T.C. Arnot, J.B. Lakeman, and F.C. Walsh, *Biofuel cells and their development.* Biosensors and Bioelectronics, 2006. **21**(11): p. 2015-2045.
17. Armstrong, F.A. and G.S. Wilson, *Recent developments in faradaic bioelectrochemistry.* Electrochimica Acta, 2000. **45**(15–16): p. 2623-2645.
18. Minteer, S.D., B.Y. Liaw, and M.J. Cooney, *Enzyme-based biofuel cells.* Current Opinion in Biotechnology, 2007. **18**(3): p. 228-234.
19. Rubenwolf, S., S. Kerzenmacher, R. Zengerle, and F. von Stetten, *Strategies to extend the lifetime of bioelectrochemical enzyme electrodes for biosensing and biofuel cell applications.* Applied Microbiology and Biotechnology, 2011. **89**(5): p. 1315-1322.
20. *RCSB Protein Data Bank.* http://www.rcsb.org/pdb/101/motm.do?momID=77.

21. Shrier, A., F. Giroud, M. Rasmussen, and S.D. Minteer, *Operational Stability Assays for Bioelectrodes for Biofuel Cells: Effect of Immobilization Matrix on Laccase Biocathode Stability.* Journal of The Electrochemical Society, 2014. **161**(4): p. H244-H248.
22. Migneault, I., C. Dartiguenave, M.J. Bertrand, and K.C. Waldron, *Glutaraldehyde: behavior in aqueous solution, reaction with proteins, and application to enzyme crosslinking.* Biotechniques, 2004. **37**(5): p. 790-806.
23. Merchant, S.A., M.T. Meredith, T.O. Tran, D.B. Brunski, M.B. Johnson, D.T. Glatzhofer, and D.W. Schmidtke, *Effect of Mediator Spacing on Electrochemical and Enzymatic Response of Ferrocene Redox Polymers.* Journal of Physical Chemistry C, 2010. **114**(26): p. 11627-11634.
24. Meredith, M.T., D.-Y. Kao, D. Hickey, D.W. Schmidtke, and D.T. Glatzhofer, *High Current Density Ferrocene-Modified Linear Poly(ethylenimine) Bioanodes and Their Use in Biofuel Cells.* Journal of the Electrochemical Society, 2011. **158**(2): p. B166-B174.
25. Dawn, A., T. Shiraki, S. Haraguchi, H. Sato, K. Sada, and S. Shinkai, *Transcription of Chirality in the Organogel Systems Dictates the Enantiodifferentiating Photodimerization of Substituted Anthracene.* Chemistry-a European Journal, 2010. **16**(12): p. 3676-3689.
26. Meredith, M.T., M. Minson, D. Hickey, K. Artyushkova, D.T. Glatzhofer, and S.D. Minteer, *Anthracene-Modified Multi-Walled Carbon Nanotubes as Direct Electron Transfer Scaffolds for Enzymatic Oxygen Reduction.* ACS Catalysis, 2011. **1**(12): p. 1683-1690.
27. Klotzbach, T., M. Watt, Y. Ansari, and S.D. Minteer, *Effects of hydrophobic modification of chitosan and Nafion on transport properties, ion-exchange capacities, and enzyme immobilization.* Journal of Membrane Science, 2006. **282**(1-2): p. 276-283.
28. Hebert, N.E., B. Snyder, R.L. McCreery, W.G. Kuhr, and S.A. Brazill, *Performance of Pyrolyzed Photoresist Carbon Films in a Microchip Capillary Electrophoresis Device with Sinusoidal Voltammetric Detection.* Analytical Chemistry, 2003. **75**(16): p. 4265-4271.
29. Daniel, R.M., M.J. Danson, R. Eisenthal, C.K. Lee, and M.E. Peterson, *The effect of temperature on enzyme activity: new insights and their implications.* Extremophiles, 2008. **12**(1): p. 51-59.
30. Moore, J., C. Stanitski, and P. Jurs, *Principles of Chemistry: The Molecular Science*. 2009: Cengage Learning.

SECTION II

PASSIVE MICROFLUIDIC FUEL CELLS MADE OF PAPER. The capillary flow of liquids

II.I MICROFLUIDIC PAPER-BASED DEVICES

It has been shown that microfluidic fuel cells using glass or plastic [1-5] can be made easily using rapid prototyping techniques. They are also simple to operate provided that an external pressure system is coupled to the device to maintain the reactants in motion. However, the need for external pressure sources, like pumps, limits severely their portability and miniaturization [6-7]. The need for external pumping has been recently overcome with the emergence of microfluidic paper devices. Paper possesses the ability to wick fluids via capillary action, allowing passive liquid transport [8]. Indeed, moving from conventional microfluidic systems to paper-based designs can provide important benefits. Paper presents good compatibility with a high number of

chemicals/biochemicals and it is an excellent means of establishing a laminar flow, which allows the confinement of liquids to specified regions [9-12]. The selection of the paper substrate material can be different depending on the specific requirements. In the context of microfluidic paper based devices, nitrocellulose and fibreglass are candidates that have proved their suitability in commercial lateral flow devices. Furthermore, paper systems can be combined with other low cost materials, such as plastics, which provide mechanical support. Another advantage of microfluidic paper-based devices is that they can provide semi-quantitative results of a measure (without the use of a reader) as it is possible to estimate the amount of analyte present in a sample by colorimetric techniques. Table II.1 presents a comparison between chip-based and paper-based microfluidic devices [13].

	Chip-based device	**Paper-based device**
Material	Glass, silicon, PDMS...	Paper, nitrocellulose and plastics
Manufacture	Microfabrication techniques	Rapid prototyping techniques
Driving force	External pumps	Capillary force
Detection	Reader	Reader or visual detection

Table II.1 Detailed comparison between chip-based and paper-based systems.

Paper has been widely employed as substrate to develop point of care (POC) diagnostics devices for many years [13]. The most widely used POC diagnostic devices are paper-based dipsticks, such as urinalysis dipsticks and lateral-flow immunoassays, such as pregnancy tests [14-17]. Lately, materials used in lateral flow devices have been adapted and reconfigured into 2D or 3D paper matrixes. This has led to the creation of new and exciting components such as valves, mixers, or separators. In this way, the capabilities of complex microfluidic functions and the simplicity of diagnostic tests strips have been combined to originate a new generation of paper-based analytical devices (µPADs) [18-22]. These devices have been identified as especially suitable for point of care purposes in the field of home health-care settings and in medical points of care in developing countries [11, 23-24]. This is because they promise to accomplish the ASSURED criteria; they are affordable, sensitive, specific, user-friendly, rapid and robust, equipment free and derivable to those who need it [18, 22, 25]. Nevertheless, the quantification of the results of a test requires the use of a hand-held reader which sometimes is not a cost effective solution. This has brought the idea of developing low cost disposable readers, however, examples in the literature are still very scarce. To realize this vision, the search of a new generation of power sources that satisfy the requirements such as high power density, low cost and disposability with minimum environmental impact has attracted lot of attention. In the last years, paper has been used as a substrate to develop different kinds of batteries. Different techniques can be found in the literature (i) electrochemical batteries [11], (ii) biofuel cells [26-27], (iii) lithium-ion batteries [28], (iv) supercapacitors [29] and (v) nanogenerators [30]. Among these, biofuel cells [31] appear to be one of the most suitable power sources for paper-based µPADs in terms of environmental impact

due to the use of biodegradable fuels. Moreover, paper-based devices can be disposed in an incinerator at a low cost.

The next chapters of this thesis combine both the advantages of enzymatic fuel cells and the benefits of microfluidic paper-based systems to obtain an enzymatic paper-based microfluidic fuel cell for single use applications [32].

II.II FLUID TRANSPORT IN PAPER DEVICES. The wicking process in a porous matrix

Paper-based devices rely on capillary forces to transport liquids through its porous matrix without external pumps. Properties of the porous material, including pore size, pore structure and surface treatments affect flow velocity inside the paper matrix [33]. The driving force inside the paper is the capillary suction pressure P_{cap} and it is given by the following equation:

$$P_{cap} = \frac{2\gamma cos\theta}{r_m} \quad \textbf{(II.1)}$$

where, γ is the surface tension, ϑ the contact angle of the liquid with the material and r_m is the mean porous radius of the paper material that remains constant throughout the strip.

In this section, different experiments on paper substrates are presented to show specific characteristics of paper networks that will be later applied to our devices. In particular, the behaviour of a liquid during its flow through two paper materials based on cellulose and glass fibre were tested. Moreover, capillary flow was investigated in two different regimes: (A) the wet out flow and (B) the fully wetted flow.

A) Capillary flow in a paper strip: the wet-out process

The wet out process refers to a fluid moving in a porous media because of a continuous pressure gradient created by capillarity. In the wicking action the main cause of absorption depends directly on the effective surface tension (that includes the contact angle dependence) and the pore diameter and inversely on the fluid viscosity [34]. The fluid in a paper channel of constant width can be described by Darcy's Law [35].

$$Q = -\frac{kwh}{\mu l}\Delta P \quad \textbf{(II.2)}$$

where, Q is the volumetric flow rate, k is the permeability of paper to the fluid, w and h are the width and the thickness of the channel perpendicular to flow, μ is the dynamic viscosity of the liquid and ΔP is the pressure difference applied at the ends of the liquid along the direction of flow over the length l [36]. This pressure difference can be defined as $P_{cap} - P_0$ being P_{cap} the capillary

pressure that forces the fluid to move and P_0 the atmospheric pressure. Figure II.1 (a) shows a representation of the process taking place. Making the assumption that at any point of the fluid front the capillary pressure is homogeneous, *Q* can be rewritten as:

$$Q = -\frac{kwh}{\mu l}(P_{cap} - P_0) \tag{II.3}$$

The flux on a paper strip can be related with the velocity as follows:

$$Q = v_{average} wh \tag{II.4}$$

combining equations 3 and 4 it can be seen that flux does not depend on the geometrical section of the paper:

$$\frac{dl}{dt} = v_{average} = \frac{k}{\mu l}(P_0 - P_{cap}) \tag{II.5}$$

considering that *k*, μ and $(P_0\text{-}P_{cap})$ remain constant trough the entire paper strip, the next relation can be obtained:

$$\frac{dl}{dt} = \frac{A}{l} \Rightarrow l^2 - l_0^2 = 2A(t - t_0) \tag{II.6}$$

and therefore:

$$l \sim A'\sqrt{(t - t_0) + l_0^2} \tag{II.7}$$

which describes the fluid progress as a function of the square root of the time. The result is the decrease of fluid flow velocity as the front penetrates the paper strip as it is shown in figure II.1 (b). In this case, Darcy's law neglects gravity-induced pressures and evaporative losses [37].

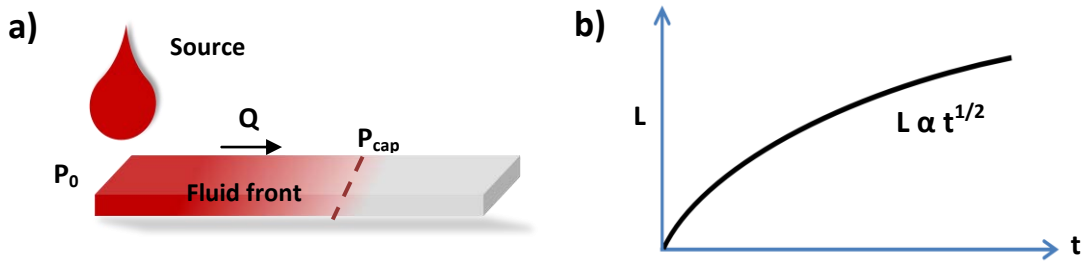

Figure II.1 (a) Schematic of the capillarity process in a paper strip where P_{cap} forces the liquid to move towards the dry zone. (b) Representation of the wicking distance versus time during the absorption of a liquid in a paper-based matrix in which the fluid front moves proportional to the square root of the time.

A.1) Experimental capillary in different paper materials and sizes

The capillary process of two papers with different compositions from Whatman® has been studied. These papers materials have been selected because of their wide use in lateral flow test applications (e.g. the home pregnancy tests). The paper materials employed in the experiments were: grade *1 Chr* (180 µm thick and porous size of 2.3 µm) made of cellulose and grade *Fusion 5* (370 µm thick and 11 µm of porous size) based on fibreglass.

In order to study and characterize the wetting process of these two paper materials they were cut with the cutter plotter with 45 mm x 5 mm dimensions and placed in parallel in the setup presented in figure II.2. The support has two reservoirs filled with a colored water-based ink. Graph paper was used to measure the distance traveled by the fluid front through the paper channel. A camera (AnimatorDV Simple) monitored the progression of the liquid along the paper by acquiring a series of pictures at a fixed the time lapse.

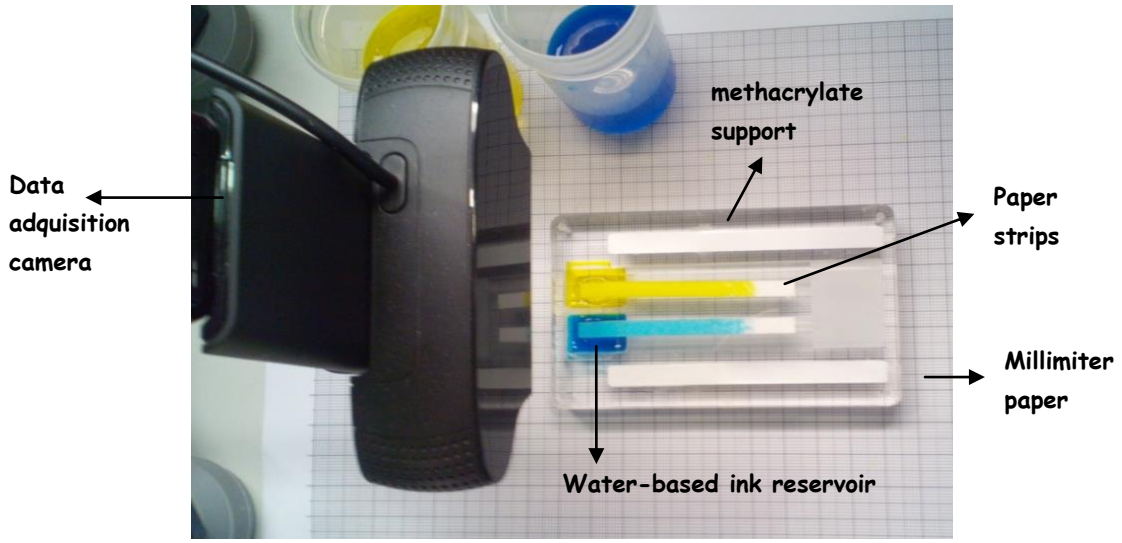

Figure II.2 Setup used for studying the progress of a liquid in a porous matrix.

In figure II.3 some images during the wetting process on these papers are presented. As it can be seen, in *1 Chr*-paper the fluid front advanced slower than in *Fusion 5* paper strip.

For the experiments, one end of the strips was submerged at time named t_0=0 and at a distance l_0=0 considered as the initial moment where liquid started to flow through the channel. Therefore, equation (II.7) can be described as:

$$l = A'\sqrt{t} \qquad \textbf{(II.8)}$$

The distance travelled by the fluid front of the ink can be measured in the paper scale at the back of the strips and it can be related to the frames per second selected in the data acquisition program of the *AnimatorDV* camera. The progression of the liquid along *1 Chr* and *Fusion 5* paper strips can be plotted as a function of the square root of the time, results are presented in figure II.4. The slopes of the graphs are attributed to the characteristics of the paper material (such as pore size) and the interaction between fluid and substrate (such as surface tension and contact angle). Then, big porous size as well as low surface tension and low contact angle have been found to be advantageous for the fast absorption of fluid. Other factors to take into account that can affect the fluid permeation are temperature, viscosity and pH values on the liquid. The graphs from figure II.4 were adjusted to the equation $y = ax$ and correlation coefficients of R > 0.98 were obtained for both. This leads to know *A'* in equation (II.8) and therefore the capillary properties of the strips can be estimated for both paper materials.

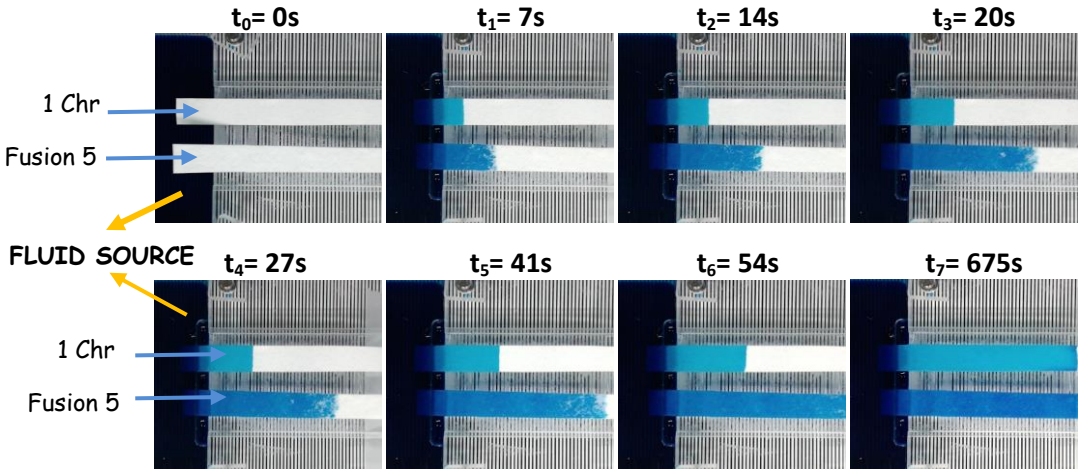

Figure II.3 Sequence of photographs showing the evolution of a water-based ink solution in two different kinds of paper strips materials. *Fusion 5* filter paper is filled up in less than 1 minute (t_6= 54 s), while *1 Chr* takes more than 10 minutes (t_7= 675 s) to be saturated, photograph (i).

It has been previously seen that the fluid penetration rate in a porous matrix depends mainly on the properties of the liquid when it is put in contact with the paper material. Therefore, the fluid progression was independent of the dimensions of the strip and it was only a function of the square root of the time. In order to test this assumption, two strips of *Fusion 5* paper were cut with 5 mm and 10 mm width and same length and then placed on the setup depicted in figure II.2. At the same time, the ends of the strips were soaked in the source solution and successive images were recorded during the fluid progress through the paper strips. Figure II.5 (a) shows some images of the liquid moving in the paper where it can be seen how the fluid fronts move together at three different times.

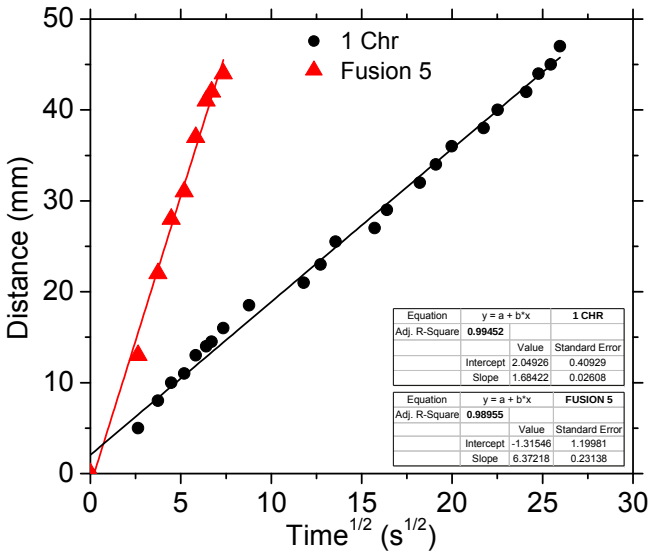

Figure II.4 Representation over time of the wicking distance of a front in *1 Chr* and *Fusion 5* paper strips of 5 mm width where fluid moves faster in the case of the filter paper *Fusion 5*. In both cases, points were adjusted to the root of t. A correlation coefficient higher than 0.9 was obtained verifying in this way the Darcy's Law.

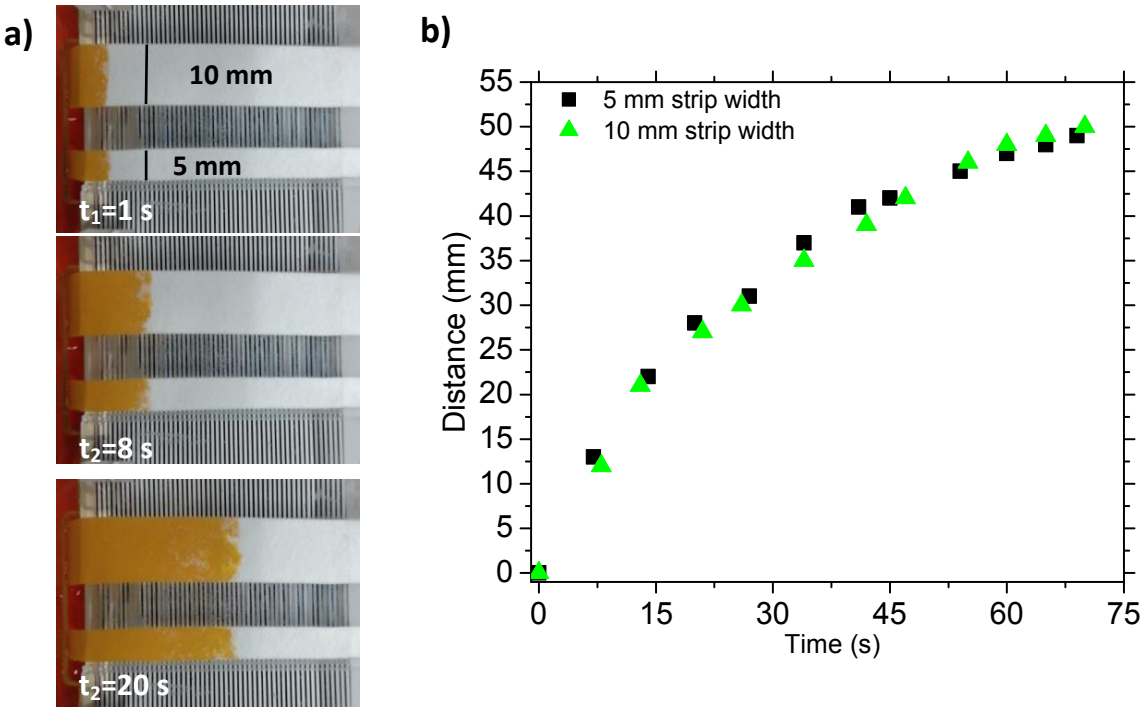

Figure II.5 Wicking process in two *Fusion 5* strips of 5 mm and 10 mm width (a) Photographs during the capillary flow of a coloured liquid recorded at different times where it can be seen the same distance moved by the fluid in both strips. (b) Representation over time of the wicking distance of the fronts in two paper strips of different widths where fluid moves with the same velocity despite of the dimensions of the paper strips and following the Darcy's law.

The wicking distance of the fronts was plotted as a function of time in figure II.5 (b). As it was predicted, the distance moved by the fluid have the same transport time in both paper strips regardless of their width. However, the amount of liquid delivered by the strips differed from one strip to the other. The volumetric flow rate, equation (II.4), depends on the paper section, therefore in a porous matrix the liquid dispensed by the strips can be adjusted by varying the paper width.

B) Capillary flow in a paper strip: the fully-wetted flow

Microfluidic fuel cells made on paper require a sustained flow along the strip to function. This is accomplished by attaching a dry absorbent pad on the distant end of the strip. In this configuration, the liquid moves through the paper strip until the liquid has filled it and reaches the wicking pad. From this point, the regime flow is called fully-wetted [38]. When the advancing liquid front reaches the pad, the liquid exits a region only of ~ 100 to 400 µm thick (the strip) and enters a second porous region that is typically >1000 µm thick (the combined thickness of both the strip and the pad). This configuration allows to establish a sustained flow across the strip [39]. The process occurring in the strip in which the absorbent pad has been attached at the end of it can be explained in more detail as follows. First, flow in the rectangular channel moves because surface tension pulls the fluid farther into the dry paper. The result is that the fluid front reduces its flow velocity as it advances through the channel following equation (II.8). Then, the liquid front reaches the absorbent pad, which offers an increase of available volume of dry paper. In this case, the restriction imposed by Darcy's law of a liquid flowing through a constant cross-sectional area is violated. Taking into account that the length of the strip should be much larger than its width, it can be assumed that the flow in the paper strip is quasi-stationary and can be expressed by equation (9). Therefore, the duration of validity of this expression depends directly on the device dimensions [39].

$$Q \approx \frac{kwP_C}{\mu L_r} \Rightarrow l \sim t \qquad \textbf{(I.9)}$$

where, k is the permeability of paper to the fluid, w the width of the channel, P_c is the capillary pressure, μ is the dynamic viscosity of the liquid and L_r is the length of the strip.

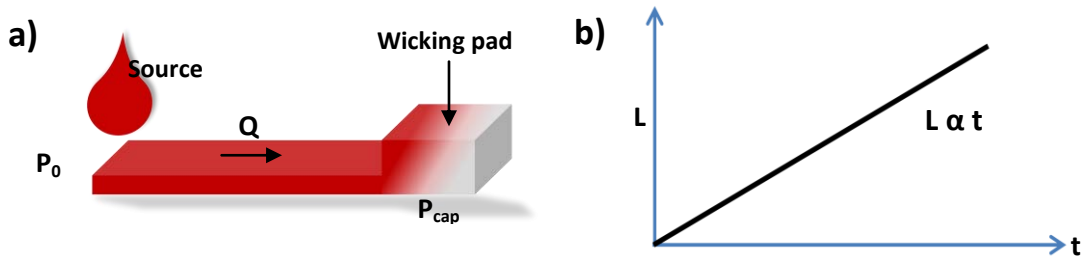

Figure II.6 (a) Schematic of the capillarity process in a paper strip when the fluid front is located in the wicking pad. (b) Representation of the wicking distance versus time for a liquid absorbed in a paper matrix for a fully wetted process.

B.1) Experimental fully-wetted flow

As it was demonstrated in previous chapters, flow rate has an important effect on the microfluidic fuel cell output power. In typical microfluidic fuel cells flow rate can be adjusted by means of an external pump (for typical microfluidic fuel cells) to maximize the delivered power.

In this section, the flow rate of a liquid that is established inside the paper strip by placing an absorbent pad at its end was characterized. *Fusion 5* paper was cut with dimensions of 5.5 cm length and 0.5 cm width and positioned on the set up shown in figure II.2. Then, approximately 1 cm of the strip end was immersed in a water-based yellow ink reservoir to ensure a continuous source of liquid. At the other side of the strip, an absorbent pad (a folded Kimwipe from Kimtech) was placed to establish a continuous flow during the experiments. Flow velocity was measured by following the movement of a drop of a water-based green ink deposited at the beginning of the strip (d=0) near the yellow ink reservoir. The first drop was deposited once the yellow ink front reached the absorbent pad and the wet out flow was established. When the drop arrived at the end of the strip (d=4.5 cm), another drop was deposited at d=0 position. This procedure was repeated several times until the wicking pad was nearly saturated. The position of the different drops during their travel from the beginning to the end of the strip was measured from the frames taken by the webcam and plotted against time. Due to diffusion, the green drop got more blurred with increasing time. Drop position was taken as the middle point of the green spot. Figure II.7 shows some of the images taken from the first drop deposited in the strip of F5. It can be seen qualitatively that the drop travels at a steady velocity.

The progression of the coloured drop in the fully-wetted mode (figure II.7) was compared with the wet out process during the fluid front advance (figure II.5) and represented in figure II.8. It can be seen that the liquid front during the wet out regime travels at a rate that is proportional to the square root of the time. However, the drop moving in the fully-wetted mode advances at a steady pace trough the paper strip. Note that in the second case the mean velocity of the drop is lower than during the wetting-out process. This is due to the fact that the capillary pressure in the *Kimwipe* pads is lower than in *Fusion 5.*

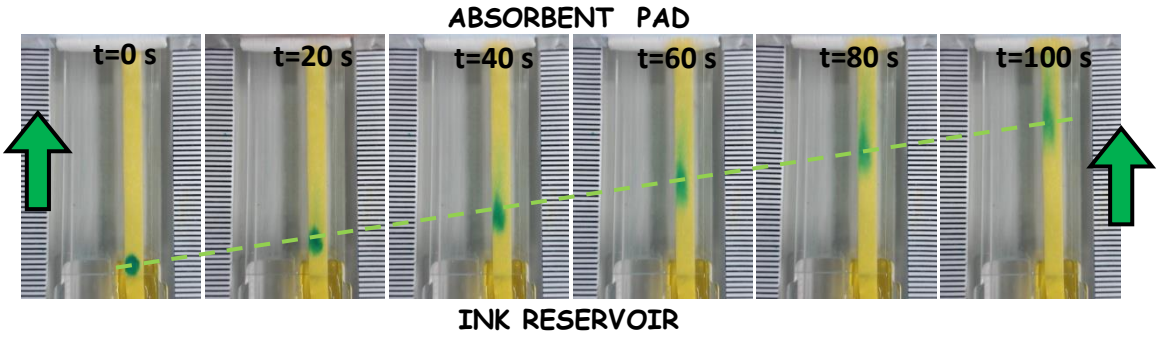

Figure II.7 Set of images showing the progress of the first coloured drop moving through a *Fusion 5* paper channel with constant dimensions and an absorbent pad placed at the end of the strip for a fully-wetted flow mode.

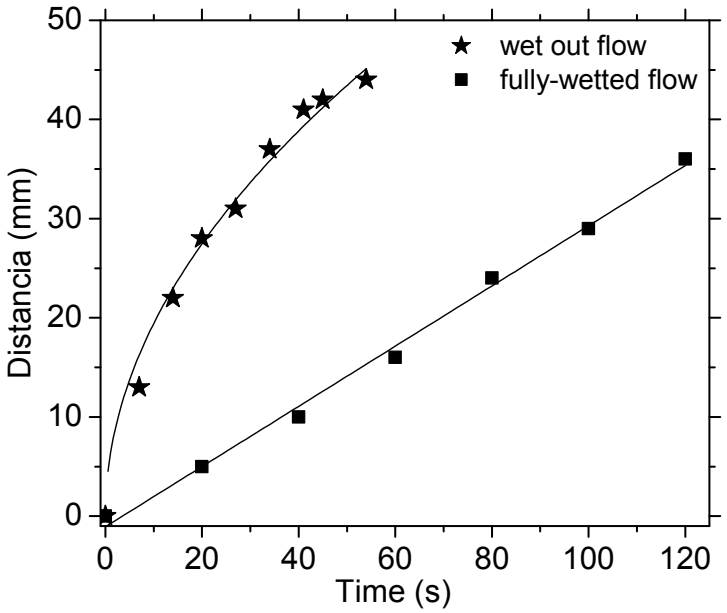

Figure II.8 Comparison of the capillary process in two paper strips of *Fusion 5* during the progression of (a) the fluid front (wet out flow) and (b) a coloured spot (fully-wetted flow) travelling through a paper channel of 4.5 cm of length.

The progress of the successive green drops along the strip was plotted as a function of the time as it is shown in figure II.9. The set of points corresponding to each drop were fitted to a linear dependence and correlation coefficients higher than 0.98 were obtained in all cases (except for the 14th drop probably due to a bad data acquisition). It can be seen that for successive drops, the slopes of the lines decrease. This means that as the fluid front advances inside the wicking pad a reduction of the flow velocity takes place. The mean flow velocity was extracted from the slopes of the lines of figure II.9 and depicted in figure II.10. It can be observed how the speed of the drops travelling through the strips ranges from 35 µl min^{-1} to 5 µl min^{-1} as the wicking pad is being gradually filled in a process that lasts approximately 100 minutes. In order to have some control over the flow rate during the characterization of the fuel cell in the following chapters, the fuel cells measurements were restricted within the time frame from minute 3 to minute 20 after the liquid front reaches the absorbent pad. In this way flow rate range was kept between 20-30 µl min^{-1} (see inset of figure II.10).

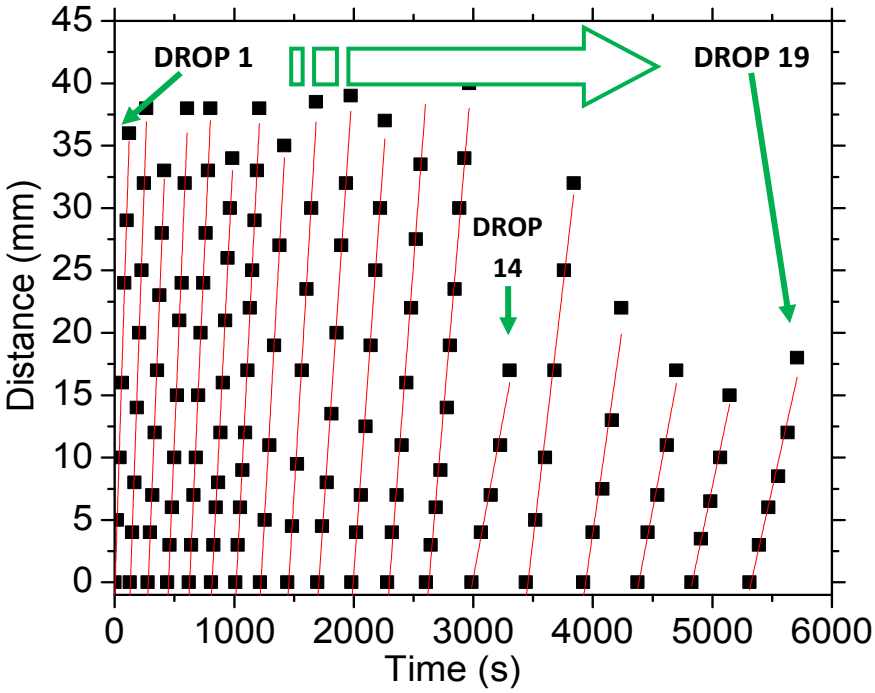

Figure II.9 Graphic of the distance moved by different drops as a function of the time. Each set of points indicate the course of a 2 µl drop moving along 4.5 cm *Fusion 5* paper strip. Points were adjusted with a liner fitting and correlation coefficients bigger than 0.98 were obtained corroborating the approximately steady flow of the drops.

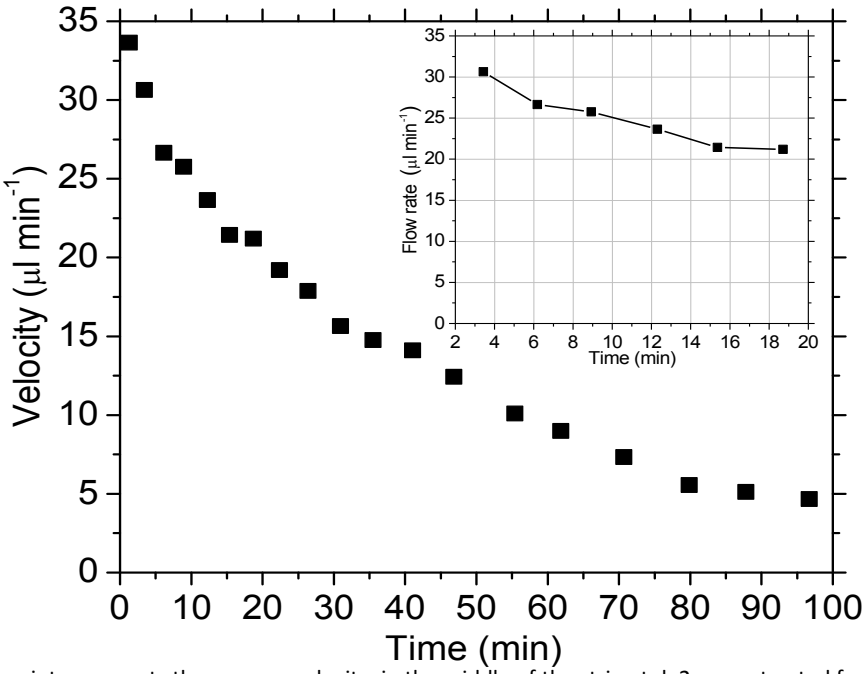

Figure II.10 Each point represents the average velocity, in the middle of the strip at d=2 cm, extracted from the slopes of figure II.9 of the successive drops travelling through a *Fusion 5* paper channel (dimensions: 0.5 cm width and 4.5 cm length) as a function of the time lapsed**.**

On the other hand, devices utilizing passive flow of reactants are a better solution to eliminate completely the balance of plant power consumption. Passive flow cells do not require external power inputs, they only need fluid delivery to an inlet region after which filling of the microfluidic device is spontaneous and the subsequent continuous flow is a function of the device design. Free from the size restrictions and power requirements of external equipment, LOC devices utilizing passive flow have great potential for use in point-of-care diagnostics and portable micro-total analysis systems [40].

CONTENTS OF SECTION II

Section II, with Chapter 4 and 5, represents a big step forward the creation of low cost passive fuel cells. The objective is to develop a paper-based microfluidic fuel cell for single-use and portable applications combining the advantages of enzymatic fuel cells and the benefits of microfluidic paper-based systems.

Chapter 4 presents the first approach towards the development and fabrication of a cost-effective enzymatic paper-based microfluidic fuel cell. The fabricated system is simplified with respect to the fuel cells presented in *Section I* because pumps are not necessary to keep liquids in movement inside the fuel cell and instead, solutions move by capillarity. With the objective to approximate the device to lateral flow test formats, the electrolyte pH used in the fuel cell are adapted to finally run the fuel cell with a single solution. The viability of the device is proved by operating the paper fuel cell with a soft drink. In **Chapter 5**, the development of a compact paper-based microfluidic fuel cell is presented. A new combination of enzymes is tested which allow to run the fuel cell with samples at neutral pH. This fact opens the possibility to operate the system using physiological fluids (such us blood, urine, serum or plasma). Furthermore its packed format allows to work with a very the limited sample volume. The output energy of the system is studied for glucose concentrations in the range found in blood resulting in a very low cost fuel cell that can be used at in-vivo applications at physiological conditions.

The current and power denisties obtained from the passive microlfuidic devices presented in these chapters are summarized in table II.2.

Fuel Cell Type	Anode material	Anolyte	Cathode material	Catholyte	J_{max} ($\mu A\ cm^{-2}$)	P_{max} (μWcm^{-2})	Chapter
Bioelectrode based and microfluidic	GOx enzyme and the mediator Fc-C6-LPEI on carbon paper	Glucose	MWCNT/lacc/ TBAB Nafion on CP	O_2	318	44	**4**
	GOx enzyme and the mediator Fc-C6-LPEI on carbon paper	Glucose & O_2 (one stream solution)	MWCNT/lacc/ TBAB Nafion on CP	Glucose & O_2 (one stream solution)	222	25	
	GDH with MWCNTs and Os-mediator on carbon paper	Glucose & O_2 (one stream solution)	BOx with MWCNTs and Os-mediator on CP	Glucose & O_2 (one stream solution)	275	91	**5**

Table II.2 Types of microfluidic fuel cells fabricated in Chapter 4 and Chapter 5 displaying the electrode material, the electrolytes and the maximum current and power densities obtained.

REFERENCES

1. Meredith, M.T. and S.D. Minteer, *Biofuel Cells: Enhanced Enzymatic Bioelectrocatalysis.* Annual Review of Analytical Chemistry, Vol 5, 2012. **5**: p. 157-179.
2. Jose Gonzalez-Guerrero, M., J. Pablo Esquivel, D. Sanchez-Molas, P. Godignon, F. Xavier Munoz, F. Javier del Campo, F. Giroud, S.D. Minteer, and N. Sabate, *Membraneless glucose/O-2 microfluidic enzymatic biofuel cell using pyrolyzed photoresist film electrodes.* Lab on a Chip, 2013. **13**(15): p. 2972-2979.
3. Kjeang, E., N. Djilali, and D. Sinton, *Microfluidic fuel cells: A review.* Journal of Power Sources, 2009. **186**(2): p. 353-369.
4. Atencia, J. and D.J. Beebe, *Controlled microfluidic interfaces.* Nature, 2005. **437**(7059): p. 648-655.
5. Song, Y., V. Penmatsa, and C. Wang. *Recent development of miniatured enzymatic biofuel cell*. in *Society of Photo-Optical Instrumentation Engineers (SPIE) Conference Series*. 2011.
6. Esquivel, J.P., F.J. Del Campo, J.L. Gomez de la Fuente, S. Rojas, and N. Sabate, *Microfluidic fuel cells on paper: meeting the power needs of next generation lateral flow devices.* Energy & Environmental Science, 2014. **7**(5): p. 1744-1749.
7. Zebda, A., C. Innocent, L. Renaud, M. Cretin, F. Pichot, R. Ferrigno, and S. Tingry, *Enzyme-Based Microfluidic Biofuel Cell to Generate Micropower*. in Society of Photo-Optical Instrumentation Engineers (SPIE) Conference Series. 2011.
8. Liana, D.D., B. Raguse, J.J. Gooding, and E. Chow, *Recent Advances in Paper-Based Sensors.* Sensors, 2012. **12**(9): p. 11505-11526.
9. Cate, D.M., J.A. Adkins, J. Mettakoonpitak, and C.S. Henry, *Recent Developments in Paper-Based Microfluidic Devices.* Analytical Chemistry, 2014. **87**(1): p. 19-41.
10. Thom, N.K., K. Yeung, M.B. Pillion, and S.T. Phillips, *"Fluidic batteries" as low-cost sources of power in paper-based microfluidic devices.* Lab on a Chip, 2012. **12**(10): p. 1768-1770.

11. Thom, N.K., G.G. Lewis, M.J. DiTucci, and S.T. Phillips, *Two general designs for fluidic batteries in paper-based microfluidic devices that provide predictable and tunable sources of power for on-chip assays.* Rsc Advances, 2013. **3**(19): p. 6888-6895.
12. Osborn, J.L., B. Lutz, E. Fu, P. Kauffman, D.Y. Stevens, and P. Yager, *Microfluidics without pumps: reinventing the T-sensor and H-filter in paper networks.* Lab on a Chip, 2010. **10**(20): p. 2659-2665.
13. Hu, J., S. Wang, L. Wang, F. Li, B. Pingguan-Murphy, T.J. Lu, and F. Xu, *Advances in paper-based point-of-care diagnostics.* Biosensors and Bioelectronics, 2014. **54**: p. 585-597.
14. Martinez, A.W., *Microfluidic paper-based analytical devices: from POCKET to paper-based ELISA.* Bioanalysis, 2011. **3**(23): p. 2589-2592.
15. Von Lode, P., *Point-of-care immunotesting: approaching the analytical performance of central laboratory methods.* Clinical Biochemistry, 2005. **38**(7): p. 591-606.
16. Chin, C.D., S.Y. Chin, T. Laksanasopin, and S.K. Sia, *Low-cost microdevices for point-of-Care testing*, in *Point-of-Care Diagnostics on a Chip*. 2013, Springer. p. 3-21.
17. Shah, P., X. Zhu, and C.Z. Li, *Development of paper-based analytical kit for point-of-care testing.* Expert Review of Molecular Diagnostics, 2013. **13**(1): p. 83-91.
18. Jane Maxwell, E., A.D. Mazzeo, and G.M. Whitesides, *Paper-based electroanalytical devices for accessible diagnostic testing.* MRS Bulletin, 2013. **38**(4): p. 309-314.
19. Martinez, A.W., S.T. Phillips, G.M. Whitesides, and E. Carrilho, *Diagnostics for the Developing World: Microfluidic Paper-Based Analytical Devices.* Analytical Chemistry, 2009. **82**(1): p. 3-10.
20. Liu, H. and R.M. Crooks, *Paper-Based Electrochemical Sensing Platform with Integral Battery and Electrochromic Read-Out.* Analytical chemistry, 2012. **84**(5): p. 2528-2532.
21. Chin, C., S. Chin, T. Laksanasopin, and S. Sia, *Low-Cost Microdevices for Point-of-Care Testing*, in *Point-of-Care Diagnostics on a Chip*, D. Issadore and R.M. Westervelt, Editors. 2013, Springer Berlin Heidelberg. p. 3-21.
22. Zhao, C., M.M. Thuo, and X. Liu, *A microfluidic paper-based electrochemical biosensor array for multiplexed detection of metabolic biomarkers.* Science and Technology of Advanced Materials, 2013. **14**(5): p. 54402-54408.
23. Dungchai, W., O. Chailapakul, and C.S. Henry, *Electrochemical Detection for Paper-Based Microfluidics.* Analytical chemistry, 2009. **81**(14): p. 5821-5826.
24. Nie, Z., C.A. Nijhuis, J. Gong, X. Chen, A. Kumachev, A.W. Martinez, M. Narovlyansky, and G.M. Whitesides, *Electrochemical sensing in paper-based microfluidic devices.* Lab on a Chip, 2010. **10**(4): p. 477-483.
25. Peeling, R.W., K.K. Holmes, D. Mabey, and A. Ronald, *Rapid tests for sexually transmitted infections (STIs): the way forward.* Sexually Transmitted Infections, 2006. **82**: p. V1-V6.
26. Zhang, L., M. Zhou, D. Wen, L. Bai, B. Lou, and S. Dong, *Small-size biofuel cell on paper.* Biosensors and Bioelectronics, 2012. **35**(1): p. 155-159.
27. Ciniciato, G.P.M.K., C. Lau, A. Cochrane, S.S. Sibbett, E.R. Gonzalez, and P. Atanassov, *Development of paper based electrodes: From air-breathing to paintable enzymatic cathodes.* Electrochimica Acta, 2012. **82**(0): p. 208-213.
28. Leijonmarck, S., A. Cornell, G. Lindbergh, and L. Wagberg, *Single-paper flexible Li-ion battery cells through a paper-making process based on nano-fibrillated cellulose.* Journal of Materials Chemistry A, 2013. **1**(15): p. 4671-4677.
29. Ge, L., P. Wang, S. Ge, N. Li, J. Yu, M. Yan, and J. Huang, *Photoelectrochemical Lab-on-Paper Device Based on an Integrated Paper Supercapacitor and Internal Light Source.* Analytical Chemistry, 2013. **85**(8): p. 3961-3970.

30. Zhong, Q., J. Zhong, B. Hu, Q. Hu, J. Zhou, and Z.L. Wang, *A paper-based nanogenerator as a power source and active sensor.* Energy & Environmental Science, 2013. **6**(6): p. 1779-1784.
31. Nguyen, T.H., A. Fraiwan, and S. Choi, *Paper-based batteries: A review.* Biosensors & Bioelectronics, 2014. **54**: p. 640-649.
32. Calabrese Barton, S., J. Gallaway, and P. Atanassov, *Enzymatic biofuel cells for implantable and microscale devices.* Chemical Reviews, 2004. **104**(10): p. 4867-4886.
33. Byrnes, S., G. Thiessen, and E. Fu, *Progress in the development of paper-based diagnostics for low-resource point-of-care settings.* Bioanalysis, 2013. **5**(22): p. 2821-2836.
34. Masoodi, R. and K.M. Pillai, *Darcy's Law-Based Model for Wicking in Paper-Like Swelling Porous Media.* Aiche Journal, 2010. **56**(9): p. 2257-2267.
35. Fu, E., S.A. Ramsey, P. Kauffman, B. Lutz, and P. Yager, *Transport in two-dimensional paper networks.* Microfluidics and Nanofluidics, 2011. **10**(1): p. 29-35.
36. Sharp, J.M. and C.T. Simmons, *The compleat Darcy: New lessons learned from the first English translation of Les Fontaines publiques de la Ville de Dijon.* Ground Water, 2005. **43**(3): p. 457-460.
37. Masoodi, R., K.M. Pillai, and P.P. Varanasi, *Effect of externally applied liquid pressure on wicking in paper wipes.* J. Engineered Fibers Fabrics, 2010. **5**(3): p. 49-66.
38. Washington, U.o. *Microfluidics 2.0. A Practical Guide to Fluid Flow in Porous Media*. Microfluidics 2.0 2010; Available from: http://www.mf20.org/practical-guide-fluid-flow-porous-media.
39. Mendez, S., E.M. Fenton, G.R. Gallegos, D.N. Petsev, S.S. Sibbett, H.A. Stone, Y. Zhang, and G.P. López, *Imbibition in Porous Membranes of Complex Shape: Quasi-stationary Flow in Thin Rectangular Segments.* Langmuir, 2010. **26**(2): p. 1380-1385.
40. Lynn, N.S. and D.S. Dandy, *Passive microfluidic pumping using coupled capillary/evaporation effects.* Lab on a Chip, 2009. **9**(23): p. 3422-3429.

CHAPTER

4

Paper-based enzymatic microfluidic biofuel cells

This chapter presents a first approach towards the development of a paper-based glucose/O_2 microfluidic system. Two microfluidic fuel cells made in paper were constructed using the knowledge presented in previous chapters on glass and plastic technologies. First, a Y-shaped paper system was fabricated in which two parallel solutions flow side by side. Next, this configuration was adapted to use a single solution containing both the fuel and the oxidant. In this way, a biofuel cell much closer to a commercial application, similar to conventional lateral flow tests strips, was designed, developed and fabricated and characterized.

4.1 FLOW WITHIN A Y-SHAPED PAPER SYSTEM

The previous section described fluid transport in paper networks due to capillarity, leading to a comprehensive understanding of the basic transport principles of a liquid in a porous matrix. Special attention was given to fluid transport inside a paper channel when an absorbent pad is placed at its end. The velocity of the fluid inside the paper matrix in this regime - labelled as fully wetted flow - was recorded. It was demonstrated that compared with the wet-out regime, the velocity of the fluid slows down very gradually, which allows to consider velocity as a constant during the fuel cell characterization.

Here this knowledge has been used to establish a capillary co-laminar flow of two different fluids inside a paper strip. For this, a *Fusion 5* paper was cut in a Y-shape that allowed to define in this way two separate inlets. The suitability of the design was tested by applying a coloured aqueous-based solution at each of the two inlets of the strip. These solutions account for the electrolytes that will be used later to implement a microfluidic fuel cell. Figure 4.1 shows two pictures of the Y-shape setup. It can be seen that the two dyes flow parallel until they reach the wicking pad placed at the end of the strip. This result is the first step towards the achievement of a pumpless microfluidic fuel cell.

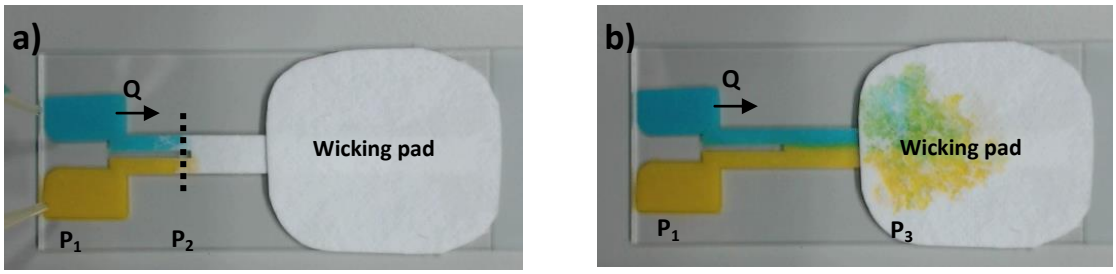

Figure 4.1 Photographs of the Y-shaped paper strip displaying the laminar behaviour of two coloured liquids moving along the paper. a) The front of the liquids is situated in the rectangular portion of the strip (wet out flow). (b) The fluid front reaches the wicking pad (fully-wetted flow) and the flow velocity is considered steady.

4.2 FUEL CELL DESIGN AND FABRICATION

After demonstrating that a co-laminar flow could be established inside a paper channel, the Y-shaped paper strip was used as a central component of a microfluidic fuel cell. In the following sections the fabrication process and its assembly in a characterization setup are described.

4.2.1 Microfluidic channels and fuel cell electrode construction

The paper selected as substrate for the microfluidic fuel cells was Whatman® paper, grade *Fusion 5*, due to its high wicking rate. The system was designed using Vectorworks 2012 student edition (Techlimits, Spain). Before the cutting process, a flexible plastic plate was added to one side of the paper sheet to provide mechanical support to it. The device was cut using a Roland

GX-24 cutter plotter with a force and speed of 30 gf at 1 cm s^{-1}, respectively, and the cutting was performed in two passes in order to prevent any tearing of the paper [1]. The thickness of the *Fusion 5* substrate (and consequently the height of the microfluidic channel) was 370 µm and the systems had final dimensions of 45 x 5 mm^2. After cutting, the paper structures were released from the plastic support.

Carbon paper from Fuel Cell Earth (type TG-H-060) was used as the electrodes of the fuel cells. They were cut in a rectangular size of 5 x 10 mm^2 and were positioned in parallel 2 cm downstream from the paper inlets with a separation of 1 mm from each other. A piece of a conducting copper tape (3M-1182) purchased from RS (Spain) was used to contact the outer part of the carbon paper electrodes. This way the electrodes were protected from the spring-loaded pins that connected the external wires. Figure 4.2 shows a picture of the Y-shaped paper strip together with the carbon electrodes on a glass slide. The glass slide held (using a two side adhesive plastic material) the paper substrate.

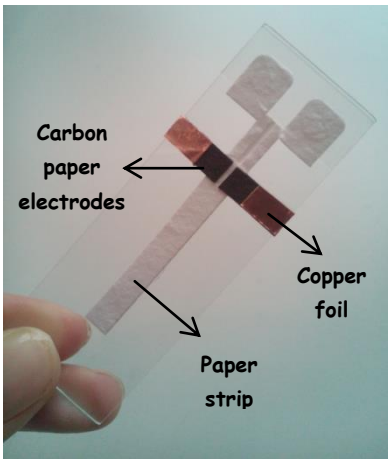

Figure 4.2 Two stream paper fuel cell with carbon paper electrodes fixed in a glass slide

4.2.2 Microfluidic device assembly

A holder made of poly(methyl methacrylate) - PMMA - was designed and made with a Roland MDX-40 milling machine (Roland DG, Spain). This component – shown in figure 4.3 – was fabricated to facilitate the connection of different elements of the measurement setup to the fuel cell. A socket milled into the holder was used to hold the glass slide that supports de paper fuel cell (figure 4.2). Two adhesive magnetic bands, placed on the sides of the PMMA block, allow to fix two PMMA fuel reservoirs at the paper inlets. Also the fuel cell wicking pad and the external electrical connections of the device are hold by PMMA pieces. All these plastic components host small magnets that keep them attached to the holder. For the external electrical connections spring-loaded pins (Preci-Dip, CH) were inserted in the PMMA plugs that at the same time were in contact with the copper foil over the electrodes. An absorbent wipe

from Kimtech Science was folded and used as a wicking pad. It ensured a continuous and steady wicking of the liquids up to a volume of 3ml.

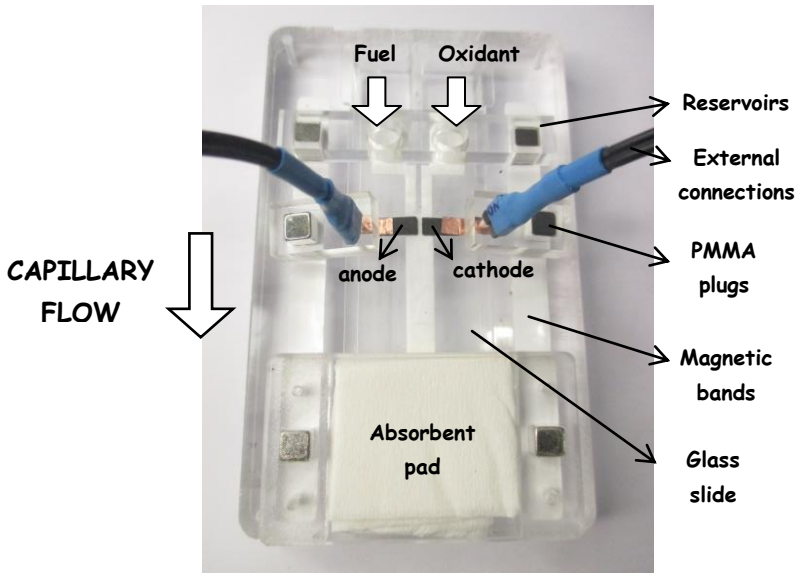

Figure 4.3 Two stream solution paper-based fuel cell showing the different parts forming the experimental setup for measurements.

4.3 PREPARATION OF ENZYMATIC BIOELECTRODE SOLUTIONS

The carbon paper working electrodes were functionalized with enzymes prior to their incorporation in the microfluidic fuel cell. The chemicals used to obtain the catalytic solutions and the process for preparing the enzyme-mixture inks are described below. The electrolyte solutions and the fuel used to run the fuel cell are also listed.

4.3.1 Chemicals and equipment

The salts required for the supporting electrolytes, the enzymes for the electrode enzyme-mixture inks, glucose, Nafion and solvents were purchased from Sigma Aldrich and used as received. Glucose oxidase from *Aspergillus niger* (EC 1.1.3.4, Type X-S, 175 units/mg of solid, 75% protein) and laccase from *Trametes Versicolor*. The proton conducting binder was Nafion 5% by wt. EW1100 in an alcoholic suspension. Hydroxylated MWCNTs (10–30 mm length, 1.6% –OH functionalization) were purchased from cheaptubes.com and used as received. Ethylene glycol diglycidyl ether (EGDGE) was purchased from Polyscience Inc., Warrington, PA. 2-Anthracenecarboxylic acid was obtained from TCI chemicals and used as received. The redox polymer Fc-C_6-LPEI used at the anode along with the glucose oxidase was synthesized as previously reported [2]. Tetrabutylammonium bromide (TBAB)-modified Nafion was prepared as previously reported [3]. Anthracene-2-carbonylchloride for anthracene-modified MWCNTs was synthesized as previously published procedures [4-5].

Phosphate buffer was prepared with sodium phosphate dibasic, sodium phosphate monobasic and sodium nitrate (Na_2HPO_4, NaH_2PO_4 and $NaNO_3$) for a final concentration of 100 mM. The pH of the buffer was adjusted with hydrochloric acid and sodium hydroxide (HCl and NaOH) to match the optimal pH required by the enzymes. A 1 M stock glucose (α-D(+)-Glucose) solution in distilled water was prepared 24 hours before use and stored at 4ºC to allow it to mutarotate.

Electrochemical measurements were conducted with an electrochemical workstation CHI model 650A (Austin TX). Ag/AgCl electrode (saturated KCl) and a commercial platinum electrode were used as reference and counter electrode respectively. All of the experiments were carried out at room temperature.

4.3.2 Enzymatic bioelectrode modification

The biocatalyst solutions to be deposited on the carbon paper electrodes were prepared as follows:

a) For the anodic side, the enzymatic solution was prepared with the blend of 3 µl of enzyme glucose oxidase (10 mg ml^{-1} in distilled water), 7 µl of redox polymer Fc-C_6-LPEI (10 mg ml^{-1} in distilled water) and 0.4 µl of the crosslinker EGDGE (10% v/v). All the previous components were mixed together by vortexing.

b) The cathodic solution was prepared by mixing 1.5 mg of laccase enzyme in 74 µl of 100 mM phosphate buffer at pH 7, 7.5 mg of anthracence modified MWCNT's and 25 µl TBAB-modified Nafion. The above components were sonicated and vortexed intermittently until the mixture was completely dissolved.

Two pieces of 10 mm^2 of carbon paper were modified with 42 µl of each enzymatic mixture by drop-casting. The electrodes were allowed to dry for 24 hours at room temperature. Then, the electrodes were positioned side by side over the paper substrate with its catalytic side in contact with the paper strip. Figure 4.4 shows a diagrammatic representation of the functionalized carbon paper electrodes together with the electrical connections between them.

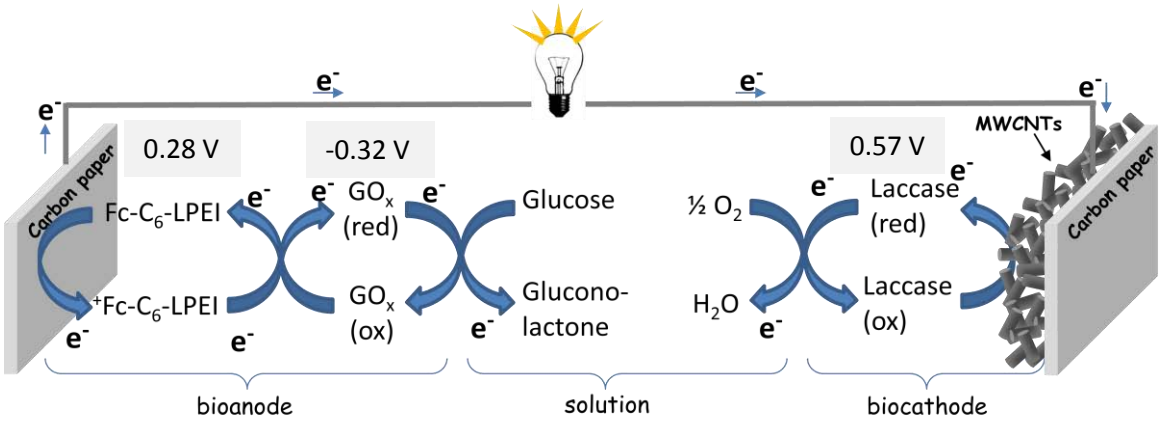

igure 4.4 Depiction of the glucose/O_2 biofuel cell after enzymatic drop-coating with the reactions that will take place. It can be seen the flow of electrons from the oxidation of glucose to the reduction of oxygen, showing the potentials involved in the reactions vs Ag/AgCl [2, 6-8]. At the anode, a mediated electron transfer (MET) occurs due to the redox polymer Fc-C_6-LPEI. At the cathode, on the contrary, a direct electron transfer (DET) step can be seen between the electrode and the enzyme because anthracene groups help to orient the active sites of laccase.

4.4 FUEL CELL OPERATION

4.4.1 Two stream solution paper fuel cell

After enzymatic electrode modification the Y-shaped paper microfluidic fuel cell was assembled in the PMMA holder (figure 4.3). For the fuel cell characterization, sodium phosphate buffer at pH 7.4 with 100 mM glucose was applied to anodic side of the device whereas buffer phosphate at pH 4.5 was introduced as catholyte.

4.4.1.1 Polarization and power curves

Figure 4.5 shows the obtained polarization and the power curves of the paper fuel cell. The open circuit voltage was 0.6V and the maximum current and power density were 320 µA cm^{-2} and 45 µW cm^{-2} (at 0.23 V) respectively. Data was taken within the first 15 minutes after having applied the anolyte and catholyte solutions to the fuel cell. According to the values obtained from paper flow characterization (figure II.10 in Section II) flow rates inside the paper range from 25 to 20 µl min^{-1} during this time interval. In order to compare the power output obtained using paper to drive the fluid with a pumped microfluidic fuel cell, the maximum power densities obtained in chapter 3 (figure 3.19) at the same flow rates have been depicted as two red stars in the polarization curves. It can be seen that the power output obtained with the paper fuel cell yields between the values previously obtained with the active microfluidic fuel cell (20 µl min^{-1} the power obtained was 41 µW cm^2 and at 25 µl min^{-1} was 48 µW cm^2). This shows that the paper fuel cell is capable of producing a comparable power output, when using the same enzymatic electrodes, as a fuel cell using an active supply of liquids (such as external pumps) without losing performance. Furthermore, since no energy is spent in pumping the solutions, all the power

generated is actually available for any other function. The paper device represents an important simplification as compared with the typical microfluidic fuel cells that use syringe pumps.

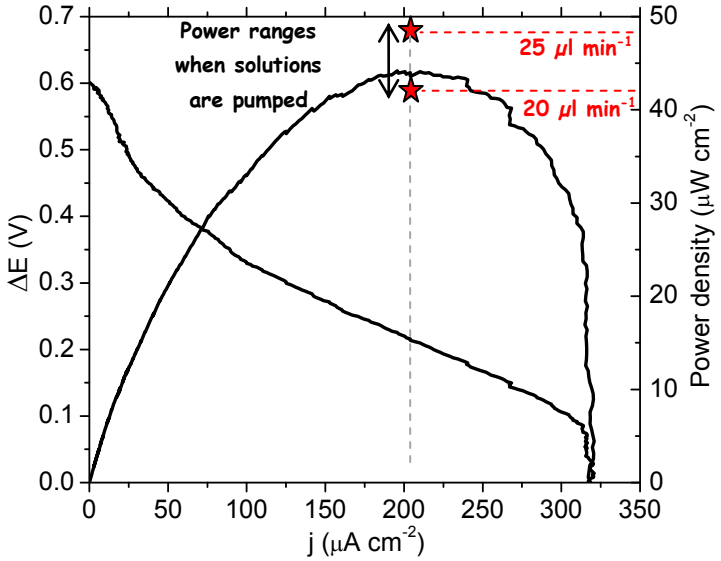

Figure 4.5 Polarization and power curve for the Y-shaped microfluidic fuel cell at a time compressed between 10 to 15 minutes representing a flow velocity of 20-25 µl min^{-1}. In red, power density values for the same ranges of velocities using a syringe pump instead of the capillary of paper.

4.4.2 One stream solution paper fuel cell

The performance of the Y-shape fuel cell prototype was validated showing that it is possible to eliminate the need of pumps in a microfluidic fuel cell. However, its operation is still of no practical use as it requires the application of two separated solutions of different pH at the fuel cell inlets. In order to gain simplicity in fuel cell operation the two inlets of the Y-shaped fuel cell may be simplified into only one inlet so that the fuel and the electrolytes could be added together in a single step. This would result in a fuel cell working with the simplicity of lateral flow test strips. In order to achieve this simplicity, the fuel cell will have to work with a single electrolyte which requires to find a compromise in the pH value between anolyte and catholyte solutions. In the Y-shaped device the fuel cell electrolytes had the optimum pH for each enzyme (i.e. the pH at which enzyme activity is maximized) at pH= 4.5 for laccase and pH=7.4 for glucose oxidase.

In order to determine the pH at which laccase and glucose oxidase can operate losing the minimum overall fuel cell performance, their electrochemical responses were studied at pHs ranging from 4.5 to 7.4. Once the optimum pH value was found, the performance of the single inlet paper fuel was evaluated by means of polarization and power curves in the setup shown in figure 4.6.

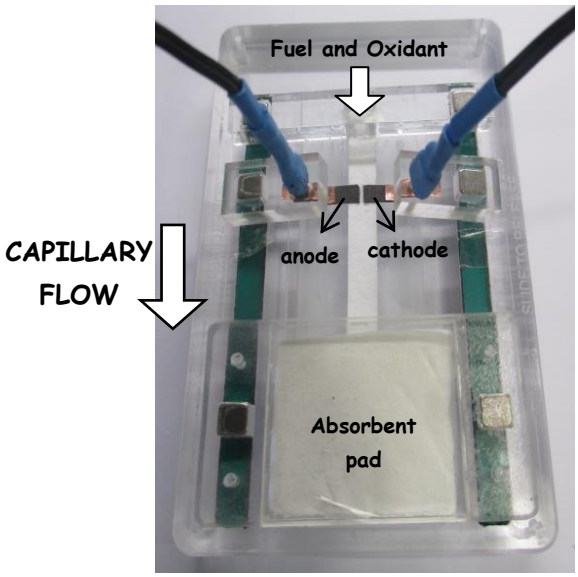

Figure 4.6 Experimental setup used for the one stream solution in a I-shaped paper-based fuel cell.

4.4.2.1 Bioelectrode characterization at different pHs

Glassy carbon electrodes (BASi, West Lafayette, IN) were modified with the appropriate enzyme-solution (depending if they were working as anode or cathode). Their catalytic responses were measured in 100 mM phosphate buffer with 100 mM glucose by cyclic voltammetry. The pH of the buffer was varied between 4.5 and 7.4 using HCl or NaOH when required. Laccases optimally operate in slightly acidic solutions, at pH values ranging from 3 to 5 [9]. In contrast, glucose oxidases show their better responses around neutral pH values [6]. The voltammograms of the bioelectrodes were recorded at different pH values and peak current values were extracted. Figure 4.7 shows the current density values obtained for both bioanode and biocathode. As it can be seen, glassy carbon modified electrodes based on glucose oxidase (bioanode) or electrodes based on laccase (biocathode) differ considerably depending on the pH of the electrolyte used. These results corroborate that the fuel cell yields the best performance when pH of the electrolytes are 7.4 (anode) and 4.5 (cathode). The obtained current densities of 635 ± 95 μA cm^{-2} and 180 ± 60 μA cm^{-2} show that the cell is limited by the cathode performance, probably due to the low concentration of dissolved O_2 as well as by the lower activity of the laccase as compared with the glucose oxidase. However, the one stream configuration requires an intermediate buffer pH that can be set around 5.5.

A comparison of the linear sweep voltammetries of the bioelectrodes working at pH 5.5 and at its optimum pH are represented in figure 4.8. At pH 5.5, the bioanode showed a current density that corresponds to 269 ± 30 μA cm^{-2}, at the cathode the current density was 120 ± 35 μA cm^{-2}. Figure 4.8 (b) shows a shift of about 0.05 V of the oxygen reduction potential towards a more negative potential when the solution at pH 5.5 was air saturated.

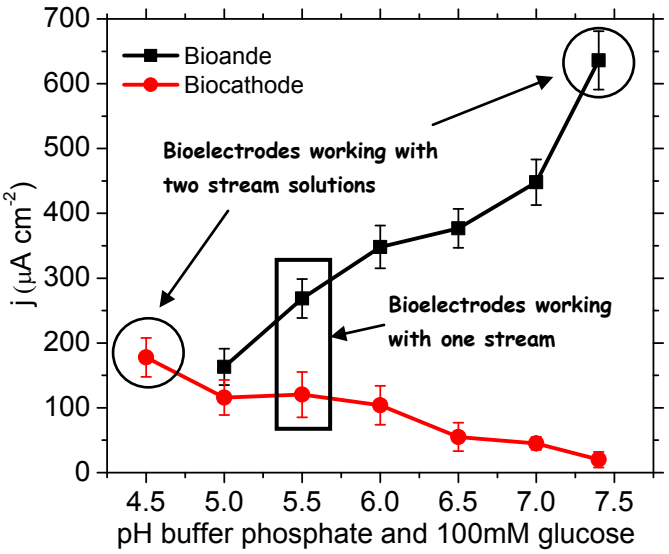

Figure 4.7 PH analysis of glassy carbon electrodes modified with the corresponding biocatalytic solutions**.** Representation of the influence of pH on the current density at room temperature in buffer phosphate at 100 mM and 100 mM glucose. Dot-line, bioanode behaviour. Square-line, response of the biocathode. The experiments were repeated three times. The errors bars correspond to the standard deviation.

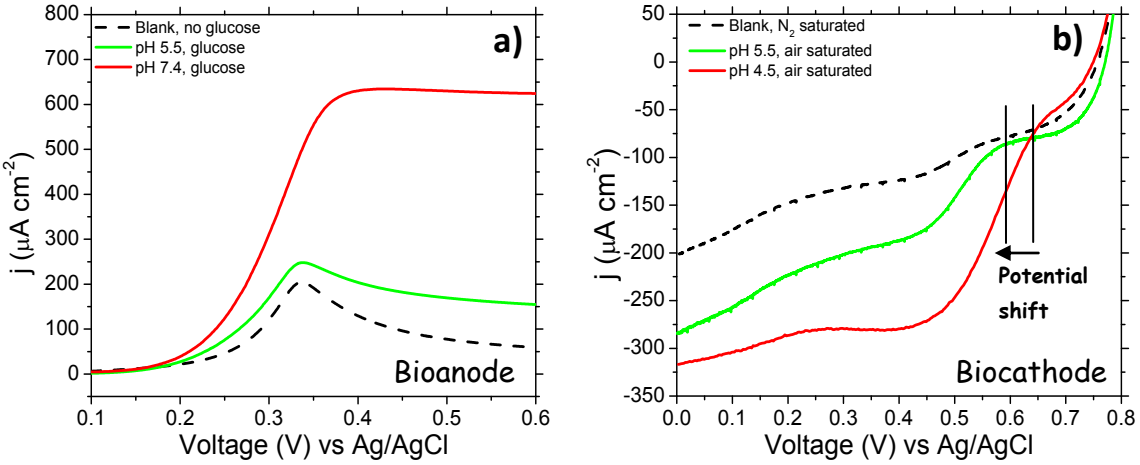

Figure 4.8 Representative linear sweep voltammetries of enzymatic GC electrodes at 5 mV s^{-1}. (a) GOx/Fc-C_6-LPEI bioanodes in 100 mM sodium phosphate at pH 7.4 (red), at pH 5.5 (green) and without glucose (dotted line). (b) An-MWCNTs/laccase/TBAB-Nafion biocathode in 100 mM sodium phosphate in air saturated conditions at pH 4.5 (red), at pH 5.5 (green) and in N_2-saturated conditions (dotted line)

4.4.2.2 Polarization and power curves

The performance of the single stream paper fuel cell (shown in figure 4.6) was measured with a solution consisting of a mixture of buffer phosphate at pH 5.5 and 100 mM glucose. The polarization and power curves obtained are represented in figure 4.7. The polarization curves previously obtained with the two stream fuel cell have been added for comparison purposes.

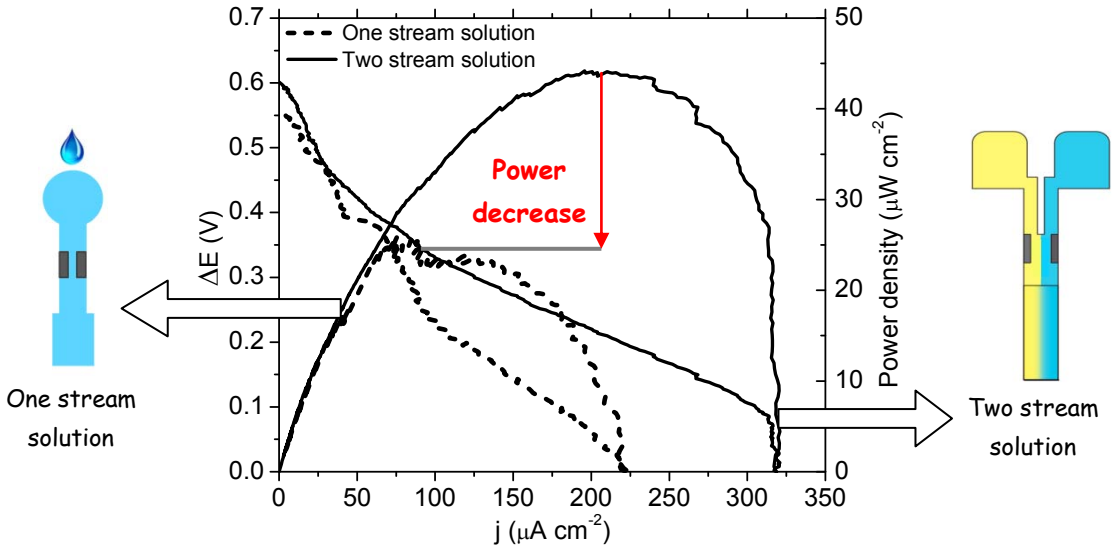

Figure 4.9 Polarization and power curves of two enzymatic paper-based fuel cells. Solid line shows the performance of the two stream fuel cell (Y-shaped) working with buffer phosphate at pH 4.5 at the cathode and pH 7.4 with 100 mM at the anode. Dotted lines correspond to the one stream fuel cell (I-shaped) working with a single solution of sodium phosphate at pH 5.5 with 100 mM glucose.

The I-shaped fuel cell yielded an open circuit voltage around 0.55 V, a slightly lower value than that at the Y-shaped system probably due to the potential shift observed in the oxygen reduction reaction (figure 4.8 (b)). The maximum current and power density were 225 μA cm^{-2} and 24 μW cm^{-2} at 0.19 V, respectively. This corresponds to a power output drop of almost 50% compared to the Y-shaped fuel cell in which the optimum pH for each enzyme was used.

To sum up, it was demonstrated that the one stream enzymatic paper-based fuel cell is able to operate properly with a single solution despite showing lower performance as compared with the Y-shape fuel cell. However, the fuel cell format presented is much closer to lateral flow test strips which gives to the system important advantages toward commercial applications [10].

4.4.2.3 Performance at different glucose concentrations

The power output of the single inlet system was studied under different glucose concentrations ranging from 50 to 400 mM in buffer phosphate at pH 5.5. Results are shown in figure 4.10 (a). It can be seen how power output increases from 15 μW cm^{-2} to 24 μW cm^{-2} when glucose concentration increases from 50 mM to 100 mM. However, when the glucose concentration goes up to 400 mM the system showed an intermediate power output (19 μW cm^{-2}) between the two referred to above. This result is consistent with those reported in the literature for similar enzymatic fuel cells. Generally, this kind of fuel cells shown a power output saturation at around 100 mM glucose and an increase in glucose concentration does not increase the performance of the fuel cell. On the contrary, in our case at high glucose concentrations (such as 400 mM) a diminution of the current and power density of the system was observed. This could

be due to an increase of the electrolyte viscosity which diminishes the velocity of the flow. It has been reported that increasing glucose concentration in an aqueous fluid from 100 mM to 400mM increases viscosity from 1.0 Pa·s to approximately 1.4 Pa·s [11]. Indeed, the volumetric flow rate (Q) is related to the viscosity (μ): $Q \sim {}^{1}/_{\mu}$. Consequently, the velocity of the liquid inside the microchannel decreases and this gives rise to a decrease of the power output of the system.

The simplicity of operation of our single-inlet paper fuel cell inspires the possibility of using ubiquitous fuel sources. Ultimately, biofuel cells should benefit from abundant fuel sources accessible to the general public that could use them to power small electronic devices [12]. In this context, soft drinks are cheap and broadly available in our daily lives. In fact, sugar is a very common ingredient in beverages, vegetables and fruits. Therefore, a commercial soft drink with high glucose content was applied to the fuel cell instead of the buffer phosphate with the glucose. The soft beverage selected for the experiments was *Coca-Cola* and it was used without the addition of any salts to improve its electric conductivity and without adjusting its pH either. Taking into account that 330 ml of that drink contain approximately 40 g of glucose, the glucose concentration was estimated to be around 670 mM with a measured pH of 2.5. As we can see from the curves shown in figure 4.7 (b), the paper fuel cell is able to generate energy from this commercial beverage. The power density at 0.23 V corresponded to 11 µW cm^{-2} and the maximum current density to 65 µW cm^{-2}.

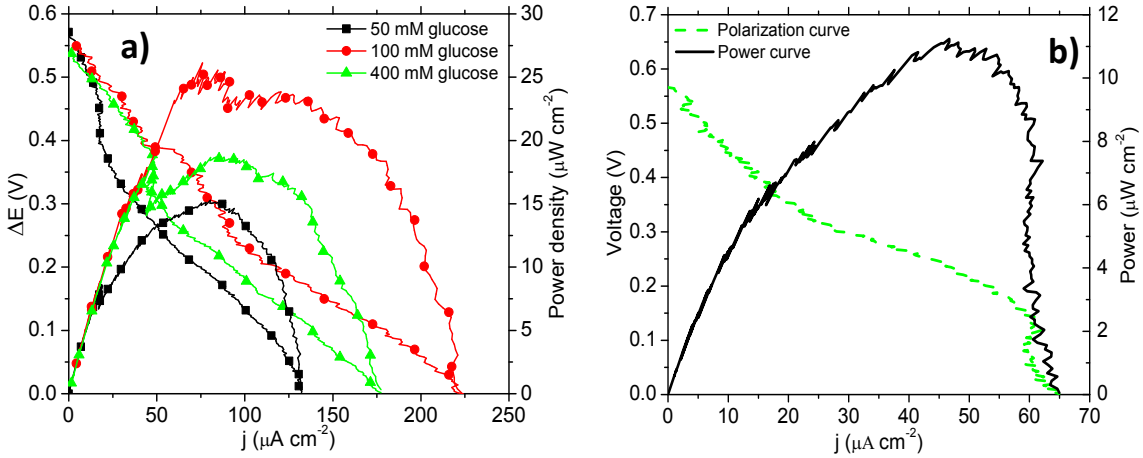

Figure 4.10 Polarization and power curves of the I-shaped paper-based enzymatic fuel cell working with a single stream solution. a) Using buffer phosphate at pH 5.5 with 50 mM, 100 mM and 400 mM glucose. b) Using a commercial drink with high levels of glucose (11.3 g in 100 ml of solution).

From these results, the versatility of the paper-based fuel cell presented in this chapter is proved being able to harvest energy from a commercial soft drink, with a very simple cell construction and very low cost fabrication.

SUMMARY AND CONCLUSIONS

This chapter has shown the first approach towards the development and fabrication of cost-effective *enzymatic paper-based microfluidic fuel cell*. The material selected as substrate for the microfluidic paper-based fuel cell was *Fusion 5* paper because of its high volumetric flow rate. Carbon paper electrodes were used to immobilize the catalysts that are responsible for the generated power. The enzymatic mixture consisted of a combination of GOx and the polymer Fc-C_6-LPEI (for the bioanode) and the blend of MWCNTs, laccase and TBAB-Nafion (at the biocathode).

The first objective of the present chapter was to show that it is possible to run a microfluidic fuel cell without the implementation of pumps, which results in a great simplification of the system. This was shown successfully in the first part of the chapter; our paper microfuel cell yields approximately the same power output that the plastic pumped microfuel cell developed in chapter 3.

The second objective of this work was to approximate the paper-based fuel cell to the simplicity of a lateral flow test format. For this purpose, the paper fuel cell was run using a single solution instead of the two streams employed in conventional Y-shaped microfluidic fuel cells. That implied the need of finding a compromise between anolyte and catholyte pH, a value that was set at 5.5 after studying carefully the enzymatic performance of both fuel cell electrodes at different pH solutions.

The single-inlet fuel cell was characterized with a mixture of glucose fuel and electrolyte at pH 5.5. It yielded an open circuit voltage of 0.55 V, a maximum current density of 225 μA cm^{-2} and a maximum power density of 24 μW cm^{-2} (at 0.19 V). It can be concluded that although the efficiency of the system decreases (as compared with the Y-shaped microfluidic fuel cell with every anode operating at its optimal pH) the single-inlet configuration is much closer to a commercial application.

The I-shaped paper device was then tested at different glucose concentrations. It was observed that very high glucose concentrations (such as 400 mM) led to a diminution of the power output. This was attributed to an increase in the liquid viscosity that causes an significant reduction in the flow rate.

Finally, a soft drink was used "out of a can" to feed the fuel cell yielding a maximum power density of 11 μW cm^{-2}. These promising results show that paper-based fuel cells using enzymes to convert ubiquitous glucose into electrical energy could be used to power real devices using the sugar from commercial drinks.

In conclusion, the *enzymatic paper-based microfluidic fuel cell* presented here exhibits multiple benefits as compared with the fuel cells developed in previous chapters. However, as a result of the enzyme limited lifetimes, the application of these devices is restricted to portable power devices where long-term operation is not required. There are still some technical challenges to

overcome for realistic and practical applications. They include (a) identifying more robust and active enzymes and mediators, (b) more effectively immobilizing enzymes and mediators in microfluidic environments; and (c) preferably increasing stability of enzymes [13]. On the other hand, a clear advantage of paper-based devices is that while conventional fuel cells use syringe pumps to move reactants, these represent an extra energy consumption and extra volume of the system that prevents the practical application of microfluidic fuel cells in real case scenarios. Consequently, the most important advantage of paper-based fuel cells is that they can get rid of external pumps because capillary action of paper maintains the liquid in movement. Moreover, these paper fuel cells are more likely to be recycled than the others made on plastic and glass. Furthermore, the materials used to implement these devices are typically used in in-vitro diagnostic sector. Thus, all the energy produced from the paper fuel cells could be potentially used to enable electrical functions of this kind of devices. In this sense, associating biological fuel cells with the advantage of paper networks could be significant for developing economical, mass-producible, and portable diagnostic devices, which may possess market value in the future.

REFERENCES

1. Cate, D.M., J.A. Adkins, J. Mettakoonpitak, and C.S. Henry, *Recent Developments in Paper-Based Microfluidic Devices.* Analytical Chemistry, 2014. **87**(1): p. 19-41.
2. Merchant, S.A., M.T. Meredith, T.O. Tran, D.B. Brunski, M.B. Johnson, D.T. Glatzhofer, and D.W. Schmidtke, *Effect of Mediator Spacing on Electrochemical and Enzymatic Response of Ferrocene Redox Polymers.* The Journal of Physical Chemistry C, 2010. **114**(26): p. 11627-11634.
3. Klotzbach, T., M. Watt, Y. Ansari, and S.D. Minteer, *Effects of hydrophobic modification of chitosan and Nafion on transport properties, ion-exchange capacities, and enzyme immobilization.* Journal of Membrane Science, 2006. **282**(1–2): p. 276-283.
4. Meredith, M.T., M. Minson, D. Hickey, K. Artyushkova, D.T. Glatzhofer, and S.D. Minteer, *Anthracene-Modified Multi-Walled Carbon Nanotubes as Direct Electron Transfer Scaffolds for Enzymatic Oxygen Reduction.* ACS Catalysis, 2011. **1**(12): p. 1683-1690.
5. Dawn, A., T. Shiraki, S. Haraguchi, H. Sato, K. Sada, and S. Shinkai, *Transcription of Chirality in the Organogel Systems Dictates the Enantiodifferentiating Photodimerization of Substituted Anthracene.* Chemistry-a European Journal, 2010. **16**(12): p. 3676-3689.
6. Meredith, M.T., D.-Y. Kao, D. Hickey, D.W. Schmidtke, and D.T. Glatzhofer, *High Current Density Ferrocene-Modified Linear Poly(ethylenimine) Bioanodes and Their Use in Biofuel Cells.* Journal of the Electrochemical Society, 2011. **158**(2): p. B166-B174.
7. Jose Gonzalez-Guerrero, M., J. Pablo Esquivel, D. Sanchez-Molas, P. Godignon, F. Xavier Munoz, F. Javier del Campo, F. Giroud, S.D. Minteer, and N. Sabate, *Membraneless glucose/O-2 microfluidic enzymatic biofuel cell using pyrolyzed photoresist film electrodes.* Lab on a Chip, 2013. **13**(15): p. 2972-2979.
8. Alkire, R.C., D.M. Kolb, J. Lipkowski, and P.N. Ross, *Bioelectrochemistry: fundamentals, applications and recent developments*. Vol. 26. 2013: John Wiley & Sons.
9. Baldrian, P., *Fungal laccases - occurrence and properties.* Fems Microbiology Reviews, 2006. **30**(2): p. 215-242.

10. Esquivel, J.P., F.J. Del Campo, J.L. Gomez de la Fuente, S. Rojas, and N. Sabate, *Microfluidic fuel cells on paper: meeting the power needs of next generation lateral flow devices.* Energy & Environmental Science, 2014. **7**(5): p. 1744-1749.
11. Kim, E., *Relationship between viscosity and sugar concentration in aqueous sugar solution using the Stokes' Law and Newton's First Law of Motion.* 2010.
12. Nolan-Neylan, F., *Harvesting energy from soft drinks.* Chemistry World, 2011. **8**(4): p. 23-23.
13. Lee, J.w. and E. Kjeang, *A perspective on microfluidic biofuel cells.* Biomicrofluidics, 2010. **4**(4): p. 041301.

CHAPTER

5

Paper-based microfluidic biofuel cells for in-vitro applications at physiological conditions

Enzymatic glucose fuel cells can become an alternative for providing energy to power small electronic devices if they work at high fuel concentration, such as 100 mM glucose, because it is when these systems produce their best performance. However, due to the possibility to operate them at low glucose and oxygen concentration levels, enzymatic fuel cells can generate power form glucose available in human physiological fluids, *e.g.* blood, plasma, saliva, tears and urine [1].

Table 5.1 shows the glucose concentration ranges typically found in these physiological fluids of a healthy person.

Body fluid	Glucose concentration (mM)
Blood	*4 - 10* [1-2]
Saliva	*0.03 – 0.2* [3]
Tears	*0.1 – 0.6* [4]
Urine	*0 - 0.8* [5]

Table 5.1 Normal glucose concentration found in human physiological fluids.

This allows envisaging the use of the enzymatic fuel cells as power sources for attachable, adhesive and floating devices operating in the presence of these physiological fluids [6]. This open the possibility to employ them in *ex-vivo* applications to generate power for self-powered biodevices, *i. e.* to use the electrical power extracted from these physiological fluids to power a sensing system with the same sample to be analysed [2, 7].

On the other hand, enzymatic fuel cell devices can also be used to supply power at *in-vivo* applications, *e. g*. implanted pacemakers, glucose sensors or prosthetic valve actuators. However, *in-vivo* systems need to overcome hurdles to become a reality as they generally require long operational lifetime and up to now enzymatic fuel cells lack long-term stability. Therefore, single-use enzymatic fuel cell devices could be a practical option to overcome the limitations imposed by enzymatic lifetime. This fact combined with the advantages of using paper-based devices can turn the system into a disposable device apart from low-cost, lightweight and portable [8].

This chapter addresses the development of a compact paper-based microfluidic glucose/O_2 fuel cell. It can be activated by a single-user step using a single and very limited sample volume (from ≈30 to 150 µl) at physiological conditions (pH 7.4). To achieve this goal, a new combination of enzymes and mediators has been developed, immobilized and tested over graphite electrodes. Once the suitability of the catalytic solutions was studied, the EFC device has been constructed using two different paper materials. Material selection allows tuning the required sample volume. The performance of the fuel cell was then measured under different content of glucose ranging from 2.5 mM up to 30 mM. The result was a flexible and low cost fuel cell that can be potentially used to power an electronic analysis device in in-vitro applications.

5.1 ENZYMATIC SOLUTIONS TO BE IMMOBILIZED ON THE ELECTRODES

The description of the chemicals, solutions and the procedure for preparing the enzymatic catalytic inks to be immobilized on the electrodes surfaces are given in next paragraphs.

5.1.1 Electrolyte and fuel

Phosphate buffer at pH 7.4 was utilized in all the studies. It was prepared by the combination of; sodium phosphate monobasic dihydrate ($NaH_2PO_4 \cdot 2H_2O$), sodium phosphate dibasic dihydrate ($Na_2HPO_4 \cdot 2H_2O$) and sodium chloride (NaCl) for a final 100 mM concentration. The pH of this solution was then adjusted adding $NaH_2PO_4 \cdot 2H_2O$ for lower or $Na_2HPO_4 \cdot 2H_2O$ for raising the pH.

The fuel utilized in the experiments was α-D(+)-glucose prepared in a stock solution of 1 M at least 24 hours before its use to establish the anomeric equilibrium between α and β forms of D-glucose. This prepared glucose was kept in the refrigerator at 4 °C and used within a week.

5.1.2 Enzymatic bioelectrode solution composition

The catalytic solutions to be deposited on the electrode surfaces consist in the mixture of: (i) the enzyme-solution, (ii) the redox mediator, (iii) the crosslinker and (iv) a solution containing multiwall carbon nanotubes.

The crosslinker and the multiwall carbon nanotubes mixture were common elements used in both anode and cathode electrode solutions. The crosslinker was poly(ethylene glycol)diglycidyl ether (PEGDGE), freshly prepared in water before its use with a concentration of 15 mg ml^{-1}. On the other hand, MWCNTs were previously acid-treated [9] and prepared with a concentration of 46 mg ml^{-1} in distilled water.

The redox mediators and the enzymes in each electrode side were different depending on the characteristics required. The redox mediators used in all the work consist of Osmium-based polymers, with a poly-vynilmidazole (PVI), synthesized according to previous published procedures [10-14]. This kind of redox-mediators was selected because of its high level of reversibility and its diffusion controlled mechanism reaction. Moreover, they present the advantage that their redox potential can be tailored by altering the ligands attached to the Osmium active site [14-16]. Therefore, the osmium polymer to be joined to the catalytic inks can be selected depending on the redox potential required in a particular application [17]. Among the most commonly used mediators, in addition to ferrocene and its derivatives, complexes of ruthenium and redox organic dyes (mainly azines) canalso be found. Ferrocene derivatives accomplished considerably success in commercial home-house devices however these Osmium complexes achieve higher efficiency mediating electron transfer reactions. Nevertheless, they have some drawbacks related with its possible toxicity [18].

The mediators used in the anode were: $[Os(4,4'\text{-dimethyl-}2,2'\text{bipyridine})_2$ $(\text{poly-vinylimidazole})_{10}Cl]^+$ and $[Os(4,4'\text{-dimethoxy-}2,2'\text{-bipyridine})_2(\text{poly-vinylimidazole})_{10}Cl]^+$ [19-20],

however for simplicity they were called Os(dmbpy)PVI or Os(dmbpy)PVI, respectively. At the cathode side, the redox polymer was the $[Os(2,2'\text{-bipyridine})_2(\text{poly-vinylimidazole})_{10}Cl]^+$ and it was named Os(bpy)PVI [19-20]. The selection of a concrete mediator lies in its formal oxidation/reduction potentials.

On the other hand, the enzyme utilized at the anode was the glucose dehydrogenase from *Aspergillus sp.* (FAD-GDH, EC 1.1.99.10 with specific activity >625 U mg^{-1}), purchased from Sekisui Diagnostics (USA). This choice was motivated due to the ability of GDH to be unaffected by molecular oxygen, therefore GDH presents high selectivity towards glucose oxidation in the presence of oxygen [21]. At the cathode side, the enzyme used was the bilirubin oxidase 'Amano-3' from *Mytothecium* (BOx, EC 1.3.3.5 with specific activity ≈2.5 U mg^{-1}), acquired from Amano Enzyme Inc. (Japan). This enzyme could work properly at neutral pH (pH≈7). Due to the particular characteristics of these enzymes, they can be used with a single solution at physiological pH.

To sum up, the enzymatic solutions were freshly prepared following table 5.2.

Solution for the anode	
i)	4.8 µl of GDH with a concentration of 10 mg ml^{-1}.
ii)	9.6 µl (5 mg ml^{-1}) of Os(dmbpy)PVI or Os(dmobpy)PVI.
iii)	2 µl of the crosslinker, PEGDGE (15 mg ml^{-1}).
iv)	9.6 µl of the MWCNTs solution (46 mg ml^{-1}).
Solution for the cathode	
i)	4.8 µl of BOx with a concentration of 10 mg ml^{-1}.
ii)	9.6 µl (5 mg ml^{-1}) of Os(bpy)PVI.
iii)	2 µl of the crosslinker, PEGDGE (15 mg ml^{-1}).
iv)	9.6 µl of the MWCNTs solution (46 mg ml^{-1}).

Table 5.2 Composition of the enzymatic solutions to be deposited on the electrode surfaces.

5.2 BIOELECTRODES: FABRICATION PROCESS AND CHARACTERIZATION

5.2.1 Working electrodes fabrication and equipment

Fabrication of the electrodes. Graphite electrodes were used to immobilize and evaluate the enzymatic solutions. These electrodes were made manually by cutting a piece of about 8 cm length from a long graphite rod of 3 mm diameter (from Graphite Store, USA). Its surface ending was polished on grit sandpaper and sonicated in distilled water. A heat-shrink tube of 6 cm in length and 5 mm diameter was then inserted within the graphite rod and the assembled plastic-graphite system was heated. On heating it, the plastic adhered to the graphite surface wall for finally obtaining a robust electrode which can be reused multiple times by cutting its ending using

a blade knife. Finally, the surface active area of the graphite electrodes was 0.07 cm^2.
Catalytic solution deposition. A drop of the corresponding enzymatic solution (prepared following table 2) was deposited over the graphite electrodes which were kept overnight at room temperature (approximately 24 °C) until the enzymatic-ink was completely dried.

Experimental equipment. The electrical connections between the electrodes and the external potentiostat were established using the end of the graphite rod. The electrodes were tested in a typical three electrode configuration using an Ag/AgCl (3M KCl) reference electrode and a platinum wire as a counter electrode [22]. Cyclic voltammetry and chronoamperometry measurements were performed using a model CHI 1030 multi-channel potentiostat or a series CHI 620A and controlled trough a personal computer.

5.2.2 Anode for glucose oxidation

Two redox mediators were studied and compared in terms of their redox potential to be utilized at the anode. The one with the more negative potential was selected as the most appropriate mediator for the anode of the fuel cell. Later, the behaviour of the couple enzyme-mediator was characterized in a solution containing different concentrations of glucose as fuel.

5.2.2.1 Fuel cell anode: Os(dmobpy)PVI

The polymers Os(dmbpy)PVI and Os(dmobpy)PVI were selected among other different Os-polymers to take part in the catalytic solution because of their low redox potentials [23]. Both polymers were studied as electron transfer mediators for the FAD-GDH enzyme. Their electrochemical responses were characterized in 100 mM phosphate buffer at pH 7.4 and room temperature and they are shown in figure 5.1.

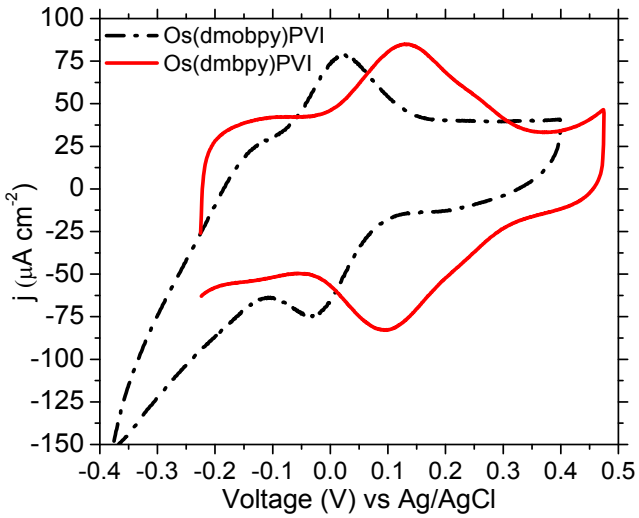

Figure 5.1 Cyclic voltammetries at 10 mV s^{-1} in 100 mM phosphate buffer at pH 7.4 and room temperature of Os(dmbpy)PVI (solid line) and Os(dmobpy)PVI (dotted line) redox polymers on graphite electrodes.

As we can see, both redox polymers exhibited well-defined oxidation and reduction peak potentials corresponding to the Os(II/III) redox couple. It can also be observed that the redox formal potential for the Os(dmbpy)PVI corresponds to $E^{0\prime}$= 0.110 V while the formal redox potential of the Os(dmobpy)PVI was $E^{0\prime}$= -0.001 V (these values were in agreement with other published potentials [23]). The oxidation potential of the anode should be as low as possible to obtain the maximum performance in a biofuel cell. Therefore, the Os(dmobpy)PVI polymer was selected as the redox-mediator for the anodic solution and subsequently used throughout all the work. The other polymer was then discarded for our application.

The behavior of the Os(dmobpy)PVI redox polymer was studied by cyclic voltammetry at different scan rates ranging from 1 mV s^{-1} to 100 mV s^{-1}, the results are shown in figure 5.2 (a). It can be observed that nearly the same peak voltage positions were maintained for all the scan rates indicating fast electron transfer. Small shoulders peaks appeared at around -0.15 V probably as a consequence of some impurity on the electrode surface. As it was expected, the height of the oxidation and the reduction peaks increased as the scan rate was enhanced. The peak currents were plotted as a function of the scan rate, obtaining figure 5.2 (b), in which a linear relation with the scan rate should appear if the catalytic solution is strictly immobilized on the electrode surface. It was observed that at slow scan rates (up to 10 mV s^{-1}) the peak currents scaled linearly with the scan rate indicating that the Osmium polymer was anchored on the electrode surface. However, at higher scan rates (>10 mV s^{-1}) peak currents scaled linearly with $v^{1/2}$ indicating a changeover from finite-diffusion (surface confined) to semi-infinite diffusion (incomplete electrolysis within the film on the time scale of the experiment) control [24]. Since mediators are small molecules and high soluble, they posses some freedom to move inside and out the catalytic layer on the electrode surface. Therefore, they can diffuse away from the immobilized film which can result in a loss of catalytic activity and long-term operational stability [25]. Under these conditions the rate of charge transport through the film can be characterized by an apparent diffusion coefficient, D_{app}. The slope of the peak current versus $v^{1/2}$ at scan rates from 20 mV s^{-1} to 100 mV s^{-1} (in the absence of enzyme substrate) corresponded to 5.58 10^{-3} A $cm^{-2}v^{-1/2}s^{1/2}$. On the other hand, the concentration of redox centers in the polymer (*C*) can be estimated by dividing the density of polymer by its formal molecular weight. The density of the dry film is approximately 1 g cm^{-3} giving a concentration of 6.25 10^{-4} mol cm^{-3}. Combining the slope and the concentration value in the *Randles-Ševčik* equation (equation 1.7) led as to estimate the D_{app} of the polymer Os(dmobpy)PVI to be $1.10\ 10^{-9}\ cm\ s^{-1/2}$, comparable with other published results [26].

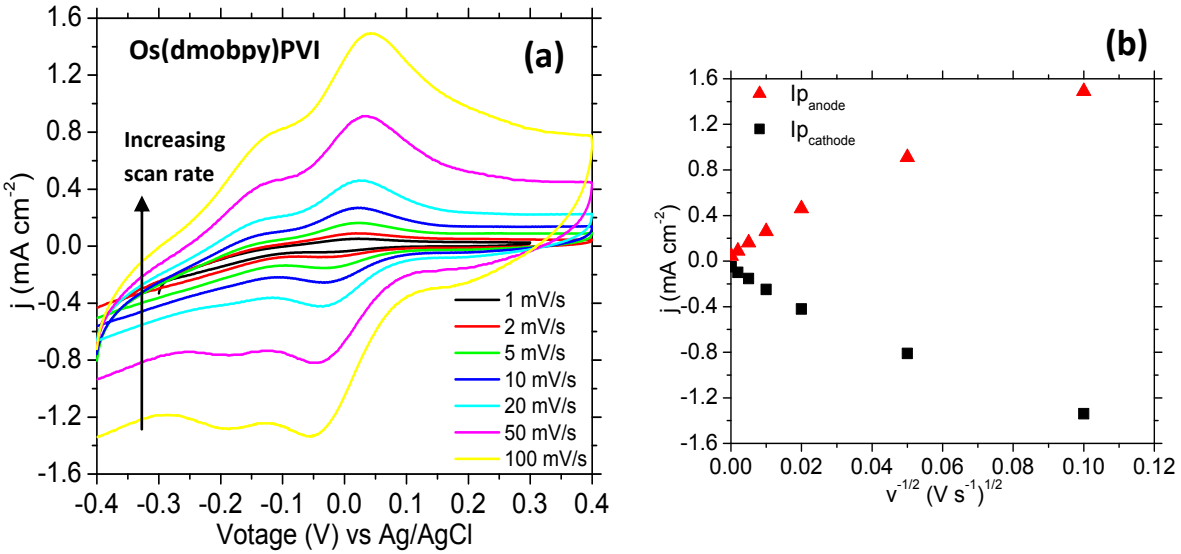

Figure 5.2 Graphite electrode modified with the anodic solution using the Os(dmobpy)PVI redox polymer and evaluated in 100 mM phosphate buffer solution at pH 7.4 and room temperature. (a) Cyclic voltammograms recorded at different scan rates ranging from 1 mV s^{-1} to 100 mV s^{-1}. (b) Dependence of the anodic and cathodic current peaks as a function of the of the scan rate.

An estimation of the surface coverage *(Γ)* over the graphite electrode can be obtained integrating the area under the peaks *(Q)*of the cyclic voltammetries for slow scan rates (up to 10 mV s^{-1}), see figure 5.2 (a), and by the use of the following equation;

$$\Gamma_{Os} = \frac{Q}{nFA} \qquad \textbf{(5.1)}$$

where, *n=1* is the number of electron passed during the redox process Os(II/III), *F* is the Faraday constant 96485 C mol^{-1}, and *A* is the surface area of the graphite electrodes, 0.07 cm^2. The estimation of the initial Γ_{Os} was found to be 111 ± 32 nmoles cm^{-2}. The same experiment was repeated without the addition of MWCNTs to the redox film. In this case the Γ_{Os} was determined to be 46 ± 18 nmoles cm^{-2}. This demonstrates that carbon nanotubes into the enzymatic solution results in an increase of the amount of osmium-polymer and enzyme immobilized over the electrodes. Therefore, an increase of the surface coverage on the electrode surfaces will lead to an increase in the current density obtained from the electrode.

Os(dmobpy)/FAD-GDH films		
MWCNTs	*Charge (C)*	*Γ (nmoles cm^{-2})*
without	$(3.4 \pm 0.4)\cdot10^{-4}$	46 ± 18
9.6 µl (480 µg)	$(8.6 \pm 1.7)\cdot10^{-4}$	111 ± 32

Table 5.3 Surface coverage estimation of the enzymatic solution layer deposited on graphite electrodes with 9.6 µl of MWCNTs in the coated enzymatic solution and without the incorporation of MWCNTs.

These results validate the use of this redox polymer in the anodic compartment to facilitate the electron-transfer reaction with the corresponding enzyme and the electrode surface.

5.2.2.2 Characterization of the couple Os-polymer/enzyme

In order to evaluate the Os(dmobpy)PVI redox polymer working along with the GDH enzyme, the graphite electrodes were immersed and tested in solution with and without glucose. The reactions taking place at the electrode surface can be describes as follows:

$$GDH_{FAD}(ox) + glucose \rightleftarrows GDH_{FADH_2}(red) + gluconolactone \quad (5.2)$$

$$2Os^{3+}(ox) + GDH_{FADH_2}(red) \rightleftarrows 2Os^{2+}(red) + GDH_{FAD}(ox) \quad (5.3)$$

$$Os^{2+}(red) \rightleftarrows Os^{3+}(ox) + 1e^- \quad (5.4)$$

The GDH oxidize glucose and 2 e^- and 2 H^+ are transferred from the glucose to the GDH (equation 5.2). The electron transfer occurs between GDH and the Os-polymer which reoxidized the reduced enzyme (equation 5.3). Finally, the reduced Os-polymer is reoxidized by the electrode [27].

The cyclic voltammetry occurring at the anode is shown in figure 5.3. When no glucose was added to the medium, the response of the electrode was only due to the presence of the mediator, figure 5.3 (a). However, upon the addition of 100 mM glucose into the electrolyte, oxidation current of 1.8 mA cm^{-2} was observed, figure 5.3 (b). This high value was attributed in part to the elevated enzymatic activity of GOx. The steady-state current represents the maximum reaction rate achieved for the oxidation of 100 mM glucose. At a potential around 0.15 V it can be considered that the anode is oxidising the glucose present in solution at its maximum rate.

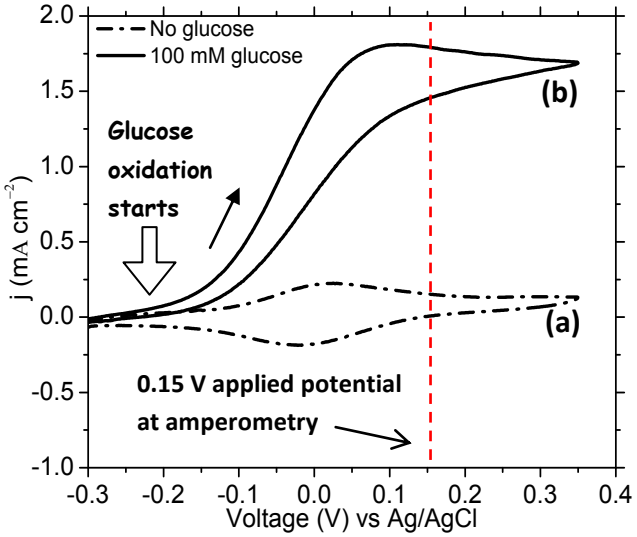

Figure 5.3 Cyclic voltammograms recorded at 1 mV s^{-1} in 100 mM buffer phosphate at pH 7.4 at a graphite electrode modified with the anodic solution. (a) No glucose in the electrolyte (-···-), and (b) after the addition of 100 mM glucose

(—). It can be observed that at approximately 0.15 V the steady current for the oxidation of glucose was reached.

To further study the performance of the couple Os(dmobpy)PVI/GDH, the glucose oxidation current was monitored over time using different concentrations of glucose. The glucose concentrations ranged from 5 mM to 100 mM, at a fixed applied potential of 0.15 V, the responses were recorded and displayed in figure 5.4 (a-1). A gradual increase in current was observed after each glucose addition until at around 50 mM a current plateau of 2.2 mA cm^2 was reached. In contrast, much less current was obtained when the chronoamperometry experiment was repeated for graphite electrode modified with the enzymatic anodic solution without carbon nanotubes, figure 5.4 (a-2). As it was predicted by the study of the Osmium surface coverage, the current increased significantly when the catalytic layer contained carbon nanotubes [24].

This experiment was repeated for 5 identical samples and the graphic 5.4 (b) was elaborated. At low glucose concentrations (5 mM to ≈20 mM glucose) a linear trend was observed. However, this linear behavior was not maintained for higher fuel concentrations where glucose saturation occurred. These results suggested that this bioanode should also work when operating in biosensor applications [28-30].

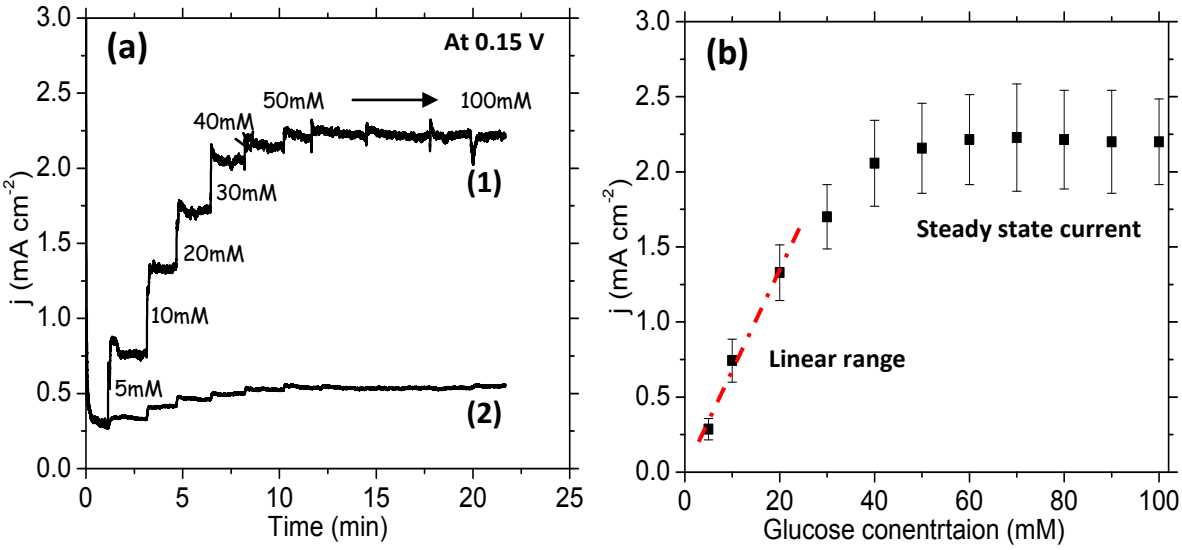

Figure 5.4 Graphite electrode, modified with the anodic solution, measured in buffer phosphate at pH 7.4 with different glucose concentrations. (a) Cronoamperometric responses, at a fixed potential of 0.15 V, for different additions of glucose (from 5 to 100 mM) with (1) and without (2) the incorporation of MWCNTs to the catalytic film. (b) Glucose oxidation currents as a function of the glucose concentration. The error bars correspond to the average of 5 electrodes.

5.2.3 Cathode for oxygen reduction

The redox polymer and the enzyme selected for the oxygen reduction reaction at the cathode were electrochemically characterized separately using cyclic voltammetry. Furthermore, the

couple enzyme-mediator was studied under different atmospheres (nitrogen, air and oxygen) as well as the influence of glucose in the medium.

5.2.3.1 Fuel cell cathode: Os(bpy)PVI

Consecutive voltammetries at different scan rates, from 1 mV s^{-1} to 100 mV s^{-1}, were performed using the mediator Os(bpy)PVI to evaluate its reversibility. Prior to the experiments, the electrolyte was bubbled for at least 5 minutes with nitrogen gas to remove the oxygen dissolved in solution to avoid oxygen reduction reaction, figure 5.5 (a) shows the results. In all cases, a pair of peaks corresponding to the transition $Os^{2+/3+}$ were obtained with a redox potential of $E^{0'}$= 0.24 V, in accordance with other reported values [9, 31].

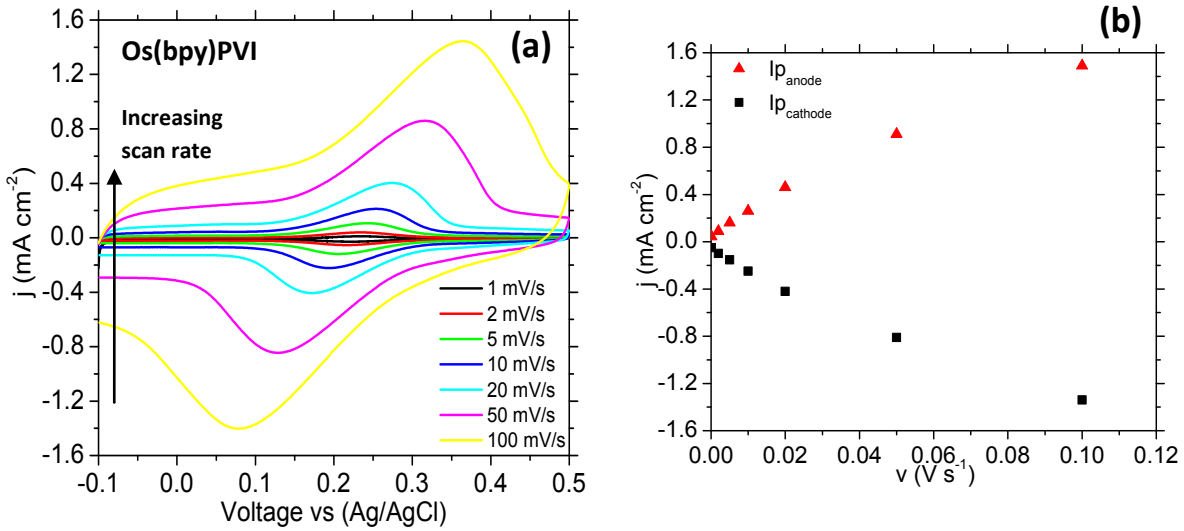

Figure 5.5 Cathodic solution immobilized on a graphite electrode in 100 mM phosphate buffer solution in the absence of oxygen at pH 7.4 and room temperature. (a) Cyclic voltammograms recorded at different scan rates. (b) Dependence of the anodic and cathodic current peaks with the scan rate.

It can be seen that at high scan rates the separation between anodic and cathodic peak potentials become wider as compared with the voltammograms at slower scan rates. This behaviour represents a quasi-reversible electrochemical process. In spite of this, the scan rate used in the experiments ranges between 1 mV s^{-1} and 5 mV s^{-2} where the Os(bpy)PVI mediator has a reversible and fast electron transfer kinetic behaviour. From these voltammograms, the anodic and cathodic heights of the peak currents were plotted against the scan rate (*v*) obtaining figure 5.5 (b). It is known that if a catalytic solution is completely immobilized on electrode surface a linear relation can be observed on this graphic [32]. However, only for high scan rates (>20 mV s^{-1}) the peak currents scaled with the square root of the scan rate indicating a semi-infinite diffusion conduct [33]. This indicates that the osmium centers on the immobilized catalytic layer have some mobility. In this particular case the reaction can be considered diffusion-controlled. The slope obtained

when the current peaks were represented versus $v^{1/2}$ (at scan rate from 20 to 100 mV s^{-1}) was 5.81 10^{-3} A cm^{-2} $V^{-1/2}$ $s^{1/2}$ and the concentration of Os(bpy)PVI redox centers, with molecular weight 1487.16 g mol^{-1}, of 6.72 10^{-4} mol cm^{-3}. By using the *Randles-Ševčik* equation (equation 1.7) the D_{app} of the polymer Os(bpy)PVI was found to be *1.03 10^{-9} cm $s^{-1/2}$,* in the order of some other reported values [26].Thus demonstrating that the mediator Os(bpy)PVI will be a good candidate to take part in the oxygen reduction reaction process along with the enzyme.

Applying equation 5.1 an estimation of the catalytic surface covering the cathodic electrode can be calculated. From figure 5.5 (a) the area under the CV peaks were integrated for slow scan rates (1, 2 and 5 mV s^{-1}) obtaining a Γ_{Os} =103 ± 20 nmoles cm^{-2}, a very similar value that obtained for the anodic surface coverage and comparable with others found in literature [24].

5.2.3.2 Bilirubin oxidase (BOx) and the Os-mediator study

To help and shuttle electrons efficiently from/to the electrode surface (in MET systems) enzymes and mediators should work together, therefore its behavior working separately will be inefficient.

To demonstrate this, the ability of the enzyme BOx reducing O_2 without the addition of redox polymer was studied. For this purpose, a graphite electrode was modified with the cathodic solution removing the redox polymer. Then, cyclic voltammetries after air, figure 5.6 (a-1) and oxygen, figure 5.6 (a-2), saturated conditions were performed. The graphic shows how effectively the BOx was able to reduce the oxygen present in solution at a potential starting at approximately 0.5 V (in accordance to the T1 site potential of the BOx [34]) and reaching a maximum current density of 150 µA cm^{-2}.

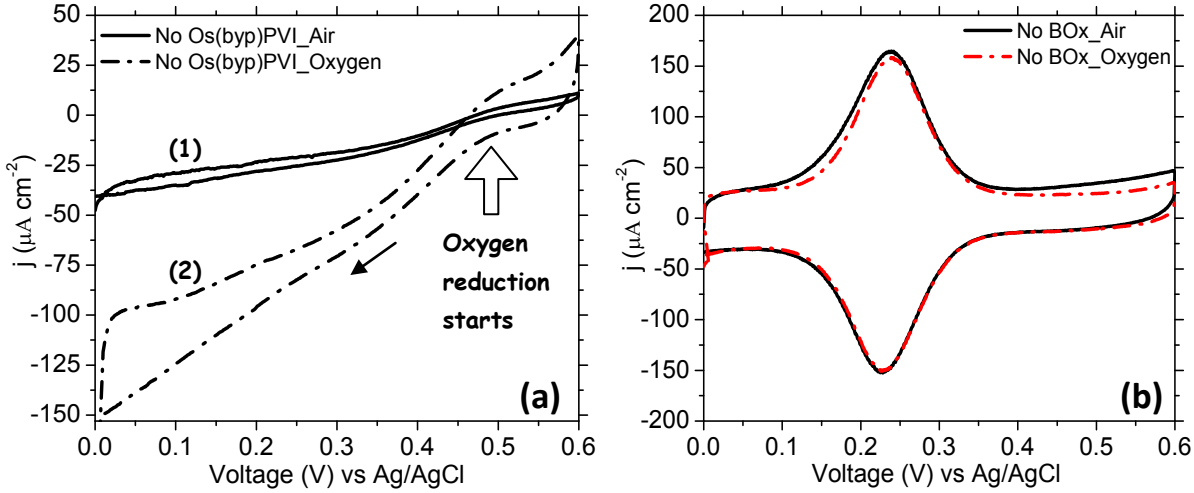

Figure 5.6 Cyclic voltammetries of a graphite electrode in 100 mM phosphate buffer at ph 7.4 and room temperature recorded at 1 mV s^{-1}. (a) Modified with the enzymatic cathodic solution without the addition of Os(bpy)PVI after bubbling air into the solution (1) and in oxygen saturated conditions (2). (b) Modified with the catalytic solution without

the addition of BOx enzyme, no difference was observed when air or oxygen were bubbled into the electrolyte solution. On the other hand, a graphite electrode was modified with the cathodic solution without the incorporation of BOx. The electrode was then studied under air and oxygen saturated conditions and figure 5.6 (b) was obtained with two identical cyclic voltammograms responses. This fact evidences that the redox polymer will not be able to interact by itself with the oxygen present in the electrolyte.

5.2.3.3 Characterization of the couple Os-polymer/enzyme

The electrochemical reaction occurring between the Os(bpy)PVI redox polymer and the BOx enzyme can be described in this way. At the cathode, the electrons are transferred from the electrode to the Osmium polymer which is reduced (equation 5.5). The reduced Os-polymer is then oxidized by the BOx (equation 5.6). Finally, bilirubin oxidase catalyzes the reduction of O_2 to water (equation 5.7).

$$Os^{3+}(ox) + 1e^- \rightleftarrows Os^{2+}(red) \quad \textbf{(5.5)}$$

$$2Os^{2+}(red) + BO_x(ox) \rightleftarrows 2Os^{3+}(ox) + BO_x(red) \quad \textbf{(5.6)}$$

$$BO_x(red) + \frac{1}{2}O_2 \rightleftarrows BO_x(ox) + H_2O \quad \textbf{(5.7)}$$

To demonstrate it is the couple enzyme/mediator the one which can effectively reduce the oxygen to water, the oxygen reduction reaction signals of the cathodic electrode were evaluated by cyclic voltammetry when nitrogen, air and oxygen were bubbled in the electrolyte, see figure 5.7.

When the electrolyte was purged with nitrogen (curve 1) the current observed was only due to the presence of the redox mediator, Os(bpy)PVI. After air-bubbling (curve 2), the voltammogram presented an increase of current up to 323 µA cm^{-2}. On the contrary, the presence of an O_2-saturated ambient (curve 3) gave a sigmoidal-shaped voltammogram with a current density of 800 µA cm^{-2} (corresponding to an oxygen concentration of 0.87 mM). Therefore, the Os(bpy)PVI coupled with the BOx becomes necessary to shuttled electrons efficiently from the electrode surface to the enzyme and help to the oxygen reduction reaction to take place. The results accomplished by the BOx-biocathode suggested that when coupled with the GDH- bioanode (previously described in figure 5.3) the enzymatic fuel cell will display high performance in terms of current and power density.

To prove the glucose was not interfering with the oxygen reduction reaction at the cathode, the response of a graphite cathode was evaluated by cyclic voltammetry with 100 mM glucose within the electrolyte. As we can see from figure 5.8, the cathode exhibited practically the same behavior with and without glucose in the solution. Therefore, the EFC working with this cathode will not diminish its performance because of the presence of glucose in the solution.

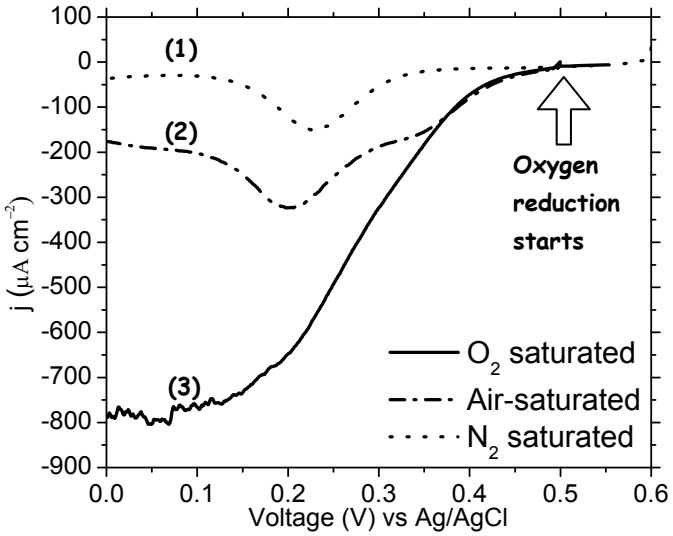

Figure 5.7 Cyclic voltammograms of a graphite electrode modified with the cathodic solution recorded at different concentrations of O_2 in the solution recorded in 100 mM phosphate buffer at pH 7.4 and room temperature with a scan rate of 1 mV s^{-1} under (1) nitrogen (2) air and (3) oxygen saturated conditions.

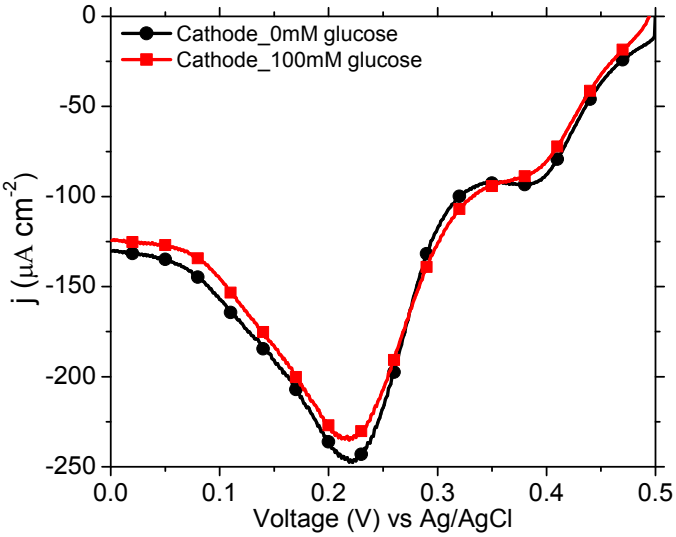

Figure 5.8 Modified graphite electrode with the cathodic ink solution measured in 100 mM buffer phosphate without and with the addition of 100 mM glucose in the electrolyte solution.

5.2.3.4 'Air breathing cathode'

It has been demonstrated in the previous section that the biocathode performance was limited mainly due to: (i) the low diffusivity of dissolved oxygen ($2 \cdot 10^{-5}$ cm^2 s^{-1}) as well as (ii) the low concentration of oxygen in an aqueous solution in equilibrium with ambient air, with values of 2-4 mM at most. This limitation can be addressed by increasing the content of oxygen by pure O_2 gas bubbling or in a more sophisticated microfluidic design with the incorporation of multiple inlets close to the cathode that enable boundary layer replenishment [35]. In our specific case, this

cathode limitation was addressed by the integration of a porous air-exposed gas diffusion electrode (GDE) that enabled direct oxygen delivery from air. In this kind of electrodes, the use of a porous carbon paper material allows the oxygen diffusion from air on one side of the electrode whereas the catalytic side remains in contact with the electrolyte solution. In this way, the content of oxygen increases up to an order of magnitude (≈ 10 mM) and it is supplied with a diffusion coefficient of 0.2 $cm^2 s^{-1}$ (diffusion in air) [36-37].

The air-breathing cathode was fabricated using a piece of Toray carbon paper (TGP-H-060) material that was cut with dimension of 5 mm x 15 mm. Then, a surface of 0.4 cm^2 was modified with 150 µl of cathodic enzymatic solution. The air-breathing cathode was characterized in a three electrode system using the specific setup described in figure 5.9. A PMMA holder was fabricated to place a glass slide with a paper strip of 6 cm long and 1 cm width on it. At the same time, the holder presented a milled cavity acting as a reservoir for electrolyte. The carbon paper electrode was placed over the paper substrate with its catalytic side in contact with the paper strip while the other side was left open to the air. The counter electrode consisted of a graphitic carbon tape positioned in contact with the paper strip. The Ag/AgCl reference electrode was dipped in the cavity containing the electrolyte and the end of the paper strip was also immersed in the reservoir. Finally, the electrical connections were enabled by attaching pieces of copper foil to the carbon strips.

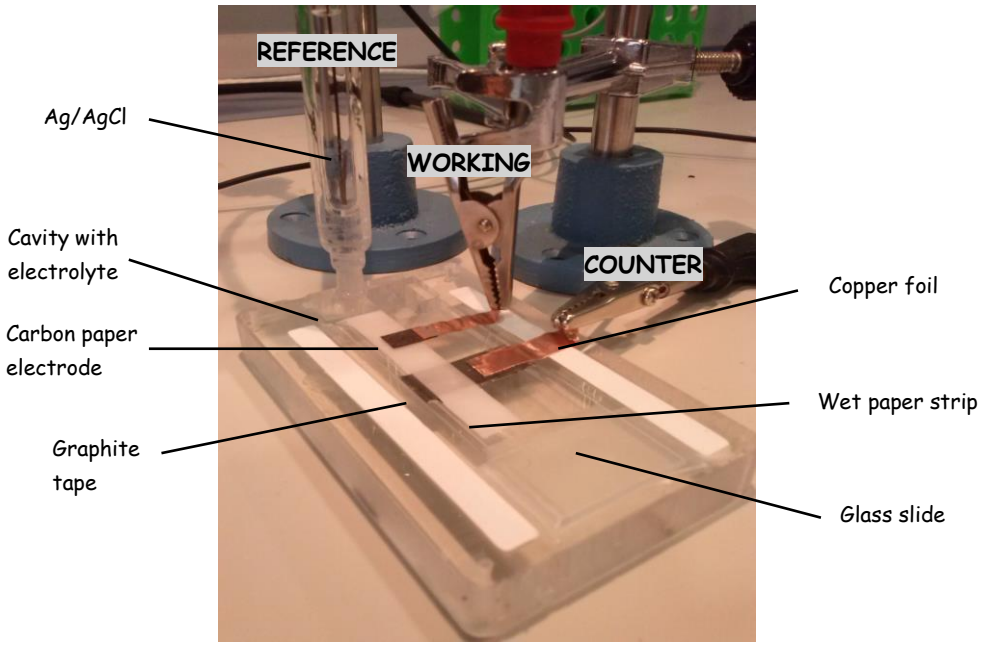

Figure 5.9 Setup for a three-electrode experiment performed with a carbon paper electrode working as an air-breathing cathode.

Cyclic voltammetries were performed with this setup in order to test the improvement of the air-breathing solution over the immerged cathode. For this, the cathode was placed on top of the

paper substrate so it could take the oxygen coming from the air. Once the measurement was done, the same cathode was laid under the paper strip, making accessible only the oxygen dissolved in solution travelling through the paper. The obtained curves are depicted in figure 5.10. As it was expected, the cathode presented higher current densities when working in an air-breathing mode displaying a reduction peak current that increases from 280 µA cm^{-2} (when the cathode was under the strip) to 400 µA cm^{-2}. Accordingly, the performance of the enzymatic paper fuel cell was improved using biocathodes working in an 'air breathing' conditions [35].

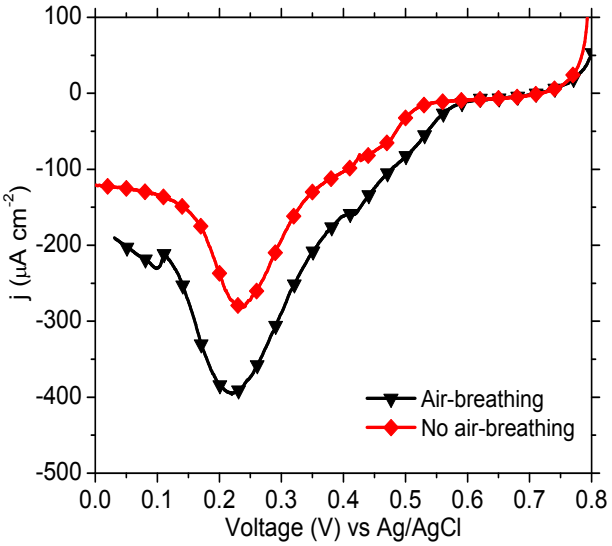

Figure 5.10 Cyclic voltammetries of a carbon paper electrode modified with the cathodic ink solution showing the differences between an air-breathing cathode (black line) and a normal one (red line).

5.3 FUEL CELL DESIGN AND FABRICATION

In this section, the design and fabrication of the paper fuel cell is described. The device construction is divided in two; (i) the core of the system, that is, the electrodes and the paper strip and (ii) the packaging of the core structure by the addition of several layers of laminated plastics.

5.3.1 The core of the fuel cell

The main structure of the device consisted of a 35 mm length and 5 mm width of *Fusion 5* (or *1 Chr*) paper strip and two carbon paper electrodes. The paper strip had a circular reception zone of 10 mm diameter and a 10 mm x 5 mm absorption region. A pair of transparent PSA layers with a thickness of 75 µm and dimensions of 30 x 15 mm^2 (bottom) and 17 x 15 mm^2 (top), were added to the previous assembly to maintain the elements together. They were cut in different lengths to allow for reception of sample and the absorption of excess liquid during the performance of the experiments. The PSA layers also define the active electrode area (4 x 5 mm^2) exposed to the

paper substrate. Carbon paper electrodes were manually cut with dimensions of 5 x 15 mm^2. However, the rest of components of the fuel cell, the plastic layers and the paper strip, were cut with a computer controlled CO_2 laser (*Epilog Mini 24*) [38-40] which presents better capabilities than the cutter plotter (used in previous chapters) because it is able to cut in one pass and much faster [41]. Figure 5.11 shows the layers shaping the fuel cell.

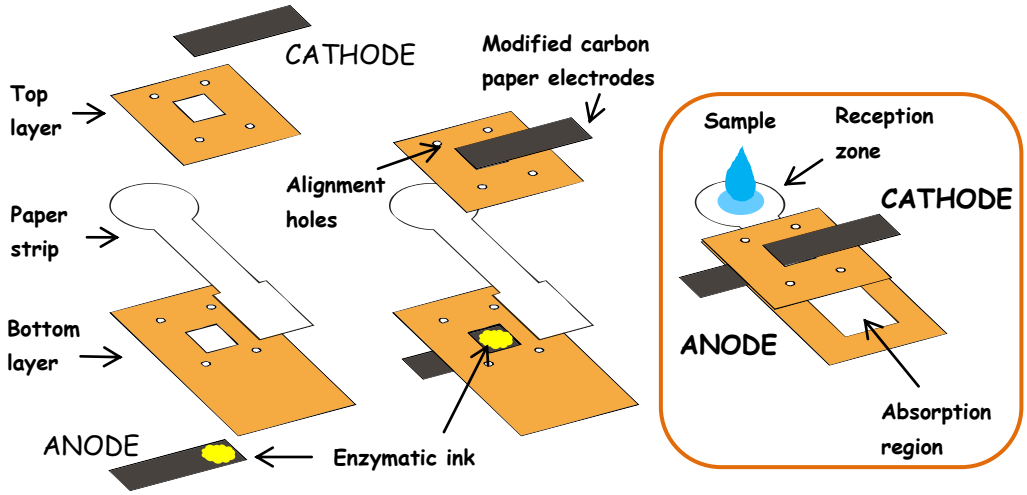

Figure 5.11 Depiction of the main core of the microfluidic paper fuel cell.

The above components were aligned and assembled with a four-pin PMMA holder that is shown in figure 5.12 (a). The external connections, see figure 5.12 (b), were made using a piece of copper foil covering the ends of the carbon electrodes. However, this last configuration was very fragile because of the pressure applied to the carbon paper electrodes by the external electrical connections. In this sense, the packaging of the fuel cell becomes necessary because (i) it prevents the evaporation of liquid when working with small sample volumes and (ii) it makes the device more robust and easier to handle because it provides an extra physical support to the system.

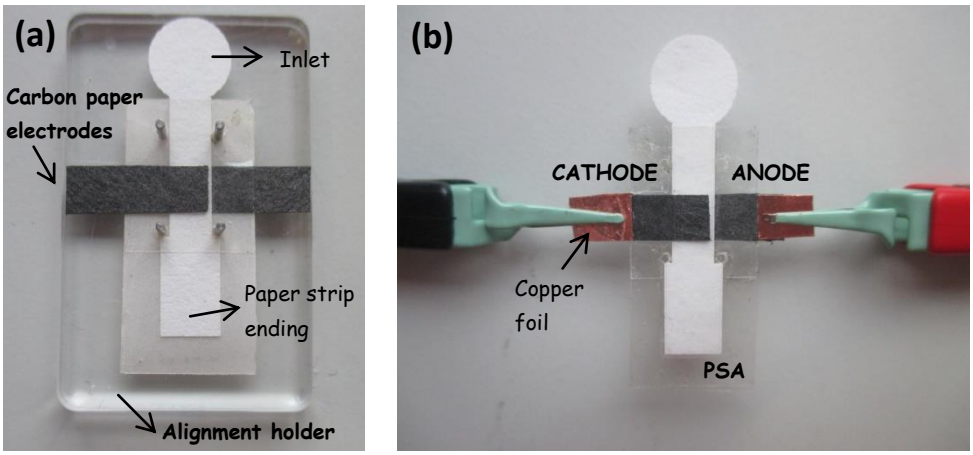

Figure 5.12 Photographs of the central body of the paper-based microfluidic fuel cell (a) after the alignment step with

the four pin holder and (b) with the external electrical connections.

5.3.2 Fuel cell packaging

The fuel cell packaging was carried out incorporating multiple layers of laminated adhesive plastic materials to the previous assembled system. Each layer of 25 x 35 mm^2 presents different functions and characteristics. A representation of this paper fuel cell is displayed in figure 5.13 (a) and for convenience a detailed description of the device construction is given below.

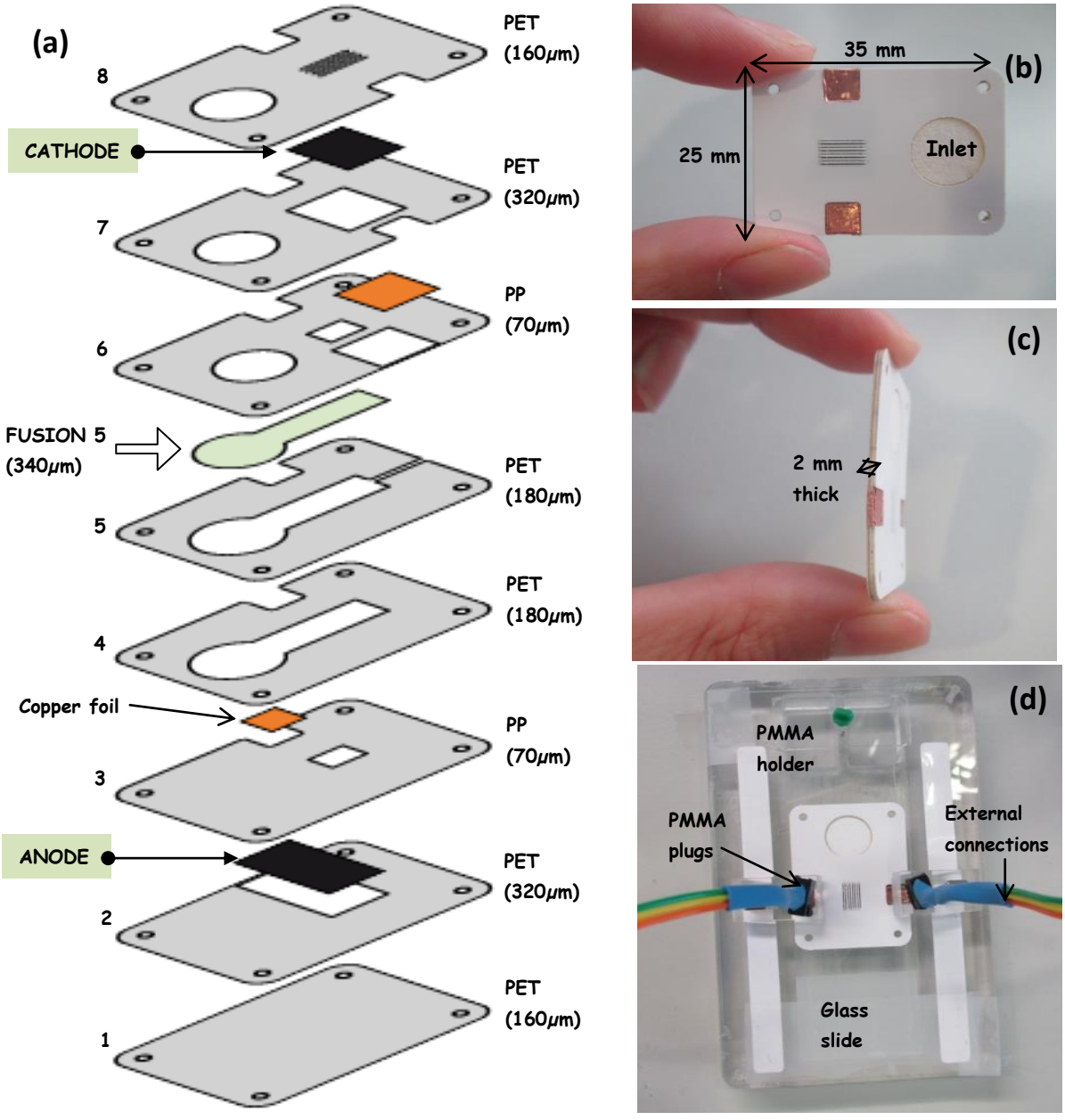

Figure 5.13 (a) Scheme of the individual layers forming the packaged microfluidic paper-based device. Numbers from 1 to 8 indicate the layer number whereas figures in μm account for the layer thickness. (b) Front-view of the sealed paper

device. (c) Side-view of the paper fuel cell. (d) External connections using a PMMA holder.

From bottom to top: layer 1 was fabricated to supply primary backing to the fuel cell. Then, the carbon paper anode was carefully fit in layer 2. Next sheet (layer 3) with an open window of 5 x 4 mm^2 was designed to define the active surface of the bioanode. Layers 4 and 5 were conceived to house the paper strip with 2.5 cm of length and final surface of 5.4 cm^2. Layer 6 with an aperture of 5 x 4 mm^2 defined the active area of the biocathode. In this layer a 8 x 8 mm^2 copper foil for the electrical connections was placed. The cathode, with dimensions of 8 x 10 mm^2, was enclosed in the slot of layer 7 that at the same time was in contact with the copper foil attached to the previous layer. In the case of using the *1 Chr* paper substrate (instead of *Fusion 5*) the layer 4 was eliminated because the thickness of this material (180 µm) allow to hold it only using layer 5.

All these components were aligned with an external PMMA holder for finally obtaining the device presented in figure 5.13 (b) with a thickness of around 2 mm, see figure 5.13 (c). At the end, the electrical connections, with PMMA plugs, allowed to fix the fuel cell during its characterization.

5.4 COMPLETE FUEL CELL OPERATION

5.4.1 Fuel cell performance at different glucose concentrations and two paper materials

The paper fuel cells developed in this chapter are intended to be fed using biological samples, which limits significantly the available volume of fuel. It is clear that this depends strongly on the nature of the sample to be used; a blood drop coming from a finger prick ranges from 0.3 µl to 20 µl whereas urine or saliva yields samples in the range of milliliters. The present chapter aims to explore the energy available in a small volume of blood, and therefore sample volumes have been restricted to 155 µl at most.

First of all*, Fusion 5* and *1 Chr* paper materials (from Whatman®) were studied in terms of their liquid absortion. Two drops of 20 µl of aqueous blue dye were deposited on the surface of these materials and the wetted area was measured. Figure 5.14 shows a picture of the experiment. The spot reached a surface of 0.7 cm^2 in *Fusion 5* while at *1 Chr* the covered surface was approximately 3 cm^2. This difference is mainly due to the different thickness of 1 *Chr* and *Fusion 5* papers (180 µm and 370 µm, respectively) and difference is porosity of both materials.

Once the absorbance of both materials was evaluated, it was possible to set the sample volume required to fill the paper fuel cells. Taking into account that the surface of the paper substrate inside the fuel cell was 5.4 cm^2 (fuel cell core) a sample volume of approximately 155 µl is required to run the cell if *Fusion 5* is used as a core material and a volume of 35 µl if it is implemented with

a *1 Chr* paper strip. After this, carbon paper electrodes modified with the appropriate enzymatic solution were assembled in the microfluidic paper device.

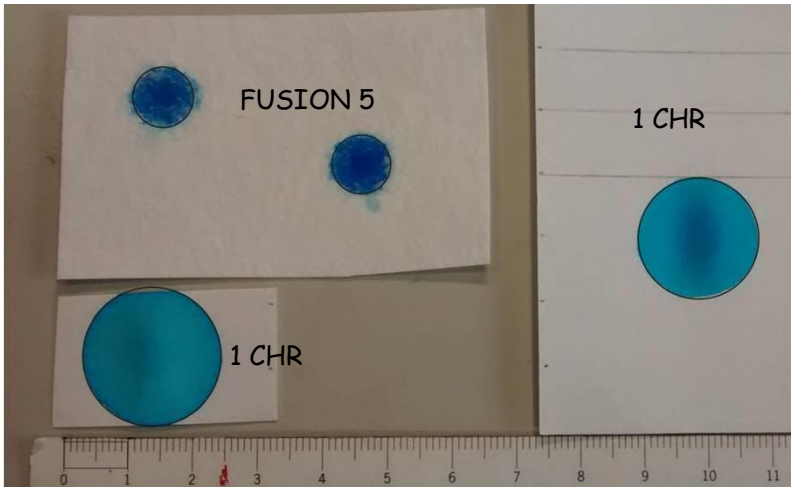

Figure 5.14 Images of the surface achieved by 20 µl of colored ink in *1 Chr* and *Fusion 5* paper materials.

The sample for the experiment consisted of 100 mM buffer phosphate with different amounts of glucose, ranging from 2.5 to 100 mM (high glucose concentrations were selected for comparison with previous Chapters). Tests were performed once the sample filled the strip, therefore the fluid was not moving during experiments. After each measurement, the tested sample was removed from the paper by adding the new concentration at the inlet of the device and absorbing the previous one by applying and absorbent pad at the end. Under these conditions the polarization and power curves were measured and represented in figure 5.15. First, the open circuit potential was allowed to stabilize at each glucose concentration for at least 300 seconds. Then, a slow I-V scan (1 mV s^{-1}) was performed.

As it can be seen, *1 Chr* paper device displayed slightly better performance as compared with the *Fusion 5* paper system. The OCP was quite stable and only variations within ±0.05 V were observed. On the other hand, in terms of maximum current and power density, *1 Chr* fuel cell showed 275 µA cm^2 and 97 µW cm^2 at 0.38 V. However, *Fusion 5* fuel cell, exhibited 250 µA cm^2 and 89 µW cm^2 at 0.38 V.

This behavior was expected since electrolyte resistance is proportional to the separation between the electrodes. In the present case, $R_{electrolyte}$(Fusion 5) >$R_{electrolyte}$(1Chr) so when using 1Chr paper, the fuel cell performance benefits from smaller electrode-to-electrode spacing. The ohmic losses of the system can be estimated from the linear region of the I-V curves (where they predominate over other losses like activation or concentration). A linear fit of this region of I-V curve obtained at 50 mM glucose obtaining slopes of 0.91 Ω cm^2 and 1.20 Ω cm^2 for the *1 Chr* and the *Fusion 5* paper-based fuel cells, respectively. It can be seen that Fusion 5 resistance is a 30% higher than 1Chr. However, the predicted results state that the ohmic resistance in *Fusion 5* material should be

twice that for the *1 Chr* as the thickness of the *Fusion 5* is double the thickness of *1 Chr*. This difference can be attributed to differences coming from manual electrode manufacturing, particularly from the drop coating of the enzyme solutions over the electrodes.

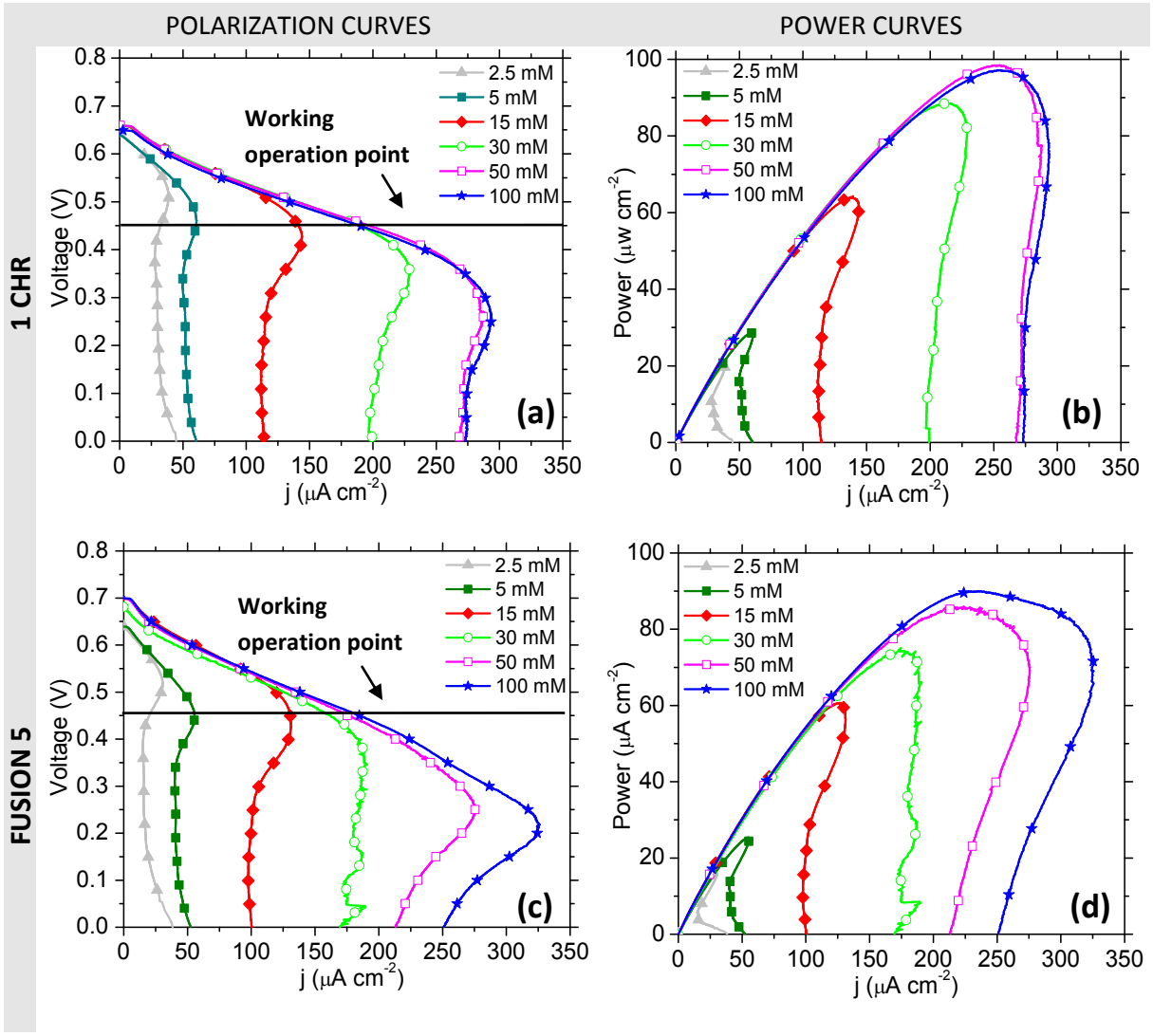

Figure 5.15 Polarization and power curves of the microfluidic paper-based fuel cell at different glucose concentrations ranging from 2.5 mM glucose to 100 mM glucose using *1 Chr* and *Fusion 5* paper materials.

5.4.2 Chronoamperometric curves

The energy that can be extracted from the paper fuel cell at a given glucose concentration can be obtained by recording the current delivered by the fuel cell when its potential is fixed at a certain value [29]. The potential should be selected as near as possible to the P_{max} (P-I curves) but before the start of the fuel cell concentration losses region (in the polarization curves). The working

potential for the experiments was chosen according to the polarization curve of figure 5.15 (a) and (c) at the lowest glucose concentration (2.5 mM). Amperometric measurements where thus performed at 0.45 V.

1 Chr and the *Fusion 5* fuel cells were fed with a fixed volume of buffer with glucose and polarized at 0.45 V. Figure 5.16 shows the output current measured over 300 seconds of experiment for glucose concentrations ranging between 2.5 and 30 mM. As it can be seen, the curves started with a large current attributed an initial fast consumption of reagents followed by a decay due to the appearance of the corresponding diffusional layer that is proportional to the glucose concentration of the sample.

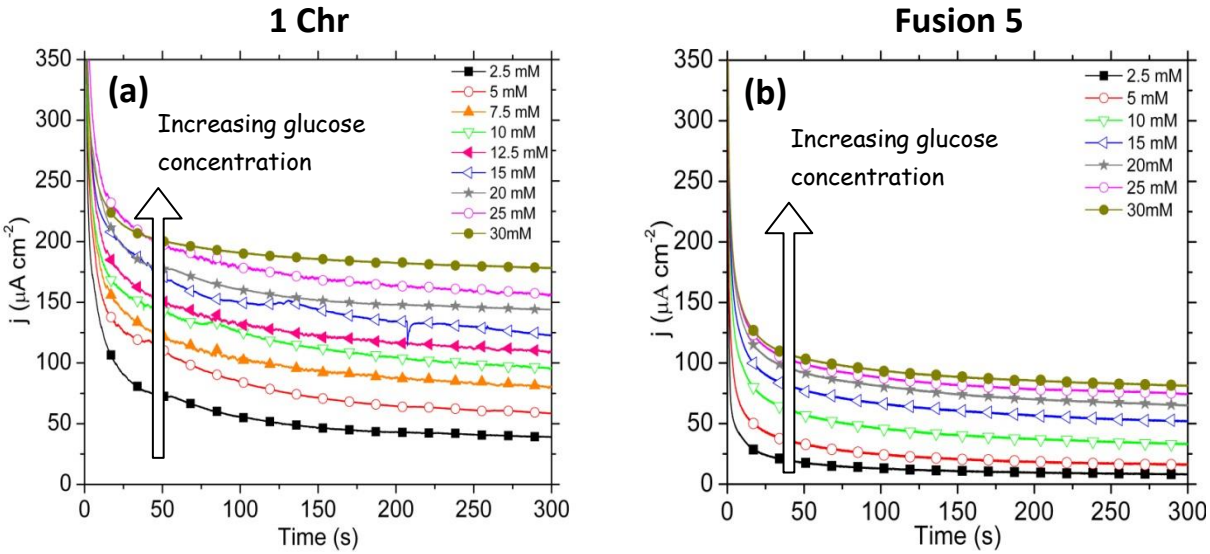

Figure 5.16 Representatives chronoamperometric curves of enzymatic paper-based fuel cell working with a fixed volume of sample using (a) *1 Chr* substrate or (b) *Fusion 5* paper substrate.

The accumulated energy obtained from each glucose concentration can be determined by integrating the area under the curves and following equation 5.8.

$$E = V \int_0^{t_m} j(t) \cdot dt \qquad \textbf{(5.8)}$$

The accumulated energy was computed for the first 120 seconds of measurement. The obtained values were plotted as a function of the glucose concentration in figure 5.17. The energy obtained from the samples varied from 3 to 17.5 mJ cm^2 with a linear range comprised from 2.5 mM to approximately 15 mM glucose (which covers the typical glucose concentrations present in blood). From here, the response reached a plateau probably due to saturation of the GOx enzyme response at the anode. In this region, the enzyme is working at its maximum rate. The error bars correspond to the same experiment repeated with four *Fusion 5* and three *1 Chr* fuel cells. The

variability of data was attributed to the low repeatability of the catalytic-solution deposition process over the electrodes.

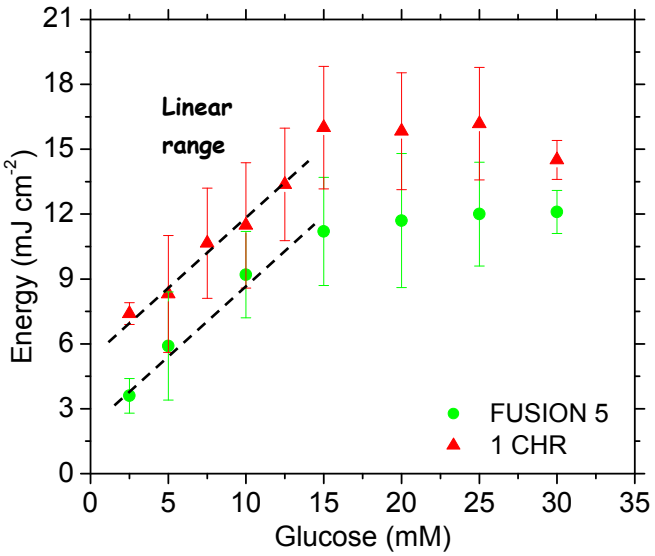

Figure 5.17 Energy accumulated during 120 seconds of experiment in fuel cells made of *Fusion 5* and *1 Chr* paper materials. The standard deviations correspond to four fuel cells made of Fusion 5 and two fuel cells made of 1 Chr.

SUMMARY AND CONCLUSIONS

In this chapter an enzymatic paper-based biofuel cell highly applicable to the development of low cost, flexible and ubiquitous energy devices was presented. The new combination of enzymes and mediators allowed the fuel cell to be operated with one stream solution at neutral pH.

The microfluidic system was composed by several layers of laminate adhesive plastic materials and at the end with a very compact device of 35 mm x 25 mm and 2 mm thick was obtained. The electrodes consisted of carbon paper material with a mixture of FAD-GDH enzyme and the redox polymer Os(dmobpy)PVI for the anode and BOx enzyme and the mediator Os(bpy)PVI at the cathode side.

Graphite rods were used to characterize the catalytic solutions prior its incorporation in the paper fuel cell. For the anode, the mediator gave a redox potential of -1 mV (vs Ag/AgCl) and a very high catalytic current of around 1.8 mA cm^{-2} when it was combined with 100 mM glucose. The electrode was evaluated for glucose concentrations ranging from 5 mM to 100 mM displaying a linear behavior at a physiological concentration range of glucose. This suggests that the bioanode can be used as biosensor for the quantitative detection of sugar in aqueous solutions including body fluids such as blood.

The mediator utilized at the cathode exhibited a redox potential of 240 mV (vs Ag/AgCl) and although the enzyme BOx catalyzed the reduction of oxygen, the combination of mediator and enzyme allowed to increase the resulting current density. Moreover, the performance of this biocathode was enhanced by turning it in an air-breathing electrode.

The bioanode and the biocathode were combined together in the paper-based fuel cell and the performance of the device was studied for *1 Chr* and *Fusion 5* paper materials. Similar behaviors in terms of polarization and power curves were obtained for both substrates. However, the *1 Chr* fuel cell needed less sample volume to function and yielded approximately a 10% higher power than F5. Then, the energy generated from the paper fuel cells was evaluated at a fixed potential (of 0.45 V) and different concentrations of glucose, displaying a linear range for concentrations up to 15mM. However, the values of energy extracted from different devices presented high dispersion. This dispersion is probably due to the low repeatability in the manual process of electrode deposition. The amplitude of the error bars could be diminished by the use of a more reliable process like inkjet printing.

In conclusion, it has been demonstrated that it is possible to develop a simple, fast and low cost fuel cell ready to power devices requiring small energy demands. Moreover, unlike devices in the literature, the energy delivered by the fuel cell represents net energy given that no external pumping was needed to move the sample through the paper.

The ability to work at neutral pH and with low volume of sample opens the possibility to work with physiological samples. Furthermore, the linear range that the fuel cell presented in terms of output energy allow for the quantification of glucose in blood within the range of medical interest (2.5-15 mM). This opens the possibility of envisaging a self-powered glucose sensor, which would have an enormous impact of the in-vitro devices domain.

Besides, the fuel cell has also shown good performance at high fuel concentrations (up to 100 mM). In order to assess the powering of small electronic devices, the recorded power output of one fuel cell can be enhanced by stacking several units in parallel.

Finally, despite further efforts have yet to be done to approach this biofuel cell to real-life scenarios as today, they do not offer enough durability. Regarding this, further work will have to be done in order to improve the enzymatic electrodes by introducing multi-enzyme systems and stabilization techniques [16].

REFERENCES

1. Falk, M., Z. Blum, and S. Shleev, *Direct electron transfer based enzymatic fuel cells.* Electrochimica Acta, 2012. **82**: p. 191-202.
2. Bullen, R.A., T.C. Arnot, J.B. Lakeman, and F.C. Walsh, *Biofuel cells and their development.* Biosensors and Bioelectronics, 2006. **21**(11): p. 2015-2045.

3. Jurysta, C., N. Bulur, B. Oguzhan, I. Satman, T.M. Yilmaz, W.J. Malaisse, and A. Sener, *Salivary glucose concentration and excretion in normal and diabetic subjects.* Journal of biomedicine & biotechnology, 2009. **2009**: p. 430426-430426.
4. Adler, A.J., *Biochemistry of the Eye.* Plenum Press, 1991. **253**(5024): p. 1153-1153.
5. McPherson, R.A. and M.R. Pincus, *Henry's clinical diagnosis and management by laboratory methods*. 2011: Elsevier Health Sciences.
6. Falk, M., D. Pankratov, L. Lindh, T. Arnebrant, and S. Shleev, *Miniature Direct Electron Transfer Based Enzymatic Fuel Cell Operating in Human Sweat and Saliva.* Fuel Cells, 2014. **14**(6): p. 1050-1056.
7. Falk, M., C.W. Narváez Villarrubia, S. Babanova, P. Atanassov, and S. Shleev, *Biofuel Cells for Biomedical Applications: Colonizing the Animal Kingdom.* ChemPhysChem, 2013. **14**(10): p. 2045-2058.
8. Yetisen, A.K., M.S. Akram, and C.R. Lowe, *Paper-based microfluidic point-of-care diagnostic devices.* Lab on a Chip, 2013. **13**(12): p. 2210-2251.
9. MacAodha, D., P.Ó. Conghaile, B. Egan, P. Kavanagh, and D. Leech, *Membraneless Glucose/Oxygen Enzymatic Fuel Cells Using Redox Hydrogel Films Containing Carbon Nanotubes.* ChemPhysChem, 2013. **14**(10): p. 2302-2307.
10. Kavanagh, P. and D. Leech, *Mediated electron transfer in glucose oxidising enzyme electrodes for application to biofuel cells: recent progress and perspectives.* Physical Chemistry Chemical Physics, 2013. **15**(14): p. 4859-4869.
11. Cardoso, F., S.A. Neto, L. Crepaldi, S. Nikolaou, V. Barros, and A. De Andrade, *Biocathodes for Enzymatic Biofuel Cells Using Laccase and Different Redox Mediators Entrapped in Polypyrrole Matrix.* Journal of the Electrochemical Society, 2014. **161**(4): p. F445-F450.
12. Conghaile, P.Ó., S. Kamireddy, D. MacAodha, P. Kavanagh, and D. Leech, *Mediated glucose enzyme electrodes by cross-linking films of osmium redox complexes and glucose oxidase on electrodes.* Analytical and Bioanalytical Chemistry, 2013. **405**(11): p. 3807-3812.
13. Ju, H.X. and D. Leech, *Os(bpy)(2)(PVI)(10)Cl Cl polymer-modified carbon fiber electrodes for the electrocatalytic oxidation of NADH.* Analytica Chimica Acta, 1997. **345**(1-3): p. 51-58.
14. Forster, R.J. and J.G. Vos, *Synthesis, characterization, and properties of a series of osmium- and ruthenium-containing metallopolymers.* Macromolecules, 1990. **23**(20): p. 4372-4377.
15. Gallaway, J.W. and S.A. Calabrese Barton, *Kinetics of redox polymer-mediated enzyme electrodes.* Journal of the American Chemical Society, 2008. **130**(26): p. 8527-8536.
16. Sakai, H., T. Nakagawa, Y. Tokita, T. Hatazawa, T. Ikeda, S. Tsujimura, and K. Kano, *A high-power glucose/oxygen biofuel cell operating under quiescent conditions.* Energy & Environmental Science, 2009. **2**(1): p. 133-138.
17. Rengaraj, S., V. Mani, P. Kavanagh, J. Rusling, and D. Leech, *A membrane-less enzymatic fuel cell with layer-by-layer assembly of redox polymer and enzyme over graphite electrodes.* Chemical Communications, 2011. **47**(43): p. 11861-11863.
18. Sekretaryova, A., *Novel reagentless electrodes for biosensing*. 2014.
19. Taylor, C., G. Kenausis, I. Katakis, and A. Heller, *"Wiring" of glucose oxidase within a hydrogel made with polyvinyl imidazole complexed with [(Os-4, 4'-dimethoxy-2, 2'-bipyridine) Cl]+/2+ 1.* Journal of Electroanalytical Chemistry, 1995. **396**(1): p. 511-515.
20. Mano, N. and A. Heller, *A miniature membraneless biofuel cell operating at 0.36 V under physiological conditions.* Journal of the Electrochemical Society, 2003. **150**(8): p. A1136-A1138.

21. Moehlenbrock, M.J., M.T. Meredith, and S.D. Minteer, *Bioelectrocatalytic oxidation of glucose in CNT impregnated hydrogels: advantages of synthetic enzymatic metabolon formation.* ACS Catalysis, 2011. **2**(1): p. 17-25.
22. *Metrohm Autolab B.V*. Available from: http://www.ecochemie.nl/download/Applicationnotes/Autolab_Application_Note_EC08.pdf.
23. MacAodha, D., P. Ó Conghaile, B. Egan, P. Kavanagh, C. Sygmund, R. Ludwig, and D. Leech, *Comparison of Glucose Oxidation by Crosslinked Redox Polymer Enzyme Electrodes Containing Carbon Nanotubes and a Range of Glucose Oxidising Enzymes.* Electroanalysis, 2013. **25**(1): p. 94-100.
24. MacAodha, D., M.L. Ferrer, P.Ó. Conghaile, P. Kavanagh, and D. Leech, *Crosslinked redox polymer enzyme electrodes containing carbon nanotubes for high and stable glucose oxidation current.* Physical Chemistry Chemical Physics, 2012. **14**(42): p. 14667-14672.
25. Bott, A.W., *Applications of "Wired" enzyme electrodes.* Current Separations, 2004. **21**(1).
26. Forster, R.J. and J.G. Vos, *Ionic interaction and charge-transport properties of metallopolymer films on electrodes.* Langmuir, 1994. **10**(11): p. 4330-4338.
27. Zafar, M.N., N. Beden, D. Leech, C. Sygmund, R. Ludwig, and L. Gorton, *Characterization of different FAD-dependent glucose dehydrogenases for possible use in glucose-based biosensors and biofuel cells.* Analytical and bioanalytical chemistry, 2012. **402**(6): p. 2069-2077.
28. Nie, Z., F. Deiss, X. Liu, O. Akbulut, and G.M. Whitesides, *Integration of paper-based microfluidic devices with commercial electrochemical readers.* Lab on a Chip, 2010. **10**(22): p. 3163-3169.
29. Nie, Z., C.A. Nijhuis, J. Gong, X. Chen, A. Kumachev, A.W. Martinez, M. Narovlyansky, and G.M. Whitesides, *Electrochemical sensing in paper-based microfluidic devices.* Lab on a Chip, 2010. **10**(4): p. 477-483.
30. Dungchai, W., O. Chailapakul, and C.S. Henry, *Electrochemical detection for paper-based microfluidics.* Analytical Chemistry, 2009. **81**(14): p. 5821-5826.
31. Jenkins, P., S. Tuurala, A. Vaari, M. Valkiainen, M. Smolander, and D. Leech, *A mediated glucose/oxygen enzymatic fuel cell based on printed carbon inks containing aldose dehydrogenase and laccase as anode and cathode.* Enzyme and Microbial Technology, 2012. **50**(3): p. 181-187.
32. Compton, R.G. and C.E. Banks, *Understanding Voltammetry*. 2011: Imperial College Press.
33. Barrière, F., P. Kavanagh, and D. Leech, *A laccase–glucose oxidase biofuel cell prototype operating in a physiological buffer.* Electrochimica Acta, 2006. **51**(24): p. 5187-5192.
34. Li, D.-a., T. Okajima, L. Mao, and T. Ohsaka, *Bioelectrocatalytic Oxygen Reduction Reaction by Bilirubin Oxidase Adsorbed on Glassy Carbon and Edge-Plane Pyrolytic Graphite Electrodes: Effect of Redox Mediators.* Int. J. Electrochem. Sci, 2014. **9**: p. 1390-1398.
35. Jayashree, R.S., L. Gancs, E.R. Choban, A. Primak, D. Natarajan, L.J. Markoski, and P.J. Kenis, *Air-breathing laminar flow-based microfluidic fuel cell.* Journal of the American Chemical Society, 2005. **127**(48): p. 16758-16759.
36. Denny, M.W., *Air and water: the biology and physics of life's media*. 1993: Princeton University Press.
37. Shaegh, S.A.M., N.-T. Nguyen, and S.H. Chan, *An air-breathing microfluidic formic acid fuel cell with a porous planar anode: experimental and numerical investigations.* Journal of Micromechanics and Microengineering, 2010. **20**(10): p. 105008.

38. Spicar-Mihalic, P., B. Toley, J. Houghtaling, T. Liang, P. Yager, and E. Fu, *CO2 laser cutting and ablative etching for the fabrication of paper-based devices.* Journal of Micromechanics and Microengineering, 2013. **23**(6).
39. Yuen, P.K. and V.N. Goral, *Low-cost rapid prototyping of flexible microfluidic devices using a desktop digital craft cutter.* Lab on a Chip, 2010. **10**(3): p. 384-387.
40. *Epilog Laser CO2 Laser Systems*. 2015; Available from: https://www.epiloglaser.com/.
41. Cate, D.M., J.A. Adkins, J. Mettakoonpitak, and C.S. Henry, *Recent Developments in Paper-Based Microfluidic Devices.* Analytical Chemistry, 2014. **87**(1): p. 19-41.

Conclusions

The thesis presents the development of different microfluidic fuel cells architectures based on enzymes that use glucose as fuel and oxygen as reductant agent. The work includes the design, fabrication and characterization of the different approaches starting with an initial microfluidic system that has been evolved toward a compact an efficient microfluidic device. This work starts with fuel cells using external pressure systems for the supply of liquids. This one leads to paper-based devices that utilize the capillary action of paper materials to cause the movement of fluids. The particular contributions to this work are presented in the following lines.

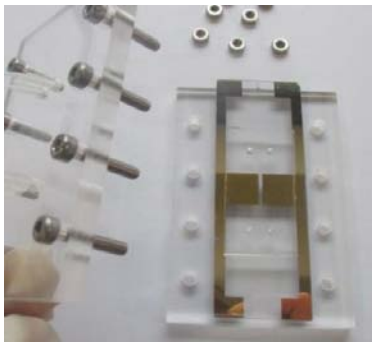

The first approximation of a microfluidic prototype device working with enzymes was achieved. The device was simple and fast to fabricate and made possible the first electrochemical measurements with enzymes. The system displayed PDMS microchannels and gold electrodes over a glass slide and the biocatalysts were introduced in solution using a syringe pump (obtaining a co-laminar flow). This device was then used as a basis for the consequent development toward an integrated microfluidic system.

However, because biocatalysts were constantly flowing through the channel of the fuel cell this device loses viability to be a commercial application. Therefore, the best way to decrease the cost of power generation is the immobilization of the catalytic solutions over the electrodes, being the fuel (glucose) and oxygen the only components continuously supplied to the fuel cell. This approximation was addressed for the fabrication of the next device.

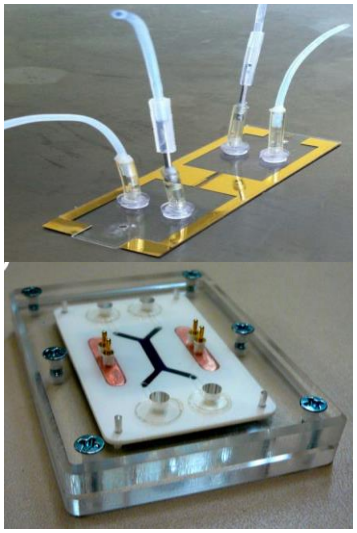

Two fuel cells made on plastic laminated materials were designed and fabricated using a cutter plotter. The use of these plastic materials turned the system light, non-rigid and compatible with large-scale manufacturing. Therefore these devices were more suitable for product development than fuel cell systems based on traditional PDMS and glass. The enzymatic-solutions were immobilized at the electrode surfaces for a better use of the catalytic solutions. The first fuel cell fabricated used gold electrodes. The second one utilized pyrolyzed photoresist film electrodes that for the first time were introduced as a suitable electrode material for the development of enzyme-based microfluidic fuel cells.

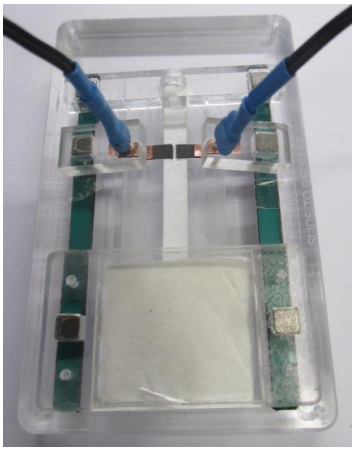

A cost-effective enzymatic paper-based microfluidic fuel cell was developed and fabricated. A very simplified device regarding the systems presented up to here. The possibility to operate a microfluidic fuel cell without the implementation of pumps was achieved yielding approximately the same power output that the plastic pumped micro fuel cell fabricated previously in this thesis. Moreover, with the objective to approximate the device to lateral flow test formats, the electrolyte pHs were adapted to run the fuel cell using a single solution. Finally, it was demonstrated that this paper-based fuel cell can convert ubiquitous glucose (using the sugar from commercial drinks) into electrical energy and this energy could be used to power real devices.

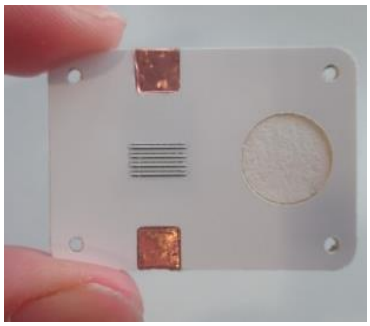

An enzymatic paper-based biofuel cell highly applicable to the development of low cost, flexible and ubiquitous energy devices was fabricated. A new combination of catalytic solutions allowed to operate the device using one stream solution at neutral pH opening the possibility to run the system using physiological fluids (blood, urine, serum or plasma). Moreover, due to its packed format it was possible to work with a very limited sample volume.

The output energy of the system was studied for glucose concentrations in the range of blood. The linear range that the fuel cell presented in terms of output energy allowed for the quantification of glucose in blood within the range of medical interest (2.5-15 mM). Therefore, the system can be used at in-vivo applications at physiological conditions as well as in self-powered glucose sensor with an enormous impact in in-vitro applications. Moreover, the energy delivered by the fuel cell represents net energy given that no external pumping was needed to move the sample through

the paper. In conclusion, it has been demonstrated that it is possible to develop a simple, fast and low cost fuel cell ready to power devices requiring small energy demands.

This work represents a significant advance toward the miniaturization of enzymatic microfluidic fuel cells. However, as a result of the enzyme limited lifetimes, the application of these devices is still restricted and further efforts have yet to be done to approach these biofuel cells to real-life scenarios.

List of acronyms and abbreviations

µDMFC	Micro Direct Methanol Fuel Cell
ABTS	2,2'-azino-bis(3-ethylbenzothiazoline-6-sulphonic acid)
AFC	Alkaline Fuel Cells
BFC	Biological Fuel Fells
BoP	Balance of Plant
BOx	Bilirubin Oxidase
CHP	Combined Heat and Power
CMOS	Complementary Metal Oxide Semiconductor
CNT	Carbon Nanotube
COP	Cyclic Olefin Polymer
CV	Cyclic Voltammetry
DET	Direct Electron Transfer
DMFC	Direct Methanol Fuel Cell
EFC	Enzymatic Fuel Cell
EGDGE	Ethylene Glycol Diglycidyl Ether
FAD	Flavin Adenine Dinucleotide (oxidized form)
$FADH_2$	Flavin Adenine Dinucleotide (reduced form)
FeMeOH	Ferrocenemethanol
GC	Glassy Carbon
GDH	Glucose Deyhrogenase
GOx	Glucose Oxidase
KB	Ketjen Black
KOH	potassium hydroxide
LoC	Lab-on-a-Chip
LPEI	Linear Poly(ethylenimine)
MCF	Microbial Fuel Cell
MCFC	Molten Carbonate Fuel Cell
MEMS	Micro Electro-Mechanical System

MET	Mediated Electron Transfer
MWCNT	Multi Wall Carbon Nanotube
NAD	Nicotinamide Adenine Dinucleotide (oxidized form)
$NADH_2$	Nicotinamide Adenine Dinucleotide (reduced form)
NADP	Nicotinamide Adenine Dinucleotide Phosphate,
OCP	Open Circuit Potential
OCV	Open Circuit Voltage
PAFC	Phosphoric Acid Fuel Cell
PDMS	Polydimethylsiloxane
PEI	Poly(ethylenimine)
PEMFC	Polymer Electrolyte Membrane Fuel Cell
PET	Polyethylene terephthalate
PMMA	Polymethyl Methacrylate
PP	Polypropylene
PPF	Pyrolyzed Photoresist Film
PQQ	Pyrroloquinoline Quinone
PSA	Pressure-Sensitive Adhesive
PTFE	Polytetrafluoroethylene
PVI	Poly-Vynilmidazole
RT	Room Temperature
RTP	Rapid Thermal Process
SCE	Saturated Calomel Electrode
SOFC	Solid Oxide Fuel Cell
SWCNT	Single Wall Carbon Nanotube
TBAB	Tetrabutylammonium bromide
TPB	Triple Phase Boundary
UV	Ultaviolet

Resumen

Esta tesis presenta el desarrollo y la fabricación de pilas de combustibles microfluídicas para aplicaciones portátiles de baja potencia. En concreto, pilas biológicas que utilizan las enzimas en la degradación de la glucosa. El trabajo está dividido en dos secciones dependiendo de si los dispositivos fabricados son activos, es decir, los reactivos son suministrados a la micropila por bombeo (Capítulo 2 y 3). O si por el contrario los reactivos fluyen sin necesidad de mecanismos externos los dispositivos serán pasivos (Capítulo 4 y 5).

En el primer capítulo de la tesis se ha llevado a cabo la primera aproximación en el desarrollo de micro pilas de combustible glucosa/O_2 con el objetivo de hacer posible las primeras medidas electroquímicas con enzimas. La pila microfluídica fue construida sobre un sustrato de vidrio en el cual se grabaron electrodos de oro mediante técnicas de microfabricación. Por otro lado, se utilizó fotolitografía suave para la fabricación de los canales (con forma de Y) en PDMS. Esta forma de canal permitió fluir dos soluciones en paralelo usando una bomba de jeringa. Como primera aproximación, las enzimas se encontraban fluyendo de manera continua a través del canal. Eso provocaba experimentos caros y dificultaba su posible aplicación portátil. De este modo, el siguiente aspecto en abordarse fue la inmovilización de los biocatalizadores sobre los electrodos de la micro pila.

El Capítulo 2 presenta la fabricación de una pila de combustible que posee los biocatalizadores inmovilizados en la superficie de los electrodos lo cual hace que los biocatalizores sean aprovechados más eficientemente que en la anterior pila. Los electrodos se han fabricado utilizando resina pirolizada y se han usado por primera vez con éxito en pilas microfluídicas enzimáticas de este tipo. La pila está compuesta por diferentes capas de material plástico laminado que han sido cortadas usando un plotter de corte. Esto hace que la fabricación del dispositivo sea rápida, barata y compatible con la manufacturación a gran escala. El canal microfluídico se ha definido también sobre este tipo de material plástico, evitando el largo proceso litográfico relacionado con el PDMS. Por otro lado, el canal (en forma de Y) permite optimizar la potencia que obtenemos de la pila cuando bombeamos dos soluciones diferentes. Por otro lado, el dispositivo necesita ser simplificado para finalmente obtener una fuente de energía portátil. Con este objetivo se abordó la siguiente fase de la tesis.

El Capítulo 4 describe la fabricación de una pila microfluídica implementada utilizando sustratos de papel a través de los cuales fluyen los reactivos (de manera pasiva) por efecto capilar. Los componentes de la pila se cortaron utilizando un plotter de corte, lo que permitía fabricar dispositivos con mucha rapidez. Se probó el buen funcionamiento de una pila de combustible de papel y enzimática obteniendo valores de potencia similares a los presentados en el Capítulo 3 (donde las soluciones eran bombeadas). A partir de aquí el trabajo se centró en aproximar la pila de papel a la simplicidad de los test de flujo lateral. Así que la micro pila fue adaptada y operada con éxito usando una única solución, generando energía de una bebida comercial.

El Capítulo 5 presenta una micropila de combustible fabricada en papel mucho más sofisticada y pequeña que la del capítulo anterior. Se probó satisfactoriamente una nueva combinación de biocatalizadores que permitió trabajar utilizando muestras a pH neutro. Además, el tamaño compacto del sistema abrió la posibilidad de operar la pila de combustible con fluidos fisiológicos como por ejemplo la sangre. Finalmente, se ha demostrado que es posible tener una pila preparada para alimentar dispositivos que requieran poca demanda de energía. Sin embargo, todavía se deben hacer esfuerzos para acercar esta pila a un mundo real, debido principalmente a que el tiempo de vida de las enzimas es todavía limitado.